2004

Gas Phase Studies of Molecular Clusters Containing Metal Cations, and the Ion Mobility of Styrene Oligomers

Edreese Housni Alsharaeh
Virginia Commonwealth University

Gas Phase Studies of Molecular Clusters Containing Metal Cations, and the Ion Mobility of Styrene Oligomers

A Dissertation submitted in partial fulfillment of the requirements for the degree of Doctor of Philosophy at Virginia Commonwealth University

by

EDREESE HOUSNI ALSHARAEH
B.Sc., Jordan University of Science and Technology, Jordan, 1993
M.Sc., Tennessee State University, USA, 1997

Director: M. SAMY EL-SHALL
PROFESSOR, DEPARTMENT OF CHEMISTRY

Virginia Commonwealth University
Richmond, Virginia
December 2004

Acknowledgement

I would like to dedicate this dissertation to my family: my parents Housni and Tamam Alsharaeh, my brothers and sisters. I like to thank my parents and my brother Dr. Saleh Alsharaeh for their endless support.

I would like to express my earnest gratitude to my adviser Dr. M. Samy El-Shall who encouraged and offered me this opportunity to pursue Ph.D. and his efforts to provide me with guidance. I also have to thank him for his support, criticism, advice and those laborious hours in correcting my grammatical and spelling errors. I also like to thank Dr. Michael Mautner, Dr. Yehia Ibrahim, Dr. Hatem Mahmoud, Dr. Victor Abdelsayed and Dr. Igor Germanenko for many discussions that benefited me greatly.

Table of Contents

Page

List of Tables

Page

List of Figures

Page

Abstract

Gas Phase Studies of Molecular Clusters Containing Metal Cations, and the Ion Mobility of Styrene Oligomers

By: Edreese Housni Alsharaeh, Ph.D.

A dissertation submitted in partial fulfillment of the requirements for the degree of Doctor of Philosophy at Virginia Commonwealth University.

Virginia Commonwealth University, 2004

Major Director: M. Samy El-Shall
Professor, Department of Chemistry

This study is divided into three parts. Part I deals with the mechanism of the self-initiated polymerization (or thermal polymerization) of styrene in the gas phase. In this work, we present the first direct evidence for the thermally self-initiated polymerization of styrene in the gas phase. Our approach is based on on-line analysis of the gas phase Oligomers by mass-selected ion mobility. The mobility measurements provide structural information on the ionized oligomers based on their collision cross-sections (Ω) which depend on the geometric shapes of the ions. Theoretical calculations of possible structural candidates of the Oligomers ions are then used to compute angle averaged Ω for comparison with the measured ones. The agreement between the measured and calculated

Ω of the candidate structures provides reliable assignments to the structures of the oligomers. Furthermore, collisional-induced dissociations of the mass-selected oligomer ions provide further support for the structures obtained from the mobility measurements. Our results indicate that the gas phase polymerization of styrene proceeds via essentially the same initiation mechanism (the Mayo mechanism) as in condensed phase polymerization. The structural evidence, the mechanism of formation and the observed fragmentation pathway of the growing dimers and trimers in the gas phase are presented

In Part II the solvation of a variety of metal cations by benzene clusters have been studied using laser vaporization, cluster beam and time-of-flight mass spectrometry techniques. In this work strong magic numbers were observed for clusters containing 10, 13 and 14 benzene molecules depending on the nature of the metal cation involved. The metal cations exhibiting preference solvation by 14 benzene molecules show a strong tendency to form sandwich structures with two benzene molecules. The interpretation of these results in view of the proposed structures and the growth patterns of the clusters are presented. In Part III, the work is focused on the investigation of the intracluster ion molecule reactions following the generation of Mg^+ within the polar clusters (water, methanol, ether and acetonitrile).

CHAPTER 1 Introduction

In the last twenty years, cluster science has become a rapidly expanding field of interdisciplinary science in both experimental and theoretical studies. Clusters are finite aggregates of atoms or molecules that are bound by forces which may be metallic, covalent, ionic, hydrogen-bonded or Van der Waals in character and may contain from a few to thousands of atoms or molecules. The study of molecular clusters has grown explosively since the early 1980's[1-8]. One of the driving forces in cluster science is the promise that studying gas phase species would provide insight into condensed phase behavior[2,3,8]. Studies so far indicate that chemical or physical properties may vary strongly with cluster size[3-6,8]. Eventually they show a gradual approach to the values that characterize the particular bulk material. This behavior, represented in Figure 1, displays the property, X (n), as a function of n, starting from a single molecule (n=1) and proceeding to the condensed phase value (n = ∞).[9] As shown, the irregular pattern observed for small clusters is responsible for the existence of "magic numbers" in the X(n) vs n plot. However for larger clusters, those specific effects vanish and $X(n)$ interpolates smoothly to the corresponding bulk value $X(\infty)$. The role of intermolecular forces in bringing about these changes in the material behavior is critical, and may provide valuable information regarding the behavior in complicated processes in the bulk materials.

Ion-molecule interactions play an important role in a diverse range of chemical and biochemical systems. Examples include substitution reactions, transmembrane ion transport, ion protein binding, upper atmospheric chemistry and nucleation phenomena[3-5]. The solvation of single ions with a selected number of neutral solvent molecules provides a unique opportunity to study intrinsic ion-neutral interactions, which can be studied in the absence of counter ions.

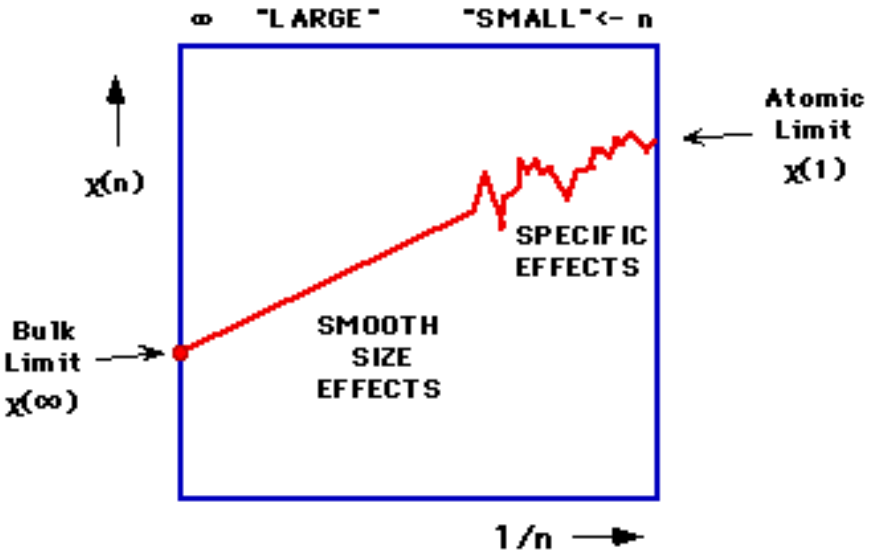

Figure 1: Physical or chemical properties as a function of the number of atoms or molecules.

The mechanism of the self-initiated polymerization (or thermal polymerization) of styrene in bulk liquids or solutions has been a challenging subject of research since the early days of polymer chemistry.[10-37] This is a phenomenon of not only fundamental and theoretical intrest but also of great commercial interest related to the industrial production of polystyrene and many of its secondary products.[38] The generally accepted mechanism for the spontaneous polymerization of styrene is known as the Mayo's mechanism[20-22]

Early studies to investigate the phenomenon in the gas phase were hampered by the condensation of the involatile polymer products and by the effects of surfaces and walls where heterogeneous polymerization took place[38]. However, the true gas phase, thermal polymerization of styrene was demonstrated more than fifteen years ago using an elegant approach based on nucleation from the vapor phase[13,29] In this approach, the thermally self-initiated oligomers growing in a supersaturated styrene vapor act as "condensation nuclei" for the formation of observable liquid drops (containing styrene oligomers and monomers) which can be detected by light scattering[14]. Due to the ultra sensitivity of the nucleation phenomena, one can in principle detect a single polymer molecule (oligomer) from the vapor phase.[5] Unfortunately, the nucleation approach provides no direct information on the initiation mechanism or on the structures of the growing oligomers. This information is still unavailable since it cannot be accurately obtained from the analysis of the condensed (deposited) polymer products from the gas phase.

The work described in this thesis is presented in six chapters. Chapter 2 deals with the experimental techniques and methods that include cluster beam generation, ionization methods, time of flight mass spectrometry (TOFMS) and Quadrupole Mass Selected-Ion Mobility-Quadrupole Mass Spectrometer (QMS-IM-QMS). Chapter 3 focuses on an experimental and theoretical study of the structures and the mechanism of the thermally self-initiated polymerization of styrene in the gas phase. Our approach is based on on-line analysis of the gas phase oligomers by mass-selected ion mobility.[39-41] The mobility of a gas phase ion is a measure of how fast it moves through a buffer gas under the effect of an electric field. The mobility measurements provide structural information on the ionized

oligomers based on their collision cross-sections (Ω) which depend totally on the geometric shapes of the ions.[42-44] Theoretical calculations are required for the average collision cross sections for the calculated geometry for comparison with the experimental one. Density Function Theory (DFT) [45] was employed to optimize the lowest energy structure of possible structural candidates of the styrene oligomer ions. These structures are based on the proposed styrene oligomerization mechanisms available in the literature. For example, the candidate structures represent structures proposed by Flory[36], complex formation proposed by Kirchner and Patat[35], cationic mechanisms[46], bimolecular formation of monoradicals[31], and finally Mayo's mechanism.[22] These structural candidates are then used to compute the angle averaged Ω for comparison with the measured ones. The agreement between the measured and calculated Ω of the lowest energy candidate structures provides reliable assignments to the structures of the oligomers. Furthermore, collisional-induced dissociations of the mass-selected oligomer ions provide further support for the structures obtained from the mobility measurements. The results show that the gas phase ion mobility is crucial for identifying the structures and to investigate the mechanisms in the bulk media. In Chapter 4, the work on the solvation of a variety of metal cations by benzene molecules using laser vaporization, cluster beam and time-of-flight mass spectrometry techniques is presented. In the benzene systems, strong magic numbers have been observed for clusters depending on the nature of the metal cation involved. This work is focused on the interpretation of these results in view of the proposed structures and the growth patterns of the clusters. Next, Chapter 5 deals with intracluster ion molecule reactions following the generation of the magnesium cation Mg^+

within the cluster. For these reactions, the work is extended to include several polar molecules such as $(H_2O)_n$, $(CH_3OH)_n$, $(CH_3OCH_3)_n$, and $(CH_3CN)_n$. The summary of the work and conclusions drawn are presented in chapter 6.

CHAPTER 2 : Experimental Techniques and Methods

The experiments were performed using a home-built Wiley-McLaren type time-of-flight mass spectrometer (TOFMS)[47,48], and a home-built quadrupole mass selected-ion mobility-quadrupole mass spectrometer (QMS-IM-QMS)[49]. The instruments, experimental techniques and methods are described in the following sections.

2.1 Cluster Generation

In our laboratory we have used pulsed supersonic adiabatic expansion[50,51], which consists of a high-pressure region (1 to $3x10^3$ torr) within a nozzle through which the sample seeded into an inert carrier gas and expands into a low-pressure region (10^{-5} to 10^{-6} torr). As the gas mixture exits through the nozzle it converts the thermal energy from within the high-pressure source into directed beam kinetics energy. If C_p is the heat capacity of the expanding gas at source temperature (T_s), and T_b is the beam temperature, then the energy balance of an ideal gas is given by:[2]

$$C_p T_s = C_p T_b + mu^2 / 2 \qquad \text{Equation 1}$$

m is the mass of the expanding gas, and u is the velocity. Since mu^2 is positive, T_b is lower than the source temperature T_s. The low temperatures in free jet expansion lead to supersaturation and the possibility of condensation[52]. In other words, as the gas mixture moves out from the nozzle, it expands, and as it does so, it cools. This cooling promotes condensation. During the condensation process neutral clusters are formed. The expansion is adiabatic, i.e. no energy is lost from the beam. As expansion increases, the collision rate falls and the result is a beam of molecules all moving in the same direction.

2.2 Ion generation

The ions are generated by two ionization techniques, namely Laser Vaporization/Ionization (LVI) and Electron Impact ionization (EI).

2.2.1 Electron Impact Ionization (EI)

In our laboratory, an Extrel axial beams ionizer model 04-11 coupled with a quadrupole mass filter is used. The Ionizer consists of tungsten filament where the electrons are generated by thermoionic emission. These electrons are then accelerated into the ion region, where they interact with the incoming neutral molecular beam, which is formed by a supersonic adiabatic expansion, resulting in the creation of ions. These ions are then extracted from the ion region and focused into the quadrupole mass filter using Einzel lenses. Electron energy in normal experimental conditions is varied between 80 – 120 eV to yield strong ion intensity.

2.2.2 Laser Vaporization/Ionization (LVI)

Laser vaporization of a metal surface is a widely used technique to generate metal cations, but the mechanism of this process is not well defined. However, thermal heating effect of the laser is believed to be the main mechanism[53]. Basically a high energy pulsed -laser beam is focused onto a very small surface area. Plume will be generated containing; ground and exited state atoms, clusters of atoms, ions[54] of the sample and electrons. In our laboratory, we used a second harmonic (λ=532 nm) pulse of a Nd:YAG laser with ~10 mJ/pulse, at a repetition rate of 5-8 Hz, focused onto a 0.01cm^2 metal surface area, using a lens with a focal length of 30 cm. The result is a very high energy flux ~ 10^7 W/cm^2,

which causes instantaneous increase in the metal surface temperature of up to approximately few thousand kelvins within 5-7 ns pulse width.[55]This temperature is so high, and because the laser pulse is short (5-7 ns), vaporization of atoms from the target becomes a very efficient process electrons will be ejected and will perhaps ionize those metal atoms, as in the electron impact process.

2.3 Time-of-Flight Mass Spectrometer (TOFMS)

The experiments are performed using a home- built Wiley-McLaren[47,48] type time-of-flight mass spectrometer (TOFMS), as shown in Figure 2. The set up consists of two vacuum chambers. The source chamber is pumped by a Varian VHS-6" diffusion pump, 3000 L/s (He). This chamber houses a metal target, which is mounted on a sample-holder placed 8 mm downstream from a pulsed valve/nozzle. The pulsed valve/nozzle, a General Valve series 9, coupled with a 200-μm diameter conical nozzle is used to generate the cluster beam by supersonic expansion of a gas mixture of the reagent vapor, seeded in He (ultra high purity Spectra Gases 99.999%) with a backing pressure of 3-8 atm, through a 0.5 mm nozzle. The molecular beam containing cluster ions skimmed through a 5mm diameter skimmer cone. This skimmer separates the first chamber and second chamber. The second chamber, the flight tube chamber, contains the extraction region, which consists of three plates arranged in the order repeller, accelerator and ground plate. There are also two deflection plates located perpendicular to these three plates. The flight tube chamber is differentially pumped by a Varian VHS-6" diffusion pump, 1500 L/s (He). The operating pressure is $5x10^{-5}$ torr for the source chamber and 1×10^{-7} torr for the flight tube chamber.

A typical experiment starts with the opening of the pulsed valve, followed by the generation of the metal cations by vaporization of a metal target inside the source chamber, using a second harmonic Nd:YAG laser at ~10 mJ/pulse, with a repetition rate of 5- 8 Hz. The laser-ablated metal ions perpendicularly cross the expansion stream 8 mm from the ablation target where they react with the neutral molecular clusters. The result is an ionic cluster beam, collimated with a 5 mm diameter skimmer 10 cm down the stream, which then travels to the second high vacuum chamber, differentially pumped, passing symmetrically between the repeller and the accelerator. This chamber is maintained at an operating pressure of 1.0×10^{-7} torr. The cationic clusters are then introduced into the extraction region, which consists of three pulsed grids: repeller, accelerator and ground plates, the accelerator and the ground plates are constructed from 90% transmission copper wire mesh. The cluster ion beam is then analyzed using a pulsed TOF mass spectrometer. Most of the cluster ions were studied using a one-Pulser setup. One Pulser setup consists of DEI GRX-3.0K-H pulsed high voltage divider. The dividing ratio is 8/10 for accelerator and repeller respectively. After acceleration, the product cations travel along the field-free 1m-flight tube, and are then detected by a microchannel- plate detector (MCP) located at the end of the flight tube. The current from the detector is then amplified and recorded by a Tektronix TDS 210 oscilloscope as a function of time. It is then converted into mass using a linear square fit. The mass spectra are usually accumulated for 128 laser shots and are transferred to the computer using a National Instrument interface board model (GPIB-PCII). The delay times between the nozzle opening, the laser firing, and the ion extraction

are adjusted to obtain the maximum signal intensities of the desired range of cluster size distribution. The time sequence for LVI-TOFMS is shown in Figure 3.

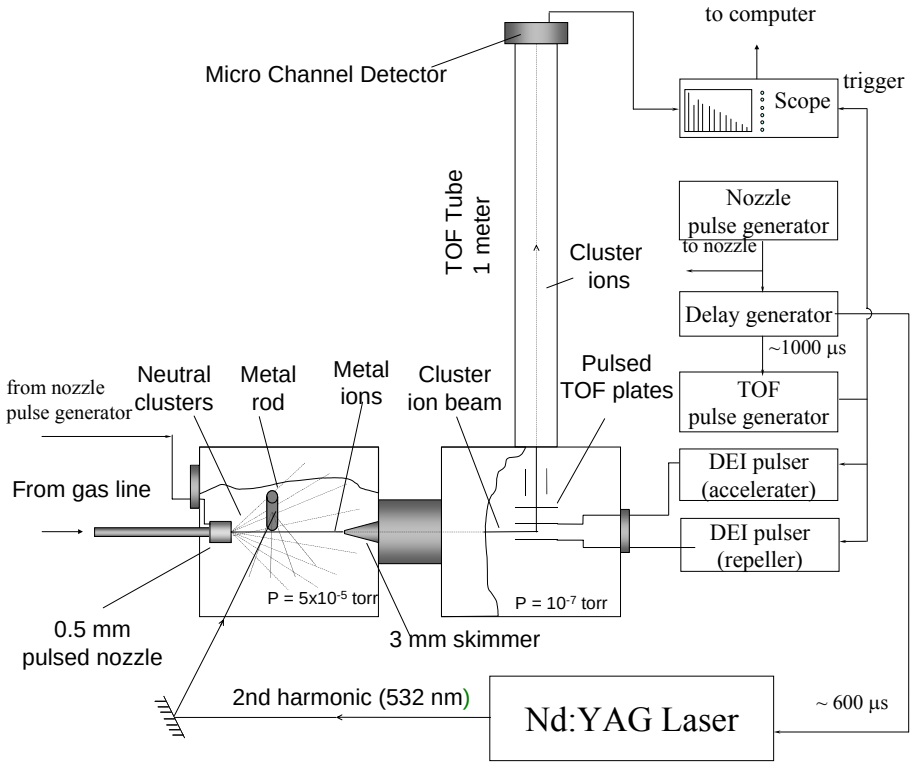

Figure 2: Experimental setup of Time-of-flight mass spectrometer (TOFMS)for the generation of metal cation – containing molecular clusters.

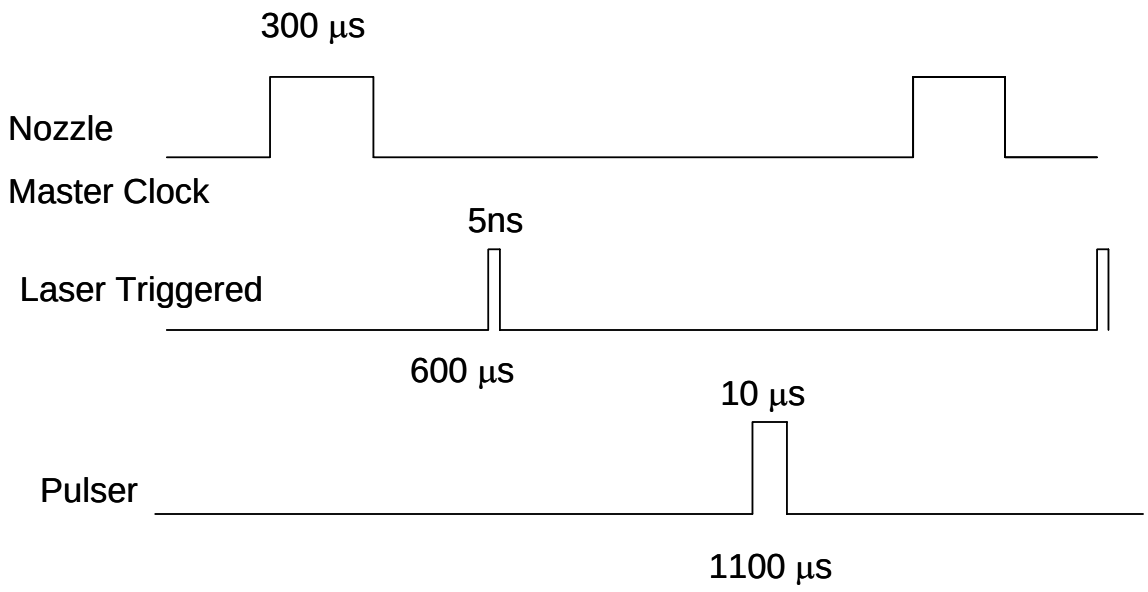

Figure 3: Timing sequence for laser vaporization/ionization experiment.

2.4 Quadrupole Mass Selected-Ion Mobility-Quadrupole Mass Spectrometer (QMS-IM-QMS)

The home-built instrument used in our laboratory [40,41] is a quadrupole mass selected-ion mobility-quadrupole mass spectrometer (QMS-IM-QMS). In the following sections, the description of the instrument, gas phase ion mobility measurements, structure determination, and the experimental approach to study the mass selected cluster ions will be described in detail.

2.4.1 Experimental Setup

Figure 4 shows the setup for the QMS-IM-QMS. This set up consists of four stainless steel chambers. The source chamber is pumped by a Varian VHS 6" diffusion. This first chamber is our source of the neutral molecular beam generated by a pulsed adiabatic supersonic expansion. In addition, this chamber houses a 5 mm skimmer that separates it from the second chamber. The operating pressure for the source chamber is $5x10^{-5}$ torr. The second chamber houses the first quadrupole (Q1). This quadrupole mass filter is equipped with an axial electron impact ionizer, which ionizes the neutral molecular beam with electron energy of 10-150 eV. An Edwards Diffstak 160/700 M diffusion pump with a pumping speed of 1300 L/s (H_2) pumps the second chamber. A typical operating pressure is $\sim 2\times10^{-6}$. After the ionization step either by laser vaporization or by electron impact the ions of interest are mass selected using the first quadrupole mass filter. This filters the ions according to their mass to charge ratio. In the case of the ions that are generated by LVI,

the filament of the Ionizer is turned off and the voltage on the Ionizer lenses is adjusted in order to focus the ions beam into the first quadrupole mass analyzer. This quadrupole can be used in mass selection mode (RF-DC mode) or an RF only mode. In mass selection mode, the ion of interest, with certain mass to charge ratio is allowed to transmit. In RF only mode, a window of mass to charge ratio ions is allowed to go through the quadrupole. After the mass selection step, the ions will be focused and injected into the drift cell using a set of three Einzel lenses located in the third chamber, which houses two sets of ion transport lenses and a drift cell. An Edwards (Diffstak 250/2000P) diffusion pump with a pumping speed of 3000 L/s (H_2) pumps this chamber. Each Einzel lens consists of a three sets of lens. The third Einzel lens is biased to the horizontal part of the electrostatic gate located just before the drift cell. This gate consists of four half-lenses two halves are horizontally opposite of each other, and other two are set vertically. One of the two functions of these sets is to steer the ion beam, horizontally or vertically, into the pinhole located at the middle of the entrance plate of the drift cell. The other function is an ion gate, which chops the wide ion beam pulse (~300 μs; proportional to the nozzle width) into 10-50 μs ions pulses. The vertical part of the set is biased to the Einzel lens 3, while the other halves are connected to a separate power supply. When the gate is closed, the two halves have equal voltages with opposite polarity (typically –200-240V and +200-240 V). This difference in polarity causes a strong deflection field, so that no ions will pass through. However, when the gate is open, polarity will be the same on both sets, therefore no deflection, and ions will pass through and enter the drift cell.

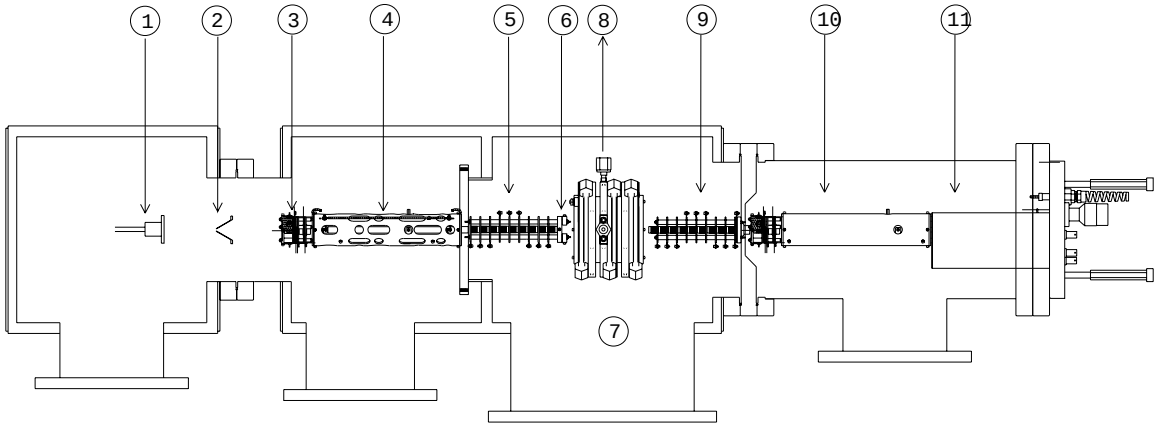

Figure 4: The experiment setup for mass-selected ion mobility spectrometer. 1) pulsed nozzle; 2) 5 mm skimmer; 3) electron-impact ionizer; 4) quadrupole mass filter; 5) ions transport lenses (Einzel Lenses 1, 2 and 3); 6) steering lens/ion gate; 7) drift cell; 8) to manometer; 9) ions transport lenses (Einzel Lenses 4, 5 and 6); 10) quadrupole mass filter; 11) electron multiplier (detector).

The drift cell is composed of entrance and exit plates as well as three oxygen-free copper rings separated by two ceramic rings. A voltage is applied to the entrance and exit plates from two independent power supplies and a homogeneous field is obtained across the cell through equal resistors (5 MΩ) that connect all the drift cell components. The entrance and exit plates have 1 mm orifice apertures. The cell can be filled with buffer gas (usually He) through electrically insulated tubing. The entrance and the exit plate's orifices and the pumping speed of the diffusion pump limit the pressure inside the cell to ~2.5 torr of He. The cell is temperature controlled. It can be heated through two heating cartridges inserted into each ring, but the Teflon gasket limits the maximum temperature. This gasket has a melting point (~ 250^{o}C). The temperature of the cell is monitored by two K type (Omega CO1) thermocouples at each ring and the seventh K-type thermocouple that is attached to the exit plate near the orifice. The temperature of the cell is controlled by three temperature controllers (Omega type CN3251), which are connected to each ring, these help maintain the cell temperature within 1^{o}C. By flowing liquid nitrogen into three copper tubes wrapped around each cell ring we can also cool the cell. The flow of nitrogen is controlled using three sets of On-OFF solenoid valves. An Omega type CNi3233 temperature controller controls the solenoid valves. The minimum cell temperature that can be achieved is -170^{o}C with a stability of ±1^{o}C. The ions that exit the drift cell are accelerated and refocused using another set of three Einzel lenses. The Einzel lenses transport and focus the exit ion beam to a second quadrupole mass filter with a mass range of 4000 amu. This second quadrupole is located in the fourth chamber, which houses a second electron impact/quadrupole mass filter and is pumped by Edwards Diffstak 160/700 M diffusion

pump with a pumping speed of 1300 L/s (H_2). A typical pressure of ~5-9×10^{-7} torr is achieved in the fourth chamber during the experiment. The second quadrupole spectrometer is coupled with a Channeltron electron multiplier detector. The detector signal flow to an ion counts preamplifier and is processed by Merlin software supplied from ABB Extrel. This quadrupole mass filter can be used either to mass scan the different ions exiting the drift cell or to monitor the intensity change for ions of certain mass to charge ratio. The arrival time of ions is obtained using a multichannel scalar. The ions arrival time distribution (ATD) represents the flight time of the ions from the ion gate to the detector. The timing sequence of the electron impact ionization experiments is shown in Figure 5.

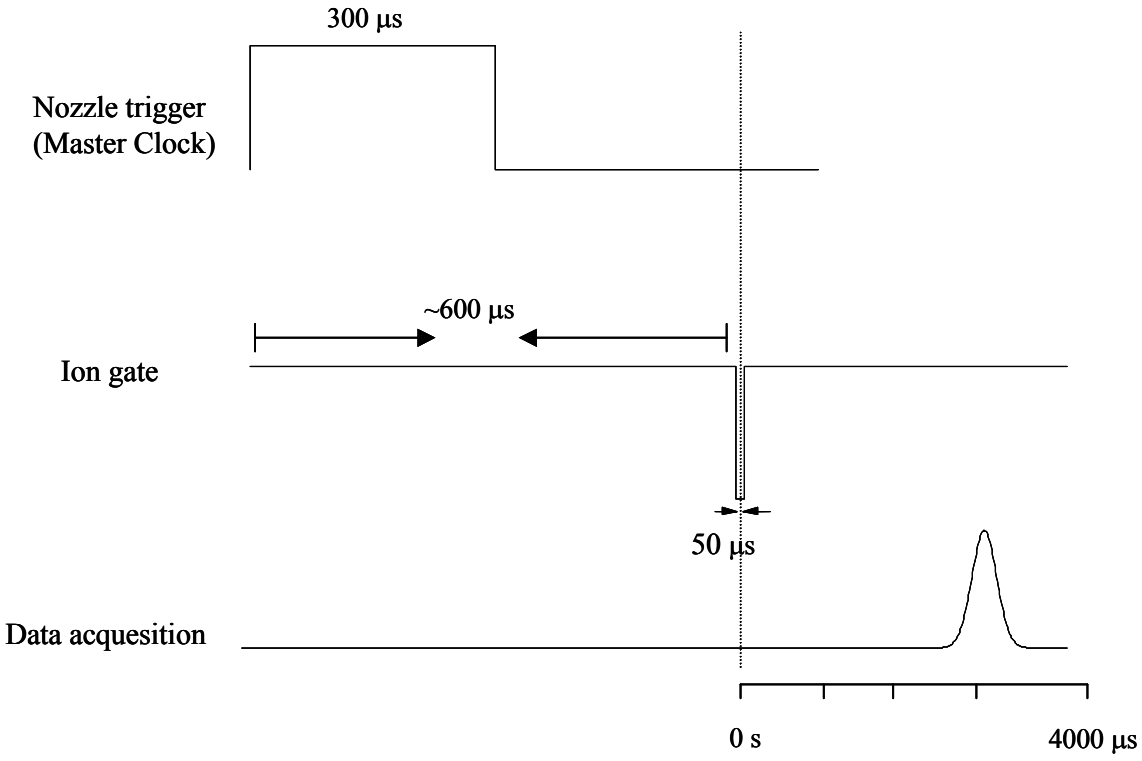

Figure 5: Timing sequence for electron impact ionization experiment.

2.4.2 Mobility measurements

The ion mobility is a measure of the velocity of the ion as it travels through non reactive buffer gas under the influence of a uniform electric field and it defined as: [44]

$$K = \upsilon_d / E \qquad \text{Equation 2}$$

K, is the mobility in $cm^2/V.s$ and E is the drift field applied along the cell ($E = V/z$, where V is drift voltage in Volt and z is the drift distance (8.9 cm in our system) and υ_d is the drift velocity.The measured mobility is proportional to the buffer gas number density and by convention it is converted to a reduced mobility (K_0) :[44,56]

$$K_0 = K\left(\frac{273.15}{T}\right)\left(\frac{P}{760}\right) \qquad \text{Equation 3}$$

Where T is the buffer gas temperature in Kelvin and P is the buffer gas pressure in torr. Combining equations (2) and (3) and substituting for E gives

$$t_d = \left(\frac{z^2 \times 273.15}{T \times 760 \times K_0}\right)\left(\frac{P}{V}\right) + t_0 \qquad \text{Equation 4}$$

t_0 is time the ions spend outside the drift cell. In the ion mobility technique, a narrow (50 μs) ions pulse is injected into the drift cell, containing buffer gas (He), then the arrival time (t_d) is collected at different cell voltages, while keeping the pressure and temperature inside the cell constant. Then a plot the ion drift time t_d vs. P/V is plotted, this should give a straight line with a slope equal to:

$$slope = \left(\frac{z^2 \times 273.15}{T \times 760 \times K_0}\right) \qquad \text{Equation 5}$$

The measured ATD can be compared with the calculated one using the transport theory (Equation 6) for flux of ions ($\phi(t)$) in the drift tube with an aperture of area *a* and with a length of z. This is given by:[56,57]

$$\phi(t) = \frac{sae^{-\alpha t}}{4\sqrt{\pi D_L t}}\left(\upsilon_d + \frac{z}{t}\right)\left(1 - exp\left(-\frac{r}{4D_T t}\right)\right)exp\left(-\frac{(z-\upsilon_d t)^2}{4D_L t}\right) \qquad \text{Equation 6}$$

The ions are introduced as a delta pulse in the form of an axially thin disk of radius r_0 and uniform surface density *s*. The term *s* can be used as a scaling factor for the signal intensity, α is a constant, *t* is the time spent inside the cell, this time is obtained with subtracting the recorded arrival time (t_d) by the time spent by the ion outside the cell (t_0), and D_L and D_T are the longitudinal and transverse diffusion coefficients, respectively, and under low field conditions are given by the equation:

$$D = D_L = D_T = K\frac{k_B T}{e} \qquad \text{Equation 7}$$

2.4.3 Structure determination

The mobility and hence the collision integral, under the low field limit, is related to the geometry, and it can be calculated from Equation 8 [42,43,58-60]. The low field limit is defined[44] as $E/N \leq 6$ Td (*N* is the buffer gas number density and Td = Townsend = 10^{-17} cm^2V),

$$K = \frac{3qe}{16N}\left(\frac{2\pi}{k_B T_{eff}}\right)^{\frac{1}{2}}\left(\frac{M_i + M_b}{M_i M_b}\right)^{\frac{1}{2}}\frac{1}{\Omega^{(1,1)}(T_{eff})} \qquad \text{Equation 8}$$

qe is the ion charge, *N* is the buffer gas number density, *m* is the ion mass, *M* is the buffer gas mass, k_B is the Boltzmann constant, T_{eff} is the effective temperature. The effective temperature is defined as:[44]

$$T_{eff} = T_g + \frac{M_b \upsilon_d^2}{3k_B} \qquad \text{Equation 9}$$

and $\Omega^{(1,1)}(T_{eff})$ is the temperature-dependent orientationally average collision integral.

In this study we have employed the DFT level of calculation with 6-31G** basis set using Gaussian 98 software[61] to optimize the geometries of selected realistic structures for styrene dimer, $^{+}C_{16}H_{16}$, and trimer,$^{+}C_{24}H_{24}$. The optimized structures are then used as input to a computer program (MOBCAL)[42] obtained from the Jarrold group[42,62,63]. This program uses the trajectory approximation (Trajectory Method) to calculate the collision integral by averaging over the impact parameter and relative velocity. The potential employed in these calculations is a sum of 12-6 potential (Lennard-Jones) plus ion-induced dipole interaction. The average collision integral ($\Omega^{(1,1)}$) is then obtained by averaging the collision integral over all possible collision geometries between the polyatomic ion and the buffer gas atom.

2.4.4 Experimental Approach

Our approach is based on on-line analysis of the gas phase oligomers by mass-selected ion mobility; this can be displayed in Figure 6. In the experiments, styrene – Helium vapor mixture is heated to well-defined temperatures (350 – 370 K), thus allowing the establishment of a distribution of oligomers grown in the vapor phase by the thermal self-initiated process. The vapor mixture is then expanded through a supersonic pulsed

nozzle into vacuum thus allowing the adiabatic cooling of the vapor and the quenching of the polymerization process. The resulting styrene oligomers are then ionized by EI, mass selected through a quadrupole mass filter, and injected into a drift cell containing buffer gas (He) for the measurement of ion mobility and to study the fragmentation of the mass selected styrene oligomers ion.

The styrene monomer ion mobility measurements were conducted at room temperature (T_{cell} = 27.3 ^{0}C) with helium as the buffer gas. First the styrene monomer ion ($C_8H_8^+$) is mass-selected by setting the first quadrupole in a mass selection mode while mass scanning the second quadrupole and the mass spectrum is collected. The resulting mass spectrum is displayed in Figure 7. Mobility measurements are made by injecting a narrow pulse (10 50 μs) of styrene monomer ions into the drift cell filled with Helium gas. Upon exiting the drift cell, the ions are collected and refocused into the second quadrupole for analysis and detection. The signal is collected on a multichannel scalar with the time zero for data acquisition set to the midpoint of the ion gate trigger. Figure 8 shows the typical set of ATDs recorded at constant temperature and pressure with different electric fields across the drift cell. The reduced mobility is determined according to equation 5 by plotting t_d versus P/V. Figure 9 shows the excellent linear correlation (R^2 = 0.9995) of the recorded data. The data shown in Figure 9 yields a slope of 1.010×10^{-2} (s·V/Torr), and an intercept of 55.66 μs (the time spent within the second quadrupole before the detection of the ions. The linear plot is inversely proportional to the reduced mobility. The reduced mobility, K_0 = 9.22 $cm^2.V^{-1}.s^{-1}$ is calculated using Equation 5. Figure 10 displays a comparison of the experimental arrival time distribution to the predicted one from

transport theory using Equation 6. This shows a good agreement between the experimental ATD and the theoretical one.

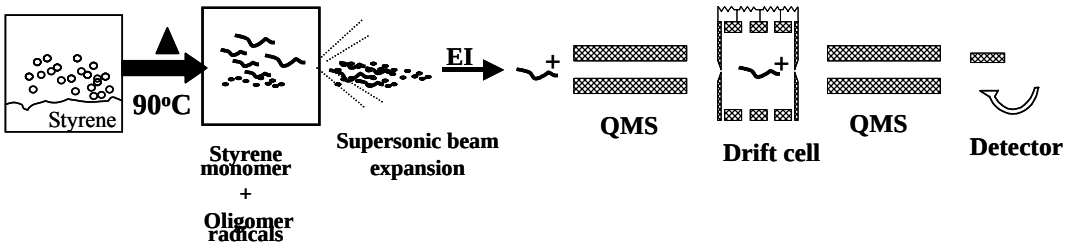

Figure 6: Schematic diagram of theexperimental QMS-IMS-QMS approach to study the thermal self-initiated styrene polymerization in the gas phase

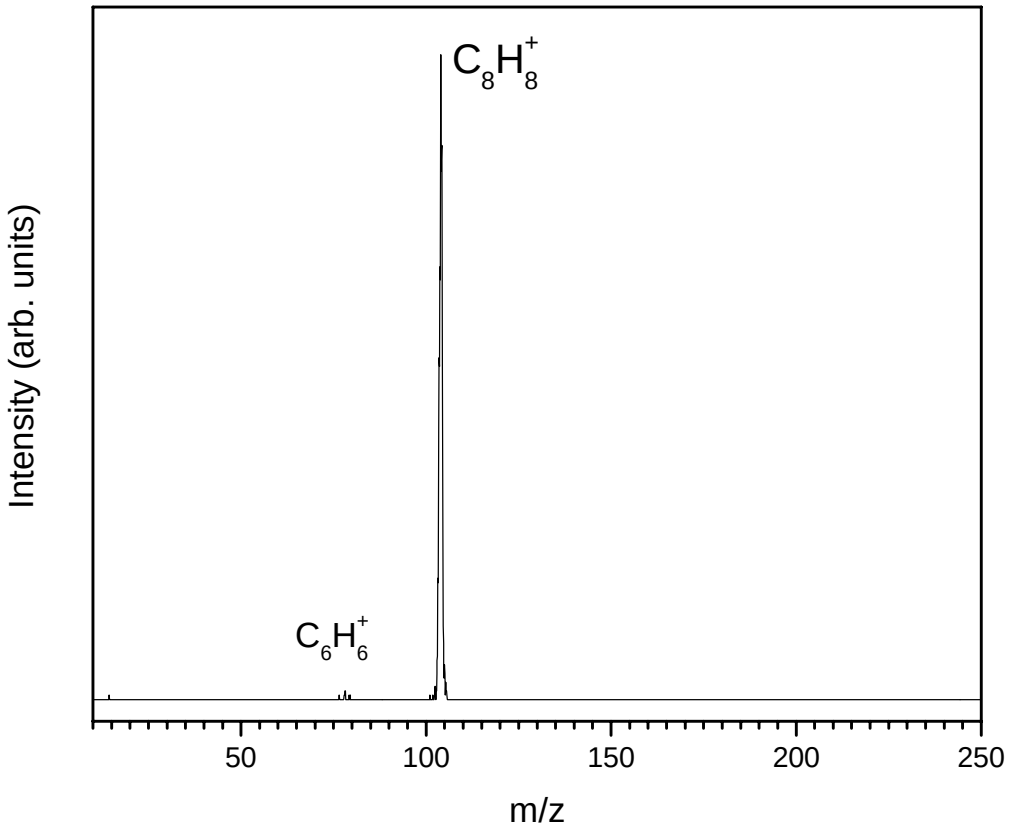

Figure 7: Mass Spectrum of the mass selected $(C_8H_8)^+$ obtained by 94 eV Electron Impact Ionization. Experimental conditions are: Source temperature is 70 ^oC, 40 psi He as carrier gas, injection energy is 15 eV, 2.007 Torr He inside the drift cell and 25 V voltage difference between the entrance and the exit lenses

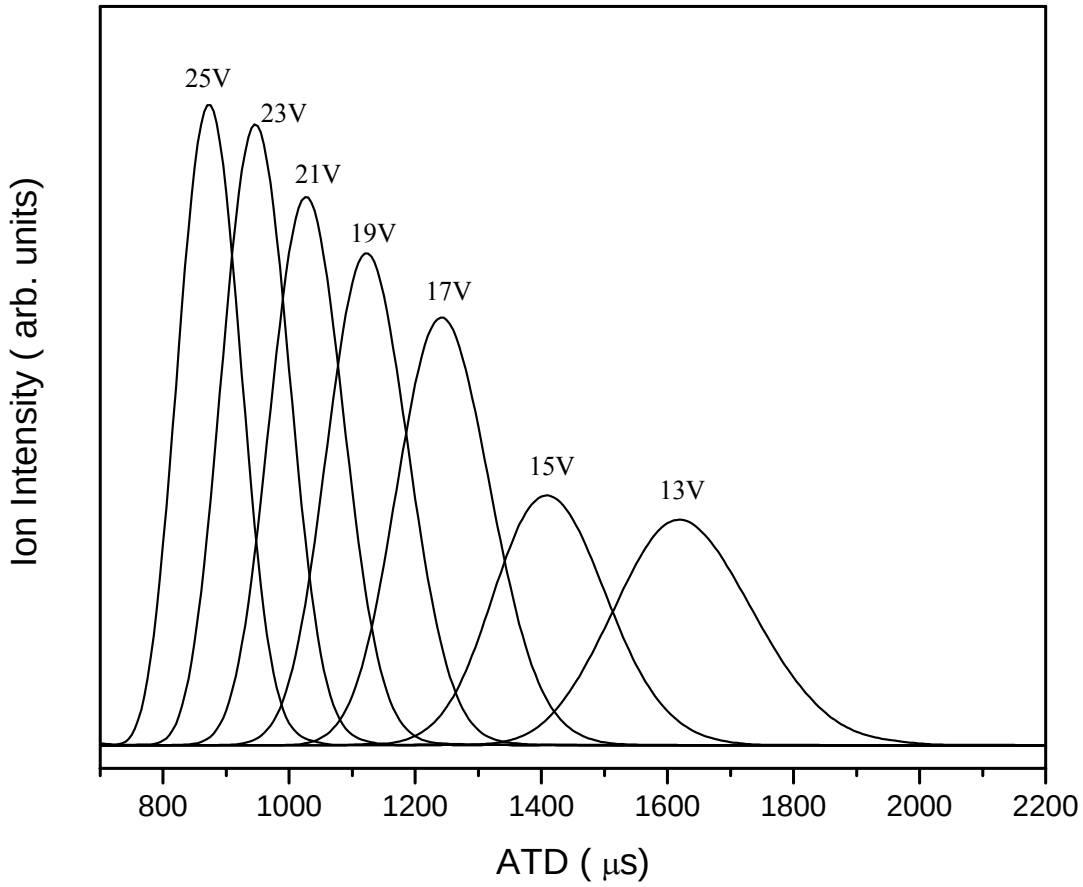

Figure 8: Arrival time distribution of mass selected $C_8H_8^+$ ions at diffrent cell voltages : Experimental conditions are: 50 μs pulse width, injection energy is 15 eV, 2.007 Torr and the drift cell tempreature is 27.3 ^oC.

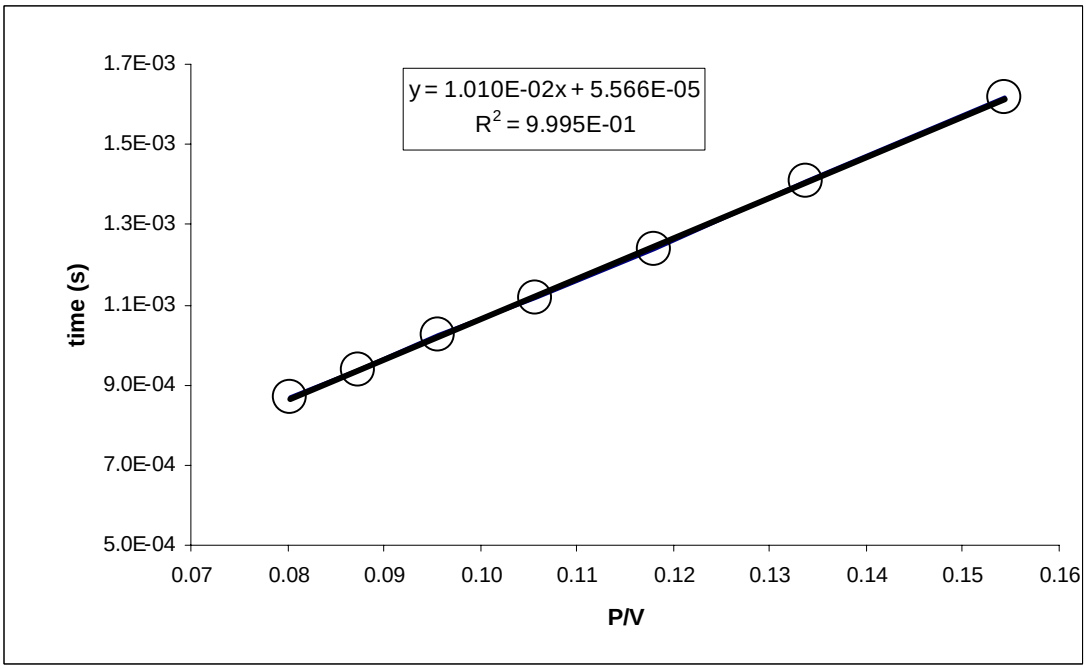

Figure 9: Plot of the arrival time vs P/V for the mass selected styrene monomer ion $C_8H_8^+$. The circles are the experimental and the solid line is the Least Square linear fit to the data points with $R^2 = 0.9995$.

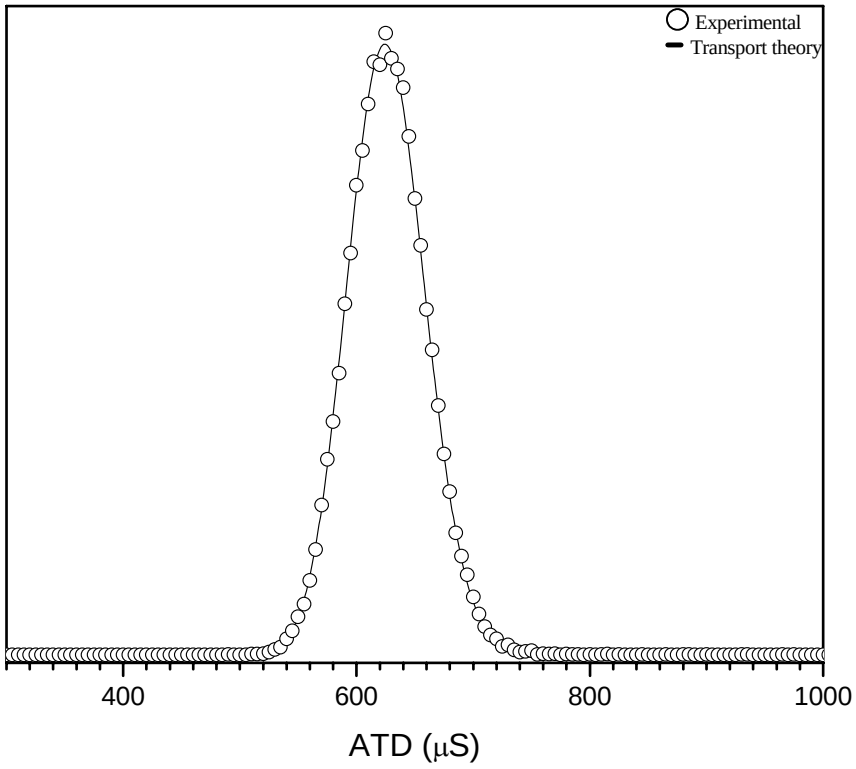

Figure 10: Arrival time distribution of mass selected $C_8H_8^+$ ions (circles) and the predicted distribution from transport theory (solid line): Experimental conditions are : 50 μs pulse width, injection energy is 15 eV, 1.136 Torr He inside the drift cell, 20 V voltage cell temperature is 31.7 ^oC, difference between the entrance and the exit lenses and E/N = 4.01 Td. The reduced mobility K_o = 9.28 $cm^2V^{-1}s^{-1}$.

CHAPTER 3 : Ion Mobility Study of Styrene Oligomers

3.1 Introduction

The mechanism of the self-initiated polymerization (or thermal polymerization) of styrene in bulk liquids or solutions has been a challenging subject of research since the early days of polymer chemistry[10-37]. Thermal polymerization or self-initiated polymerization of styrene has been studied extensively in bulk liquid and in solutions, and it is well known that styrene polymerizes upon standing[33]. In 1937, Flory[36] studied the thermal polymerization of styrene. He determined the experimental activation energy to be 32 kcal/mol and ruled out the unimolecular initiation step; such as dissociation of a C-C or C-H bond, or the opening of the double bond to yield divalent free radicals. He showed these processes to be highly endothermic. For example, the value for $D_{C\text{-}C}$, the heat of dissociation of carbon - carbon bond, is about 75 kcal/mol and for C-H is about 95 kcal/ mol while the opening of double bond requires about 60 kcal/ mol. Flory proposed a second order initiation- mechanism in which two styrene monomers coupled "tail-to tail" to form di-free radical stabilized by resonance and converted to monoradicals by H transfer. This can be summarized in equation 1.

$$PhCH{=}CH_2 + PhCH{=}CH_2 \rightarrow [PhC^{\bullet}HCH_2CH_2HC^{\bullet}Ph]$$

$$[PhC^{\bullet}HCH_2CH_2C^{\bullet}HPh] + PhCH{=}CH_2 \rightarrow Ph^{\bullet}CH\text{-}CH_3 + PhCH{=}CH_2{}^{\bullet}CH\text{-}Ph \quad (1)$$

In 1946, Mayo [30] studied the rate of thermal polymerization of styrene at 127.3 ^{o}C as a function of the vapor pressure of the monomer in the polymerizing system. The rate was measured over the range 0-95% reaction. The rate was found to be closely proportional to the square of the styrene concentration over the entire range. This is in agreement with the bimolecular mechanism proposed by Flory [36]. In 1953, Mayo [20] also studied the rate and degree of the thermal polymerization of styrene at different temperatures (60, 155, and 176^{o}C) in bromobenzene as the solvent, with styrene concentrations ranging from 7.6 to 0.05M. The general conclusion was that the overall thermal polymerization was a second order reaction. However, at certain concentration ranges from 0.05 to 1.6M, the rate of higher polymer formation agreed much better with the 5/2-order relation. Mayo proposed a termolecular reaction of styrene to give two monoradicals:

$$3\,(C_8H_8) \rightarrow CH_3(Ph)C^{\bullet}H\ (105\ amu) + CH_3(Ph)C{=}CH\text{-}(Ph)C^{\bullet}H \quad \ldots\ldots\ldots(2)$$

This proposed reaction was supported by the observed activation energy of 29 kcal/mol[20]. At this point, Mayo could not rule out the diradical mechanism since the number of double bonds lost is the same as in reaction 1. In addition, the results showed that the dimer is 90 % saturated; which led to the conclusion that the dimer is cyclic. In 1961, Mayo [21] identified the dimer products. The major products were 1-phenyltetralin (1-PhT) (70%) and Diphenylcyclobutene (DCB) (15%). This important result was then verified in 1968, when Mayo and co-workers [22] isolated the styrene dimer products by gas – liquid partition chromatography, and then distinguished the products by their infrared absorption. The major dimers were DCB and derivatives of 1-PhT. Mayo proposed that these products

correspond to a non-radical thermal process with a Diels-Alder adduct type intermediate (AH)[22]. The effect of the addition of Iodine on styrene polymerization was also investigated[22]. The results showed that Iodine acted as a retarding agent for the styrene polymerization process. However, the addition of Iodine accelerates the formation of 1-PhT and decreases the formation of DCB[22]. The results were rationalized by proposing that the role of Iodine is to assist in the isomerization of the proposed unstable (AH) intermediate, and that it converts this intermediate into 1-PhT. These results were supported by Brown *et al*[11]. Mayo proposed reaction pathways, as shown in Scheme 1, to account for the third-order initiation in the thermal polymerization of styrene.

Scheme 1: Proposed mechanism by Mayo to account for the third-order initiation in the thermal polymerization of styrene

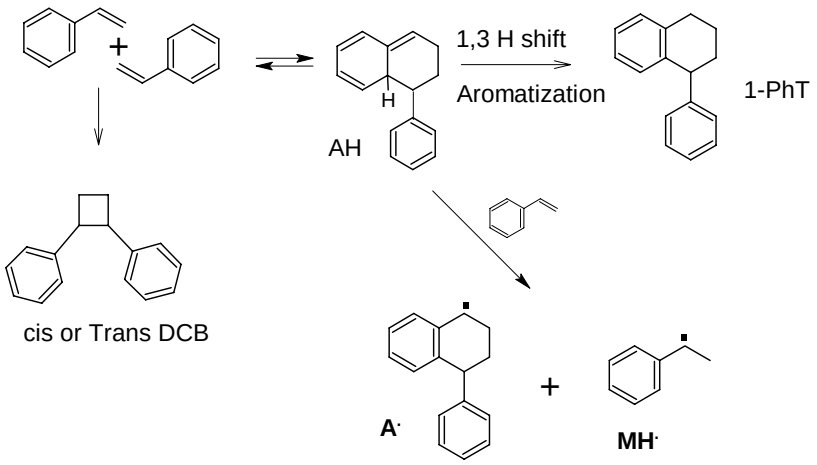

Kopecky *et al* [18,19] and Pryor *et al* [24-26,32,64] studied the mechanism of thermal initiation of styrene and the isotope effect of the thermal polymerization of deuterated styrene. They compared the results with those of polystyrene initiated with Azo

compounds. The ratio of k_H/k_D in the first case was found to be 1.8 and the major product was 1-PhT. In cases where the reaction was chemically initiated, the ratio was found to be $k_H/k_D = 1.29$. The isotope study led to a conclusion that the hydrogen transfer to the third styrene molecule happens through concerted dimerization of two molecules of styrene.

Pryor *et al* [26] also studied the thermal polymerization of 2, 3, 4, 5, 6-Pentaflourostyrene (PFS) , and identified the oligomers from PFS. The major product was 1, 2-diphenylcyclobutenes resulting from of 2+2 cycloaddition to form a 1, 4-diradical. This experimental result ruled out the Diels –Alder mechanism (AH) in PFS polymerization, since there was no condensation product such as 1-PhT. They also measured the transfer constant of PFS and found it to be zero. The authors [32]explained this result with the fact that the bond strength of C-F is higher than that of C-H bond strength. This is an important and useful clue in understanding the transfer mechanism for styrene's monomers. The work pointed out the important role of the unique H-atom in the AH adduct that is both tertiary and allylic. The loss of this hydrogen atom is considered the driving force, since it allows the rearomatization to produce a resonance stabilized benzylic radical. In an excellent review by Pryor [28] [27], he discussed the question of diradical contributions in the transition state for Diels-Alder reaction. He concludes that the actual mechanism of AH formation needs not to be specified in order to derive reasonable mechanisms for thermal initiation, which utilize AH. In this review, Pryor summarizes the steps of the dimer and trimer formation as following: After the formation of the AH intermediate, it will either react with a styrene molecule to produce two monoradicals in a solvent cage through Molecule Assisted Homolysis [33] (MAH), or form a styrene trimer (A-

Sty) through an ene reaction or through combination. In this cage, disproportionation occurs and 1-PhT will be produced, or these two monoradicals diffuse out of the cage and then propagate into a polymer. In addition, he explains the formation of DCB side products through the diradical formation followed by its cyclization. This can be summarized in Scheme 2 below:

Scheme 2:

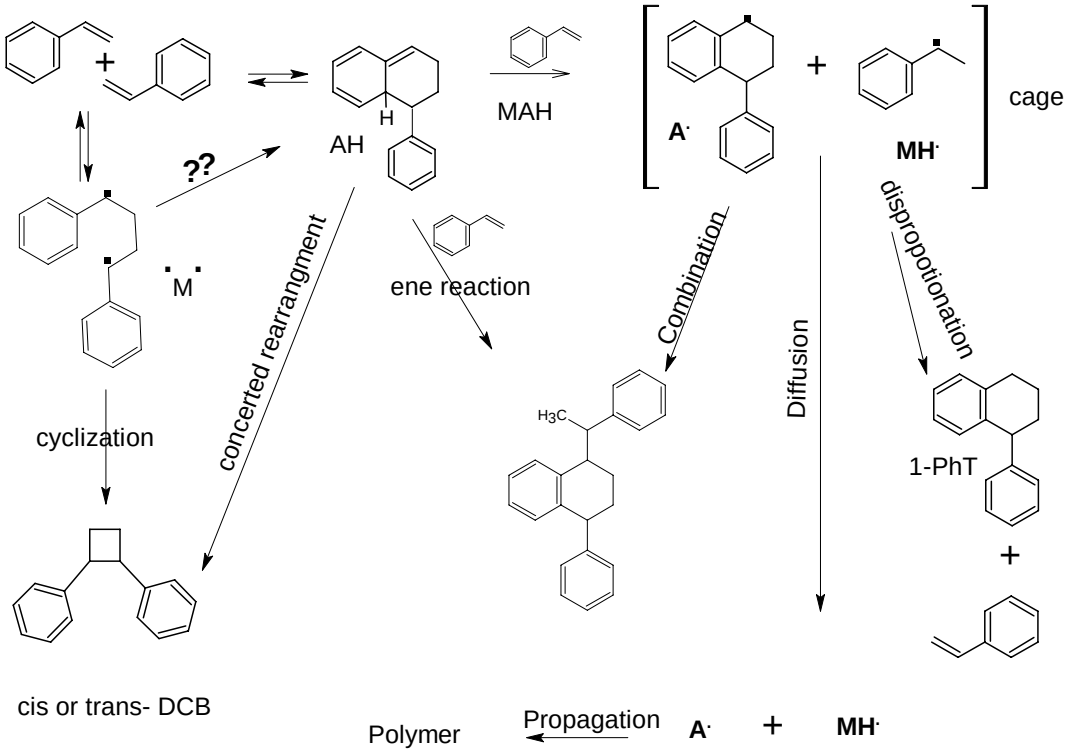

In 1979 Barr *et al* [10] studied the thermal initiation of styrene polymerization from 60-140 ^{0}C. In this study, they measured the rate of free radical formation in the presence of free radical scavengers, Diphenylpicrylhydrazyl DPPH. Their results strongly support the diradical mechanism for the thermal initiation of styrene polymerization. In 1983

Solomon etal [65] studied the propagation step in the thermal polymerization in styrene. In this study oligomers composed of 6-14 repeating units were extracted by HPLC and identified by ^{1}H NMR[66]. The spectra revealed that the styrene trimer has the structure below:

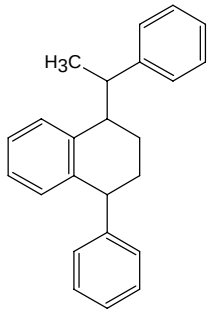

Styrene Trimer

Their results described and established the identity of the initiating radicals. This, in addition to the previous studies, as mentioned above, confirmed Mayo's mechanism for the initiation process[12]. In 2001 Kothe *et al*[37] studied the formation rate constant for styrene dimers 1-PhT and DCB and obtained the associated Arrhenius plot. Their main finding was that the styrene dimer formed via 2 + 4 Diels-Alder additions. Their conclusion was based on the fact that the Arrhenius parameters (log $(A)(M^{-1}s^{-1})$) are known for various 2 + 4 Diels-Alder additions and range between 4.1 – 7.5. The value they obtained was (log $(A)(M^{-1}s^{-1}) = 4.4$, which falls in the acceptable range. This lends additional support to the dimer formation by a concerted Diels-Alder process.

The work presented above involved the thermal polymerization of styrene in bulk liquids and solutions. Few studies were concerned with the thermal self-initiated polymerization of styrene in the gas phase[13,14,16,17,29]. This process was demonstrated in 1986 – 1987[13]

using a nucleation approach where styrene vapor condenses on the growing polymers in supersaturated styrene vapor. However, no direct information on the initiation mechanism or on the structures of the small oligomers are available to date.

In this work, we present the first direct evidence for the thermally self-initiated polymerization of styrene in the gas phase. In addition, we report structural evidence that support and confirm the Mayo mechanism of thermally- self initiated of styrene polymerization in bulk phase.

3.2 Experimental Results

Figure 11 displays the mass spectrum of gas phase styrene clusters, $^{+}(C_8H_8)_n$, formed by a supersonic beam expansion. In this case, the neutral styrene clusters travel 80 cm in vacuum (10^{-7} Torr, no buffer gas inside the cell) then ionized with the second EI ionization located just before the second quadrupole of the mass-selected ion mobility system (see Figure 4 in the experimental section). This mass spectrum shows $(styrene)_n^{+}$, n = 1-28, and doubly charged styrene clusters, $(styrene)_n^{++}$. These doubly charged styrene species begin to appear at n = 9. Figure 12 shows the mass spectrum of the EI-ionized styrene clusters, $^{+}(C_8H_8)_n$ following their injecting into the drift cell, filled with 1.5 Torr He gas, with injection energy (lab) 15 eV. The mass spectrum was obtained when the first quadrupole was set in RF only mode while mass scanning the second quadrupole. The mass spectrum displayed in Figure 12 shows styrene clusters contain up to nine molecules. The observation of large styrene clusters ions following the injection of the clusters into the drift cell containing 1.5 Torr of helium suggest that these ions are strongly bound can survive collisions with high injection energies

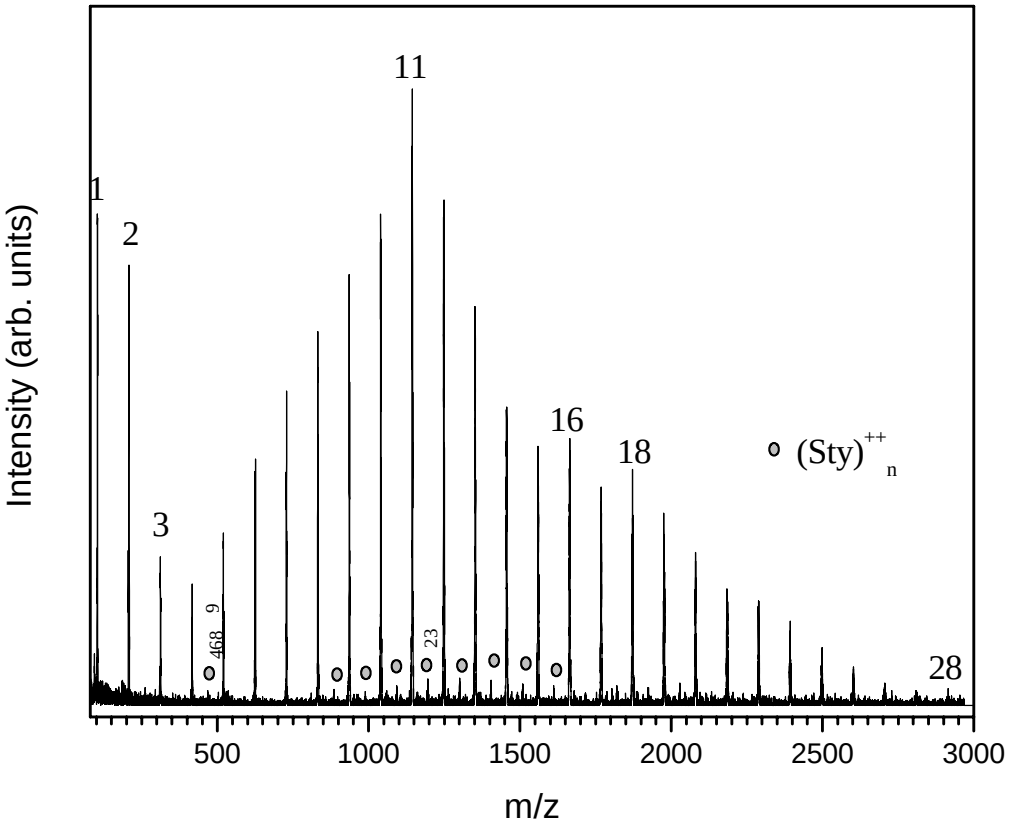

Figure 11: Mass Spectrum of $(C_8H_8)_n^+$ clusters ions obtained by 65 eV Electron Impact ionization (No He In the Drift Cell). Experimental conditions are: Source temperature is 70 ^oC120 psi He as carrier gas. First quadrupole was off and second quadrupole was optimized at 936 amu.

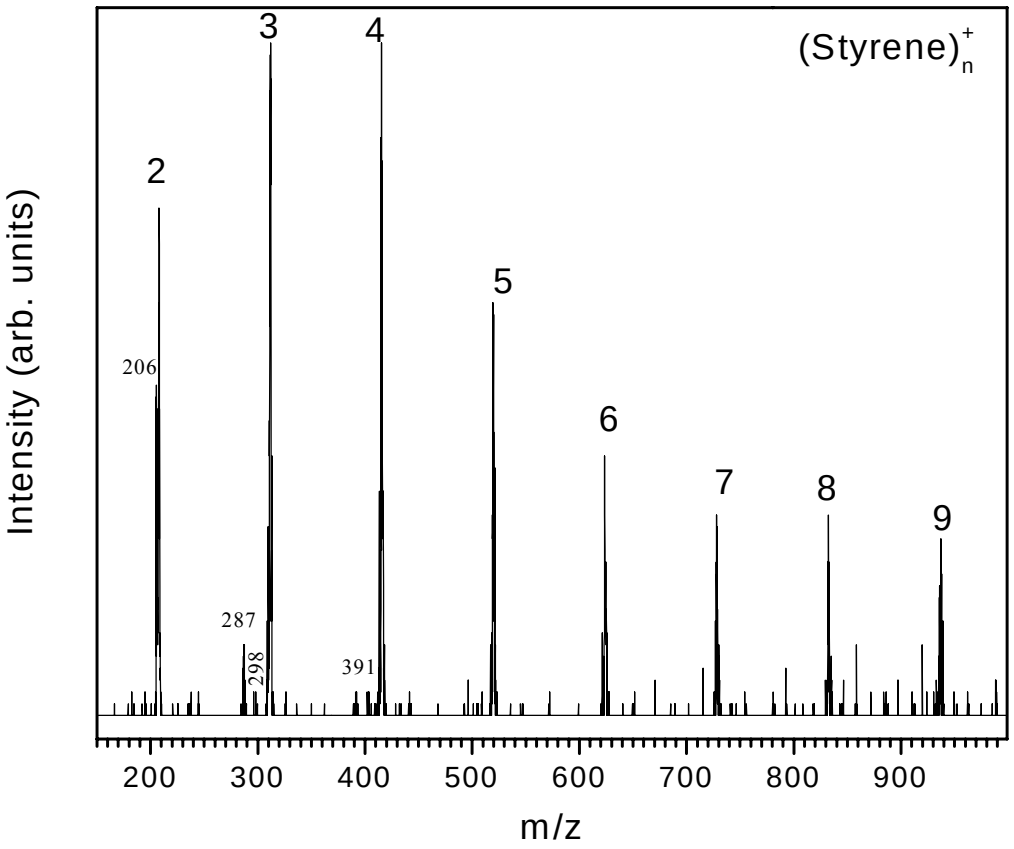

Figure 12: Mass Spectrum of $(C_8H_8)_n^+$ clusters ions produced by 90 eV Electron Impact ionization, and then injected into1.159 Torr He with 15 eV injection energy.

3.2.1 Dissociation products of mass selected styrene oligomer ions

3.2.2 Dissociation products of styrene monomer ion, $C_8H_8^+$

Figure 13 shows the mass spectra when the mass selected styrene monomer is injected into pure helium with injection energies of (E_{lab}) 10, 30, and 70 eV. At 10 eV the styrene monomer survived without fragmentation, however at 30 eV the mass spectrum shows masses at 104 with the highest intensity, and small fragments with m/z 103, 78 and 77. These fragments represent the loss of hydrogen, C_2H_5, and C_2H_4, respectively. At 70 eV the mass spectrum shows peaks with m/z of 103, 78 and 77 with the highest intensity, and small fragments with m/z 104, 102, 95, 89, 65, 63, 52, 39, and 27. The results are summarized in Table 1.

Table 1: Dissociation products of mass selected styrene ion $C_8H_8^+$.

Observed Massed (m/z)	Formula
104	$C_8H_8^+$
103	$C_8H_7^+$
102	$C_8H_6^+$
89	$C_7H_5^+$
78	$C_6H_6^+$
77	$C_6H_5^+$
65	C_5H_5
63	$C_5H_3^+$
52	$C_4H_4^+$
27	$C_2H_3^+$

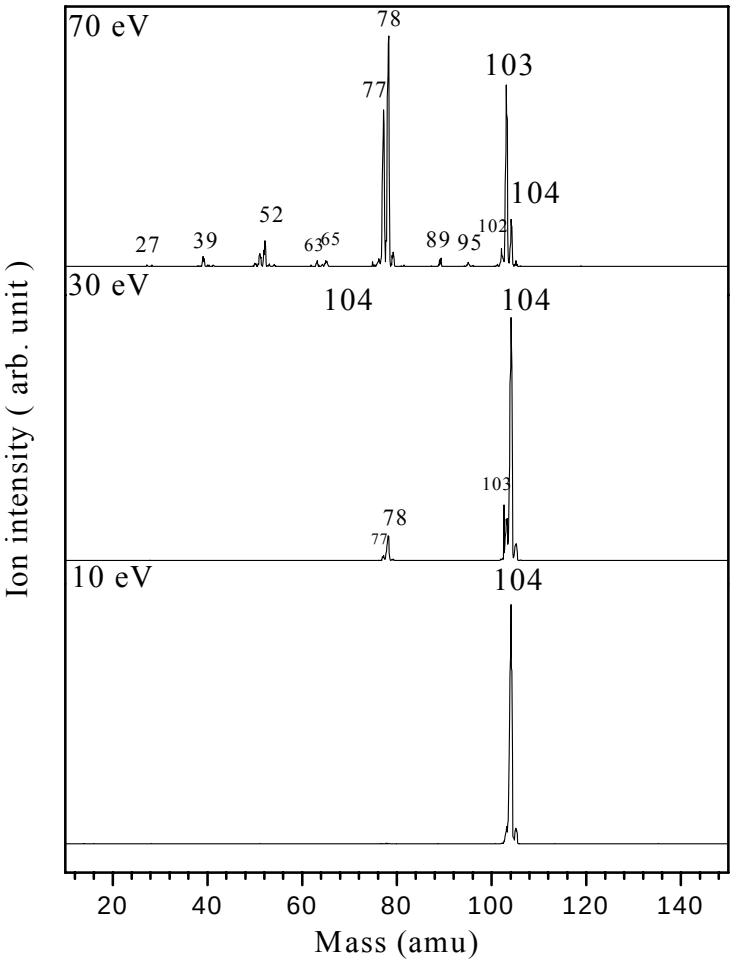

Figure 13 : Mass spectra of the mass selected Styrene monomer ions $(C_8H_8)^+$ obtained by 90 eV Electron Impact ionization, then Injected into 1.182 Torr He with different injection energies (lab) (10, 30 and 70 eV). Experimental conditions are: Source temperature is 70 ^oC, 60 psi He as carrier gas, drift cell temperature is 32.1 ^oC and first quadrupole was set in mass selection mode at 104 amu.

3.2.3 Dissociation products of styrene dimer ion, $C_{16}H_{16}^{+}$

Figure 14 shows the mass spectra when the mass selected styrene dimer was injected into pure helium with energies of 10,15, 50 and 70 eV. At 10 eV, the mass spectrum shows the styrene dimer ion $C_{16}H_{16}^{+}$ (~90 %),(~10 %) styrene monomer $C_8H_8^{+}$. At 50 eV, the mass spectrum shows peaks with m/z of 104 (~90%) with the highest intensity, and small fragments with m/z = 193, 180 130 and 117, corresponding to the loss of CH_3, C_2H_4, C_6H_6 and C_7H_7, respectively. At 70 eV, in this case, the mass spectrum shows new peaks with m/z = 179, 178, 167, 166, 165, 115, 92, 91 78 and 77. These observed peaks and their relative intensities are summarized in Table 2.

Table 2: Dissociation products of mass selected styrene Dimer ion $C_{16}H_{16}^{+}$.

Observed mass (m/z)	Formula.	Relative Intensity			
		10 eV	15 eV	50 eV	70 eV
208	$C_{16}H_{16}^{+}$	1000	1000	14	7
193	$C_{15}H_{13}^{+}$	5	2	6	7
180	$C_{14}H_{12}^{+}$	5	4	17	20
179	$C_{14}H_{11}^{+}$	5	2	2	10
178	$C_{14}H_{10}^{+}$	5	2	2	3
167	$C_{13}H_{10}^{+}$	5	2	2	3
166	$C_{13}H_{9}^{+}$	5	2	2	10
165	$C_{13}H_{9}^{+}$	5	2	2	7
130	$C_{10}H_{10}^{+}$	5	2	17	17
117	$C_{9}H_{9}^{+}$	0	2	8	10
115	$C_{9}H_{7}^{+}$	0	0	0	13
104	$C_{8}H_{8}^{+}$	77	154	1000	1000
92	$C_{7}H_{8}^{+}$	0	2	4	7
91	$C_{7}H_{7}^{+}$	0	2	14	17
78	$C_{6}H_{6}^{+}$	0	2	0	7
77	$C_{6}H_{5}^{+}$	0	2	0	0

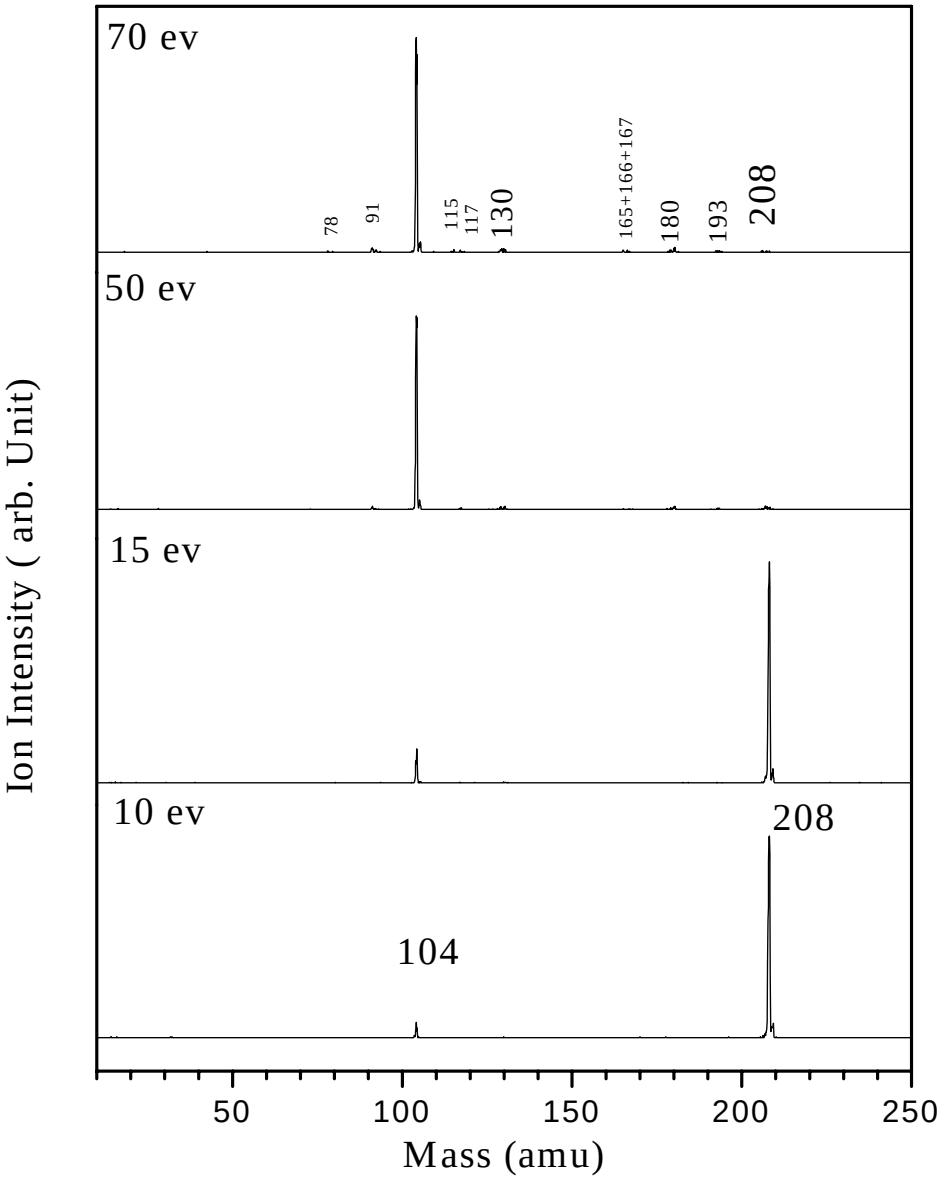

Figure 14: Mass spectra of the mass selected styrene dimer ions, $C_{16}H_{16}^{+}$ obtained by 90 eV Electron Impact ionization injected into 1.182 Torr He with different injection energies (lab) (10, 30 and 70 eV). Experimental conditions are: Source temperature is 70 ^{o}C, 60 psi He as carrier gas, Drift cell temperature is 32.1 ^{o}C and first quadrupole was set on mass selection mode at 208 amu.

The fragmentation pattern and dissociation products of mass selected styrene dimer, $C_{16}H_{16}^{+}$, is summarized in Scheme 3.

Scheme 3: Dissociation products of mass selected Styrene dimer ion $C_{16}H_{16}^{+}$

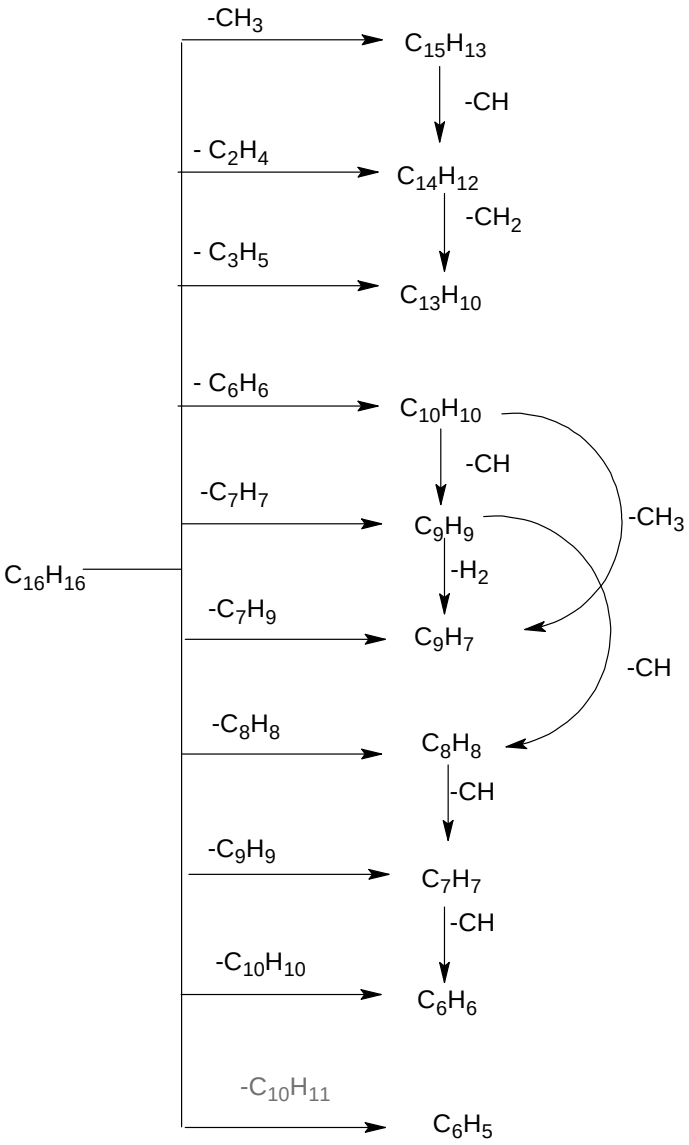

By comparing the mass spectra of the mass selected styrene dimer to the monomer, it is worth noting that the peak with m/z of 91 (C_7H_7) was not observed in the case of the monomer fragments.

A preliminary study was conducted where the $(styrene)_n^+$ was mass selected for n = 1and 2 and injected into the drift cell which contains He gas with different injection energies (10 - 70 eV). The ionization energy was varied from 30-120 eV at each injection energy and the ATDs were collected as well as the mass spectra. This is demonstrated in Figure 15. No difference was observed in the dissociation products when the ionization energy was increased. Also, the ATDs were collected for both the monomer and the dimer at different injection energies and different electron impact energies. This is illustrated in Figure 15. There was no difference in the arrival time or in the peak shape. These results suggest that no isomer formation was produced by the EI ionization process. Of course, this dose not eliminates the possibility of having isomer ions that exhibit similar arrival time distributions.

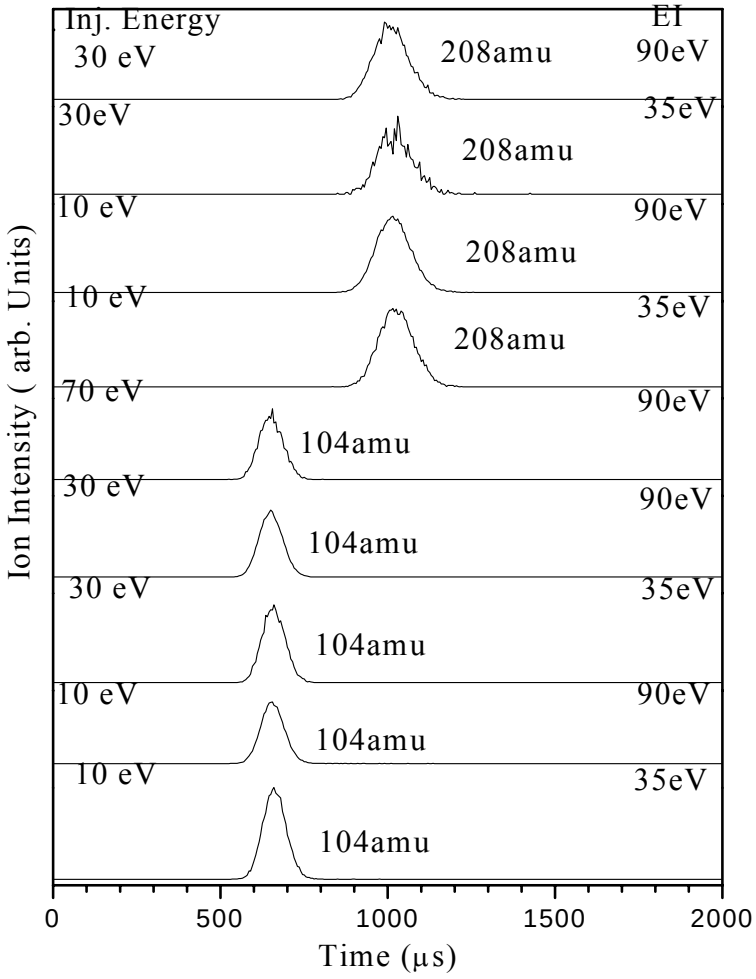

Figure 15: Arrival time distribution of mass selected $C_8H_8^+$ ions (lower five panels) and the styrene dimer ions $C_{16}H_{16}^+$ (upper four panels). Experimental conditions are : 50 μs pulse width, injection energy is as shown , 1.182 Torr He inside the drift cell, 20 V voltage difference between the entrance and the exit lenses and and the cell Temperature at 32.1 ^oC (E/N = 5.97 Td).

3.2.4 Dissociation Products of Mass Selected Styrene Trimer ion, $C_{24}H_{24}^+$

Figure 16 shows the mass spectra of the mass selected styrene trimer $C_{24}H_{24}^+$ that was injected into pure helium with injection energies 15, 30 and 70 eV. At 15 eV the mass spectrum shows three masses, the m/z 312 amu with the highest peak of 90%, m/z 208 with a peak of 4%, and m/z 206 with a peak of 6%. There are no fragments corresponding to the loss of CH_3 or C_2H_4, as in the case of the styrene dimer ion.

In the case of injection energy of 30 eV, the mass peak at m/z 312 remains the most intense peak, followed by several peaks at m/z = 208, 207, 206, 234, 221, 193, 180, 130, 129, 128, 104, 92, 91,and 85. At an injection energy of 70 eV, the m/z 180 amu has the most intense peak, and there are new peaks at m/z of 166,143, and 117. This is summarized Table 3.

In general, the dissociation products of mass selected styrene trimer, $C_{24}H_{24}^+$ (312), correspond to the loss of C_6H_6 , C_7H_7, C_8H_8, and $C_{10}H_{12}$ thus generating the peaks at m/z = 234, 221, 208 and 180 respectively. At the highest injection energy, the highest intense peak is the m/z 180 ($C_{14}H_{12}$), which corresponds to the loss of $C_{10}H_{12}$ from $C_{24}H_{24}^+$. The fragmentation pattern and the dissociation products are summarized in Scheme 2.

Table 3: Dissociation products of mass selected styrene trimer ion $C_{24}H_{24}^{+}$

Observed mass (m/z)	Formula.	Relative Intensity		
		15 eV	30 eV	70 eV
312	$C_{24}H_{24}^{+}$	908	519	12
234	$C_{18}H_{18}^{+}$	27	90	12
221	$C_{17}H_{17}^{+}$	0	45	35
208	$C_{16}H_{16}^{+}$	27	139	82
207	$C_{16}H_{15}^{+}$	0	45	94
206	$C_{16}H_{14}^{+}$	38	60	59
193	$C_{15}H_{13}^{+}$	0	4	47
180	$C_{14}H_{12}^{+}$	0	60	165
166	$C_{13}H_{9}^{+}$	0	4	12
143	$C_{11}H_{11}^{+}$	0	0	59
130	$C_{10}H_{10}^{+}$	0	4	24
129	$C_{10}H_{9}^{+}$	0	0	71
128	$C_{10}H_{8}^{+}$	0	0	0
117	$C_{9}H_{9}^{+}$	0	0	35
104	$C_{8}H_{8}^{+}$	0	15	141
92	$C_{7}H_{8}^{+}$	0	10	71
91	$C_{7}H_{7}^{+}$	0	0	82

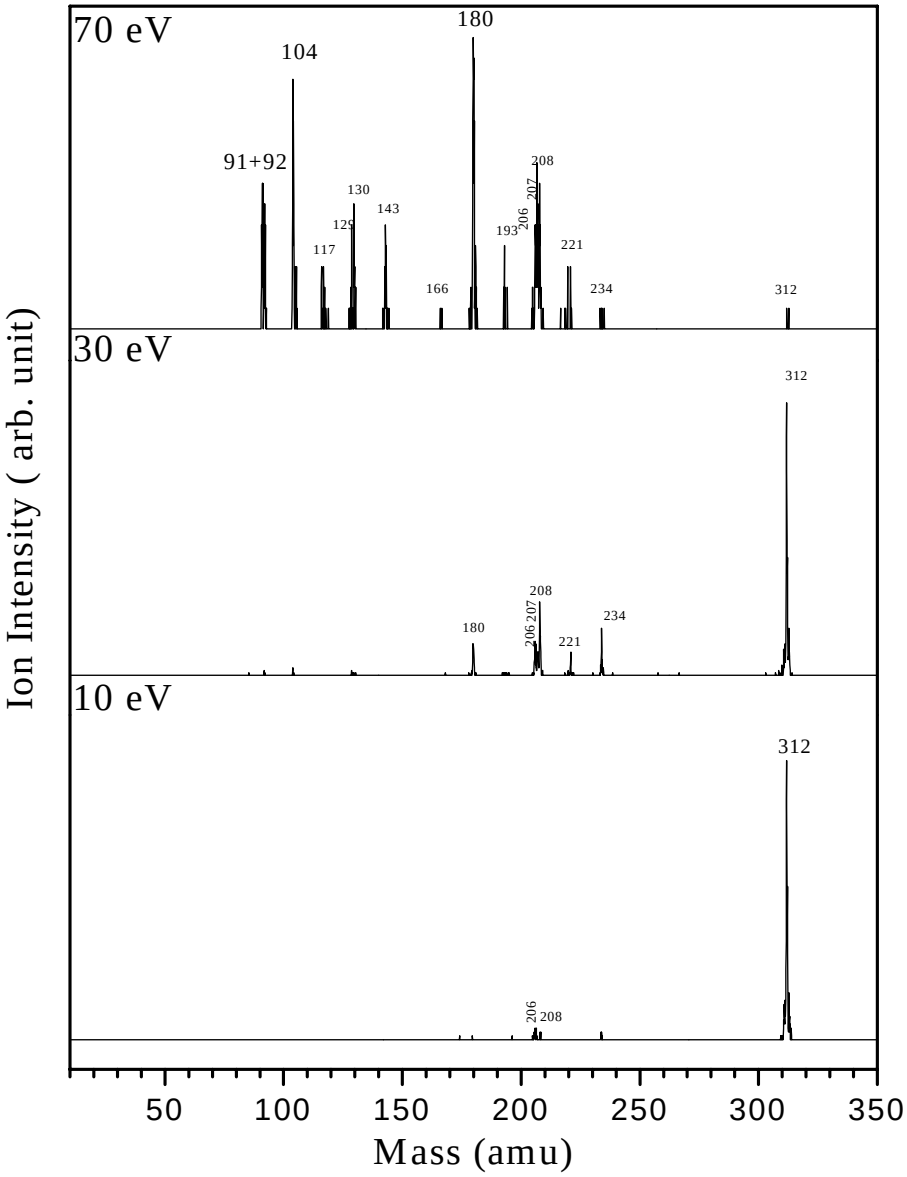

Figure 16: Mass spectra of the mass selected styrene trimer ions, $C_{24}H_{24}^{+}$ obtained by 90 eV Electron Impact Ionization injected into 1.154 Torr He with different injection energies (lab) (10, 30 and 70 eV). Experimental conditions are: Source temperature is 80 ^{o}C, 60 psi He as carrier gas, drift cell temperature is 30.7 ^{O}C and first quadrupole was set on mass selection mode at 312 amu.

Scheme 4: Dissociation products of mass selected Styrene trimer ion $C_{24}H_{24}^{+}$.

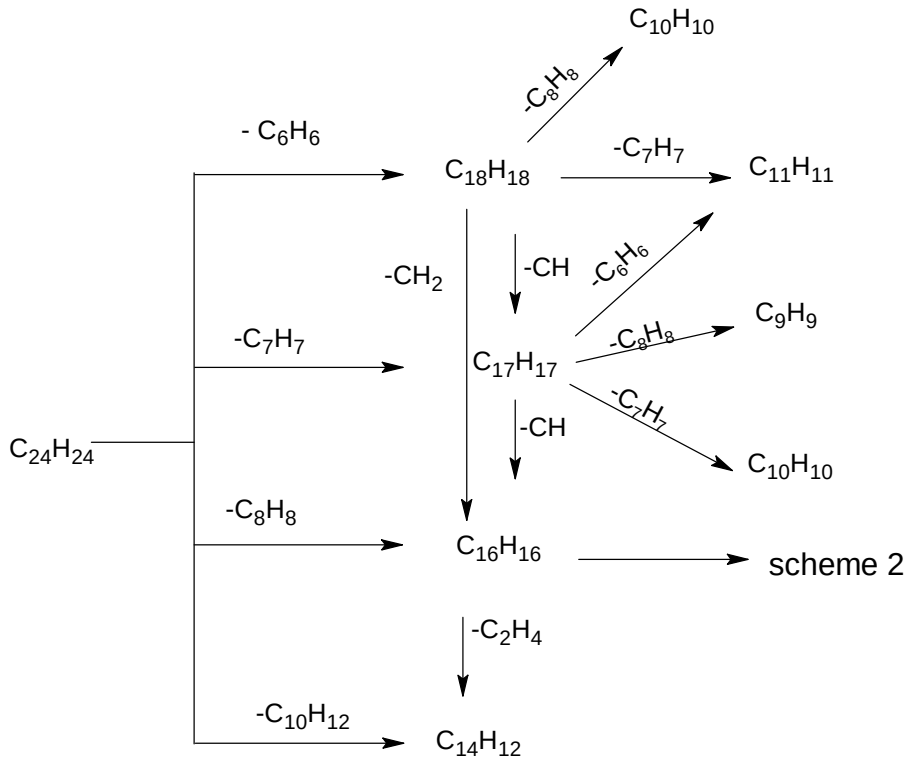

3.2.5 Dissociation Products of Mass selected Styrene tetramer ion, $C_{32}H_{32}^{+}$

Figure 17 shows the mass spectra, when the mass selected styrene tetramer was injected into pure helium with injection energies 15, 30 and 70 eV. At 15 eV the mass spectrum shows peaks m/z = 416 (the most intense peak), 208, 206, 312, 221, and 130, in intensity decreasing order.

At 30 eV the mass spectrum shows peaks at m/z 416 amu (still the most intense peak), followed by 208, 206, 312, 193 and 104. At 70 eV the m/z 104 is the most intense peak, followed by the peaks at m/z = 208, 311, 312, 416, 206, 207, 180, 325, 338, 193, 145, 129, 117, 92 and 91. This is summarized in Table 4.

Table 4: Dissociation products of mass selected styrene tetramer ion $C_{32}H_{32}^{+}$.

Observed m/z (amu)	Formula.	Observed m/z (amu)	Formula
416	$C_{32}H_{32}^{+}$	208	$C_{16}H_{16}$
338	$C_{26}H_{26}^{+}$	207	$C_{16}H_{15}$
325	$C_{25}H_{25}^{+}$	206	$C_{16}H_{14}$
312	$C_{24}H_{24}^{+}$	193	$C_{15}H_{13}$
311	$C_{24}H_{23}^{+}$	180	$C_{14}H_{12}$
310	$C_{24}H_{22}^{+}$	141	$C_{11}H_{11}$
297, 298 299	$C_{23}H_{23}^{+}$ $C_{23}H_{22}^{+}$ $C_{23}H_{21}^{+}$	130	$C_{10}H_{10}$
284	$C_{22}H_{20}^{+}$	117	$C_{9}H_{9}$
246	$C_{19}H_{18}^{+}$	104	$C_{8}H_{8}$
234	$C_{18}H_{18}^{+}$	92	$C_{7}H_{8}$
221	$C_{17}H_{17}^{+}$	91	$C_{7}H_{7}$

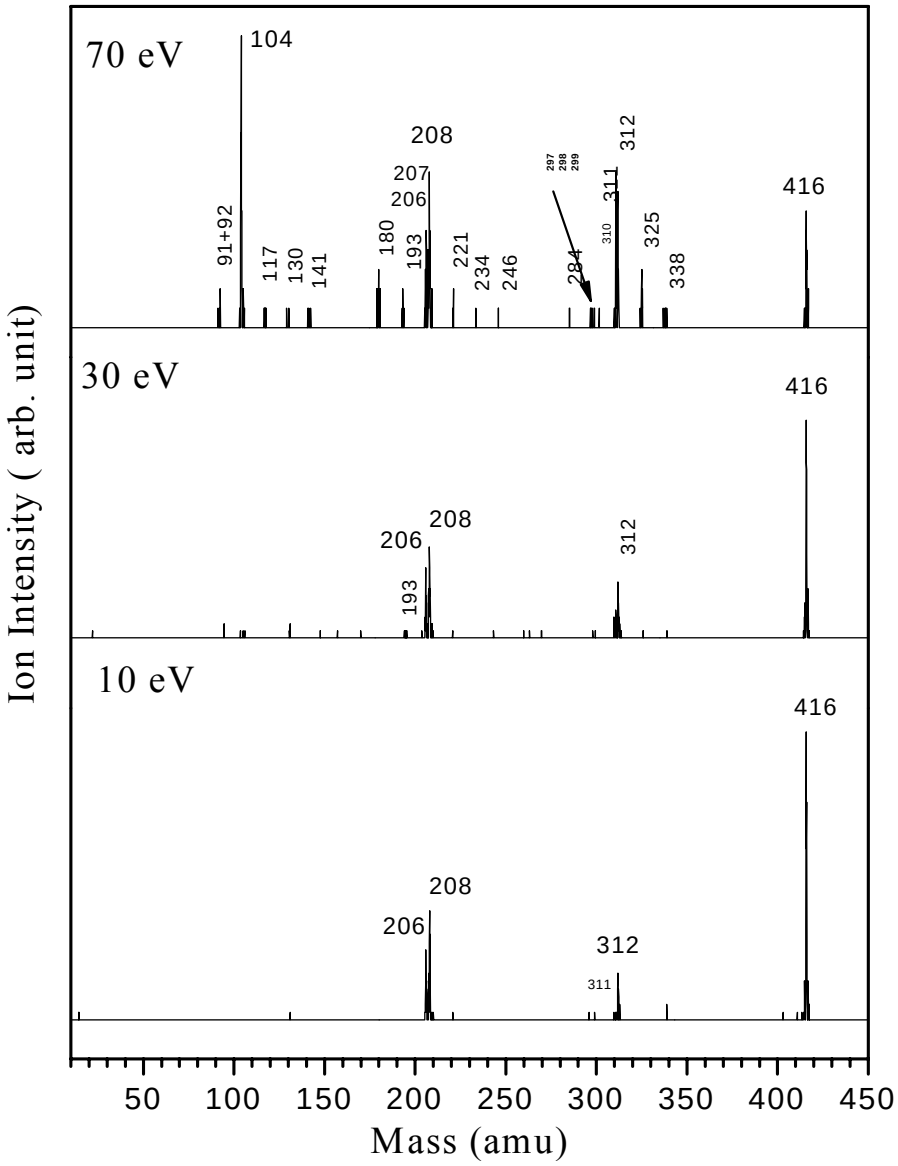

Figure 17: Mass spectra of the mass selected styrene tetramer ions, $C_{32}H_{32}^{+}$ obtained by 90 eV Electron Impact Ionization injected into 1.154 Torr He with different injection energies (lab) (15, 30 and 70 eV). Experimental conditions are: Source temperature is 80 ^{o}C, 60 psi He as carrier gas, drift cell temperature is 30.7 ^{o}C and first quadrupole was set on mass selection mode at 416 amu.

Simple comparisons between the mass selected styrene tetramer and trimer dissociation products ions to those in styrene dimer ion, indicate that no fragments corresponding to the loss of CH_3 or C_2H_4 are observed. In the case of mass selected tetramer dissociation products, peaks at m/z = 299, 298, and 297 were observed. This can be explained by the loss of CH from the m/z peaks 312, 311, and 310 respectively. However, none of these peaks were observed when styrene trimer was mass selected. This suggests that these fragments are produced from the dissociation of the styrene tetramer. The fragment at m/z of 284 can be explained by the loss of C_2H_4 from the styrene trimer, but again this peak at m/z 284 was not observed in the dissociation products of the mass selected styrene trimer ion. This strongly suggests that the m/z 284 peak corresponds to the loss of $C_{10}H_{12}$ from the styrene tetramer ion. This conclusion is supported by the fact that the mass selected styrene trimer dissociates mainly to $C_{14}H_{12}^+$ (m/z 180), as displayed in Figure 16, which correspond to a loss of $C_{10}H_{12}$ from the styrene trimer ion, $C_{24}\ H_{24}^+$.

In general, the dissociations products of the mass-selected styrene tetramer, $C_{32}H_{32,}^+$(m/z 416) show fragments corresponding to the loss of C_6H_6 , $C_7H_{7,}$ $C_8H_{8,}$ C_9H_9 and $C_{10}H_{12}$ to give m/z peak at 338, 325, 312 , 299 and 284, respectively. The fragmentation pattern and the dissociation products are summarized in Scheme 3.

Scheme 5: Dissociation products of the mass selected styrene tetramer ion, $C_{32}H_{32}^{+}$.

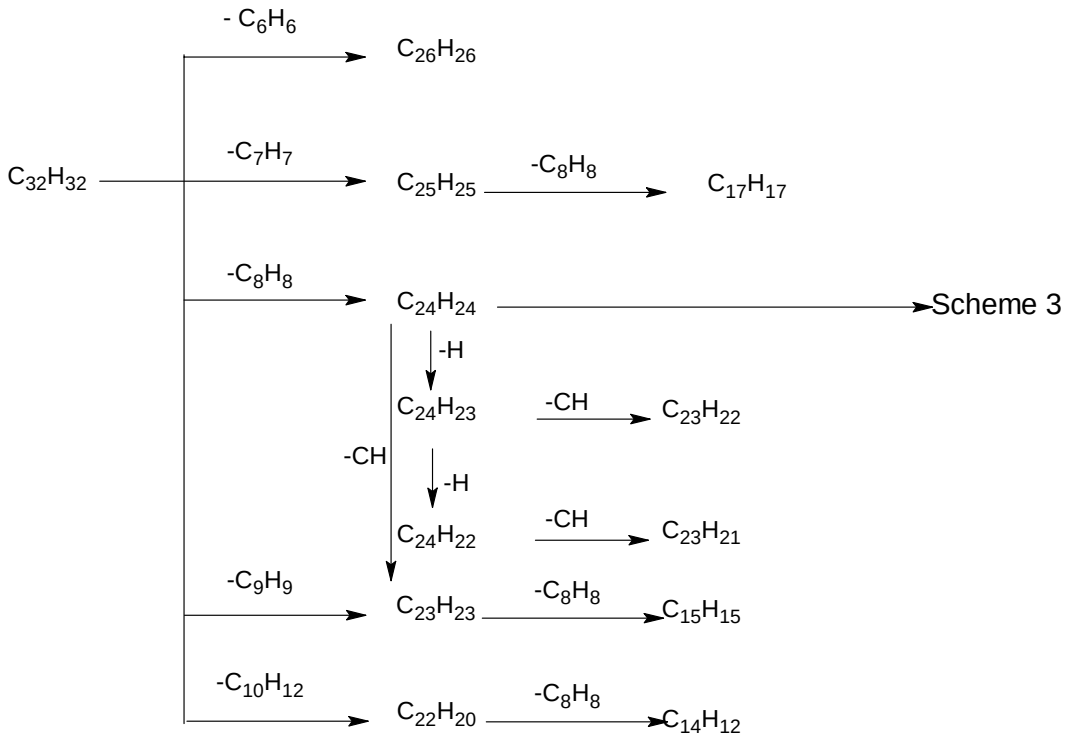

3.2.6 Dissociation Products of Styrene pentamer ion, $C_{40}H_{40}^{+}$

Figure 18 shows the mass spectra when the mass selected styrene pentamer ion, $C_{40}H_{40}^{+}$ was injected into pure helium with injection energies of 10,15, 30 and 60 eV. At injection energy of 10 eV the mass spectrum shows m/z peaks at 520, the most intense peak, followed by 312, 208, and 206. At 15 eV, 512 amu is still the most intense peak, followed by 312, 311, 206, 208, and 416. At 30 eV 520 m/z is still the most intense peak followed by peaks at m/z = 312, 311, 208, 206, 416,and 297. At 65 eV the m/z 520 peak is still the most intense peak followed by peaks at m/z = 312, 311, 310, 208, 206, 416, 415, 414, 234 and 324. The mass spectrum also shows small peaks at m/z = 505, 478, 442, 428, 130, 117, 104 and 91. This is summarized in Table 5.

Table 5: Dissociation products of mass selected styrene pentamer ion $C_{40}H_{40}^{+}$

Observed m/z (amu)	Formula.	Observed m/z (amu)	Formula
520	$C_{40}H_{40}^{+}$	234	$C_{18}H_{18}^{+}$
505	$C_{39}H_{37}^{+}$	221	$C_{17}H_{17}^{+}$
478	$C_{37}H_{34}^{+}$	208	$C_{16}H_{16}^{+}$
442	$C_{34}H_{34}^{+}$	207	$C_{16}H_{15}^{+}$
429	$C_{33}H_{33}^{+}$	206	$C_{16}H_{14}^{+}$
416	$C_{32}H_{32}^{+}$	193	$C_{15}H_{13}^{+}$
338	$C_{26}H_{26}^{+}$	180	$C_{14}H_{12}^{+}$
325	$C_{25}H_{25}^{+}$	141	$C_{11}H_{11}^{+}$
312	$C_{24}H_{24}^{+}$	130	$C_{10}H_{10}^{+}$
311	$C_{24}H_{23}^{+}$	117	$C_{9}H_{9}^{+}$
310	$C_{24}H_{22}^{+}$	104	$C_{8}H_{8}^{+}$
297, 298 299	$C_{23}H_{23}^{+}$ $C_{23}H_{22}^{+}$ $C_{23}H_{21}^{+}$	92	$C_{7}H_{8}^{+}$
284	$C_{22}H_{20}^{+}$	91	$C_{7}H_{7}^{+}$
246	$C_{19}H_{18}^{+}$		

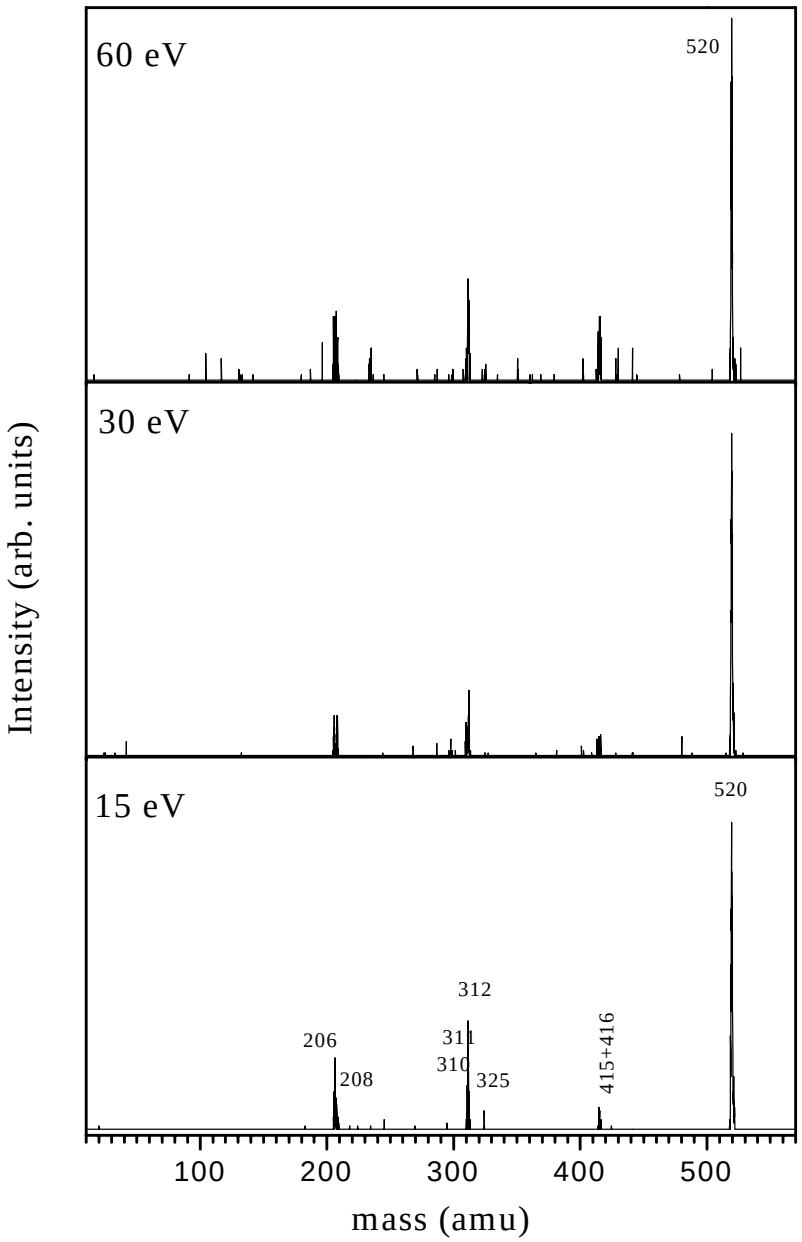

Figure 18: Mass spectra of the mass selected styrene pentamer ions, $C_{40}H_{40}^{+}$ obtained by 90 eV Electron Impact Ionization injected into 1.154 Torr He with different injection energies (lab) (15, 30 and 60 eV). Experimental conditions are: Source temperature is 70 ^{o}C, 100 psi He as carrier gas, drift cell temperature is 30.0 ^{o}C and first quadrupole was set on mass selection mode at 520 amu.

In general, the mass selected styrene pentamer ion $C_{40}H_{40}^{+}$ dissociates mainly to dimer and trimer, a small amount to the tetramer, with no dissociation into the styrene monomer. The dissociation products of the mass-selected styrene pentamer $C_{40}H_{40}^{+}$ (m/z 520) also show fragments corresponding to the loss of CH_3, C_3H_6, C_6H_6 , C_7H_7, and C_8H_8 giving m/z peaks at 505, 478, 442, 429, and 416, respectively. The fragmentation pattern and the dissociation products are summarized in Scheme 4. It should be noted that the loss of CH_3 was only observed in the dissociation products of styrene dimer and pentamer ions.

Scheme 6: Dissociation products of mass selected Styrene pentamer ion $C_{40}H_{40}^{+}$

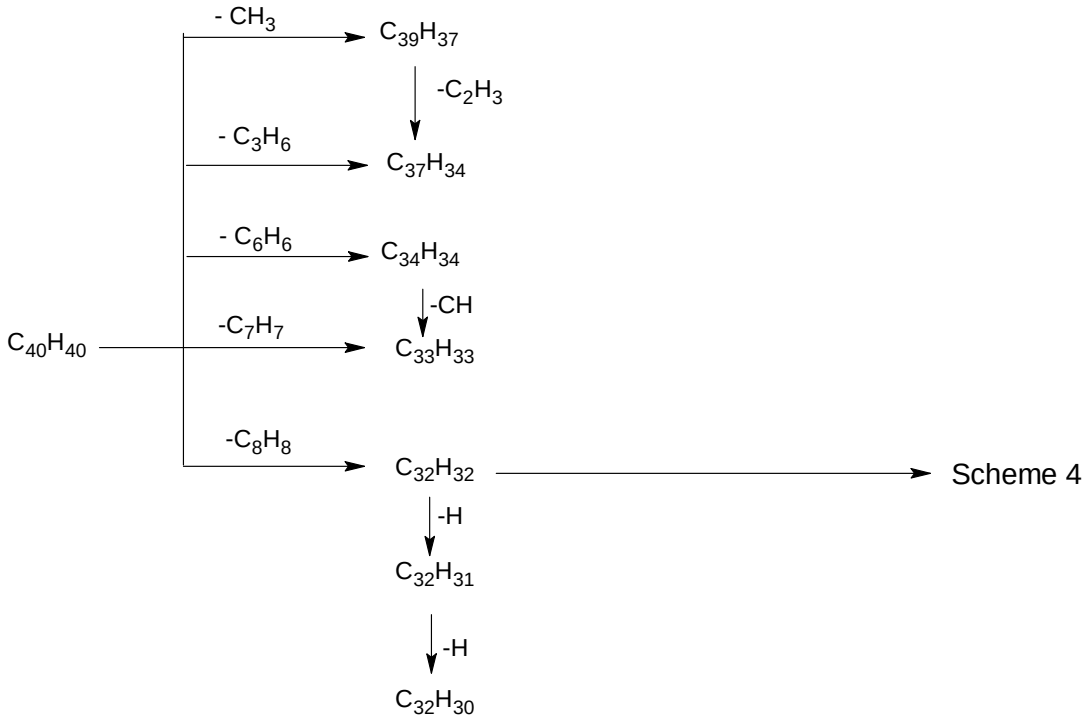

3.3 Mobilities of the Styrene Cluster ions

In this section the mobility measurements for styrene ions $(C_8H_8)_n^+$ are summarized for n = 1-8 . The first part summarizes the mobility measurements at room temperature; the second part summarizes the mobility measurements for styrene dimer and trimer ions at different temperatures.

3.3.1 Mobility of Styrene cluster ions (1-8) at room temperature

The mobility of the styrene oligomers cation $(C_8H_8)_n^+$, for n = 1-8 were measured. In the case of the Oligomer ions with n = 1-5, the source was operated in pulsed beam mode. The measurements were conducted using mass selection in the first quadrupole, and the second quadrupole was operated in the mass selection mode. In the case of n = 6- 8, the first quadrupole was operated in RF only mode. All of the experiments were conducted using a 50 μs gate width. In the case of the styrene monomer, ion mobility measurements were described in chapter 2, section 2.4.

In the case of the styrene dimer ion mobility measurements were conducted at room temperature with helium as the buffer gas. First the styrene dimer ion was mass- selected by setting the first quadrupole in mass selection mode and mass scan with the second quadrupole, and then the mass spectrum was obtained. The mass spectrum is shown in Figure 19. The typical set of ATDs was then recorded at constant temperature and pressure with different electric fields across the drift cell. These were obtained by setting the second quadrupole in single ion mode and the average arrival times were recorded. The results are shown in Figure 20. Figure 21 shows the excellent linear correlation (R^2 =

0.9999) of the recorded data when plotted as t_d vs. *P/V*. The data shown in Figure 21 yields a slope of 1.553×10^{-2} (s·V/Torr), and an intercept of 88.02 μs (time spent out side the cell). The average reduced mobility, $K_o = 5.8 \pm 0.2$ $cm^2.V^{-1}.s^{-1}$ is calculated using Equation 5. Figure 22 displays a comparison of the experimental arrival time distribution to the predicted one from transport theory using Equation 6. The comparison shows an excellent agreement between the experimental and the predicted ATDs. This may suggest that only one structure is present or that there is more than one structure, which exhibt the same mobility. The mobilities of the higher styrene oligomers ion $(C_8H_8)_n^+$, with n = 3-8 were measured and the measurements were repeated several times, Figure 23 displays typical ATDs of the styrene oligomers ions $(C_8H_8)_n^+$ for n = 1-8 and Figure 24 shows the corresponding plots of t_d Vs P/V used to calculate the mobilities of the styrene oligomers ions $(C_8H_8)_n^+$. Table 6 summarizes the gas phase mobilities of $^+(Styrene)_n$ for n = 1-8 at room temperature. Figure 26 through Figure 30 display the comparisons of the experimental arrival time distribution to the predicted distributions from transport theory assuming that the ATD peak contains only one structure for $(Styrene)_n^+$ for n = 3-8, respectively.

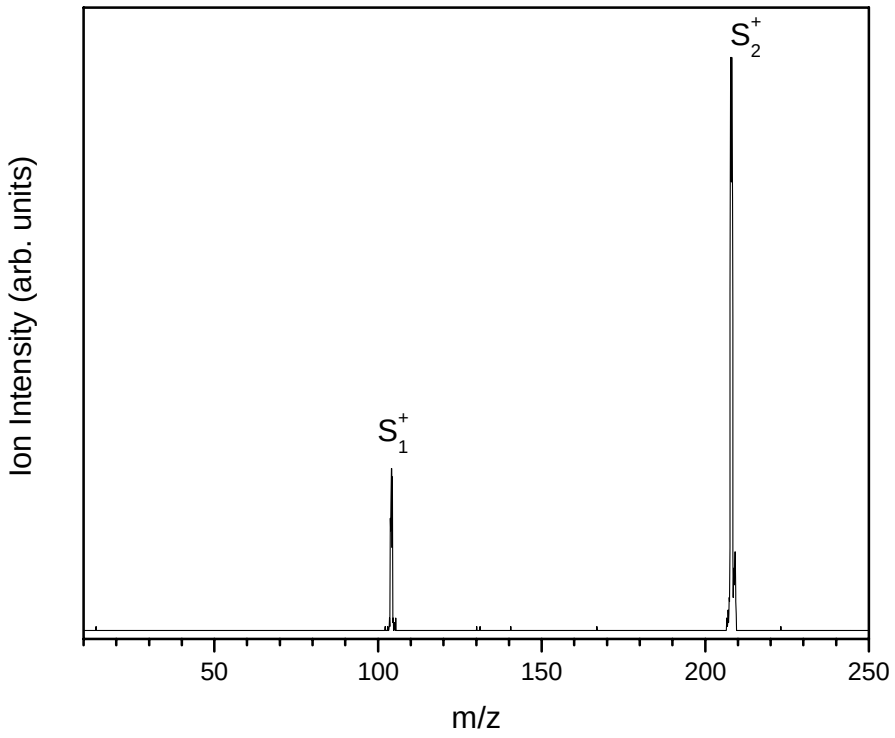

Figure 19: Mass Spectrum of the mass selected $(C_8H_8)_2^+$ obtained by 94 eV Electron Impact ionization. Experimental conditions are: Source temperature is 70 ^oC, 40 psi He 50 μs pulse width, injection energy is 15 eV, 1.136 Torr He inside the drift cell, cell temperature is 31.9 ^oC, 25 V .

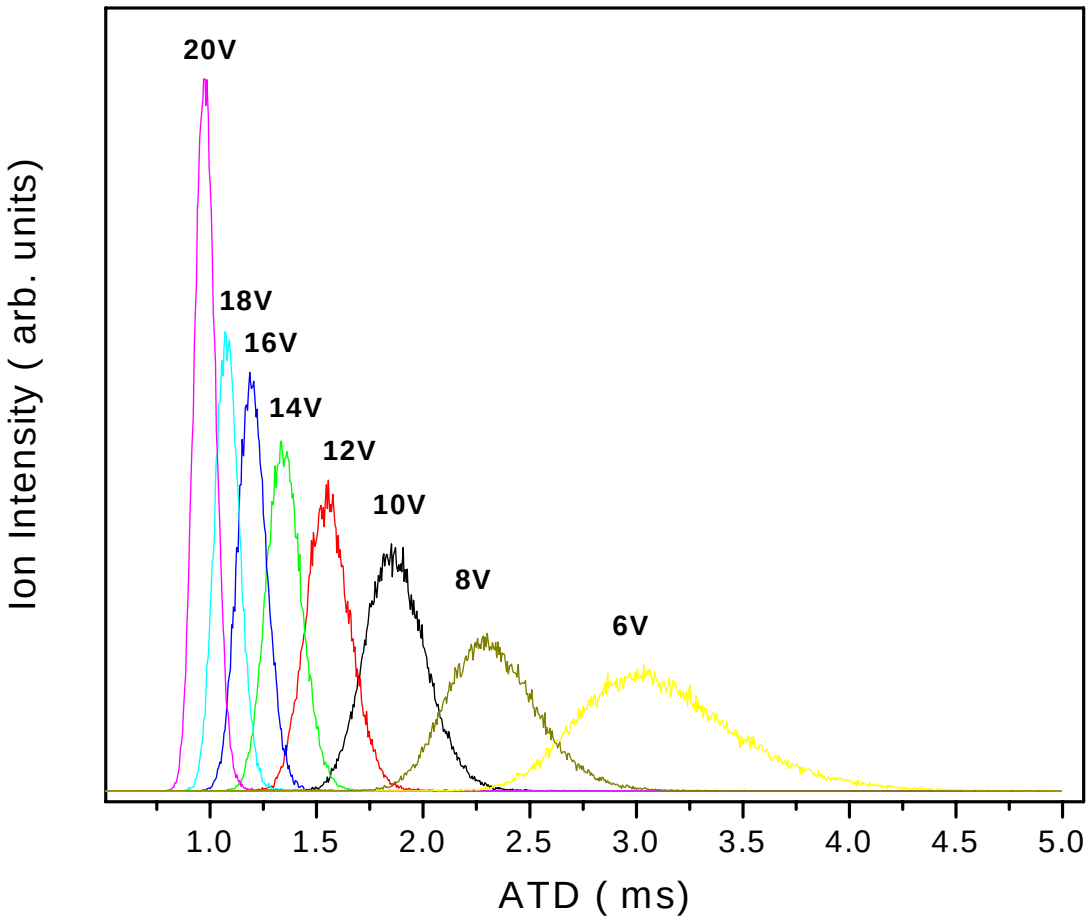

Figure 20: Arrival time distributions of the mass selected $C_{16}H_{16}^{+}$ ions. Experimental conditions are: 50 μs pulse width, injection energy is 15 eV, 1.136 Torr He inside the drift cell, cell temperature is 31.9 ^{o}C, 25 V the voltage difference between the entrance and the exit lenses varies from 20 V to 6 V.

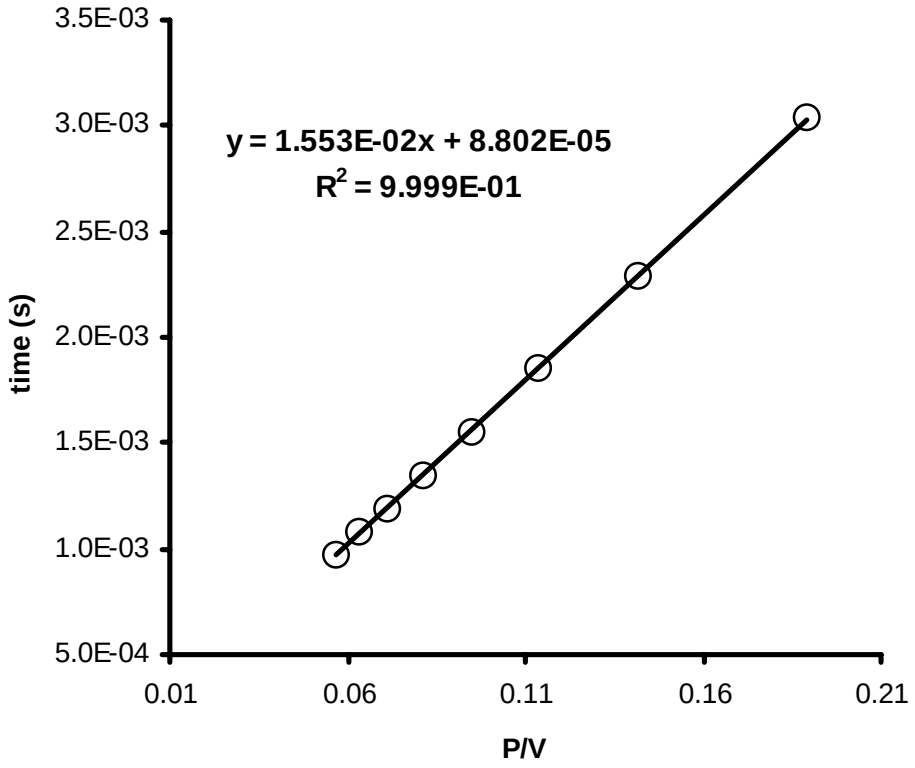

Figure 21: Plot of the arrival time vs P/V for the mass selected styrene dimer ions $C_{16}H_{16}^{+}$. The circles are the experimental and the solid line is the Least Square linear fit to the data points with $R^2 = 0.9999$.

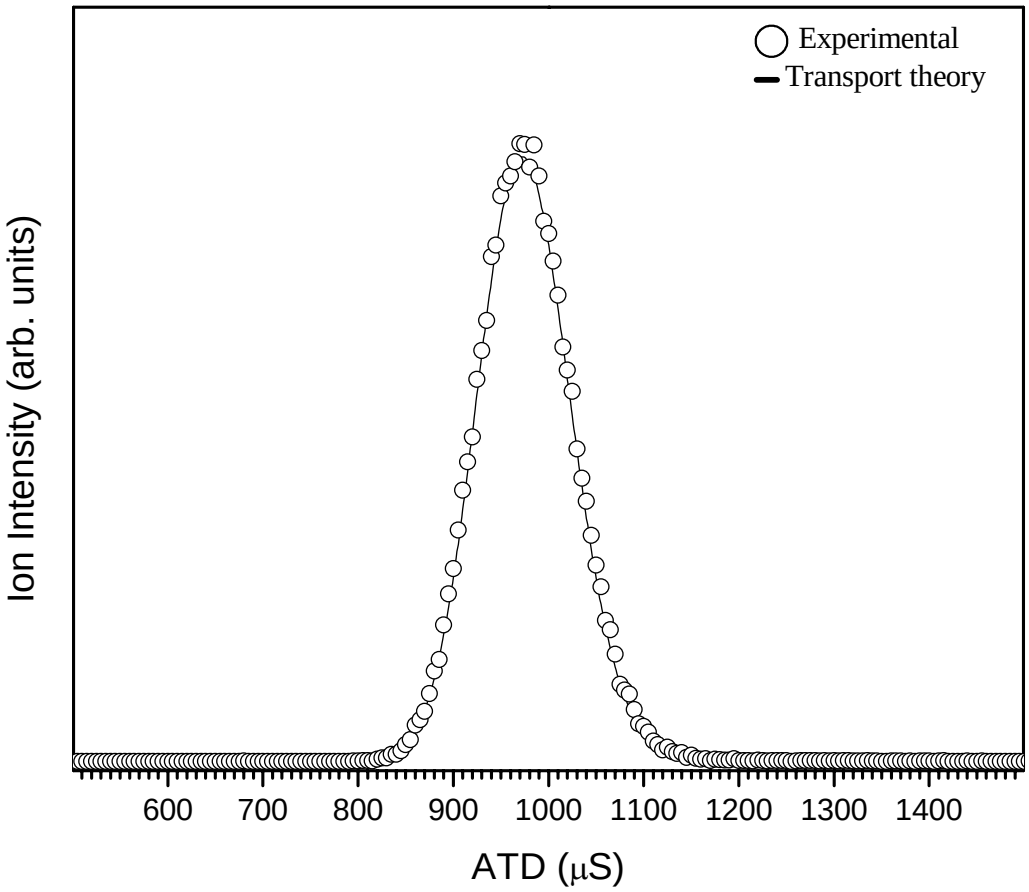

Figure 22: Arrival time distribution of mass selected $(C_8H_8)_2^+$ ions (circles) and the predicted distribution from transport theory (solid line). Experimental conditions are : 50 μs pulse width, injection energy is 15 eV, 1.136 Torr He inside the drift cell, cell temperature is 31.9 ^oC, 25 V the voltage difference between the entrance and the exit lenses and E/N = 6.26 Td. The reduced mobility $K_o = 5.86\ cm^2V^{-1}s^{-1}$.

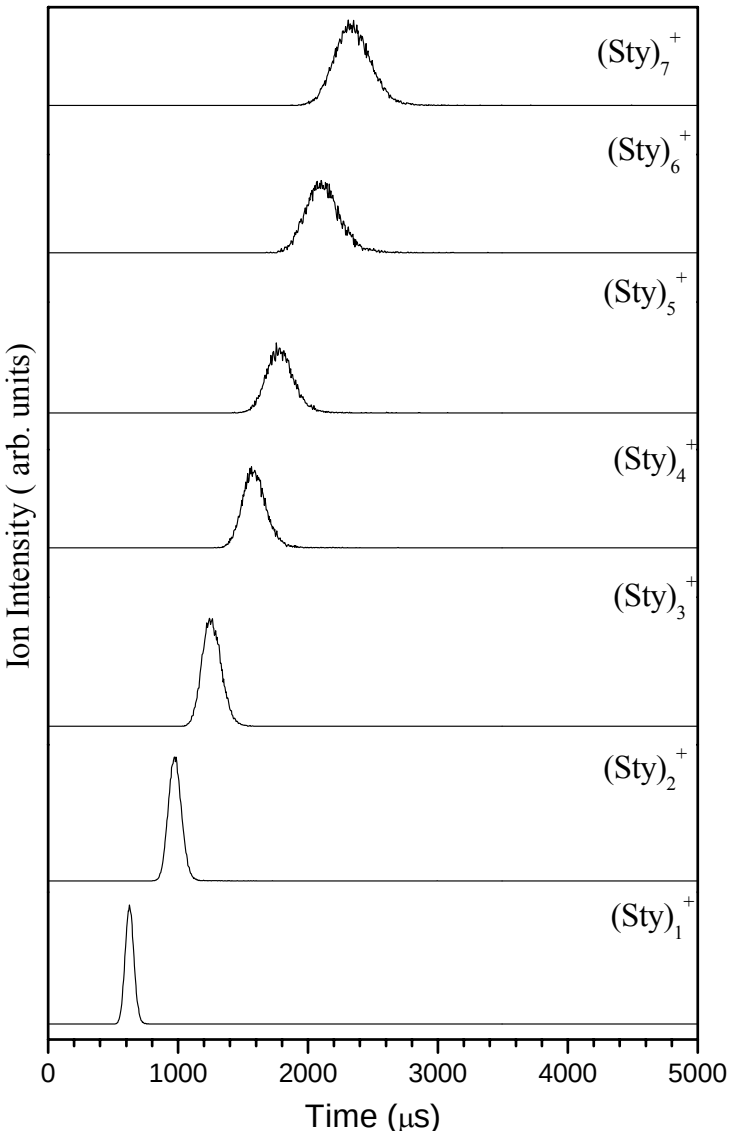

Figure 23 : The measured Arrival time distribution of $(C_8H_8)_n^+$ ions, with n = 1-7 with same E/N = 6.2 3 0.1.

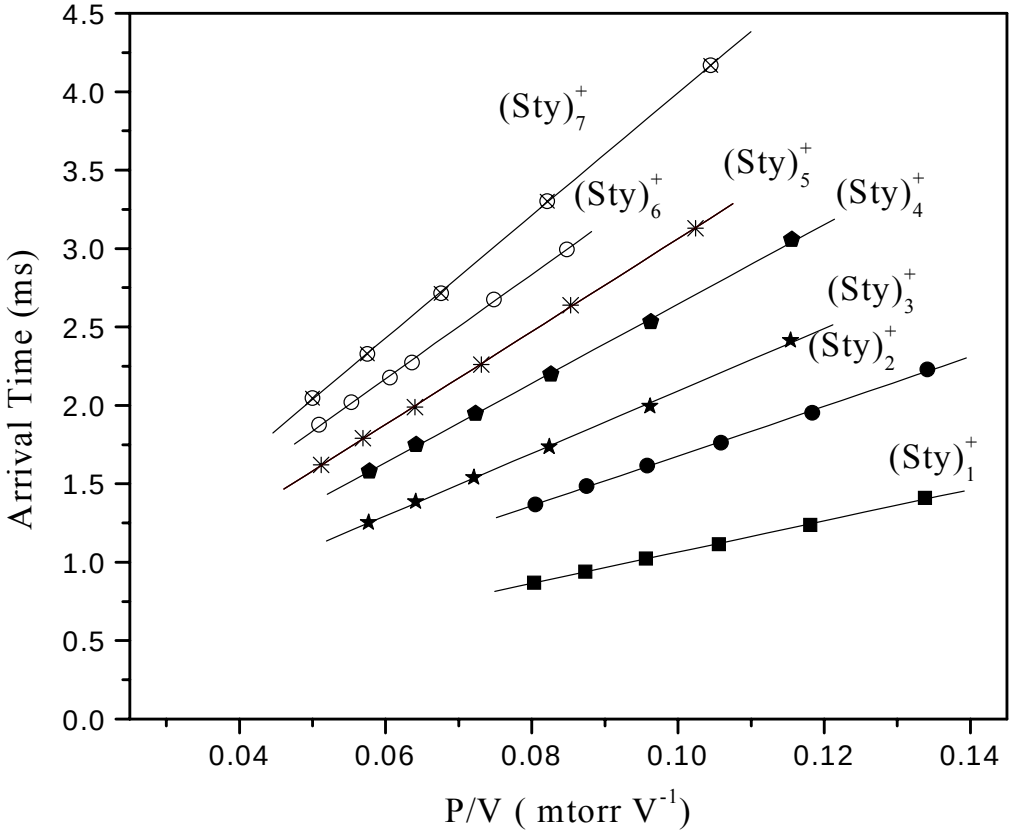

Figure 24: Plot of P/V vs average arrival time for styrene clusters ions (1- 7). Legends are experimental data points and solid lines are the Least Square linear fit to the data points.

Table 6: Summary of the gas phase ion mobilities, of $(Styrene)_n^+$, n = 1-8 at room temperature.

n	$K_o(cm^2V^{-1}s^{-1})$	Ω (/^{2})
1	9.2 ± 0.4	58.6 ± 2.3
2	5.8 ± 0.2	92.2 ± 3.7
3	4.6 ± 0.2	118.6 ± 4.7
4	3.6 ± 0.1	148.1 ± 5.9
5	3.2 ± 0.1	166.4 ± 6.7
6	2.6 ± 0.1	204.7 ± 8.1
7	2.3 ± 0.1	231.3 ± 9.3
8	2.28 ± 0.06	

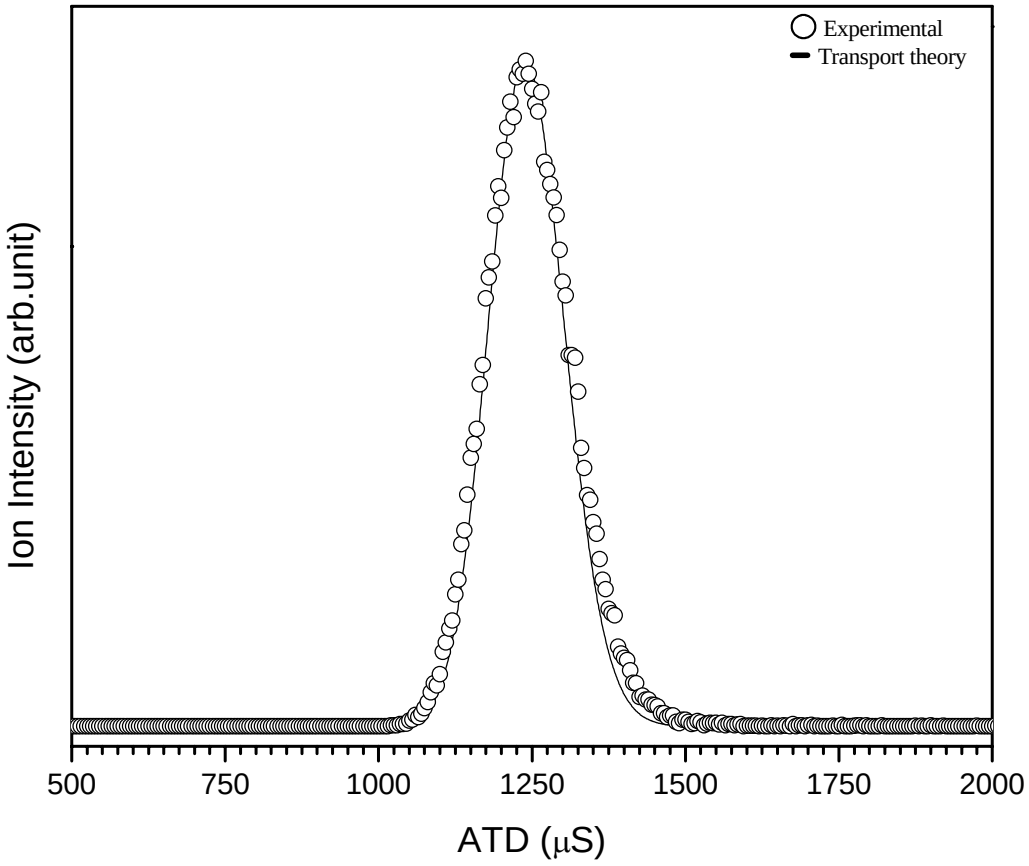

Figure 25: Arrival time distribution of mass selected $(C_8H_8)_3^+$ ions (circles) and the predicted distribution from transport theory (solid line). Experimental conditions are: 50 μs pulse width, injection energy is 15 eV, 1.141 Torr He inside the drift cell, cell temperature is 30.88 ^oC, 20 V voltage difference between the entrance and the exit lenses and E/N = 6.21 Td. The reduced mobility $K_o = 4.54\ cm^2V^{-1}s^{-1}$.

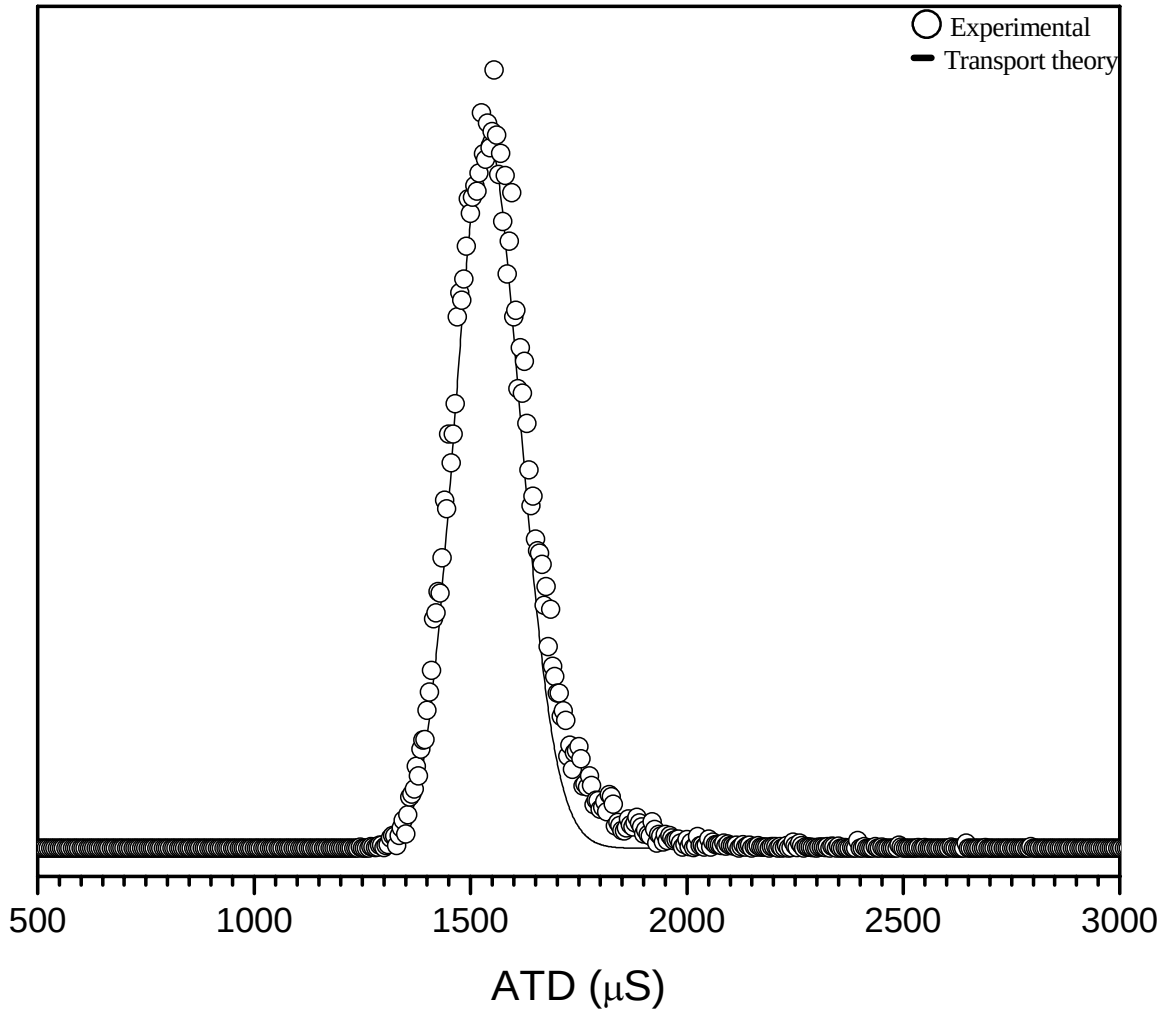

Figure 26: Arrival time distribution of mass selected $(C_8H_8)_4^+$ ions (circles) and the predicted distribution from transport theory (solid line). Experimental conditions are: 50 μs pulse width, injection energy is 15 eV, 1.098 Torr He inside the drift cell, the drift cell temperature is 30.80 ^oC, 20 V voltage difference between the entrance and the exit lenses and E/N = 6.45 Td. The reduced mobility K_o = 3.55 $cm^2V^{-1}s^{-1}$.

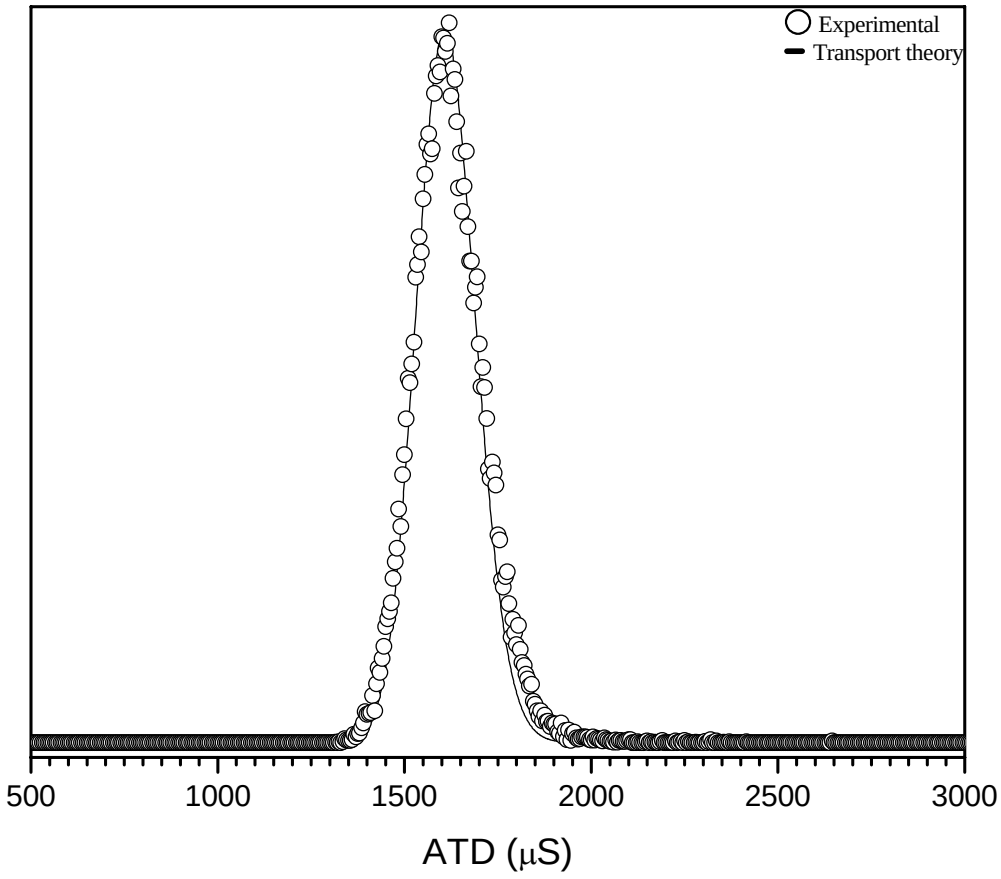

Figure 27: Arrival time distribution of mass selected $(C_8H_8)_5^+$ ions (circles) and the predicted distribution from transport theory (solid line).Experimental conditions are : 50 μs pulse width, injection energy is 15 eV, 1.024 Torr He inside the drift cell, the drift cell temperature is 31.5 ^oC, 20 V voltage difference between the entrance and the exit lenses and E/N = 6.45 Td. The reduced mobility K_o = 3.15 $cm^2V^{-1}s^{-1}$.

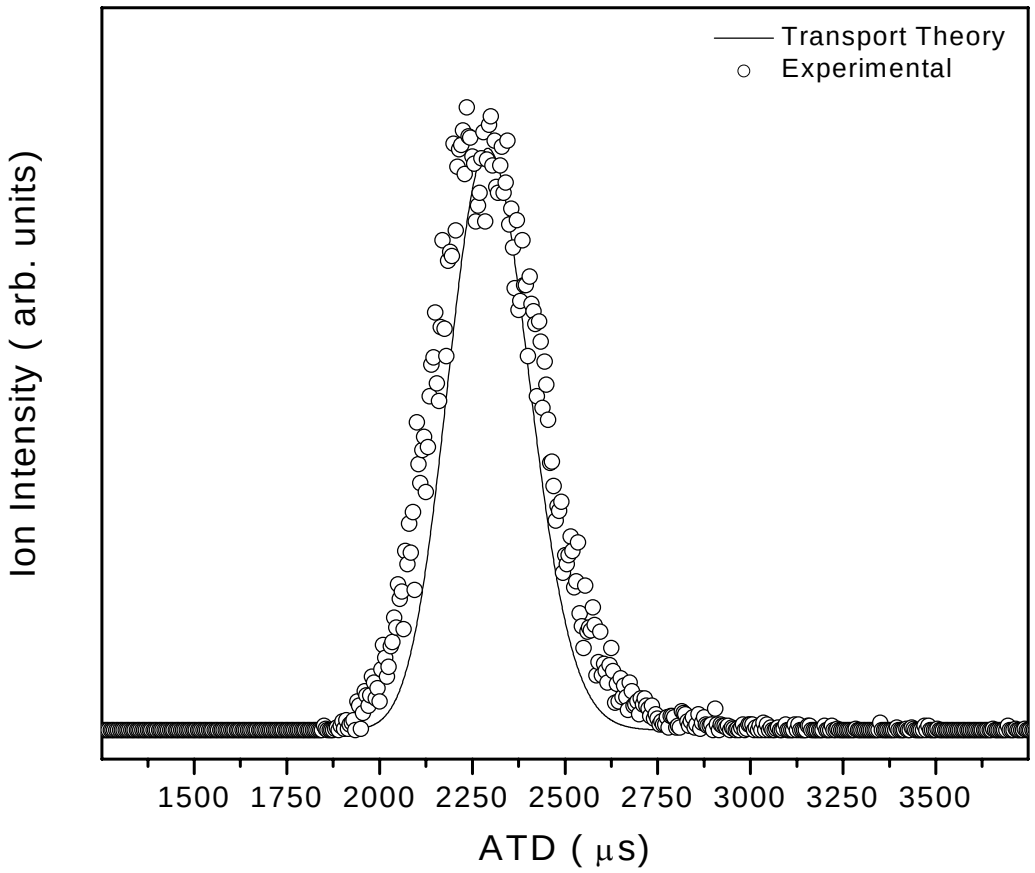

Figure 28: Arrival time distribution of $(C_8H_8)_6^+$ ions (circles) and the predicted distribution from transport theory (solid line). Experimental conditions are : 50 μs pulse width, injection energy is 15 eV, 1.272 Torr He inside the drift cell, the drift cell temperature is 29.9 ^oC, 20 V voltage difference between the entrance and the exit lenses and E/N = 5.55 Td. The reduced mobility K_o = 2.79 $cm^2V^{-1}s^{-1}$.

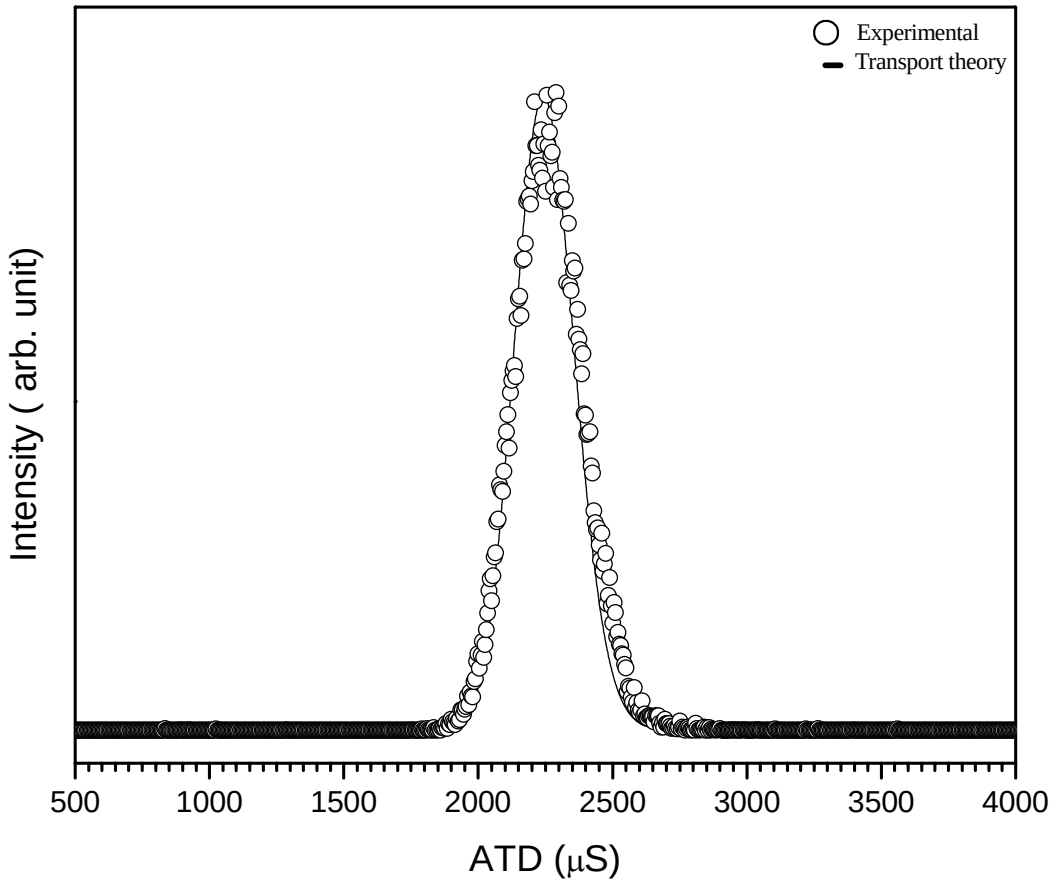

Figure 29: Arrival time distribution of $(C_8H_8)_7^+$ ions (circles) and the predicted distribution from transport theory (solid line). Experimental conditions are: 50 μs pulse width, injection energy is 15 eV, 1.152 Torr He inside the drift cell, the drift cell temperature is 28.6 ^oC 20 V voltage difference between the entrance and the exit lenses and E/N = 4.88 Td. The reduced mobility K_o = 2.50 $cm^2V^{-1}s^{-1}$.

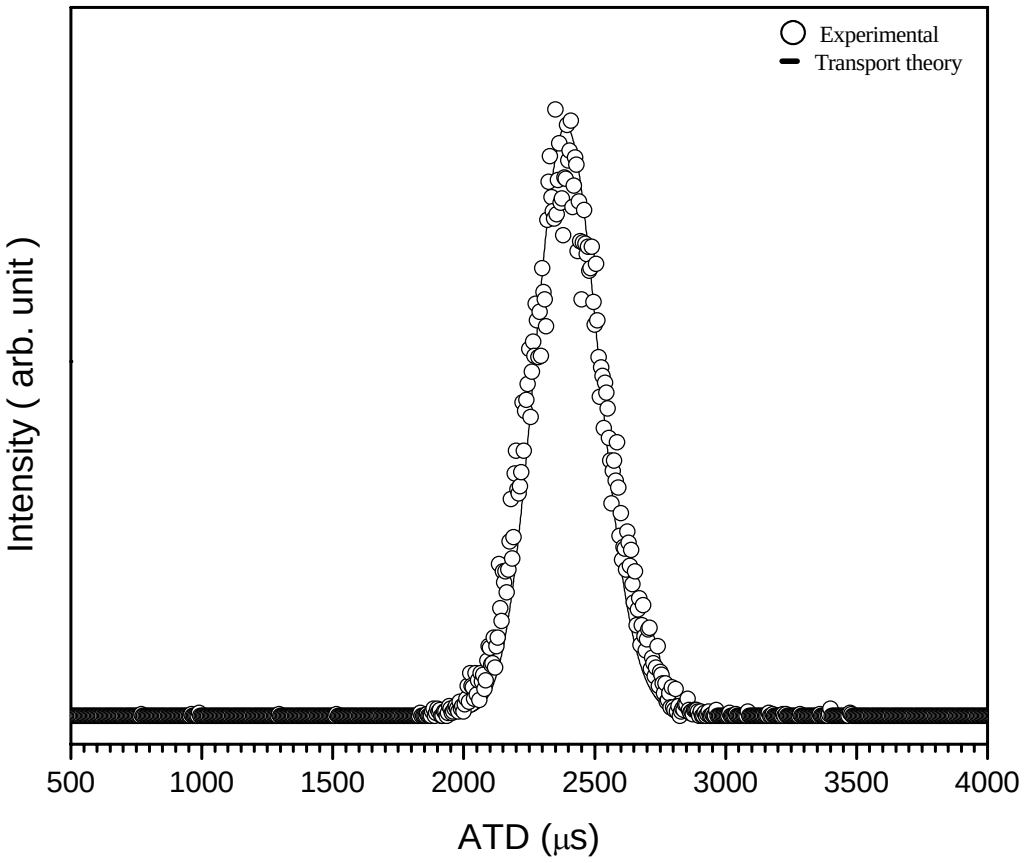

Figure 30: Arrival time distribution of $(C_8H_8)_8^+$ ions (circles) and the predicted distribution from transport theory (solid line). Experimental conditions are: 50 μs pulse width, injection energy is 15 eV, 1.152 Torr He inside the drift cell, the drift cell temperature is 28.6 ^oC, 25 V voltage difference between the entrance and the exit lenses and E/N = 6.10 Td. The reduced mobility K_o = 2.28 $cm^2V^{-1}s^{-1}$.

3.3.2 Mobility of mass selected ions at different temperature

The mobility of the mass selected styrene dimer ion $(C_8H_8)_2^+$ was measured at 453, 373, 173, and 125 K. Figure 31-34 show the observed ATDs and the predicted distribution from transport theory for a single isomer of styrene dimer ion $(C_8H_8)_2^+$. A simple comparison of the ATDs with the predictions from transport theory revealed that the distributions are significantly broader at low temperatures (at 173 and 123K).

In addition the mobility of the mass selected styrene trimer ion $(C_8H_8)_3^+$ was measured at 123 K. Figure 35 shows the experimental ATDs for styrene trimer compared with the predicted distribution from the transport theory for a single isomer. The broadening of the distribution from the experimental compared to the theory suggests the presence of other structures for styrene trimer. Table 7 summarizes the measured reduced mobilities (K_o) for the styrene dimer and trimer ions.

Table 7: Summary of the average gas phase ion mobilities for the styrene dimer and the trimer at different drift cell temperatures.

Drift Cell Temp.(K)	$K_o(cm^2V^{-1}s^{-1})$(Styrene)$_2$	$K_o(cm^2V^{-1}s^{-1})$ (Styrene)$_3$
453	4.88	N/A
373	5.34	N/A
173	7.27	N/A
125	7.78	6.20

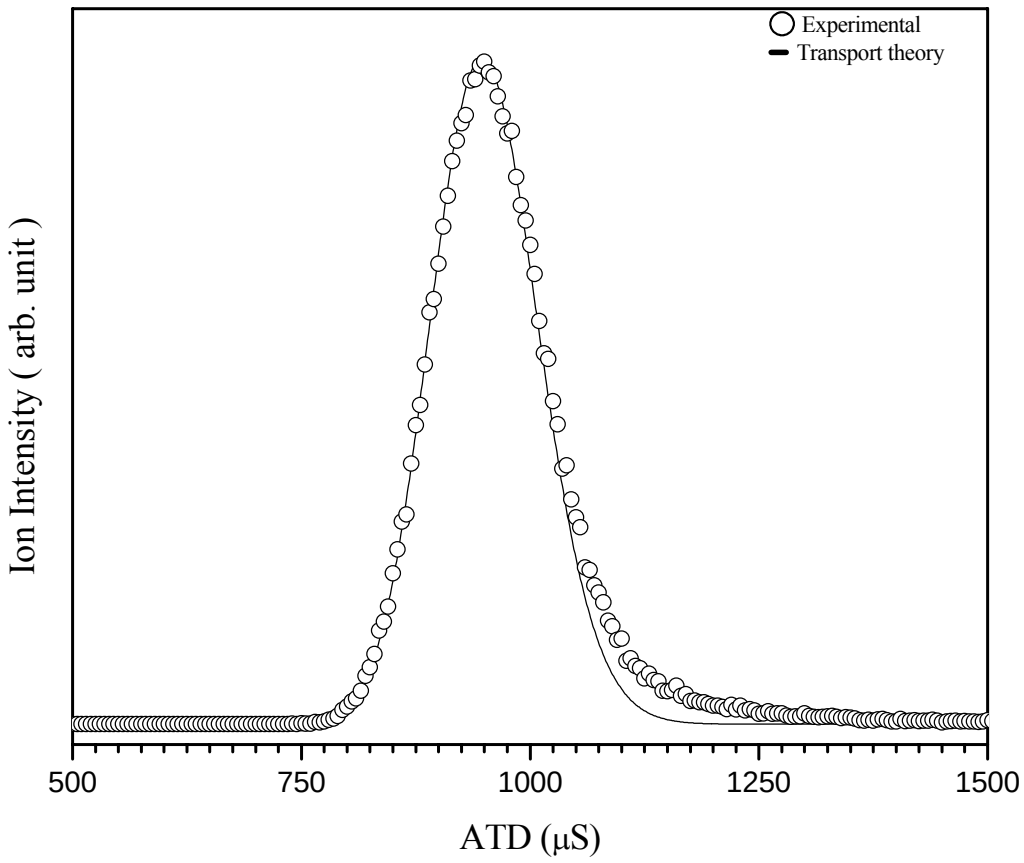

Figure 31: Arrival time distribution of $(C_8H_8)_2^+$ ions at drift cell temperature of 453 K (circles) and the predicted distribution from transport theory (solid line).Experimental conditions are: 50 μs pulse width, injection energy is 15 eV, 1.417 Torr He inside the drift cell, the drift cell temperature is 180.0 ^oC, 16 V voltage difference between the entrance and the exit lenses and E/N = 5.96 Td. The reduced mobility $K_o = 4.88\ cm^2V^{-1}s^{-1}$.

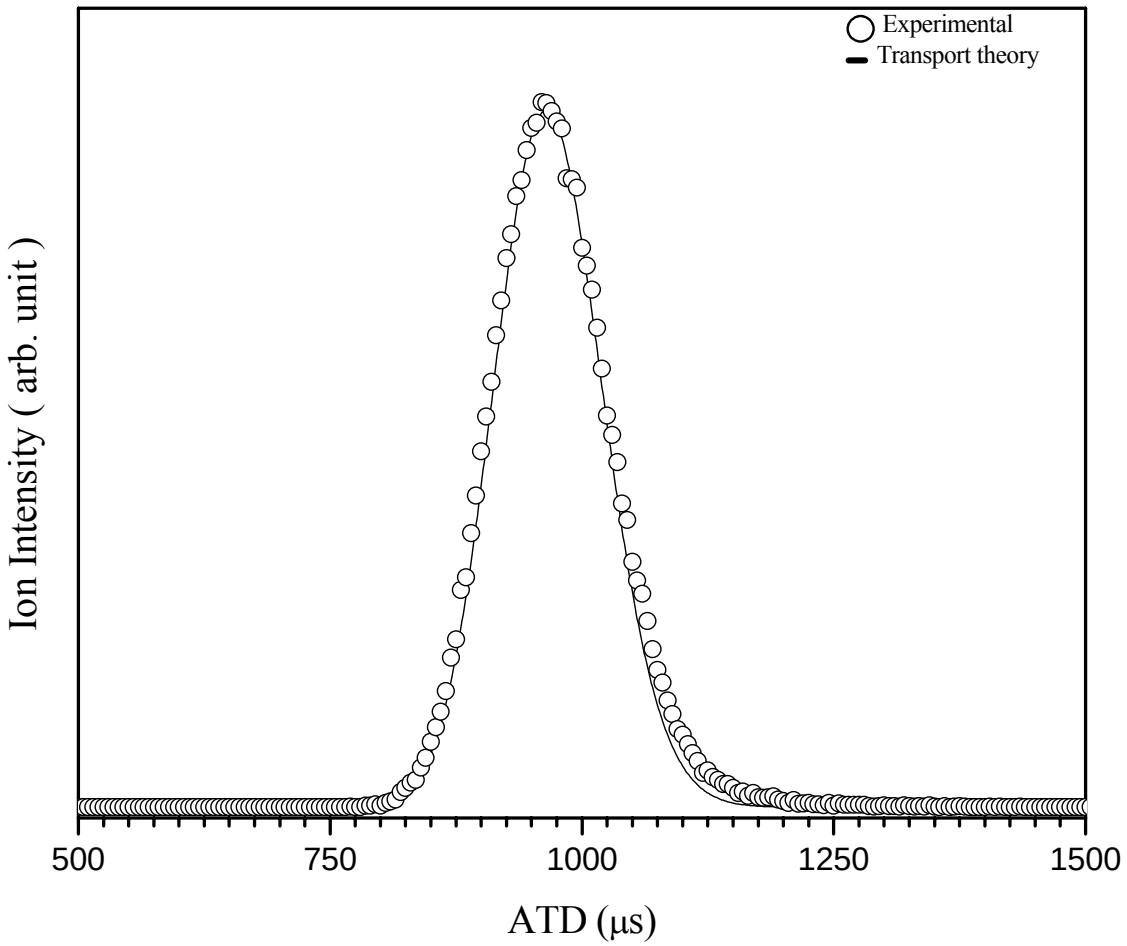

Figure 32: Arrival time distribution of $(C_8H_8)_2^+$ ions at drift cell temperature of 373 K (circles) and the predicted distribution from transport theory (solid line).Experimental conditions are: 50 μs pulse width, injection energy is 15 eV, 1.278 Torr He inside the drift cell, the drift cell temperature is 99.70 ^oC 18 V voltage difference between the entrance and the exit lenses and E/N = 6.12 Td. The reduced mobility $K_o = 5.34\ cm^2V^{-1}s^{-1}$.

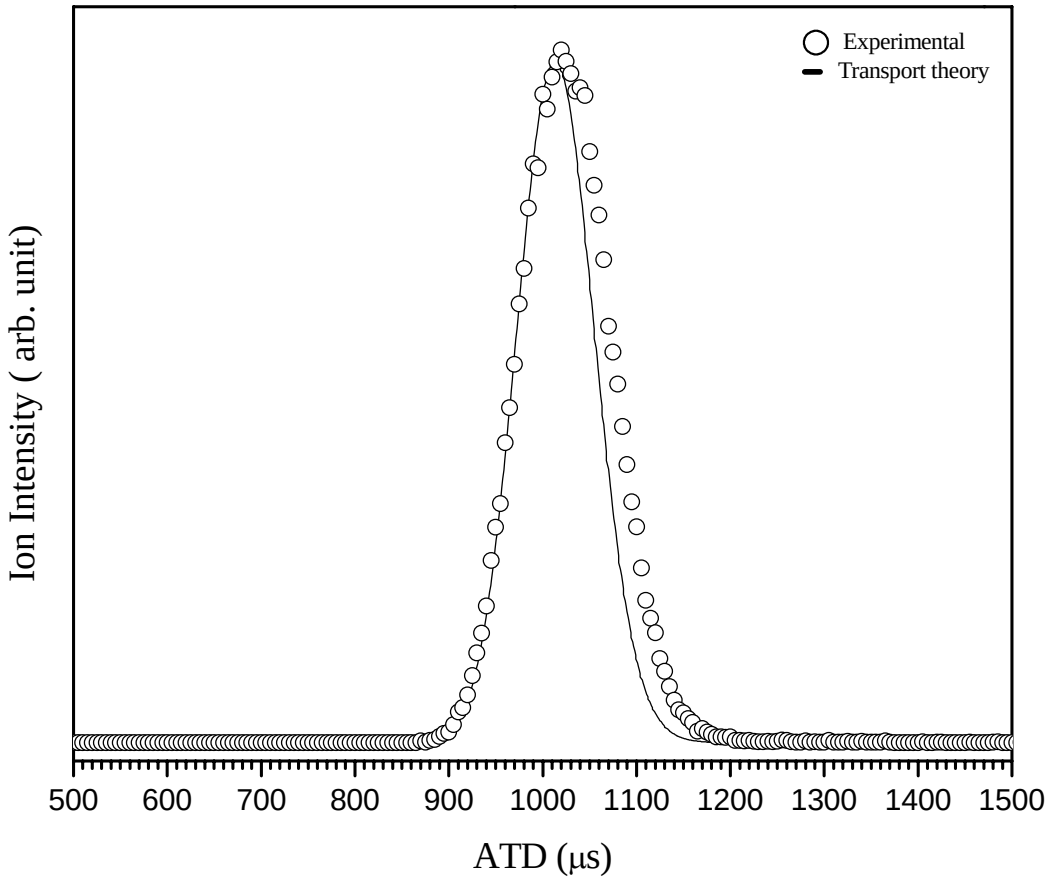

Figure 33: Arrival time distribution of $(C_8H_8)_2^+$ ions at drift cell temperature of 174.85 K (circles) and the predicted distribution from transport theory (solid line).Experimental conditions are: 50 μs pulse width, injection energy is 15 eV, 0.812 Torr He inside the drift cell, the drift cell temperature is -98.3 ^oC, 20 V voltage difference between the entrance and the exit lenses and E/N = 5.02 Td. The reduced mobility K_o = 6.82 $cm^2V^{-1}s^{-1}$.

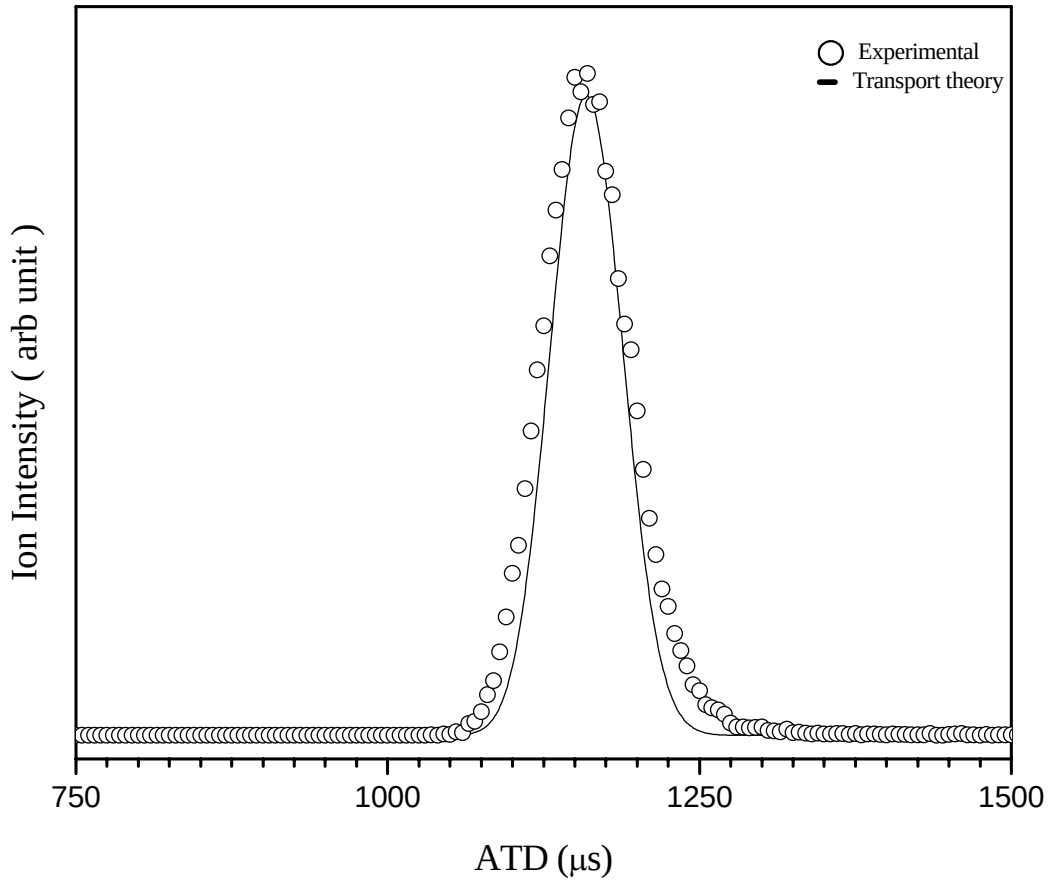

Figure 34: Arrival time distribution of $(C_8H_8)_2^+$ ions at drift cell temperature of 125.4 K (circles) and the predicted distribution from transport theory (solid line).Experimental conditions are: 50 μs pulse width, injection energy is 15 eV, 1.430 Torr He inside the drift cell, the drift cell temperature is -147.25 ^oC ,40 V voltage difference between the entrance and the exit lenses and E/N = 4.09 Td. The reduced mobility K_o = 7.78 $cm^2V^{-1}s^{-1}$.

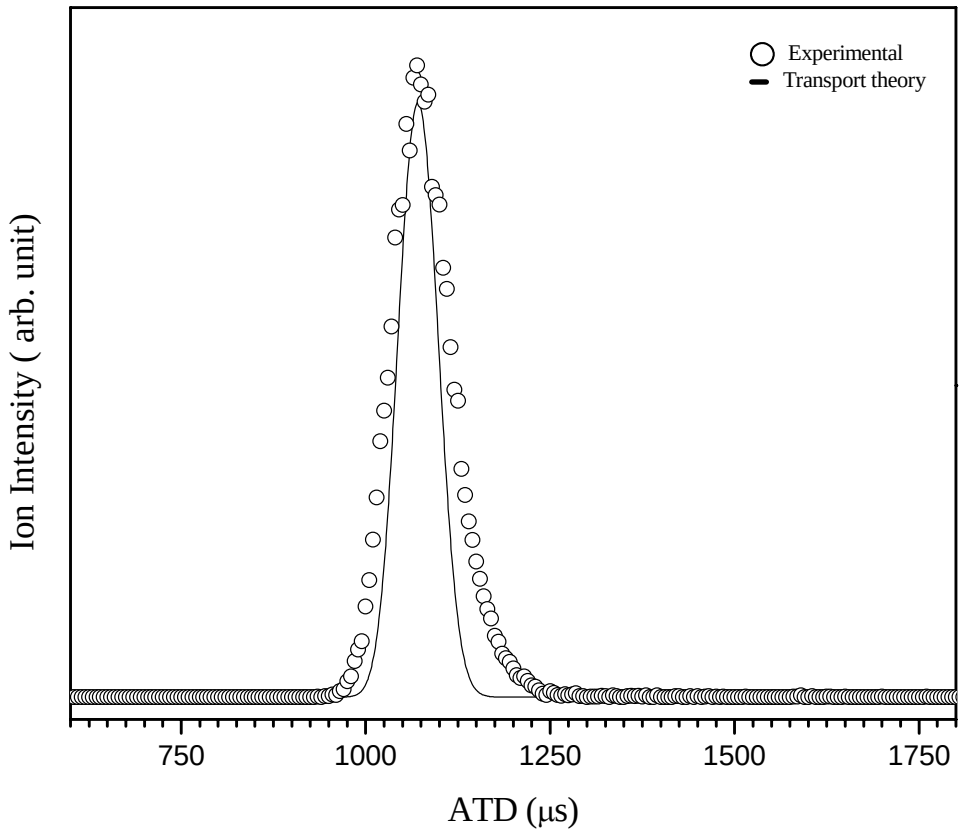

Figure 35: Arrival time distribution of $(C_8H_8)_3^+$ ions at drift cell temperature of 125.40 K (circles) and the predicted distribution from transport theory (solid line). Experimental conditions are: 50 μs pulse width, injection energy is 15 eV, 1.026 Torr He inside the drift cell, the drift cell temperature is -147.75 ^oC 40 V voltage difference between the entrance and the exit lenses and E/N = 5.69 Td. The reduced mobility K_o = 6.20 $cm^2V^{-1}s^{-1}$.

3.4 Styrene Oligomers Containing Cu^+ and Ag^+ Generated by LVI

3.4.1 Ion Mobility Measurements of the Styrene Oligomers Containing Cu^+

Figure 36 shows the mass spectrum of $Cu^+(C_8H_8)_n$. These cluster ions were produced by pulsed supersonic adiabatic expansion, followed by LVI of the Copper target. These ions were allowed to pass the first quadrupole mass filter, which was set in an RF only-mode, and then injected into the drift cell (containing He as a buffer gas) with the lowest injection energy possible. After exiting the cell, the ions were focused into the second quadrupole where they were mass-scanned. The mass spectrum in Figure 36 shows the $Cu^+(C_8H_8)_n$, (for n= 2-4), and the Styrene cluster ions $(C_8H_8)_n^+$, (for n= 2-9). It is worth noting that $Cu^+(C_8H_8)_2$ (271 m/z) is extremely high in intensity compared to the other ions, and that a peak with m/z 269 is also observed, which can be assigned to $Cu^+C_{16}H_{14}$. Although similar mass spectra were collected on many different occasions, yet the $Cu^+(C_8H_8)_1$ peak was never observed.

Ion mobility experiments were preformed on $Cu^+(C_8H_8)_2$, $Cu^+(C_8H_8)_3$ and $(C_8H_8)_2^+$ that observed in the mass spectra. The average reduced mobilities (K_o) for these ions are summarized in Table 8

Figure 37-Figure 39 show the observed ATDs of $Cu^+(C_8H_8)_2$, $Cu^+(C_8H_8)_3$ and $^+(C_8H_8)_2$ at room temperature. In addition, these figures display excellent agreements of the experimental arrival time distributions to the predicted ones from the transport theory. This suggests that only one structure is present in each case or if these are multiple structures, they must have essentially the same mobility. In the case of $Cu^+(C_8H_8)_2$ the

comparison suggests that only one isomer is present. To investigate this possibility, the mobility of the $Cu^+(C_8H_8)_2$ was measured at 173 K. The experimental arrival time distribution of the $Cu^+(C_8H_8)_2$ and the predicted distribution from transport theory are displayed in Figure 40 which shows an excellent agreement between the experimental and calculated distributions. This further supports the suggestion that only one isomer is present for $Cu^+(C_8H_8)_2$. The mobility of the styrene trimer ion $Cu^+(styrene)_3$ could not be measured at low temperatures due to the very weak signal intensity.

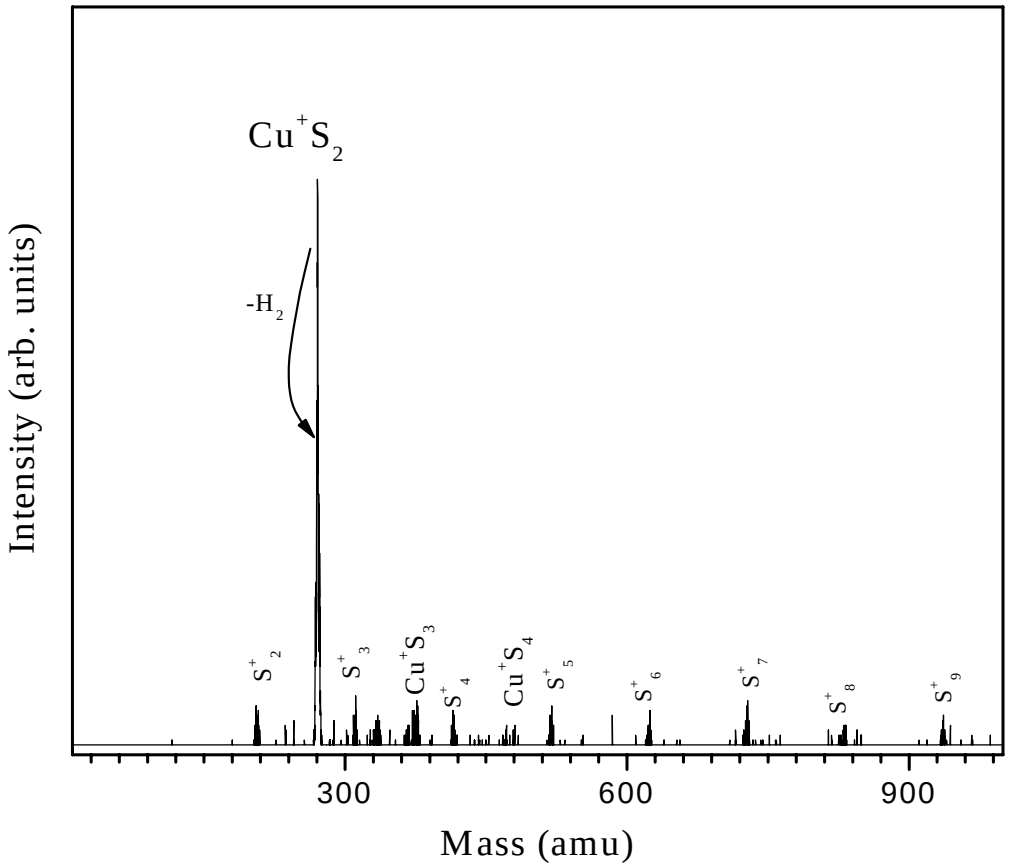

Figure 36: LVI Mass spectrum of $Cu^{+}(C_8H_8)_n$ injected into pure He. Experimental conditions are: 0.124 W Laser power,10 μs pulse width, gate entrance 100 V, 1.520 Torr He inside the drift cell, the drift cell temperature is 26.3 ^{o}C, voltage difference between the entrance and the exit lenses is 60 V.

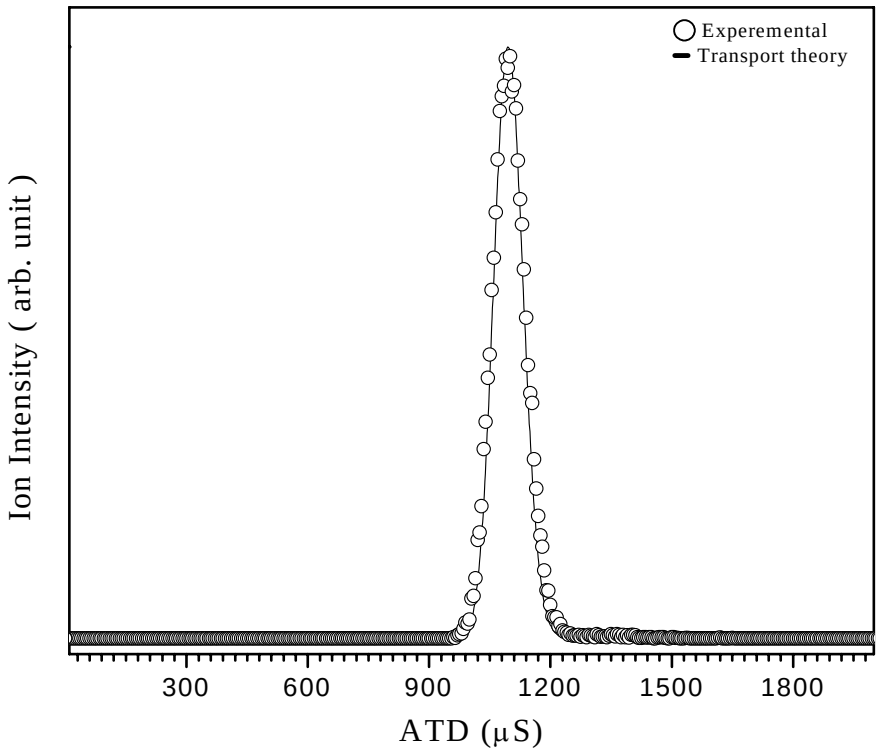

Figure 37: Arrival time distribution of $Cu^{+}(C_8H_8)_2$ ions (circles)at drift cell temperature of 300 K and the predicted distribution from transport theory (solid line). Experimental conditions are: 0.124 W Laser power,10 μs pulse width, gate entrance 100 V, 1.520 Torr He inside the drift cell, the drift cell temperature is 26.48 ^{o}C, voltage difference between the entrance and the exit lenses is 20 V.E/N = 4.59 Td. The reduced mobility K_o = 5.71 $cm^2V^{-1}s^{-1}$.

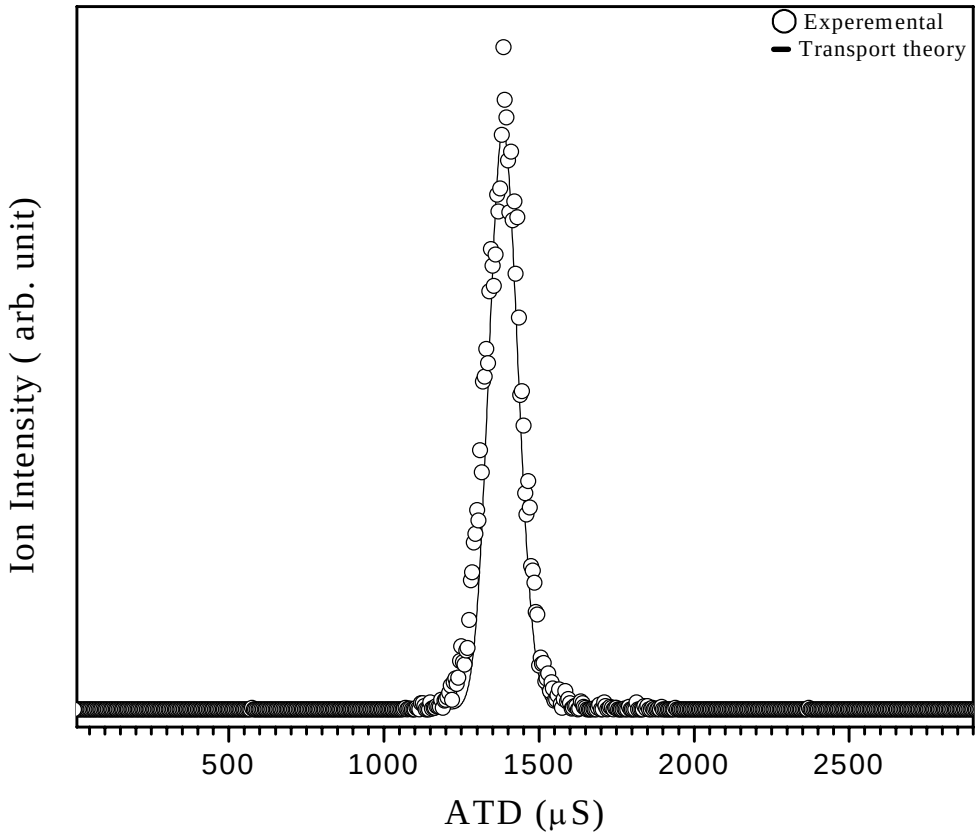

Figure 38: Arrival time distribution of $Cu^{+}(C_8H_8)_3$ ions (circles) at drift cell temperature of 300 K and the predicted distribution from transport theory (solid line). Experimental conditions are: 0.124 W Laser power,10 μs pulse width, gate entrance 100 V, 2.524 Torr He inside the drift cell, the drift cell temperature is 26.58 ^{o}C, voltage difference between the entrance and the exit lenses is 40 V.E/N = 5.53 Td. The reduced mobility K_o = 4.90 $cm^2V^{-1}s^{-1}$.

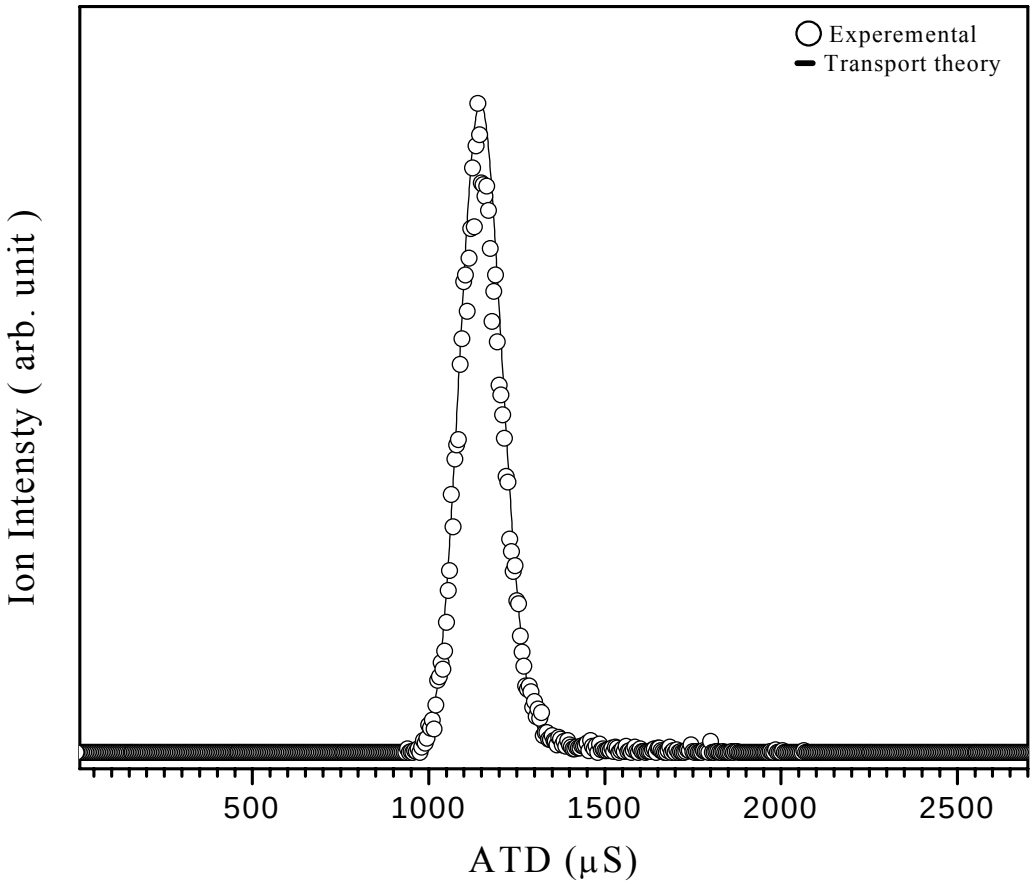

Figure 39: Arrival time distribution of $(C_8H_8)_2^+$ ions (circles) at drift cell temperature of 299 K and the predicted distribution from transport theory (solid line). Experimental conditions are: 0.15 W Laser power, 10 μs pulse width, gate entrance 70 V, 1.384 Torr He inside the drift cell, the drift cell temperature is 26.73 ^oC, voltage difference between the entrance and the exit lenses is 20 V.E/N = 5.53 Td. The reduced mobility K_o = 5.72 $cm^2V^{-1}s^{-1}$.

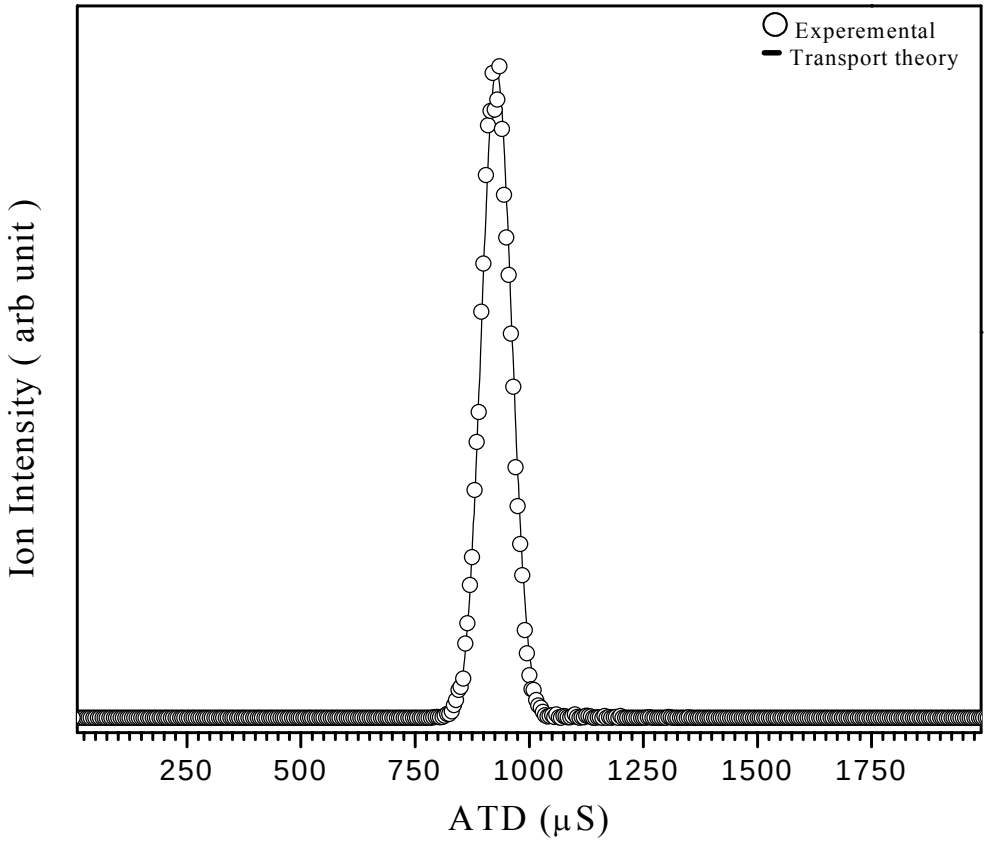

Figure 40: Arrival time distribution of $Cu^{+}(C_8H_8)_2$ ions (circles) at drift cell temperature of 173 K and the predicted distribution from transport theory (solid line). Experimental conditions are: 0.130 W Laser power,100 μs pulse width, gate entrance 110 V, 0.895 Torr He inside the drift cell, the drift cell temperature is -98.55 ^{o}C, voltage difference between the entrance and the exit lenses is 25 V. E/N = 5.70 Td. The reduced mobility K_o = 6.96 $cm^2V^{-1}s^{-1}$.

Table 8: Summary of the average gas phase ion reduced mobilities (K_o) $Cu^+(C_8H_8)_2$, $Cu^+(C_8H_8)_3$ and $(C_8H_8)_2^+$ produced by LVI.

Species Ion	K_o ($cm^2V^{-1}s^{-1}$) at 304 K	K_o($cm^2V^{-1}s^{-1}$) at 173 K
$Cu^+(C_8H_8)_2$	5.7	6.96
$Cu^+(C_8H_8)_3$	4.42	----
$(C_8H_8)_2^+$	5.7	-----

3.4.2 Ion Mobility Measurements of Styrene Oligomers Containing Ag^+

Figure 41 shows the mass spectrum of $Ag^+(C_8H_8)_n$. The ions formed were the same as with Cu-styrene system, as described above. It shows the $Ag^+(C_8H_8)_n$, (for n= 2 and 3), and the styrene dimer ion $(C_8H_8)_2^+$. In addition, a peak with m/z 313 is observed and is assigned to $Ag^+C_{16}H_{14}$. As in the case of the Cu^+/styrene system, the intensity of the $Ag^+(C_8H_8)_2$ (m/z 315) is extremely high compared to the other ions. Several mass spectra were collected on many occasions at different experimental conditions but in all cases the $Ag^+C_8H_8$ was never observed only when the $Ag^+(C_8H_8)_2$ (first quadrupole set in RF only mode) was injected with high injection energy (entrance gate voltage set at 100 V) into He, the $Ag^+C_8H_8$ was observed with a very weak intensity. Additionally, there were peaks with m/z 207 ($C_{16}H_{15}^+$) , 417 ($Ag^+C_{24}H_{22}$) and 455 ($Ag^+C_{24}H_{24}.2H_2O$). Figure 42 displays the observed mass spectrum under the high injetion energy of $Ag^+(C_8H_8)_2$.

The ion mobilities for $Ag^+(C_8H_8)_n$, for n = 2 and 3 at room temperature, and at 176 K for $Ag^+(C_8H_8)_2$ were measured. These can be summarized in Table 9.

Figure 43-Figure 45 show the observed ATDs of $Ag^+(C_8H_8)_2$, $Ag^+(C_8H_8)_3$ and $(C_8H_8)_2^+$ at room temperature. These figures show small deviations of the experimental arrival time distributions from the predicted ones from the transport theory. This suggests either more than one structure is present, or some of these species dissociate from higher channel (from larger oligomers). In the case of $Ag^+(C_8H_8)_2$ there is tailing in the experimental arrival time compared to the predicted one. To investigate this phenomenon, the mobility of $Ag^+(C_8H_8)_2$ was measured at drift cell temperatures of 173 and 123 K. The

comparisons of $Ag^+(C_8H_8)_2$ arrival time distributions to the predicted distributions from transport theory (fitted to one isomer I) are displayed in Figure 45 and Figure 46 for temperatures 173 K and 123 K, respectively. These Figures demonstrate the existence of a second small peak, which assigned to isomer II. It remains to be seen if this peak corresponds to the existence of another isomer (isomer II) or it represents a dissociation product from higher oligomers. The arrival time of $Ag^+(C_8H_8)_3$ was collected at the same temperature (176 K) and compared to ATDs of $Ag^+(C_8H_8)_2$ under the same experimental conditions. The arrival time of the $Ag^+(C_8H_8)_3$ matches well the arrival time of the small peak observed in the case of the $Ag^+(C_8H_8)_2$. This may explain the tailing in the case of $Ag^+(C_8H_8)_2$. This comparison is shown in Figure 47. The ion mobilities for $Ag^+(C_8H_8)_n$ at different conditions are summarized in Table 9.

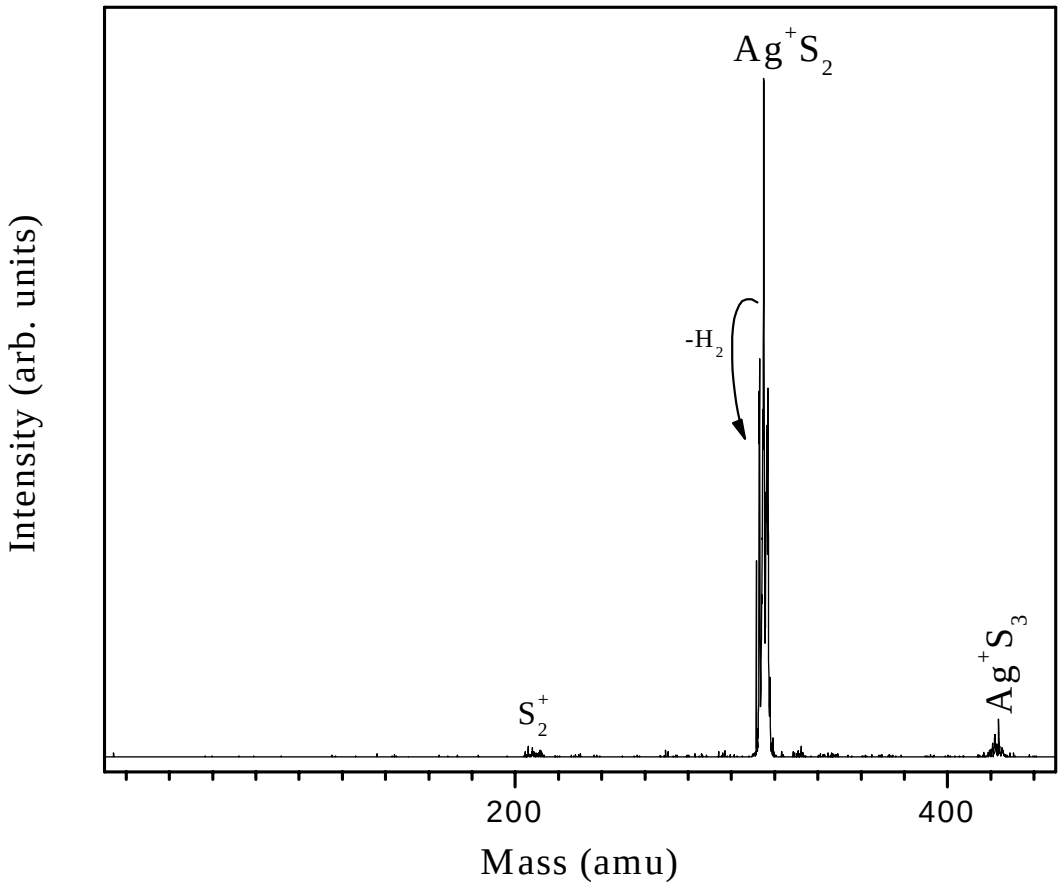

Figure 41: LVI Mass spectrum of of $Ag^+(C_8H_8)_n$ injected into pure He with the lowest injection energy (entrance gate set at 140V) where the first quadrupole set at 315 amu in RF only mode.

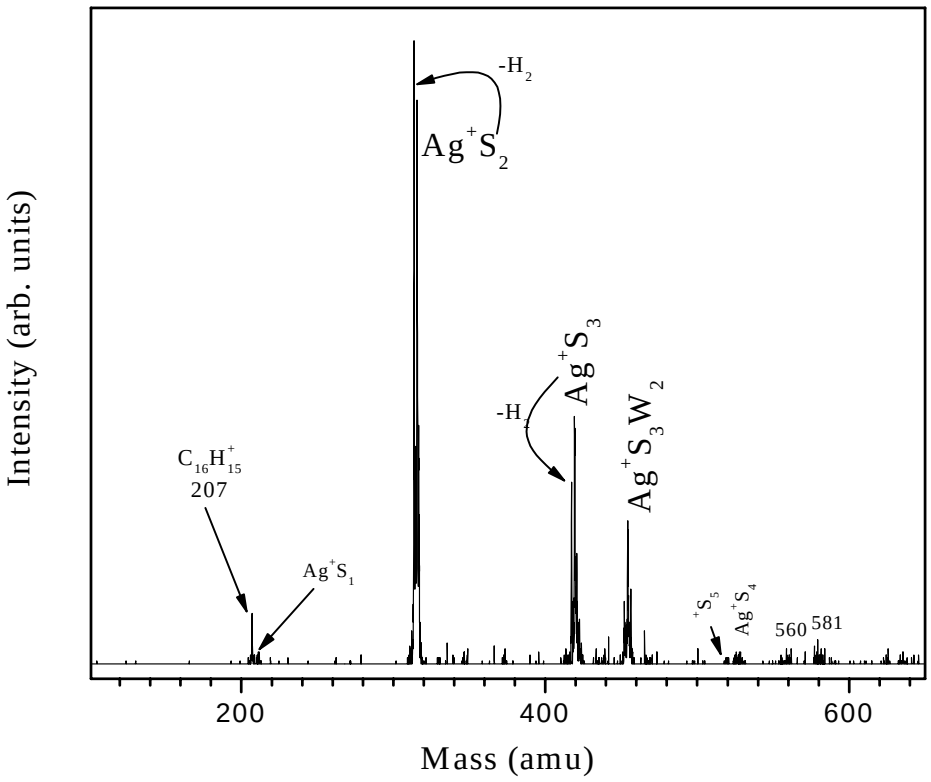

Figure 42: LVI Mass spectrum of of $Ag^+(C_8H_8)_n$ injected into He with the entrance gate set at 100V, the first quadrupole set at 419 amu in RF only mode.

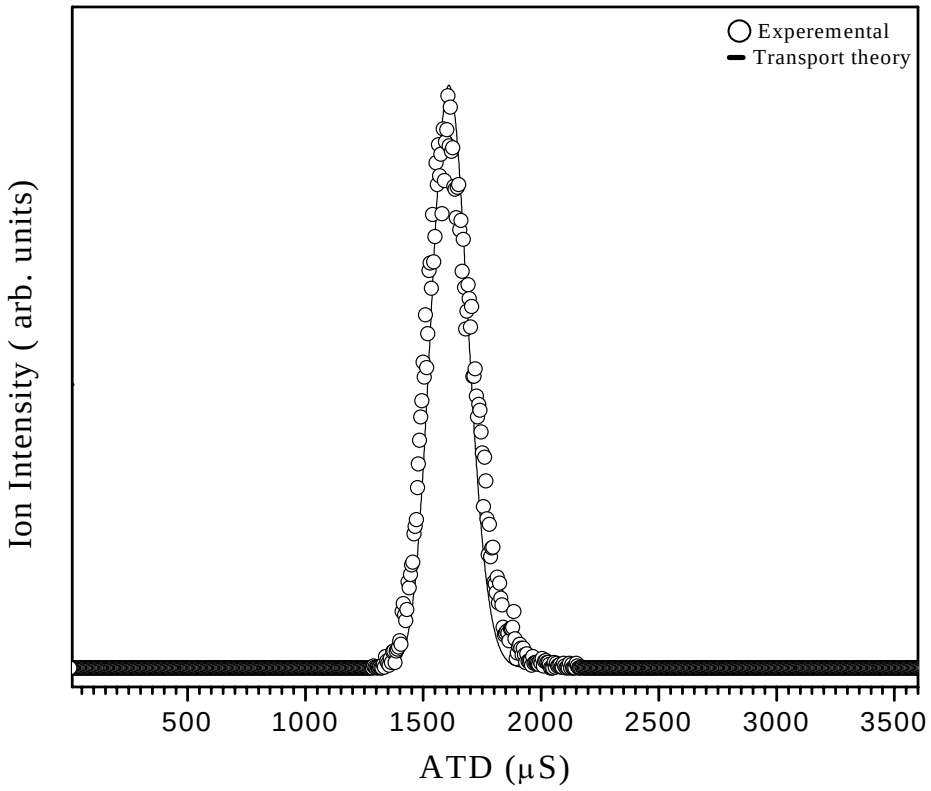

Figure 43: Arrival time distribution of $Ag^{+}(C_8H_8)_2$ ions (circles)at drift cell temperature of 300 K and the predicted distribution from transport theory (solid line). Experimental conditions are: 0.141 W Laser power, 20 μs pulse width, gate entrance 140 V, 1.548 Torr He inside the drift cell, the drift cell temperature is 26.73 ^{o}C, voltage difference between the entrance and the exit lenses is 18 V.E/N = 4.06 Td. The reduced mobility K_o = 5.62 $cm^2V^{-1}s^{-1}$.

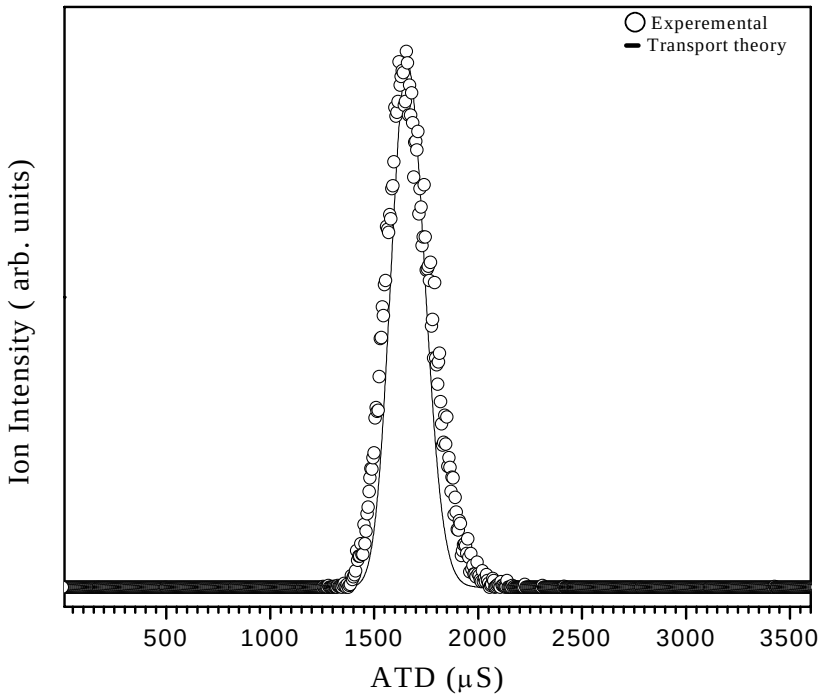

Figure 44: Arrival time distribution of $Ag^{+}(C_8H_8)_3$ ions (circles)at drift cell temperature of 300 K and the predicted distribution from transport theory (solid line). Experimental conditions are: 0.141 W Laser power, 20 μs pulse width, gate entrance 140 V, 1.552 Torr He inside the drift cell, the drift cell temperature is 26.73 ^{o}C, voltage difference between the entrance and the exit lenses is 20 V. E/N = 4.50 Td. The reduced mobility K_o = 4.64 $cm^2V^{-1}s^{-1}$.

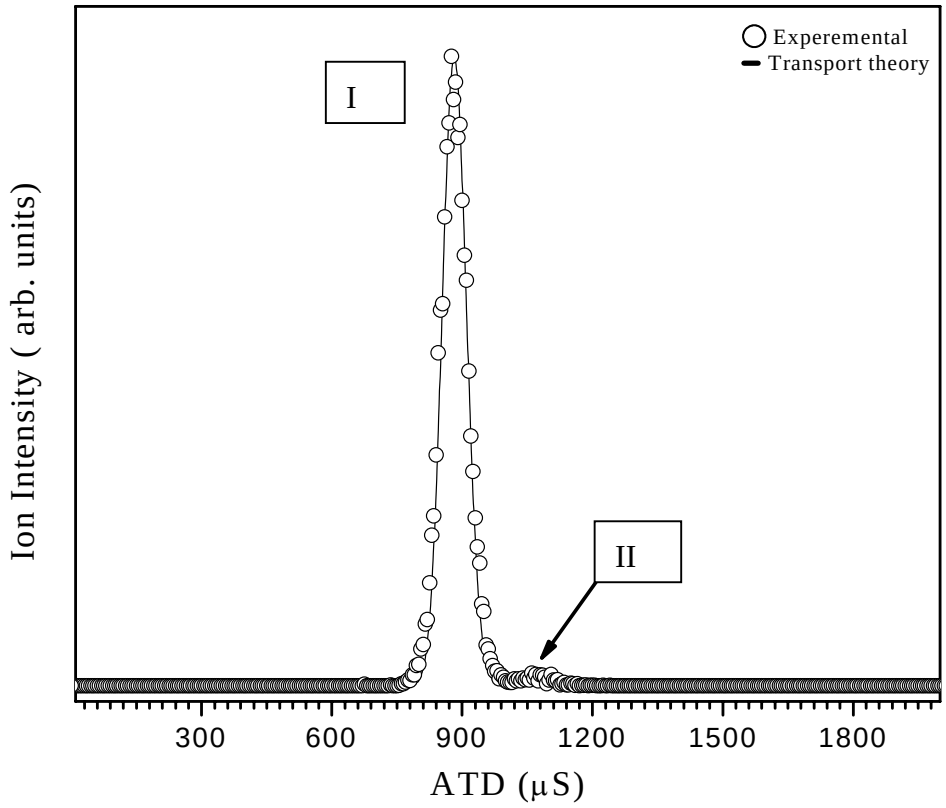

Figure 45: Arrival time distribution of $Ag^{+}(C_8H_8)_2$ ions (circles)at drift cell temperature of 176 K and the predicted distribution (for I isomer) from transport theory (solid line). Experimental conditions are: 30 μs pulse width, entrance gate-voltage energy is 100 eV, 0.908 Torr He inside the drift cell, the drift cell temperature is -97.0 ^{o}C ,40 V voltage difference between the entrance and the exit lenses and E/N = 6.10 Td. The reduced mobility K_o = 7.0(I) and 5.65(II) $cm^2V^{-1}s^{-1}$.

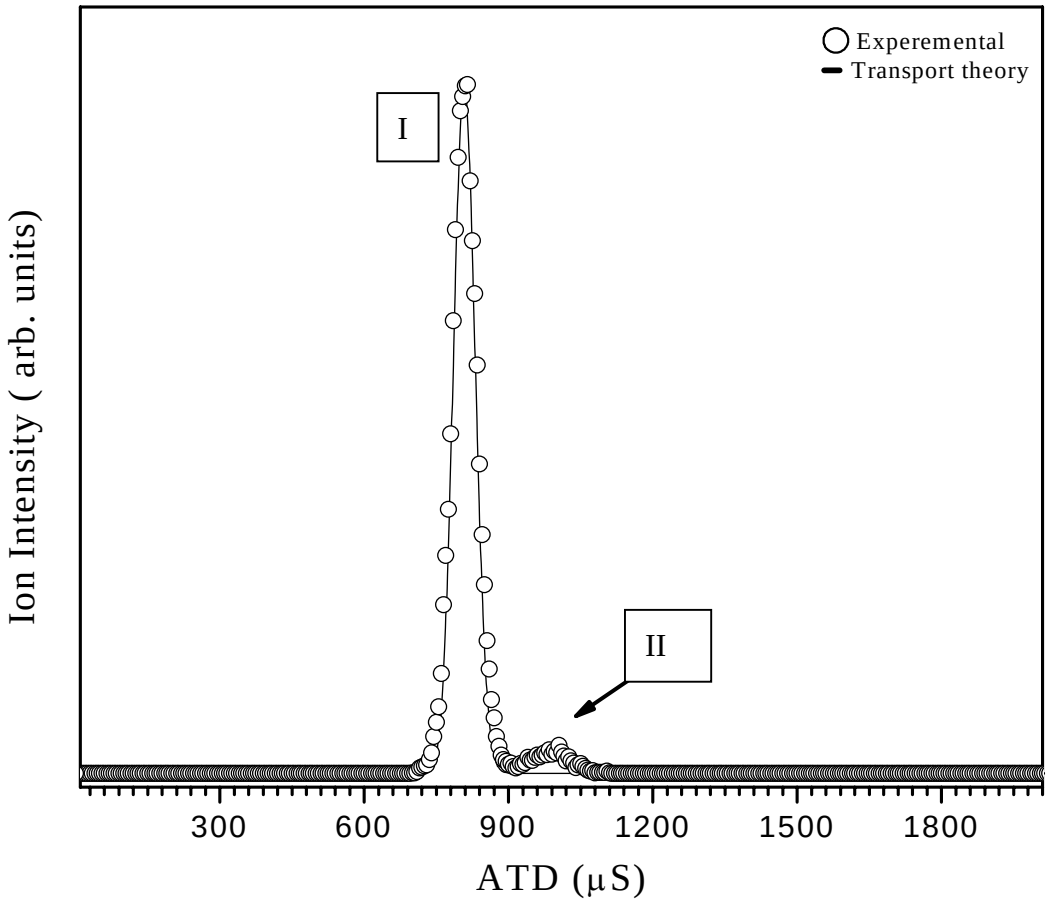

Figure 46: Arrival time distribution of $Ag^{+}(C_8H_8)_2$ ions (circles)at drift cell temperature of 124 K and the predicted distribution (for I isomer)from transport theory (solid line). Experimental conditions are: 30 μs pulse width, gate entrance-voltage 100 V, 0.643 Torr He inside the drift cell, the drift cell temperature is -149.0 ^{o}C, 27 V voltage difference between the entrance and the exit lenses and E/N = 6.04 Td. The reduced mobility K_o = 7.26 (I) and6.23 (II) $cm^2V^{-1}s^{-1}$.

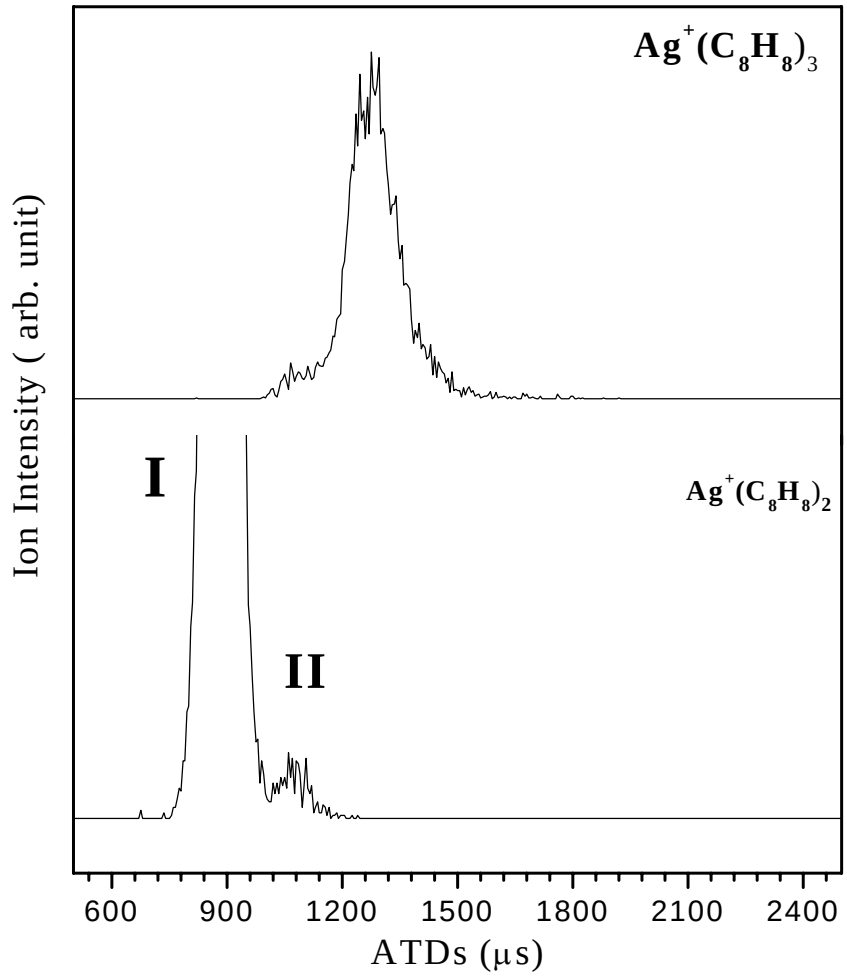

Figure 47: ATDS of $Ag^{+}(C_8H_8)_2$ (lower inset) and $Ag^{+}(C_8H_8)_3$ at drift cell temperature of 176 K.

Table 9: Summary of the average reduced mobilities (K_o) $Ag^+(C_8H_8)_2$, and $Ag^+(C_8H_8)_3$ produced by LVI

Species Ion	K_o ($cm^2V^{-1}s^{-1}$) at 300 K	K_o ($cm^2V^{-1}s^{-1}$) at 176 K	K_o ($cm^2V^{-1}s^{-1}$) at 123 K
$Ag^+(C_8H_8)_2$	5.6	7.0(I), 5.65(II)	7.6 (I), 6.23(II)
$Ag^+(C_8H_8)_3$	4.6	----	

3.5 Structure Determination of The Styrene Dimer and Trimer Cations

We have employed DFT level of calculations with the 6-31G** basis set using the Gaussian 98 software[61] to optimize the geometries of different styrene dimer, $C_{16}H_{16}^{+}$, and trimer $C_{24}H_{24}^{+}$ isomers. These geometries are based on the proposed formation mechanisms available to us from the literature[18,19,27,28,30,31,33,35-37,46]. Eleven different isomers for the styrene dimer and four different isomers for the styrene trimer were considered. The structures of the dimer isomers (Sty2 a-k) and for the trimer isomers (Sty3 a-d) are shown in Table 10Table 11, respectively. The dimer isomers a and b were proposed by Flory[36], isomer c was proposed by Kirchner and Patat[35] isomer e can be formed via a cationic mechanism[46], isomers g, h and i can be formed by bimolecular reactions of monoradicals[31], and finally isomers j and k were proposed by the Mayo's mechanism.[22] The DFT calculations were conducted by Dr. Yehia Ibrahim (yibrahim@vcu.edu), as part of the collaboration in this project.

The theoretical calculations of the possible structural candidates of the oligomers ions are then used to compute angle averaged cross sections (Ωs) for comparison with the measured ones[42]. The calculations of Ωs at different temperatures using the MOBCAL program[42]. Table 10Table 11 list the total energies of the optimized structures of the styrene dimer and trimer cations and the calculated reduced mobilities (K_o) and collision cross sections (Ω) using the trajectory methods (TM)[42] at different temperatures. The discussion of the calculated results and the correlation with the experimental value will be presented in section 3.7.

3.5.1 Styrene Dimer cation $C_{16}H_{16}^{+}$

Table 10: Optimized structures for styrene dimer cations at B3LYP/6-31** level, total energy E (in atomic units), calculated cross sections (Ω) and reduced mobility (K_o) using the trajectory methods(TM) at different temperatures.

		E (au)	T (K)	Ω (Å^2)	Ko ($cm^2.V^{-1}.s)^{-1}$
Sty2 a	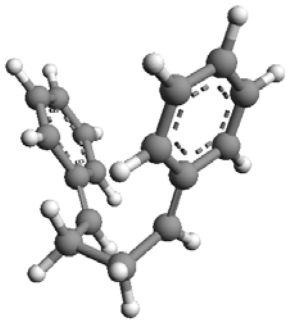	-619.068894309	125	109.07	7.66
			174	101.08	7.01
			303	91.52	5.86
			373	88.74	5.45
			453	86.38	5.08
Sty2 b	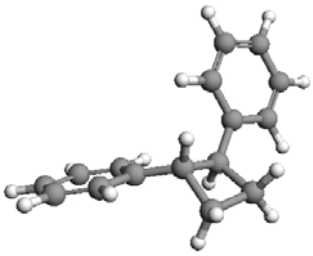	-619.058438800	125	110.17	7.58
			174	101.59	6.97
			303	90.96	5.90
			373	88.18	5.48
			453	85.90	5.11
Sty2 c	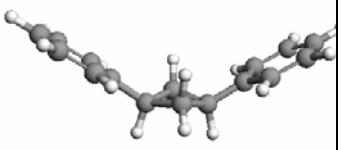	-619.061030344	125	111.86	7.47
			174	102.96	6.88
			303	92.76	5.78
			373	90.16	5.36
			453	88.17	4.98

			T (K)	Ω (Å^2)	K_o $(cm^2V^{-1}.s)^{-1}$
Sty2d	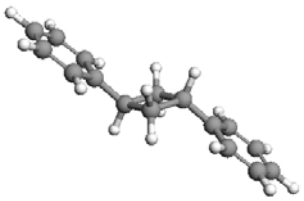	- 619.057829871	125	108.30	7.71
			174	100.41	7.05
			303	91.18	5.88
			373	88.71	5.45
			453	86.68	5.06
Sty2e	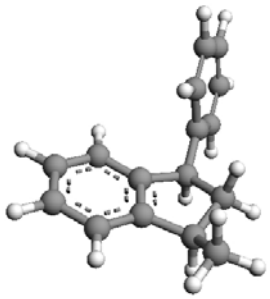	- 619.094975347	125	109.36	7.64
			174	100.44	7.05
			303	90.26	5.95
			373	87.48	5.53
			453	85.20	5.15
Sty2f	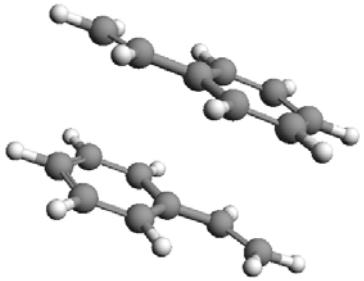	- 619.058892784	125	105.91	7.89
			174	97.49	7.26
			303	87.54	6.13
			373	84.71	5.71
			453	82.55	5.32
Sty2g	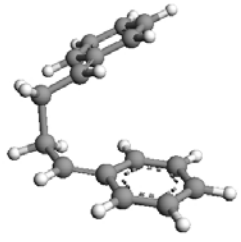	- 619.072926115	125	111.83	7.47
			174	103.03	6.87
			303	92.60	5.79
			373	89.68	5.39
			453	87.27	5.03

			T (K)	Ω (Å^2)	K_o $(cm^2V^1s)^{-1}$
Sty2h	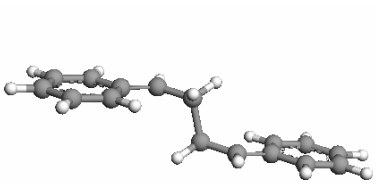	-619.074115409	125	112.87	7.40
			174	104.60	6.77
			303	95.00	5.65
			373	92.39	5.23
			453	90.35	4.86
Sty2i	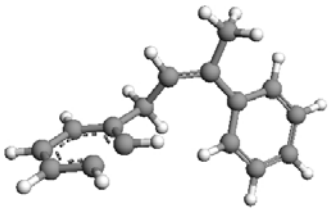	-619.082484334	125	110.53	7.56
			174	102.34	6.92
			303	92.56	5.80
			373	89.81	5.39
			453	87.52	5.01
Sty2j	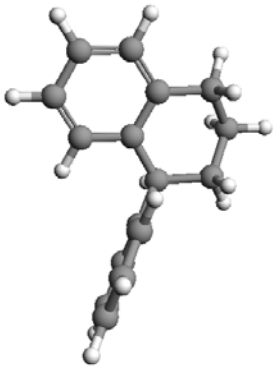	-619.097408849	125	107.11	7.80
			174	98.41	7.20
			303	88.36	6.07
			373	85.68	5.64
			453	83.48	5.26
Sty2k	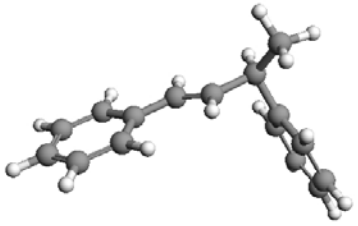	-619.089475991	125	115.94	7.21
			174	106.48	6.65
			303	95.49	5.62
			373	92.55	5.23
			453	90.25	4.86

3.5.2 Styrene Trimer cation $C_{24}H_{24}^{+}$

Table 11: Optimized structures for styrene trimer cations at B3LYP/6-31** level, total energy E (in atomic units), calculated cross sections (Ω) and reduced mobility (K_o) using the trajectory methods(TM) at different temperatures.

		E (au)	T (K)	Ω (Å^2)	K_o $(cm^2V^1s)^1$
Sty3a	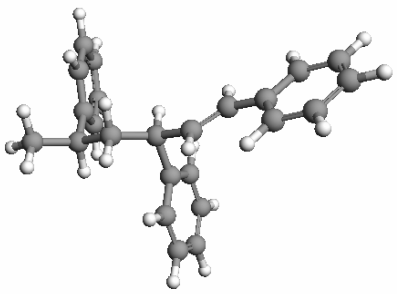	-928.780538965	125 303	154.95 127.01	5.44 4.20
Sty3b	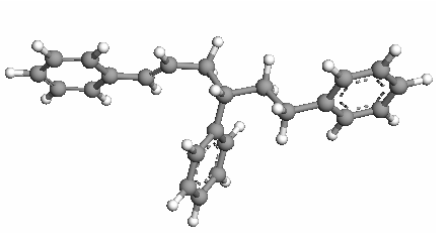	-928.781075445	125 303	153.47 128.11	5.47 4.17
Sty3c	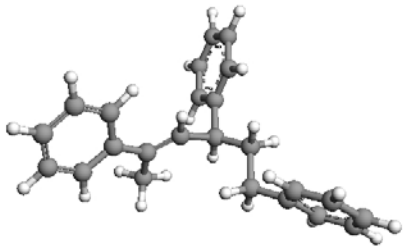	-928.781338626	125 303	157.42 128.09	5.33 4.17
Sty3d	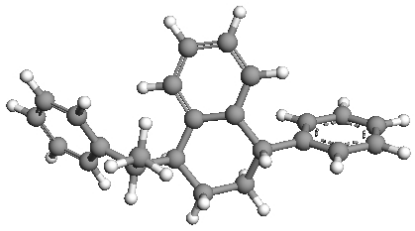	-928.784490035	125 303	142.95 119.05	5.87 4.49

3.6 Exploratory Study of the Gas Phase Polymerization of Styrene Initiated with a Free Radical Initiator

3.6.1 Experimental Results

In order to explore the possibility of the initiating the gas phase polymerization of styrene using a free radical initiator, we used the AIBN (2,2'-Azo-bis-isobutyronitrile ($C_8H_{12}N_4$)) initiator. First, the AIBN was allowed to decompose in the gas phase at T = 94.7 ^oC and the EI mass spectrum was collected as shown in Figure 48-a. The main m/z peaks observed are assigned to $C_8H_{12}N_2^+$, $C_4H_7N^+$, $C_4H_6N^+$ and $C_3H_4N^+$. Second, styrene vapor was allowed to polymerize in absence of the initiator at T = 93.3 ^oC and the EI mass spectrum was collected as shown in Figure 48-b. The mass spectrum shows the formation of the styrene dimer and its fragments ions. Finally, when both styrene and AIBN vapors were heated to T = 95.4 ^oC, the resulting mass spectrum clearly indicated the formation of higher styrene oligomers up to styrene tetramer as shown in Figure 48-c. In addition, a minor series [$C_8H_{12}N_2(C_8H_8)_n^+$, for n = 1-2] corresponding to the addition of styrene on $C_8H_{12}N_2^+$ was also observed. Other species observed correspond to $C_4H_6N(C_8H_8)_2^+$ and $C_4H_7N(C_8H_8)_2^+$, respectively. It is very interesting to note that m/z peak 206 corresponds to $C_{16}H_{14}^+$is observed with significant intensity in the presence of styrene and AIBN. This quiet different from the result obtained by heating styrene vapor in the absence of AIBN where the 206 m/z is a minor peaks as shown in Figure 48-b.

Mobility measurement was carried out for the mass-selected styrene dimer (produced from a continuous flow of the heated styrene and AIBN vapors at T = 92.3^oC) The measured

reduced mobility in He at 303 K was K_o= 5.82 $cm^2V^{-1}s^{-1}$. The Arrival time distribution of the mass-selected $(C_8H_8)_2^+$ ions and the predicted distribution from transport theory are displayed in Figure 49.

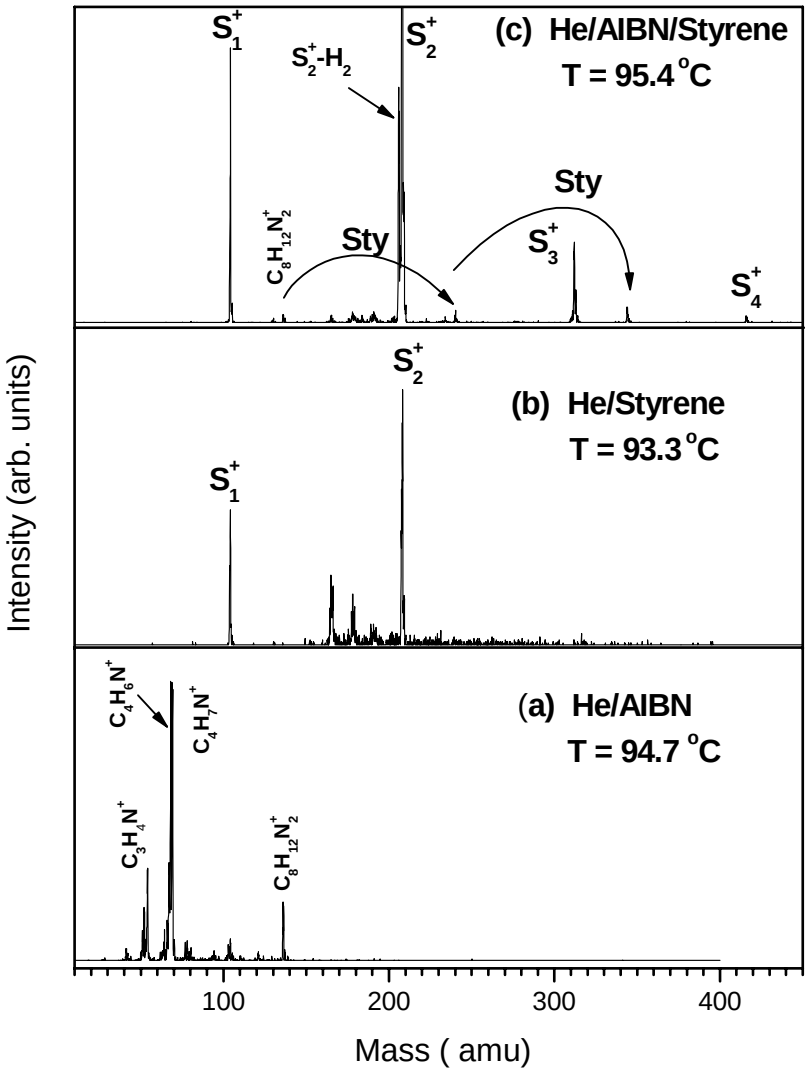

Figure 48: Mass spectra when the source contained: (a) only the initiator AIBN (2,2'-Azo-bis- iso butyronitrile ($C_8H_{12}N_4$) at T = 94.7 °C; (b) only styrene vapor at T = 93.3 °C and (c) styrene + AIBN at T = 95.4 °C.

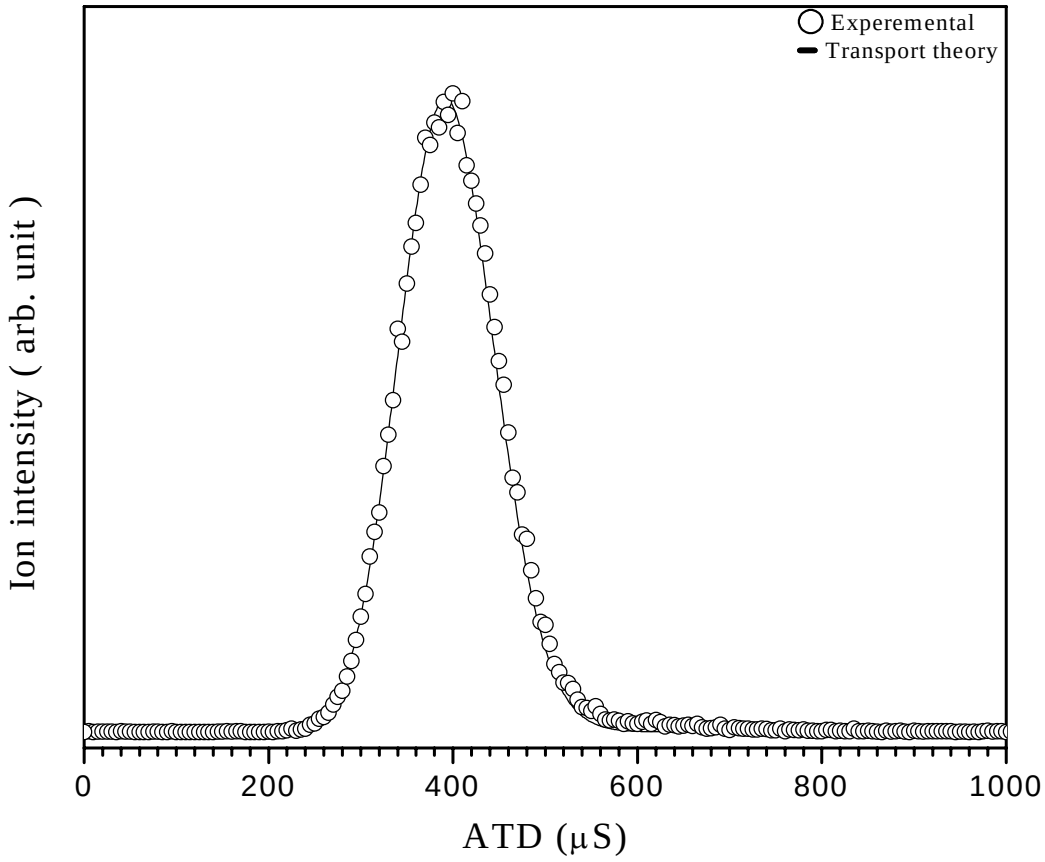

Figure 49: Arrival time distribution of mass selected $(C_8H_8)_2^+$ (formed by EI of the continuous flow of the heated styrene and AIBN vapors at T = 92.3 ^oC)(circles) and the predicted distribution from transport theory (solid line). Experimental conditions are: the source temperature is 92.3 ^oC, 50 μs pulse width, injection energy is 14 eV, 1.682 Torr He inside the drift cell, the drift cell temperature is 29.65 ^oC 25 V voltage difference between the entrance and the exit lenses. The measured reduced mobility K_o = 5.82 $cm^2V^{-1}s^{-1}$.

3.7 Discussion of the Results for Styrene Dimers and Trimers

The styrene dimer formed in the gas phase has been a subject of several studies that established the covalent bonded nature of the dimer and suggested several cyclic structures for the dimer[14,29]. However, to date no direct evidence has been reported to confirm the structure of the gas phase dimer. In this work, we followed a systematic investigation to establish the nature of bonding and confirm the structures of the styrene dimers and trimers in the gas phase. First, a dissociation energy (injection energy) study of the non-covalent benzene dimer was carried out and compared to the mass-selected styrene dimer ion. This comparative study was carried out by the injection of the mass-selected benzene dimer under the same experimental conditions as in the styrene dimer. The mass spectrum displayed in Figure 50 indicates that only 17 % of the benzene dimer population survived the 15 eV injection energy. However, in the case of the styrene dimer ion 90 % of styrene dimer population survived the collisions with an injection energy of 15 eV. Using the binding energy argument, the benzene dimer has a binding energy of 17.8 kcal/mol [40], which implies with a good confidence that the styrene dimer binding energy is significantly higher than 18 kcal/mol. Secondly, when the mass-selected styrene dimer ion was injected into the drift cell, the ratio of styrene dimer to the dissociated monomer did not to change as the drift cell temperature was increased from 303 K to 453 K. The resulting mass spectrum is displayed in Figure 51. From the dimer/monomer intensity ratio displayed in Figure 51 a binding energy of at least 28 Kcal/mol for the styrene dimer could be estimated assuming a non-covalent interaction. Finally, further evidence was obtained

from the dissociation products the mass-selected styrene dimer ($C_{16}H_{16}^{+}$)(displayed in Figure 14), which shows the sequential loss of CH_3, C_2H_4, C_2H_5, and C_6H_6 from the dimer. This reveals that the styrene dimer ion ($C_{16}H_{16}^{+}$) is a covalently bonded, since it dissociated with a characteristic loss of stable chemical fragments. The injection energy and temperature studies together lead us to the conclusion that the styrene dimer is covalently bonded. In the case of higher oligomers as in the case of styrene trimer ion ($C_{24}H_{24}^{+}$), the dissociation products of the mass-selected trimer show the sequential loss of CH_3, C_2H_4, C_2H_5, C_6H_6 and C_7H_7. This mass spectrum (displayed in Figure 16) shows that the styrene trimer ion mainly dissociates into m/z = 180 (C_{14} H_{12}^{+}). If this is weakly bonded it will dissociate into its monomer. This indicates that the structure of m/z 180 must represent a stable molecular ion resulting from the dissociation of the styrene trimer ion. Similar conclusions can be drawn based on the dissociation products of the higher styrene oligomer ions presented in Figure 17 and Figure 18.

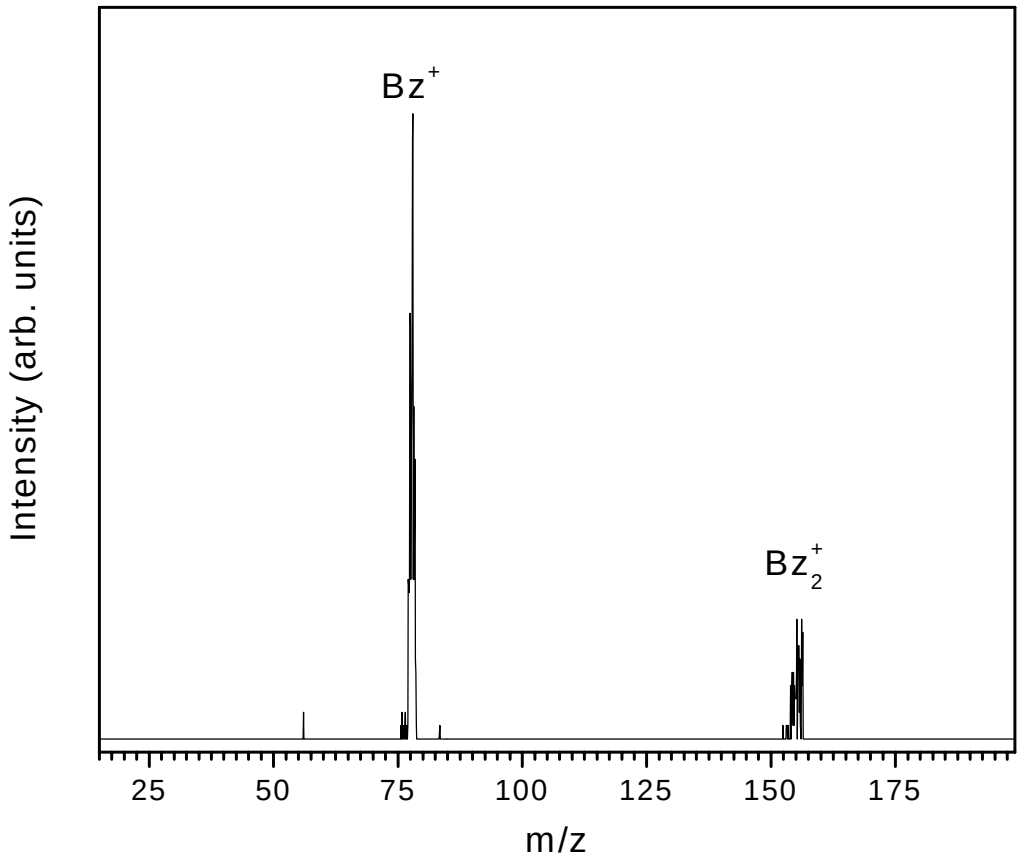

Figure 50: Mass spectra of the mass selected Benzene dimer ion, $C_{12}H_{12}^{+}$ injected into He with 15 eV injection energy .

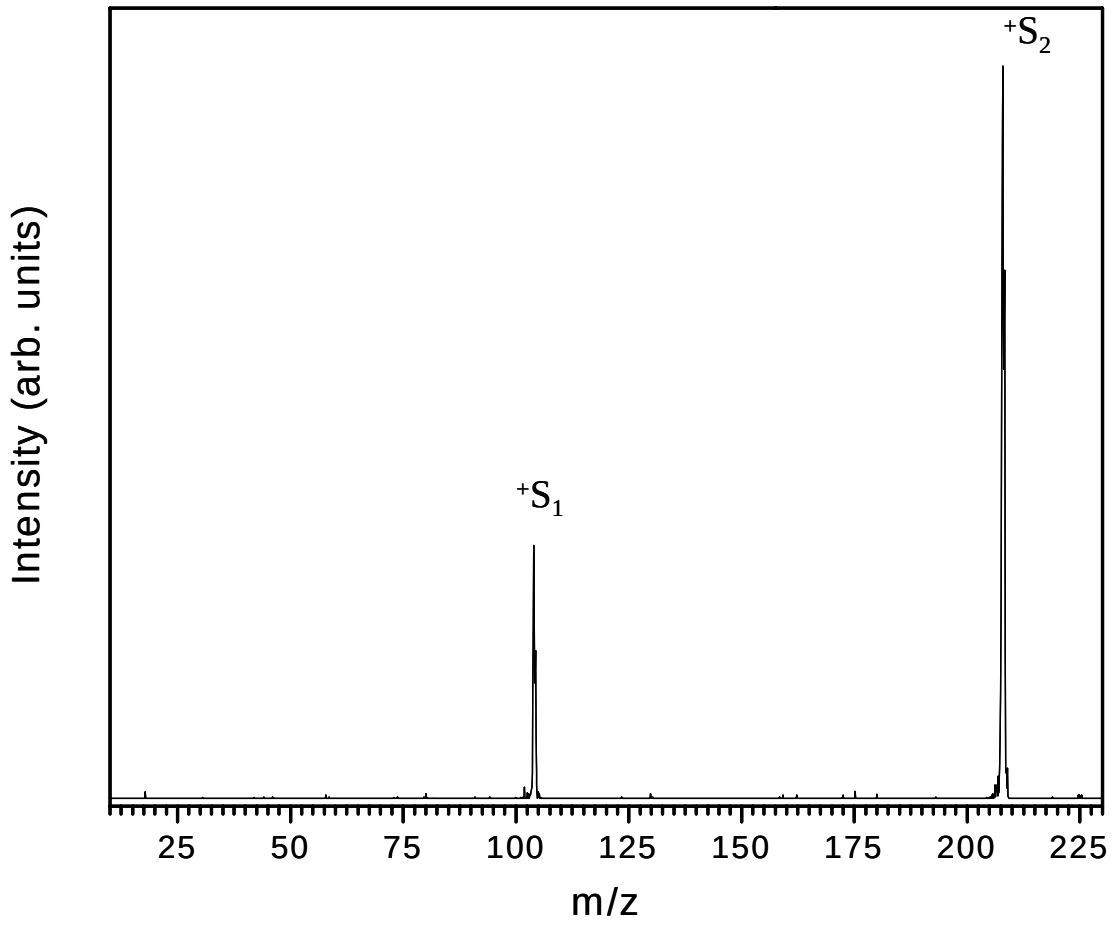

Figure 51: Mass Spectrum of the mass selected $C_{16}H_{16}^{+}$ obtained by Electron Impact ionization. Injected with 15 eV into He, the drift cell temperature is 180.0 ^{o}C.

After establishing the covalent nature of the gas phase styrene oligomers observed in our experiments, it is important to provide direct structural information on these oligomers. The combination of the measured collision cross sections and theoretical calculations can provide accurate structural information on the ionized styrene oligomers. The experimental based structure can be further confirmed by the analysis of the dissociation products of the mass-selected styrene oligomers ions. The comparisons of the measured cross sections of styrene dimer and trimer ions at different temperatures with those calculated for the lowest energy structures representing different formation mechanisms are summarized in Table 10 and Table 11.

In the case of styrene dimer ion, the measured and the calculated cross sections at different temperatures are displayed in Figure 52-Figure 55. Figure 52 shows that the measured cross section at 125 K agrees with the calculated cross sections of structures j, e, i, a, d, f and b within the experimental error (5%). However, isomer j (1-Phenyltetralin) is the lowest in energy structure closest to the measured cross section at 125 K. At 174 K the measured cross section is still in agreement with the theoretical one of the lowest energy isomer j as shown in Figure 53. At room temperature (303 K) the lowest energy structure that matches the measured cross section is structure e (1-methyl 3-phenyl indane) as shown in Figure 54. At the highest temperature used of 453 K, the measured cross section is in agreement with the theoretical structures corresponding to isomer k (1, 3 diphenyl but-1-ene) and h (1, 4 diphenyl but-1-ene) as shown in Figure 55, however isomer k is the lower in energy compared to isomer h, and therefore, isomer k is the proposed structure at 453 K.

The comparison between the measured and the calculated cross-sections of the styrene dimer at different temperatures is shown in Table 12.

Table 12: Summary of the experimental and theoretical cross sections for the styrene dimer.

Temperature (K)	Ω(exp) ($Å^2$)	Ω(Calc) ($Å^2$)	Structure
125	108	107.1	j
173	97.5	98.4	j
303	92.2	90.3	e
453	89.9	90.3	k

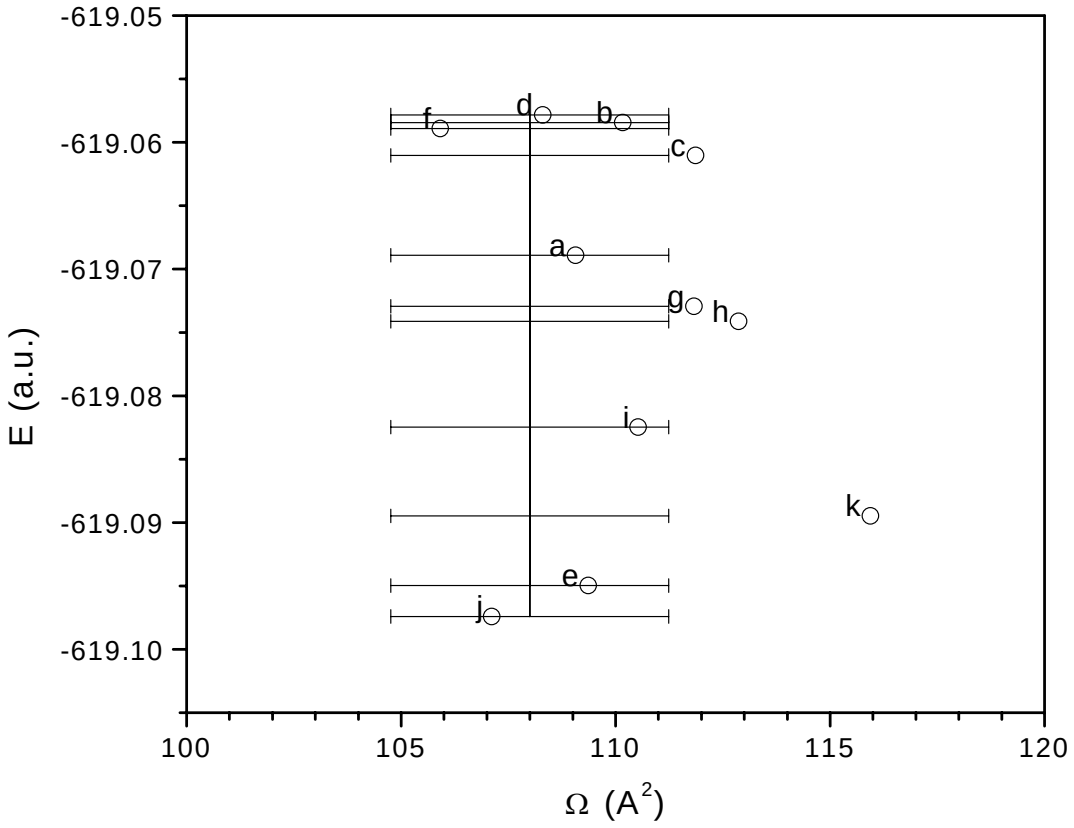

Figure 52: The calculated cross section vs the energy of the optimized structures of $C_{16}H_{16}^{+}$ at 125 K. The solid line is the measured cross section. The calculated cross sections were obtained for the optimized structures using the trajectory methods[42].

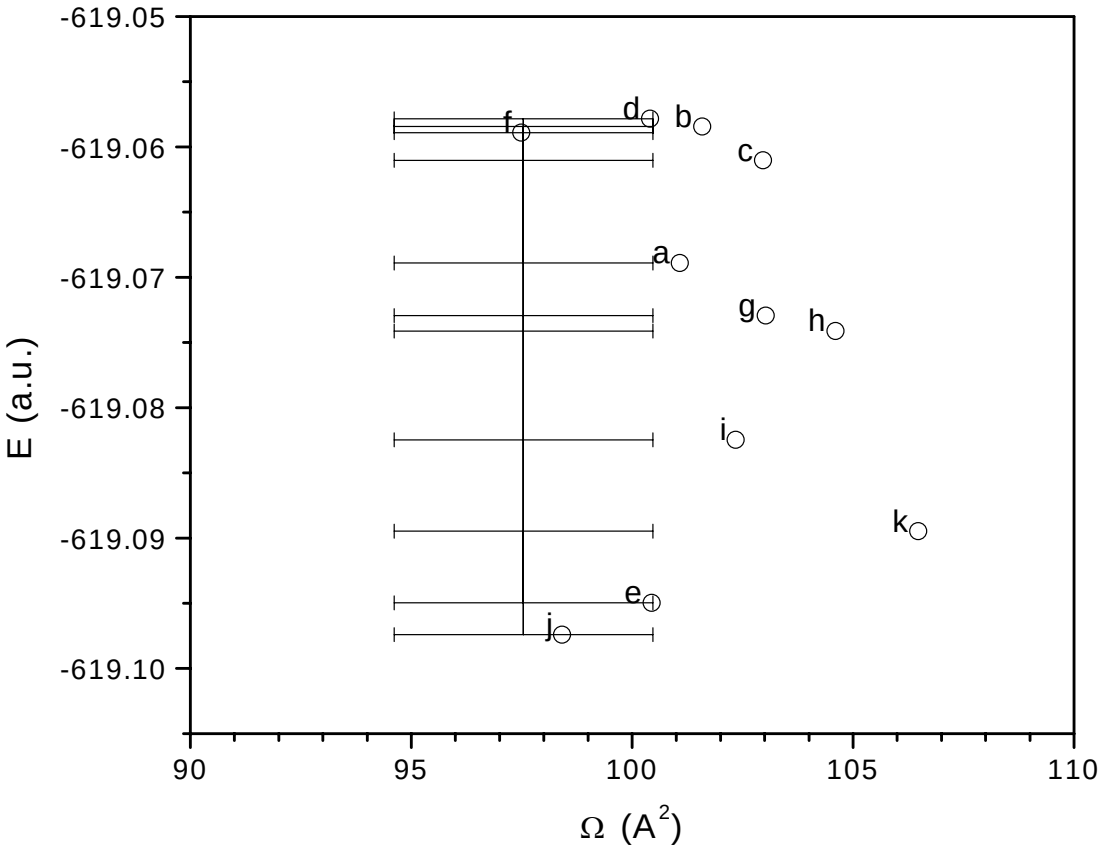

Figure 53: The calculated cross section vs the energy of the optimized structures of $C_{16}H_{16}^{+}$ at 174 K. The solid line is the measured cross section. The calculated cross sections were obtained for the optimized structures using the trajectory methods.[42]

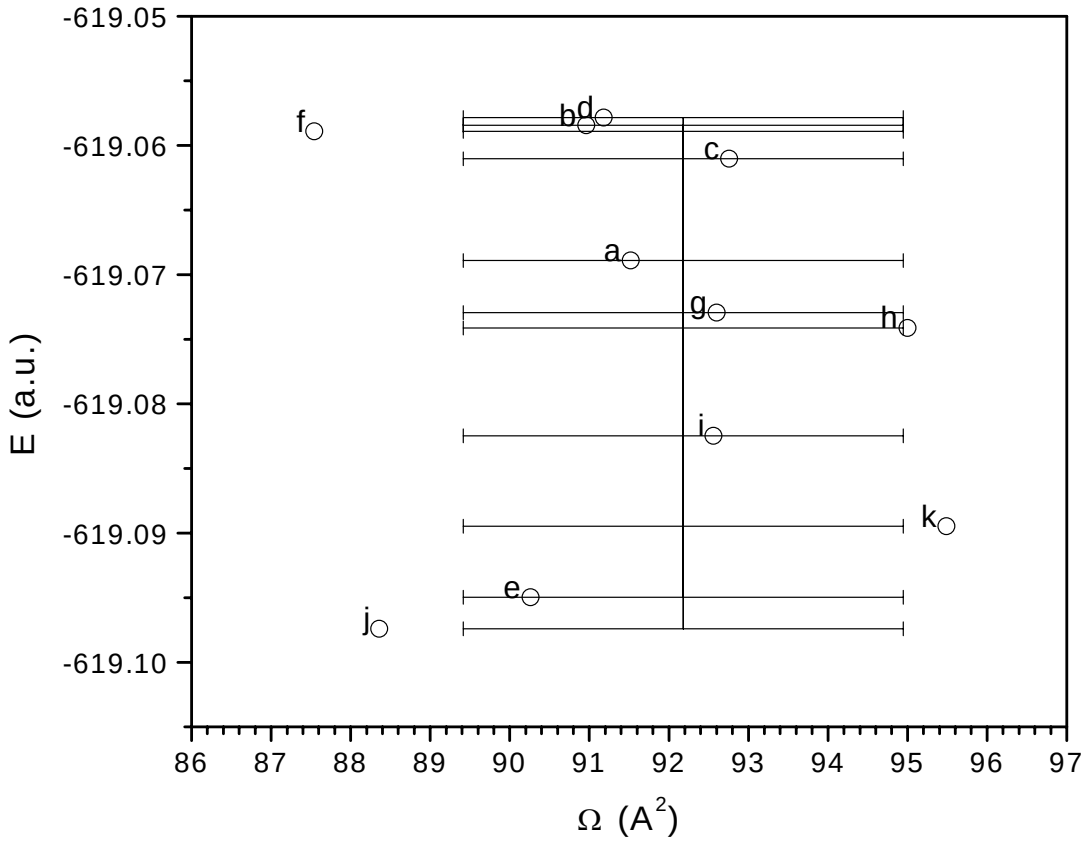

Figure 54: The calculated cross section vs the energy of the optimized structures of $C_{16}H_{16}^{+}$ at 303 K. The solid line is the measured cross section. The calculated cross sections were obtained for the optimized structures using the trajectory methods.[42]

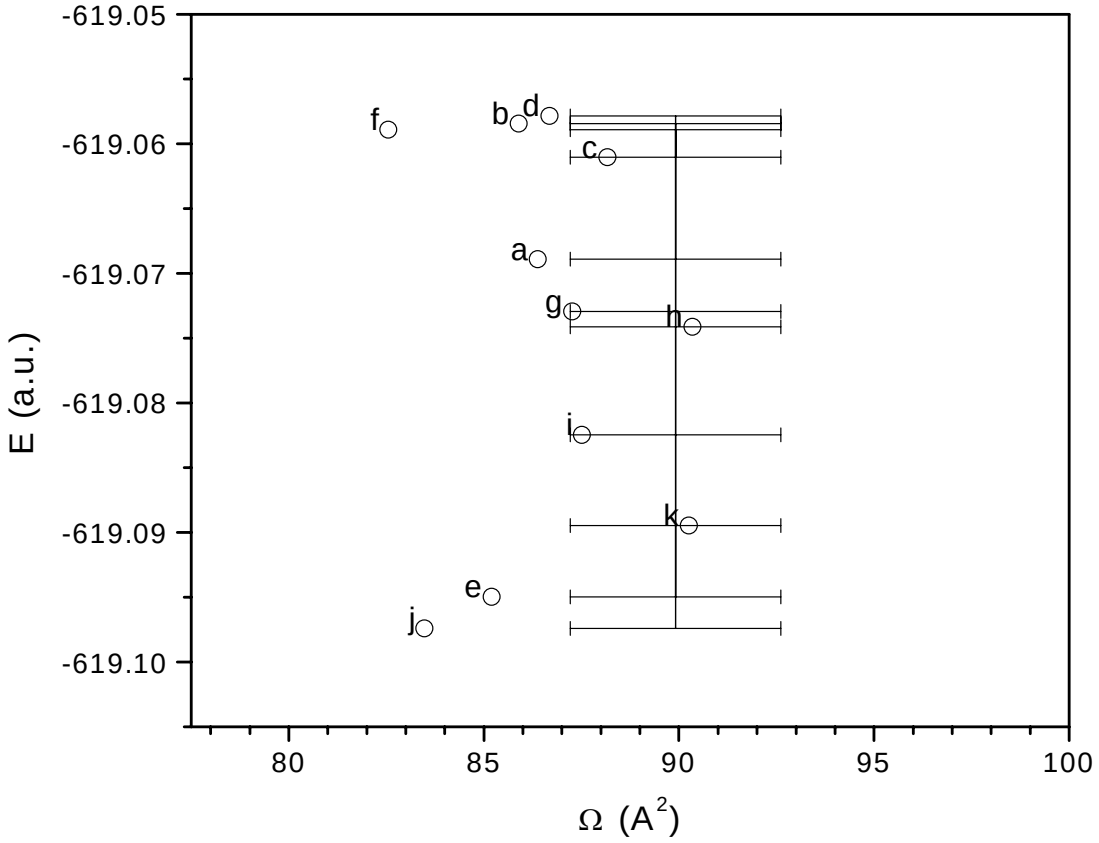

Figure 55: The calculated cross section vs the energy of the optimized structures of $C_{16}H_{16}^{+}$ at 453 K. The solid line is the measured cross section. The calculated cross sections were obtained for the optimized structures using the trajectory methods.[42]

The results shown in Table 12 indicate that there are three different isomers for the styrene dimer present under our experimental conditions. However, only one peak in the arrival time distributions (ATDs) was observed even at a lower cell temperature of 125 K. Since the measured cross sections for most of the proposed structures are very close, within 5 %, a well-resolved peak for each isomer cannot be observed. This is because our drift cell, has a resolving power of about 20. Thus only isomers with more than 5% difference in cross sections can be separated. However, using the cross section of the three lowest energy isomers j, e and k in Table 12, we can construct composite of ATDs, which reproduce the measured ATDs. Figure 56 displays a comparison of the measured ATD at 305 K, of the styrene dimer cation $(C_8H_8)_2^+$ with the predictions of transport theory for the three structural isomers j, e and k. This Figure displays an excellent fit to the sum of the isomers j (1-phenyltetralin)(dashed line), k (1,3 diphenyl but 1-ene) (dots) and e (1-methyl 3- phenyl indane) with a relative abundance of 36, 36 and 28%, respectively. This suggests that at room temperature we have three structures j, k, and e. This may also be verified by examining the dissociation products of the mass selected styrene dimer. For example, the loss of the CH_3 group supports the presence of isomers k and e. The loss of the benzene, C_6H_6 and C_2H_4 fragments supports the presence of both isomers j and e. Figure 57 and Figure 58 display the comparison of the measured ATDs, at 125 K and 453 K, of the styrene dimer cation $(C_8H_8)_2^+$ to the predictions of transport theory for the three structural isomers j, k and e. At temperature of 125 K the best fit is obtained when the relative abundance of j, k and e isomers is 63, 31, and 6% respectively. At a temperature of 453 K, Figure 58 indicates an excellent fit for isomers j, e and k when the relative

abundance is 11, 5 and 84 %, respectively. The temperature study and the good comparison to the calculated ATDs for the three different structural isomers with the proper relative abundance indicate that upon injection and heating the cyclic isomers j and e are and converted into the linear structure k. Unfortunately, those isomers could not be separated because of the resolving power of the current mobility cell. It should be possible to separate the broad ATDs using high resolution drift tube with resolving power of 50-100[67].

Now, that the structures for styrene dimers have been determined, the mechanism of formation and the observed fragmentation pathways can be explained. In the case of isomers j (1-phenyl tetralin) and k (1,3 diphenyl but 1-ene), they both can be formed via the Mayo's mechanism[21,22]. In the case of the j isomer, two styrene molecules cyclize via Diels -Alder addition forming an intermediate (AH) followed by 1,3 H-Shift. Upon ionization and then injection of the j radical cation, it losses C_6H_6 and C_2H_4 fragments to generate the dissociated products $C_{10}H_{10}^+$ and $C_{14}H_{12}^+$, respectively. These fragments (with m/z = 180 and 130) were both observed in the mass spectrum as shown in Figure 14. Finally, in the case of isomer k, it can be formed upon a free radical attack (m/z 105) to a second styrene molecule followed by termination through disproportionation. Upon ionization followed by injection, this radical cation can lose a CH_3 fragment to generate the ion $C_{15}H_{13}^+$ (m/z = 193). The $C_{15}H_{13}^+$ ion is observed in the dissociation products of the styrene dimer cation as shown in Figure 14. Finally, isomer e (1-methyl 3phenyl indane) can be formed via a cationic mechanism[68]. Upon injection, this dimer can be dissociated into $C_{15}H_{13}^+$ (m/z 193) by the loss of CH_3, and into $C_{10}H_{10}^+$ (m/z 130) by the loss of C_6H_6.

Both of these product ions were observed in the mass spectrum of the mass selected styrene dimer as shown in Figure 14. The formation mechanism and the fragmentation pathways are summarized in Scheme 7

In the case of styrene trimer ion, the measured cross section at room temperature (118.4 ± 4 Å^2) agrees well with the 1-phenyl-4 (1-phenyl ethyl tetralin) structure (structure d). At a lower temperature, 125 K, the measured cross section is (135.6 ± 5 Å^2). This favorably agrees with the cross section calculated at 125 K for the same structure d. This structure is among the four structures investigated as shown in Table 11.

Table 13 compares the experimental cross sections of the styrene trimer ion to the calculated ones for the four proposed structures a, b, c and d shown in Table 11. The comparison of the measured ATDs and the styrene trimer ions with those calculated based on structure (d) are shown in Figure 59 and Figure 60 at temperature 125 K and 303 K, respectively. At 303K, isomer (d) results in an excellent agreement between the measured and the calculated ATDs are obtained as shown in Figure 59. However, at 125 K Figure 60 indicates that there are probably other isomers present, although isomer d still contributes significantly to the ATD's. The resolution of the mobility measurements is enhanced that is why Figure 60 provides strong indication that other trimer structures are present. The other calculated structures shown in Table 11 (isomers a, b and c) result in ATDs quiet different from the experimental one at 125 K as shown in Figure 61. Future calculations should focus on identifying other possible trimer isomers that can reproduce the ATD. It should be noted that the proposed structure (d) for the gas phase styrene

trimer is identical to the structure of the trimer isolated from the solution polymerization of styrene and identified using NMR.[65]

Based on the 1-phenyl-4 (1-phenyl ethyl tetralin) structure of the styrene trimer ion, a scheme was constructed to explain the dissociation products observed in the mass spectrum of the mass selected styrene trimer cation (Figure 16). The formation mechanism of the styrene trimer ion and the explanation of the observed dissociation products are summarized in the Scheme 8.

Table 13: Summary of the experimental and theoretical cross sections for styrene trimer.

Theoretical	Structure				Experimental (Ω)
	a	b	c	d	
Ω (304 K) ($Å^2$)	127.0	128.1	128.1	119.1	118.4 ± 4
Ω(125 K) ($Å^2$)	155.0	153.4	157.4	143.0	135.6 ± 5
Stabilization Energy (kcal/mol)	2.48	2.14	1.98	0.00	

The above results indicate that the observed represent ionized neutral oligomers formed by vapor phase thermal polymerization of styrene. This is supported by several specific considerations: first, the styrene liquid contained in the bubbler used to supply the styrene vapor in the experiments formed a gel-like solution when heated. In addition, a thick film was deposited on the wall of the bubbler and inside the delivery line located before the expansion nozzle. Second, the appearance of larger oligomer ions in the mass spectrum depends on the temperature and the duration of heating of the styrene vapor.

Third, the same ions were observed (although with much weaker intensity) by directly ionizing the heated styrene vapor (with no beam expansion), thus eliminating the possibility of styrene clusters. This was achieved by removing the cluster source, the pulsed nozzle, thereby minimizing any expansion that would lead to cluster formation. Continuous flow was accomplished by using either a continuous nozzle or a capillary tube.

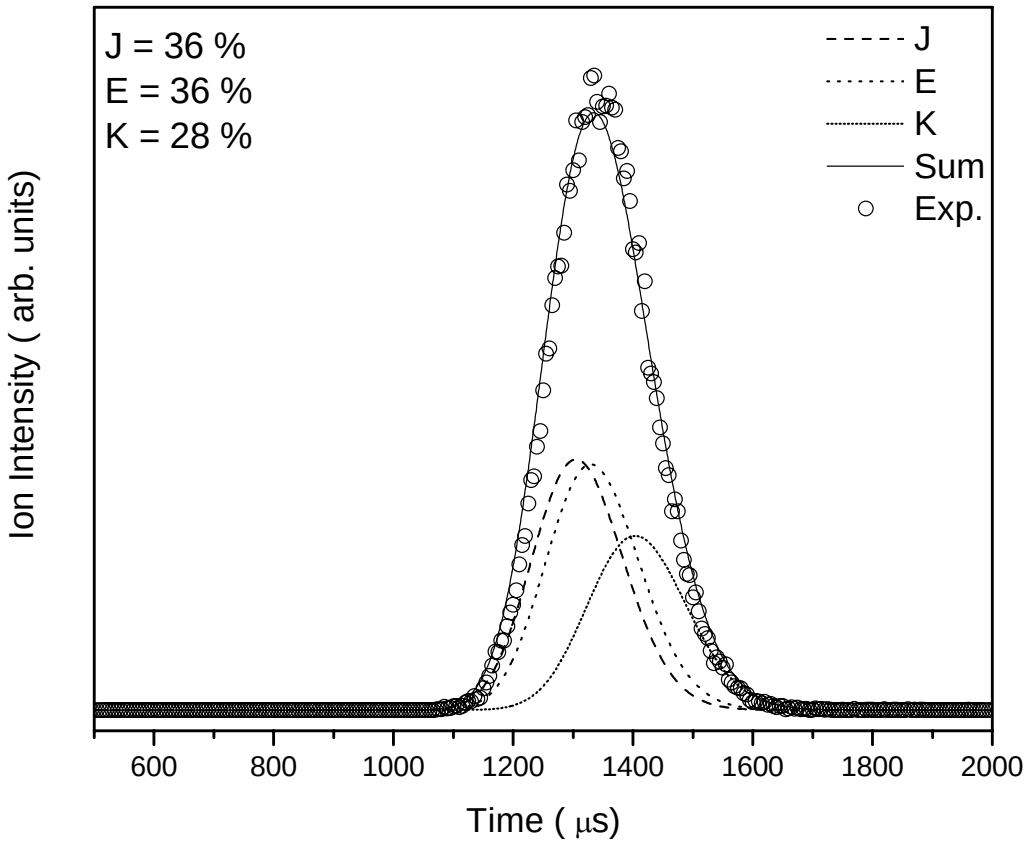

Figure 56: Comparison of the measured ATD of Styrene dimer $(C_8H_8)_2^+$(circles) drifting in 1.136 Torr He at 303 K (E/N = 4.38 Td), with the predictions of the transport theory for three structural isomers. These isomers are j (1-phenyltetralin) (dashed line), e (1methyl 3-phenyl indane) (dots) and k (1,3 diphenyl but 1-ene) (short dots).

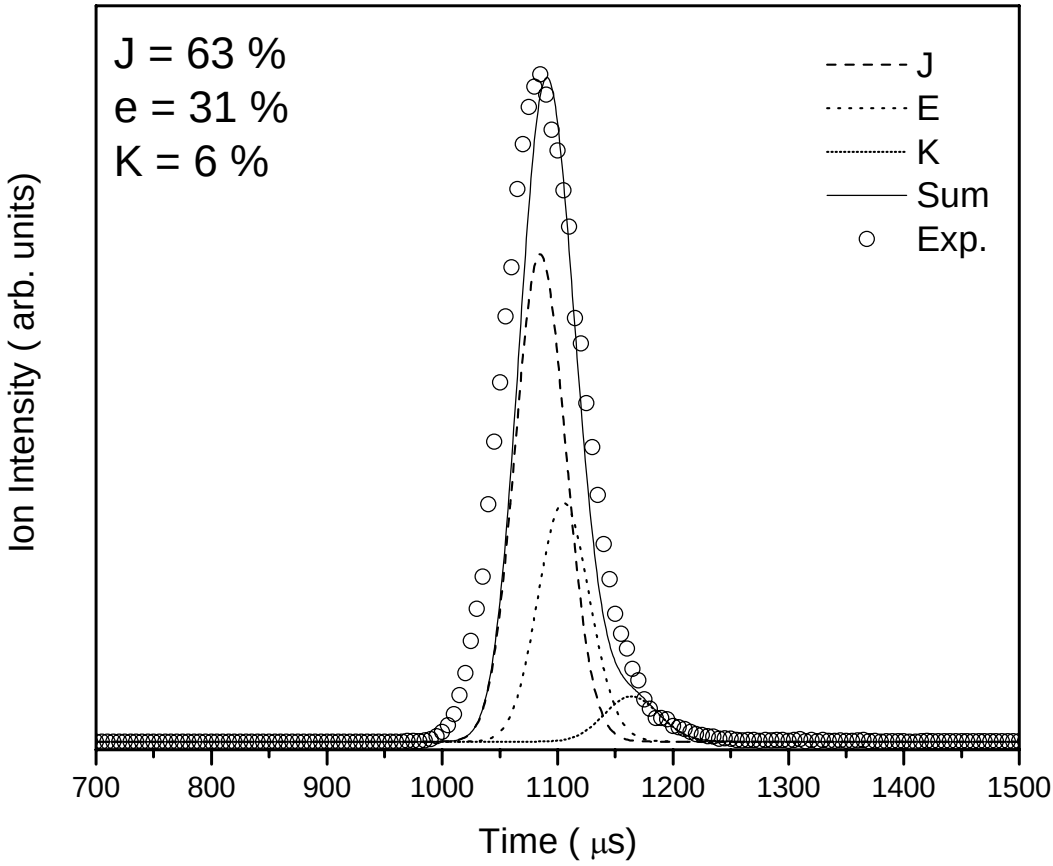

Figure 57: Comparison of the measured ATD of Styrene dimer $(C_8H_8)_2^+$(circles) drifting in 1.430 Torr He at 125 K (E/N = 4.38 Td), with the predictions of the transport theory for three structural isomers. These isomers are j (1-phenyltetralin) (dashed line), e (1-methyl 3-phenyl indane) (dots) and k (1,3 diphenyl but 1-ene (short dots).

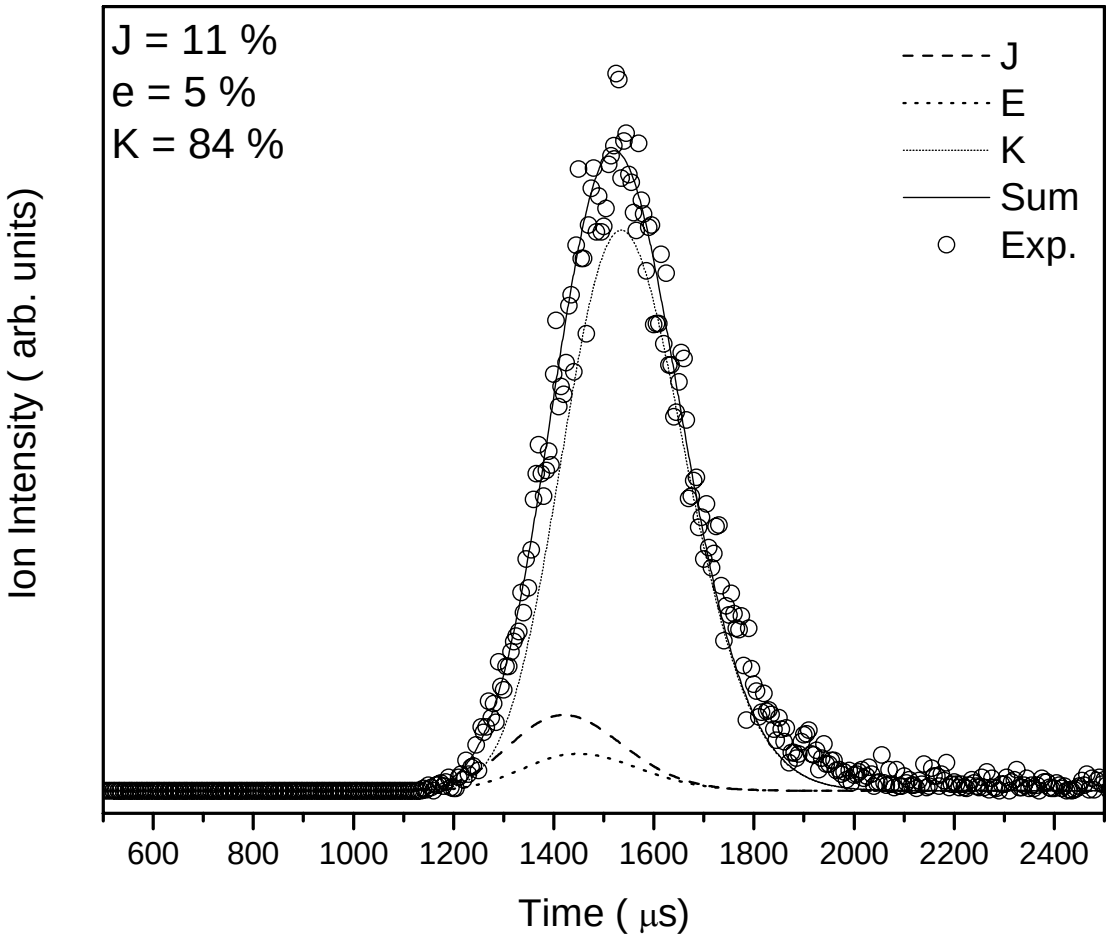

Figure 58: Comparison of the measured ATD of Styrene dimer $(C_8H_8)_2^+$(circles) drifting in 1.418 Torr He at 453 K (E/N = 4.47 Td), with the predictions of the transport theory for three structural isomers. These isomers are j (1-phenyltetralin)(dashed line), e (1-methyl 3-phenyl indane) (dots) and k (1,3 diphenyl but 1-ene) (short dots).

Scheme 7: Mechanism of the styrene dimers' formation and the explanation of the observed fragmentation pathways

1. Formation of styrene dimer (j) from the Mayo's mechanism:

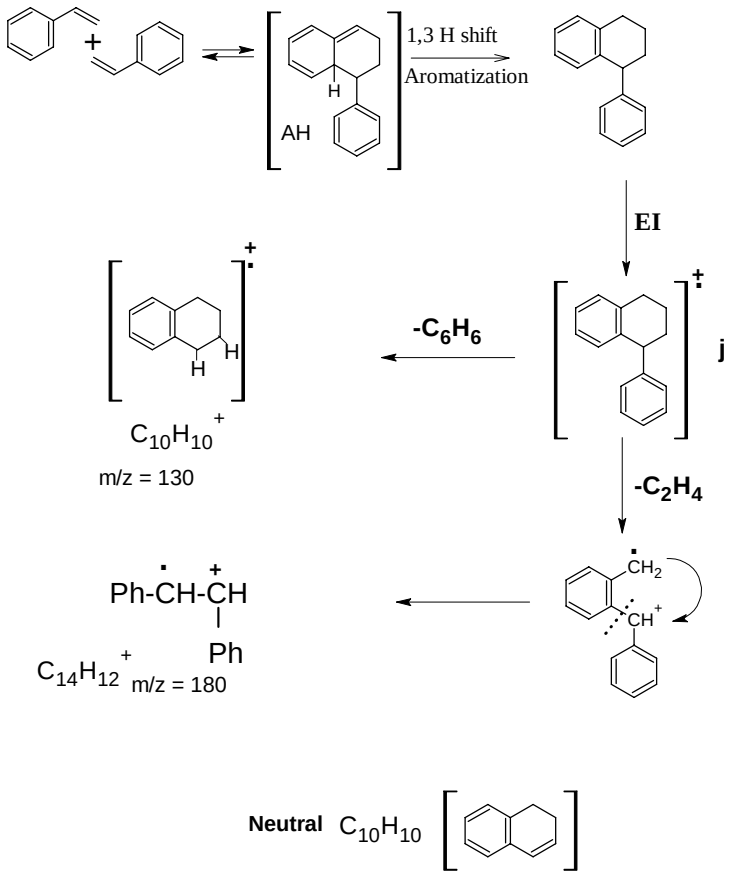

2. Formation of isomer (k) in the gas phase through the Mayo's mechanism:

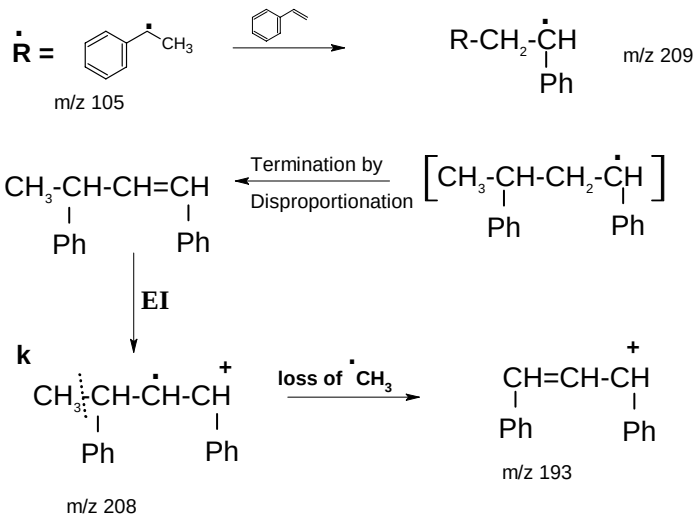

3. Formation of isomer (e) by intracluster cationic polymerization:

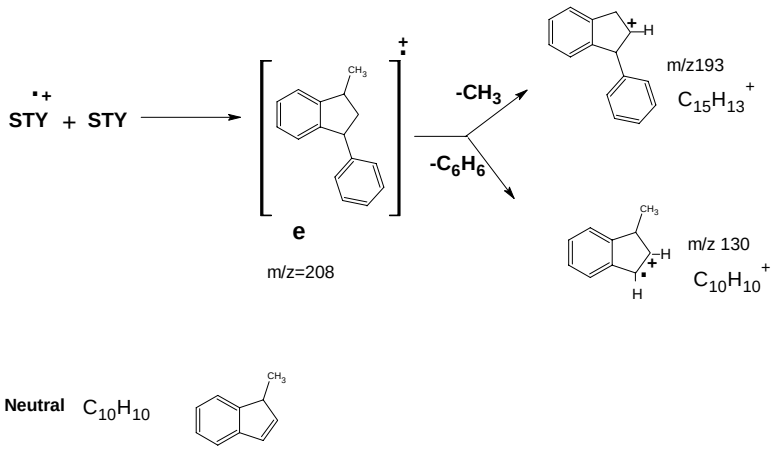

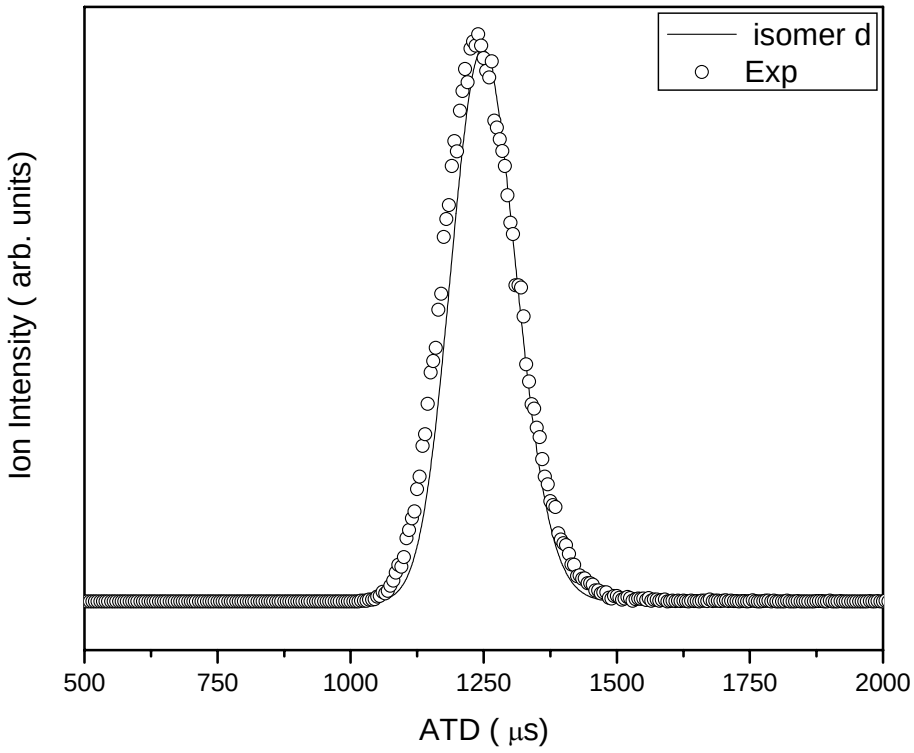

Figure 59: Comparison between the experimental and the calculated ATD for the styrene trimer (d) at room tempreature (303 K). Arrival time distribution of mass selected $(C_8H_8)_3^+$ ions (circles) and the predicted distribution from transport theory (solid line). Experimental conditions are: 50 μs pulse width, injection energy is 15 eV, 1.141 Torr He inside the drift cell, cell temperature is 30.88 ^oC, 20 V voltage difference between the entrance and the exit lenses and E/N = 6.21 Td. The reduced mobility $K_o = 4.54\ cm^2V^{-1}s^{-1}$.

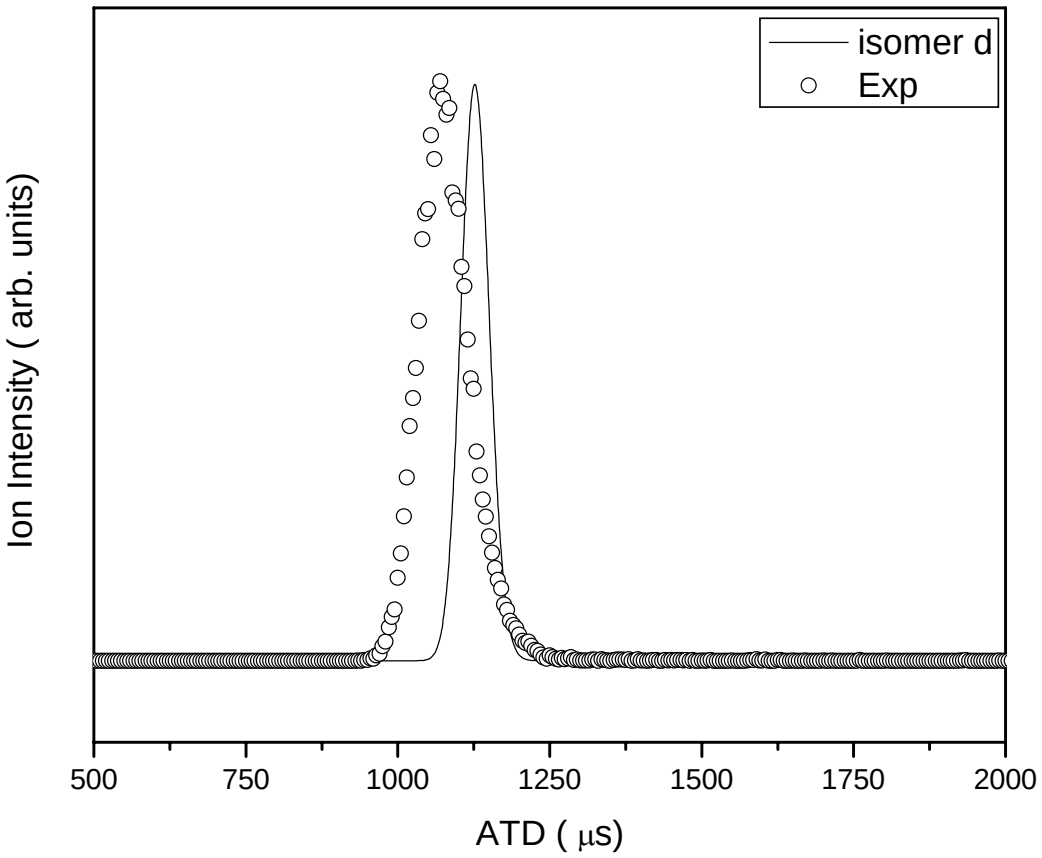

Figure 60: Comparison between the experimental and the calculated ATD for the styrene trimer (d) at 125 K (solid line).Arrival time distribution of $(C_8H_8)_3^+$ ions at drift cell temperature of 125.40 K (circles). Experimental conditions are: 50 μs pulse width, injection energy is 15 eV, 1.026 Torr He inside the drift cell, the drift cell temperature is -147.75 ^oC 40 V voltage difference between the entrance and the exit lenses and E/N = 5.69 Td. The reduced mobility K_o = 6.20 $cm^2V^{-1}s^{-1}$.

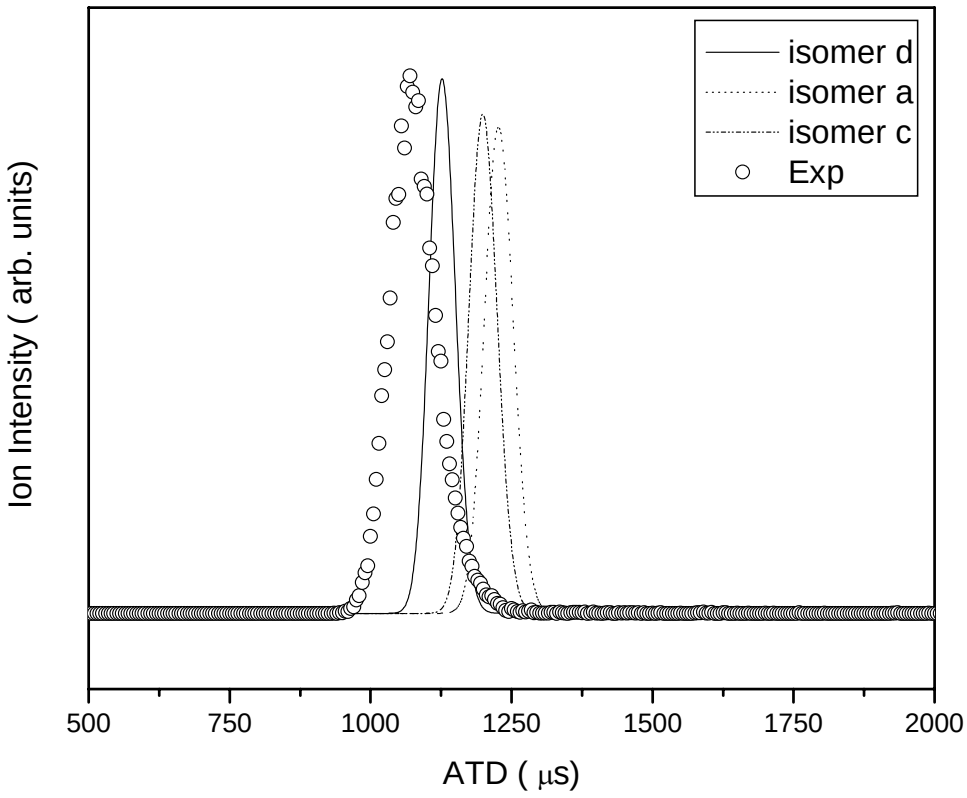

Figure 61: Comparison between the experimental and the calculated ATD for the styrene trimer (a, c and d) at 125 K .Arrival time distribution of $(C_8H_8)_3^+$ ions at drift cell temperature of 125.40 K (circles). Experimental conditions are: 50 μs pulse width, injection energy is 15 eV, 1.026 Torr He inside the drift cell, the drift cell temperature is -147.75 ^oC 40 V voltage difference between the entrance and the exit lenses and E/N = 5.69 Td. The reduced mobility K_o = 6.20 $cm^2V^{-1}s^{-1}$.

Scheme 8: Mechanism of the styrene styrene trimer ions ($C_{24}H_{24}^{+}$) formation and the explanation of the observed fragmentation pathways:

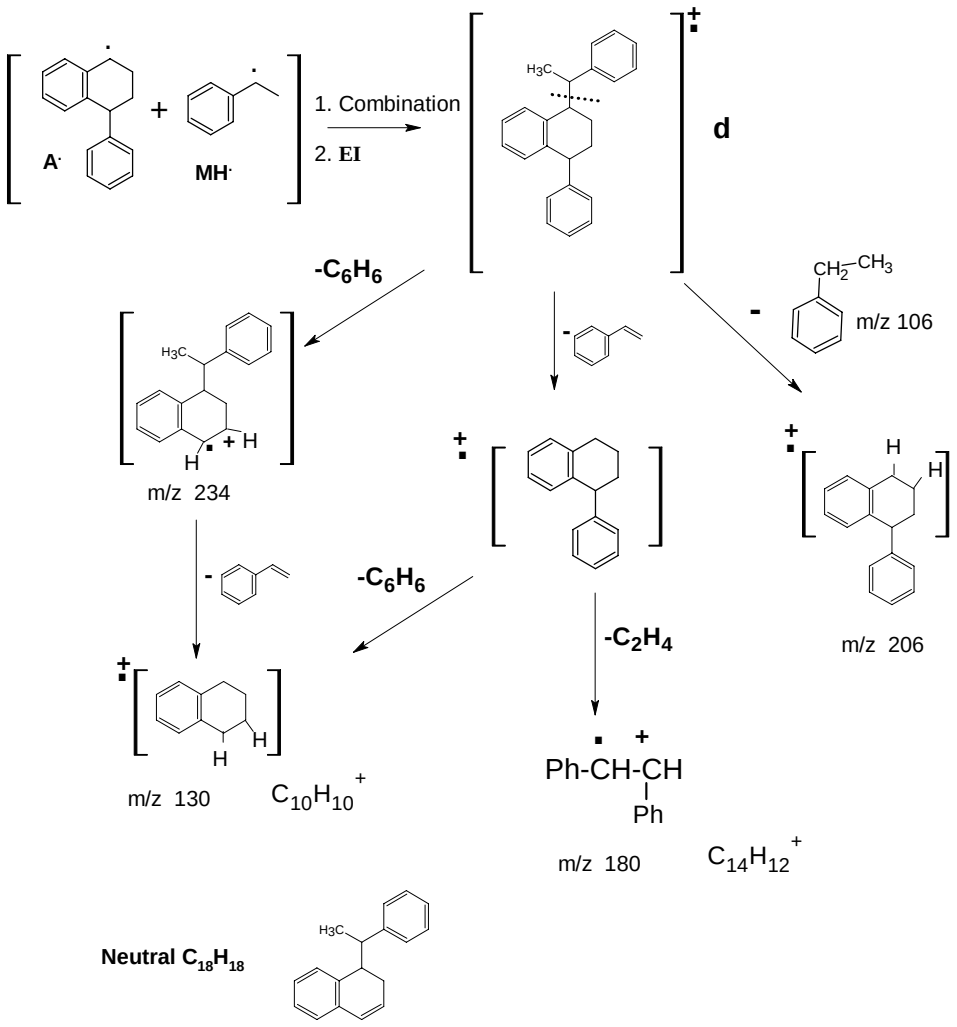

The mass spectrum showed only styrene monomer, styrene dimer and their fragments as shown in Figure 48. However, when the styrene vapor was passed over AIBN, the mass spectrum showed $(styrene)_n^+$, n = 1-4 as shown in Figure 48. This provides clear evidence that AIBN enhances the polymerization of styrene vapor. AIBN is well known initiator that initiates styrene free radical polymerization in bulk the phase. We were able to mass select the styrene dimer formed by AIBN initiator, and measure its mobility. The measured mobility (K_o=5.82 $cm^2V^{-1}s^{-1}$) is comparable to the ones obtained using the pulsed nozzle experiment.

A final experiment was performed to capture the actual initiating species in the gas phase thermal polymerization of styrene in the absence of any added free radical initiators. Styrene vapor was heated to 70-90 ^oC in a continuous flow using a capillary tube. The resulting mass spectrum is shown in Figure 62. It should be noted that under these experimental conditions, no expansion takes place and the number of collision. between the gas phase radicals and neutral styrene molecules should be very small. It is interesting to note that the major ions formed in this experiment are the even-electron ions $C_{16}H_{15}^+$(m/z 207), $C_{15}H_{11}^+$(m/z 191) and $C_{13}H_9^+$(m/z 165). This suggests that these ions are produced by the ionization of the free radical 207 amu and fragmentations of the generated $C_{16}H_{15}^+$ ion. These fragmentations involved the loss of CH_4 and C_3H_6 to generate the ions $C_{15}H_{11}^+$(m/z 191) and $C_{13}H_9^+$(m/z 165), respectively. The observation of $C_{16}H_{15}^+$ ion (m/z 207) provides another strong evidence for the generation of the 207 amu free radical.

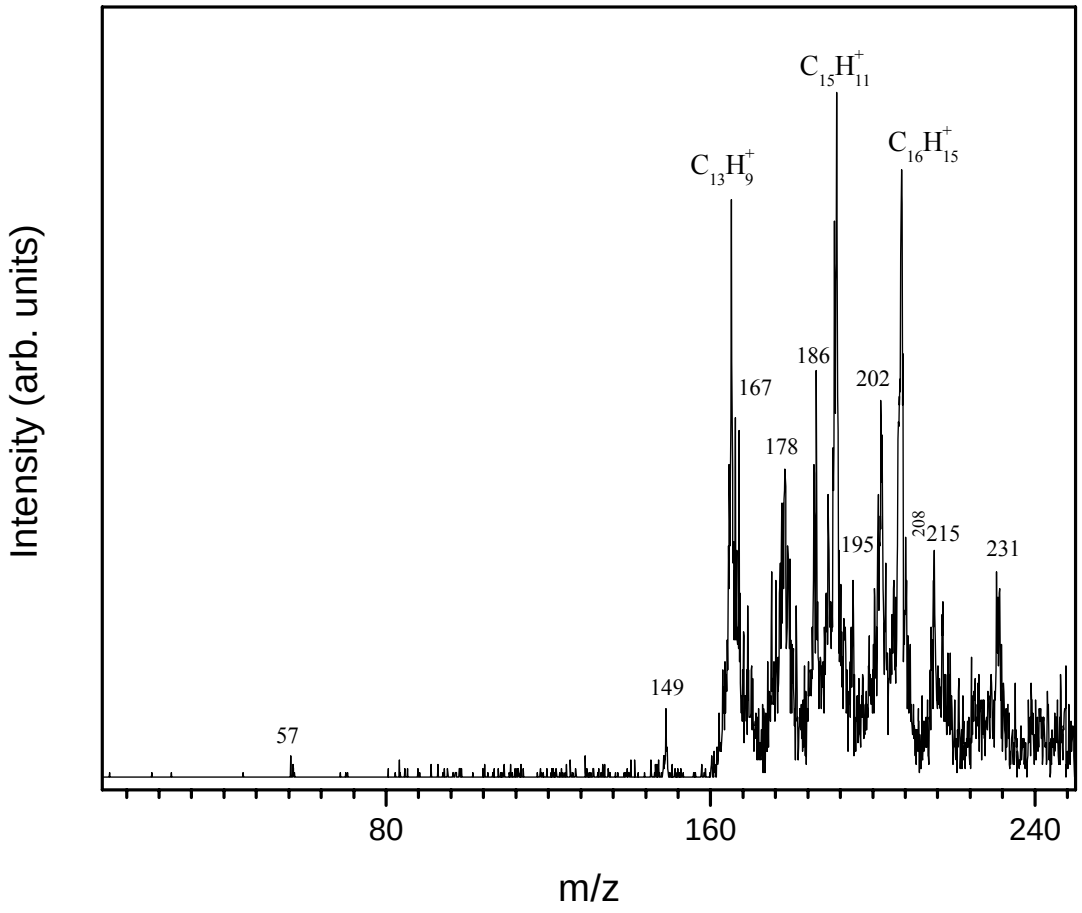

Figure 62: Mass Spectrum of $^+(C_8H_8)_n$ clusters ions produced by Electron Impact of the continuous flow of styrene vapor flown through a100 micron- needle.

($C_{16}H_{15}^{\bullet}$) in the gas phase. This is actually one of the primary radicals proposed by Mayo as initiator of the thermal polymerization of bulk styrene liquid.

These results support the assertion that styrene is thermally polymerized in the vapor phase. This conclusion is supported by collision induced dissociation experiments of the mass-selected oligomer ions. These experiments show elimination of specific molecular fragments (end groups) similar to typical polymer fragmentation[69] thus confirming the covalent nature of the oligomer ions. Additionally, it is supported by the experimental mobility measurements, which agreed with the mobility calculated for the lowest energy structures.

The results also indicate that the electron impact ionization of expanded styrene vapor may induce styrene polymerization initiated by styrene radical cation within the generated styrene clusters. This can be drawn from the fact that, one of the styrene dimer structures is 1-methyl 3-phenyl indane, which known to be produced by cationic mechanism.

Our results present direct evidence that supports and confirms the Mayo's mechanism for styrene thermal polymerization. As mentioned above Mayo proposed a termolecular reaction of styrene to form two primary radicals A ($C_{16}H_{15}^{\bullet}$) 207 amu and MH ($CH_3CHC_6H_5^{\bullet}$) 105 amu. In the mass spectrum of the continuous flow of styrene vapor using a capillary tube, we observed the ion ($C_{16}H_{15}^{+}$) m/z 207 correspond to the free

radical A•. This indicates that styrene vapor contains the initiating radicals A•. We did not observe the $CH_3CHC_6H_5$•) which correspond to m/z105. This may explain the gel-like film on the wall of the bubbler and inside the delivery lines. The ($CH_3CHC_6H_5$•) radical has been reported to be more reactive than A ($C_{16}H_{15}$•). In addition, it may explain the dominance of the phenyltetralin derivative in gas phase styrene oligomers.

For the structure of the gas phase styrene trimer, strong evidence drawn from the experimental and theoretical mobility and the dissociation products of the styrene trimer ion indicates that the observed trimer has the structure of the lowest energy isomer (d). The formation of this isomer represents the combination of the two monoradicals ($C_{16}H_{15}$•) and (C_8H_9•). This is consistent with Solomon's work [65]and Pryor proposed -solvent cage[28]. Based on the results and discussion above, we propose the following mechanism for thermally initiated vapor-phase polymerization styrene: After the formation of the AH adduct through Diels- Alder reaction, it will reacts with a third styrene molecule via Molecule Assisted Homolysis (MAH) to produce the two monoradicals A•($C_{16}H_{15}$•) and MH•(C_8H_9•), or it forms a styrene trimer through a combination process. If disproportionation occurs within the styrene clusters 1-PhT can be produced as dimer j. However, if the two radicals A•($C_{16}H_{15}$•) and MH•(C_8H_9•) diffuse out of the clusters, they can propagate with styrene molecules to generate styrene oligomers. This mechanism is summarized in Scheme 9.

Scheme 9: Proposed mechanism for styrene vapor phase thermal polymerization.

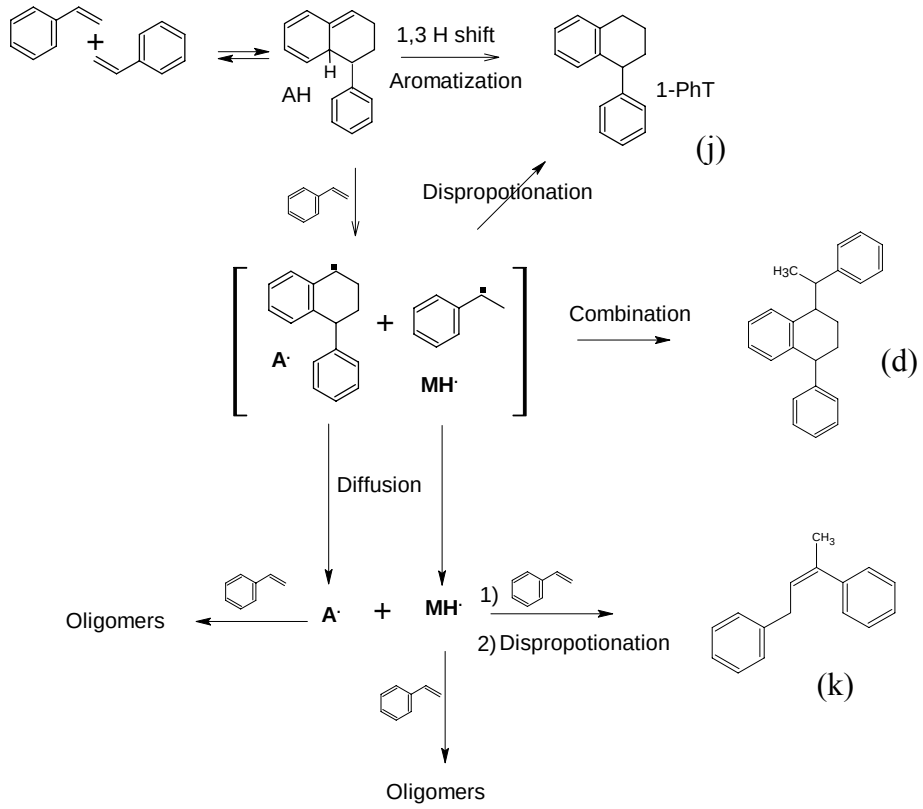

.

CHAPTER 4 : Metal Cations containing Benzene Clusters.

4.1 Introduction

Ion-molecule interactions play an important role in a diverse range of chemical and biochemical systems. Examples include substitution reactions, transmembrane ion transport, ion protein binding, upper atmospheric chemistry and nucleation phenomena[2-6,70]. With a gas phase ion and an experimentally selectable number of neutral solvent molecules, intrinsic ion neutral interaction can be studied in the absence of counter ions and as a function of size. After the discovery of Ferrocene [71,72]and the revealing of its bonding ability to form a sandwich structure , researchers around the world studied metal-benzene complexes in the condensed phase. In the gas phase these complexes were studied experimentally through Equilibrium high pressure mass spectrometry,[73-75] Collision-induced dissociation(CID)[73-75], photodissociation spectroscopy[7,76-81], and theoretical calculations to reveal the electronic structures[82]. Kaya and coworkers[83-93] studied transition metal-benzene complexes and found that early elements in the first row have the tendency to form sandwich structures and multiple-Decker sandwiches especially in the case of vanadium. They also measured the ionization energy using the photoionization method by using a tunable UV laser. This study showed that the gas phase metal-sandwich structure is the same as the studied structure in the condensed phase. Bowers and coworkers confirmed this result[94]. They used the ion mobility technique to

study V-benzene complexes, confirming that $V_n^+(C_6H_6)_{n+1}$ cluster ions also possessed the sandwich structures[94]. Recently Duncan and coworkers studied V-Benzene complexes using vibrational spectroscopy for V-mono and dibenzene complexes[7,76-80]. They showed that the first and the second benzene molecule were directly attached to the vanadium cation and that it possesses the sandwich structure. The study also shows that the third benzene is weakly bonded to the sandwich structure.[77]

In this Chapter, cluster beam- time of flight mass spectrometry, coupled with laser-vaporization ionization techniques were used to study the interactions between singly charged metal ions and benzene clusters. The mass spectra of the metal cation-containing benzene clusters $M^+(C_6H_6)$ for M = Na, K, Mg, Ca, Ba, B, Si, Al, Ga, Ge, Sc, Ti, V, Cr, Mn, Fe, Co, Ni, Cu, Zn, Zr, Nb, Ag, Hf, W, Pt, Au and Pb, were investigated.

4.2 Experimental Results

The metal cations were generated by vaporization/ionization of a metal target inside the source chamber using the second harmonic of Nd:YAG laser at ~10 mJ/pulse. Neutral clusters of benzene were produced by adiabatic expansion through the 0.5 mm pulsed nozzle at a repetition rate of 8 Hz. The distance between nozzle and the metal rod is ~8 mm. The jet was skimmed by a 3 mm conical skimmer and passed to the second high vacuum chamber maintained at 2.0×10^{-7} torr. The cluster ion beam was then analyzed using the pulsed TOF mass spectrometer.

Figure 63 displays the TOF mass spectra and ion intensity distribution as a function of cluster size of M^+ $(benzene)_n$ where M = Na and K. In the case of Na^+, the mass spectrum

shows that the major series observed is $Na^+(C_6H_6)_n$ with local maxima at n = 3, 7, 13, and 19. In the case of K^+, the mass spectrum shows the major series is $K^+(C_6H_6)_n$ with local maxima at n = 1, 4, 13, 19, and 23. In all conditions (mostly deflection voltage, nozzle opening and delay) $M^+(C_6H_6)_{13}$ is the strongest peak.

Figure 64 displays the product distribution mass spectra and ion intensity distribution as a function of cluster size of M^+ $(Benzene)_n$ where M is Mg, Ca and Ba. In the case of Mg^+ the major series is $Mg^+(C_6H_6)_n$ with local maxima at n =2, 13, 19, 21, 23. At different conditions (mostly deflection voltage, nozzle opening and delay) $Mg^+(C_6H_6)_n$, with n = 2 and n = 13 are the strongest peaks. In case of Ca^+ and Ba^+ the mass spectra and ion intensity as function of cluster size distribution, also show local maxima at n = 1, 3, 7, 13, 19 and 23. The mass spectra also show a minor series due to ionized benzene clusters $(C_6H_6)_n^+$ series.

Figure 65 displays the mass spectra and ion intensity distribution as a function of cluster size of M^+ $(benzene)_n$ where M is Ga and Al. In the case of Al^+ the major series is $Al^+(C_6H_6)_n$ with local maxima at n = 13, 19, 23, 26, 29. At certain conditions $Al^+(C_6H_6)_{13}$ is the strongest peak formation of $Al_m^+(C_6H_6)_n$ with m = 1-3 cluster series can be observed. The intensity plot for $Al_2^+(C_6H_6)_n$ series exhibit local maxima at n = 3 and 13 . The intensity plot for $Al_3^+(C_6H_6)_n$ series shows local minimum at n = 9.There are no $(C_6H_6)_n^+$ or $(C_6H_6)_nH^+$ series in this case. In the case of Ga^+, the mass spectrum displays the major series as $Ga^+(C_6H_6)_n$ with local maxima at n = 3, 13, 19, 23, 26, 29, 32, 37. At certain conditions (mostly deflection voltage and nozzle regime) $Ga^+(C_6H_6)_{13}$ is the strongest peak. At high laser ablation power, $(C_6H_6)_n^+$ series and fragments of benzene

(m/z 51, 63) can be observed . These series are stronger at high laser power. This can be an indication of plasma ionization or direct multiphoton ionization of benzene.

Figure 66 displays the mass spectra and ion intensity distribution as a function of cluster size of M^+ $(benzene)_n$ where M = W and Mn and Cr. In the case of W^+ the mass spectrum shows that the major series is $W^+(C_6H_6)_n$ with local maxima at n = 6, 13, 19, 23, 26. Formation of $W_2^+(C_6H_6)_n$ cluster series can be observed starting from n = 1 . In the case of Mn^+, the mass spectrum shows that the major series is $Mn^+(C_6H_6)_n$ with local maxima at n = 1, 7, 13, and 19. In the case of Cr^+ the mass spectrum shows that the major series is $Cr^+(C_6H_6)_n$ with local maxima at n = 1, 13, 19, 23, 26, 29 and 32. At all conditions $M^+(C_6H_6)_{13}$ is the strongest peak for M = W, Mn and Cr.

Figure 67 displays the mass spectra and ion intensity distribution as a function of cluster size of M^+ $(benzene)_n$ where M^+ is Sc and Zr. In both cases the mass spectrum shows that the major series is $M^+(C_6H_6)_n$ with local maxima at n = 2 and 13.

Figure 68 displays the mass spectra and ion intensity distribution as a function of cluster size of M^+ $(benzene)_n$ where M^+ is Ni, Cu and Ag. In the case of Ni^+, the mass spectrum shows that the major series is $Ni^+(C_6H_6)_n$ with local maxima at n = 1, 6, 13, 19 and 23. At all conditions, $Ni^+(C_6H_6)_{13}$ is the strongest peak In the case of Cu^+, the mass spectrum shows that the major series is $Cu^+(C_6H_6)_n$ with local maxima at n = 1, 7, 13, 19, 23, 26. At all experimental conditions $Cu^+(C_6H_6)_{13}$ is strongest peak. In the case of Ag^+, the mass spectrum shows that the major series is $Ag^+(C_6H_6)_n$, with local maxima at n = 1, 13, 19, 23, 26 and 29. At all experimental conditions, $Ag^+(C_6H_6)_{13}$ is strongest peak. Under a variety of experimental conditions, there is strong minimum at n = 3 in the case of Ni^+ and at n = 4

for Ag^+ and Cu^+. This can be shown in Figure 68, which displays the product distribution as a function of cluster size.

Figure 69 displays the mass spectra and ion intensity distribution as a function of cluster size of M^+ (benzene)$_n$ where M = Ti,V and Nb. In the case of Ti^+ the mass spectrum shows the major series is $Ti^+(C_6H_6)_n$ with local maxima at n = 2, 10, 14, 20, 24 and 27. At all experimental conditions, $Ti^+(C_6H_6)_{14}$ is the strongest peak. In addition, we observed the formation of $Ti_m^+(C_6H_6)_n$ for m = 2, 3. Local maximum at m = 2 and n = 3 is observed in the intensity distribution for $Ti_m^+(C_6H_6)_n$. The $(C_6H_6)_n^+$ series and fragments of benzene (m/z 51 and 63) can be observed. These series are stronger at high laser power. This can be an indication of plasma ionization or direct multiphoton ionization of benzene. In the case of V^+ product distribution, the major series is $V^+(C_6H_6)_n$ with local maxima at n = 2, 14, 20, 24, 27,30 . At all conditions (mostly deflection voltage and nozzle regime) $V^+(C_6H_6)_{14}$ is the strongest peak. In addition, we observed the formation of $V_2^+(C_6H_6)_n$ cluster series starting from n = 1. No clear magic numbers are observed in the intensity distribution for $V_m^+(C_6H_6)_n$ series. In the case of Nb^+ product distribution, the major series is $Nb^+(C_6H_6)_n$ with local maxima at n = 2, 14 and 24.

Figure 70 displays the mass spectra and ion intensity distribution as a function of cluster size of M^+ (benzene)$_n$ where M^+= Fe, Co and Pb. In all cases the mass spectra show that the major series are $M^+(C_6H_6)_n$ with local maxima at n = 2, 14, 20, 24 and 27. In addition we observed the formation of $Fe_m^+(C_6H_6)_n$ for m = 2, 3 series starting from n = 2 for $Fe_2^+(C_6H_6)_n$ and from n = 0 for $Fe_3^+(C_6H_6)_n$. No clear magic numbers are observed in the intensity distribution for the $Fe_m^+(C_6H_6)_n$ series.

Figure 71 displays the mass spectra and ion intensity distribution as a function of cluster size of M^+ (benzene)$_n$ where M = Si, Pt and Au. In the case of Si^+ the mass spectrum shows that the major series is $Si^+(C_6H_6)_n$ with local maxima at n = 10, 16, 20 and 24. At all experimental conditions, $Si^+(C_6H_6)_{10}$ is the strongest peak. In the case of Au^+ and Pt^+ the mass spectra show the major series are $M^+(C_6H_6)_n$ with local maxima at n = 11, 17, 21, 24 and 27. Table 14 summarizes the magic numbers observed in TOF mass spectra of the M^+ (benzene)$_n$ clusters for all the metal cations studied.

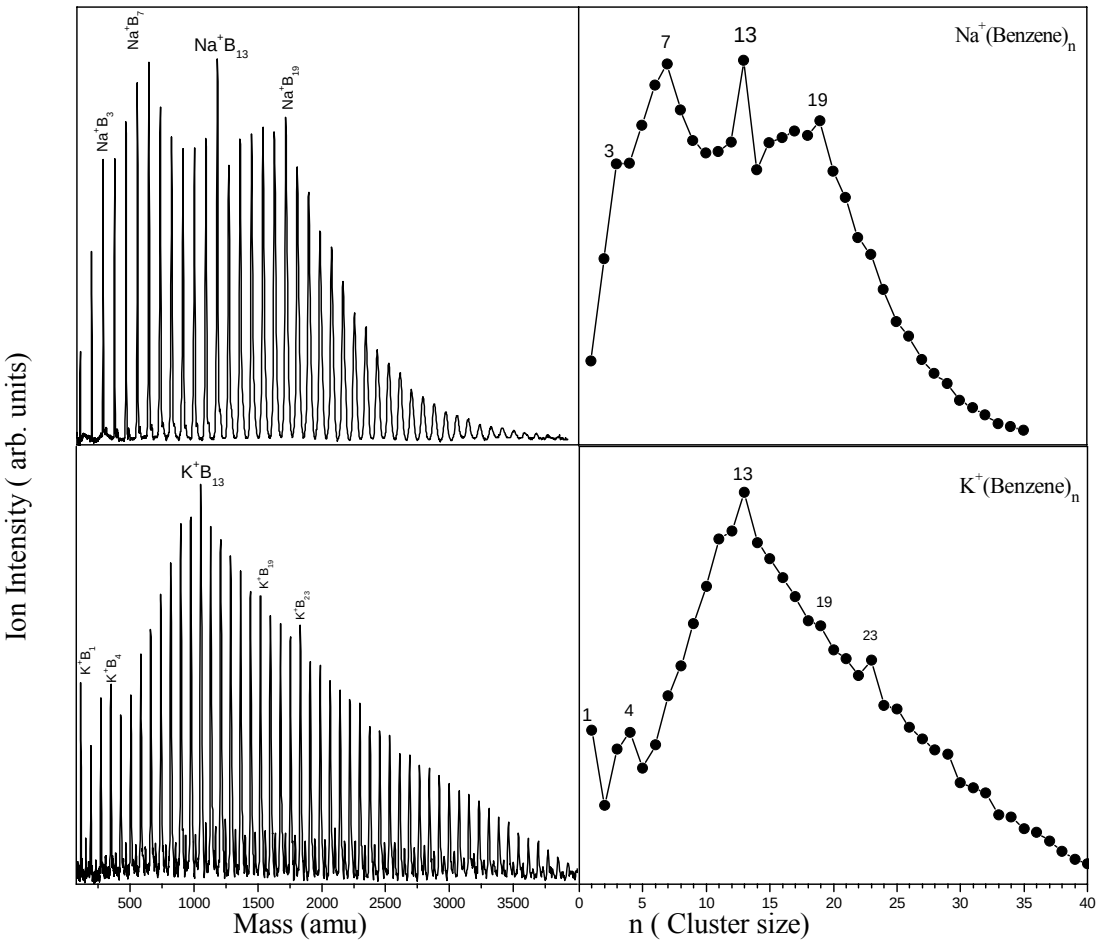

Figure 63: TOF mass spectra and ion intensity distribution as a function of cluster size of M^+ $(Benzene)_n$ where M = Na and K.

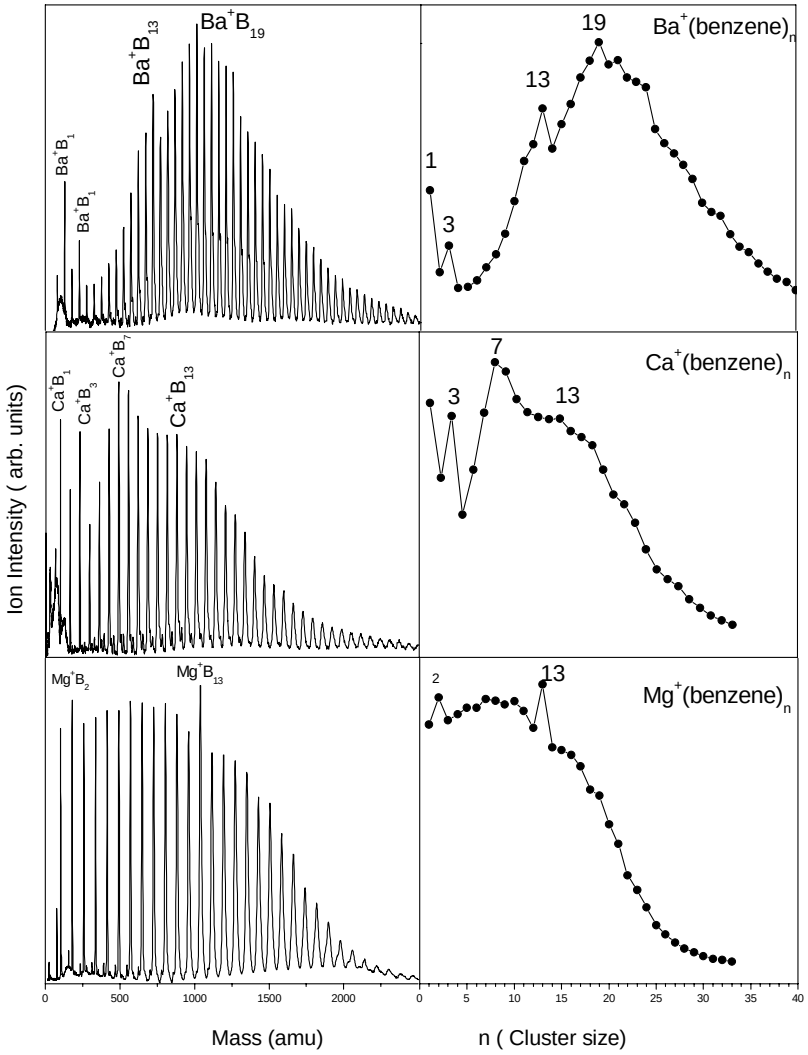

Figure 64: TOF mass spectra and ion intensity distribution as a function of cluster size of M^+ $(Benzene)_n$ where M =Mg, Ca and Ba.

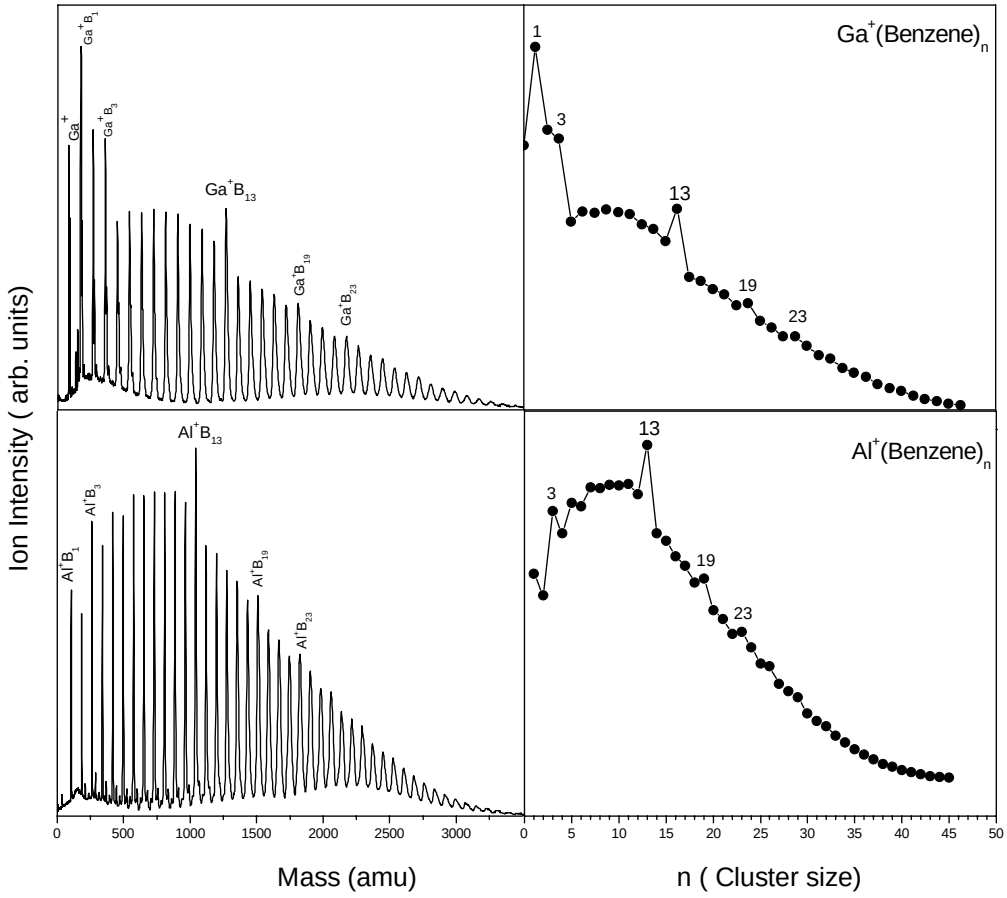

Figure 65: TOF mass spectra and ion intensity distribution as a function of cluster size of M^+ (Benzene)$_n$ where M = Al and Ga.

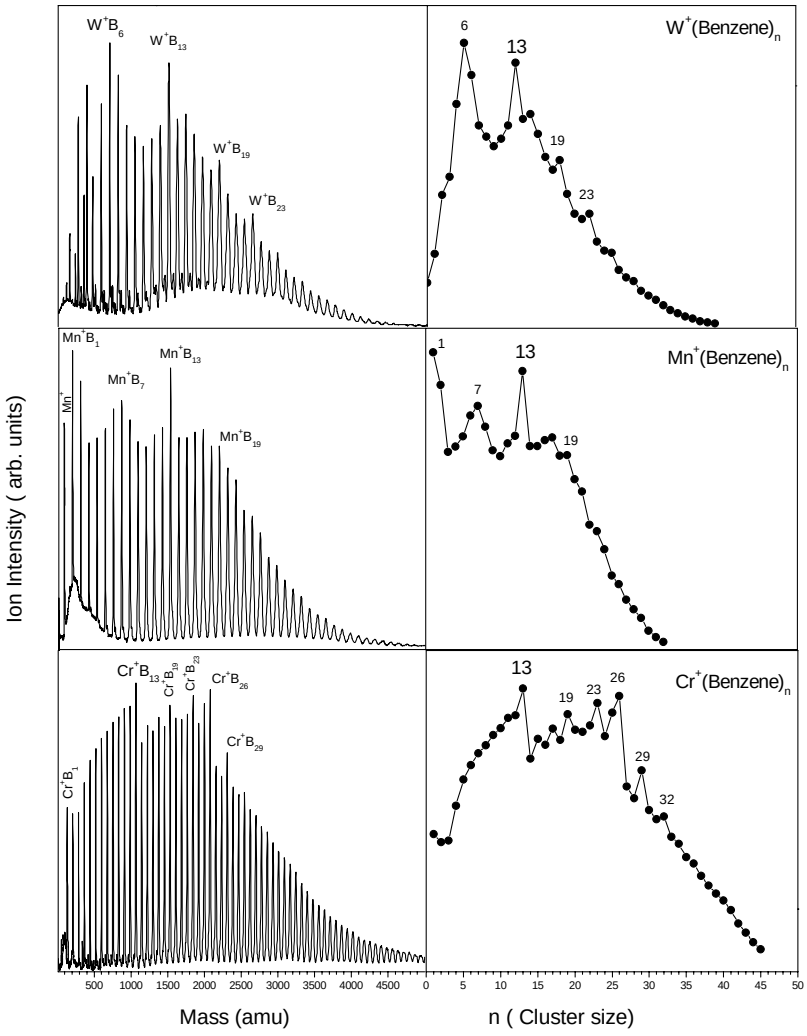

Figure 66: Mass spectra and ion intensity distribution as a function of cluster size of $M^+(Benzene)_n$ where M = Cr, Mn and W.

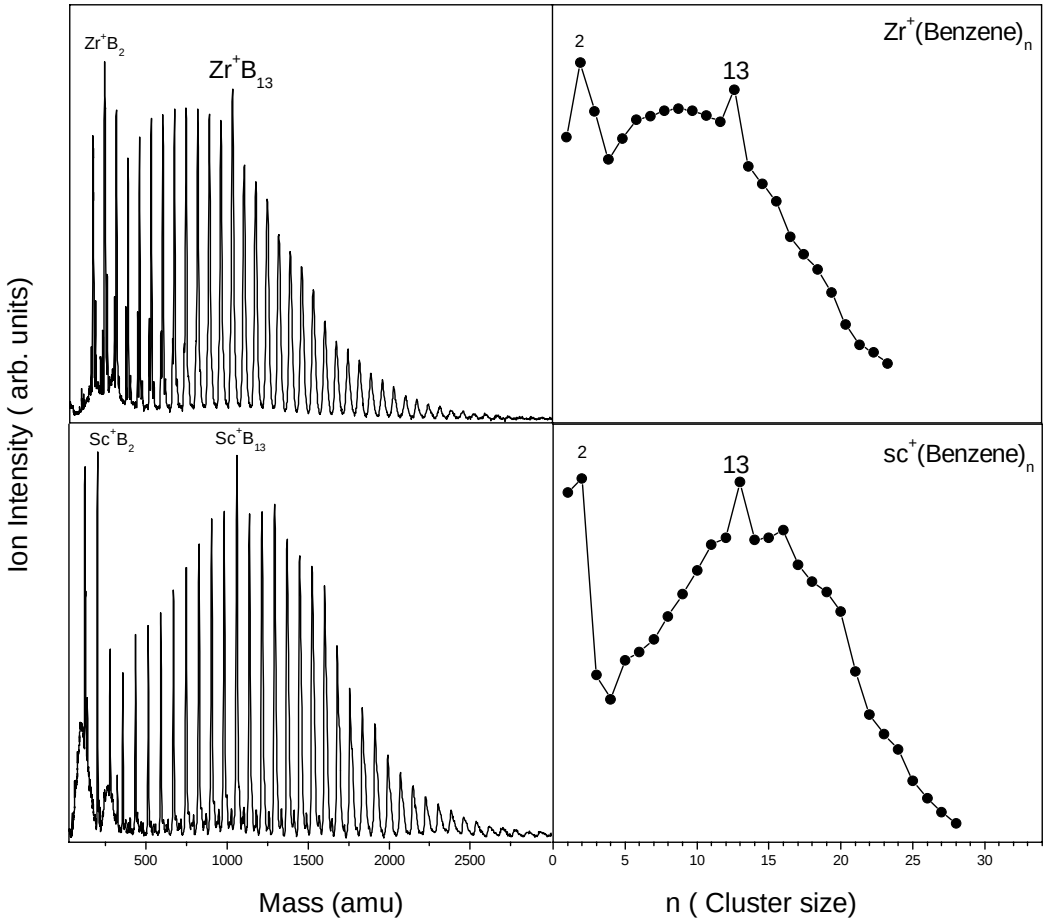

Figure 67: TOF Mass spectra and ion intensity distribution as a function of cluster size of M^+ $(Benzene)_n$ where M = Sc and Zr.

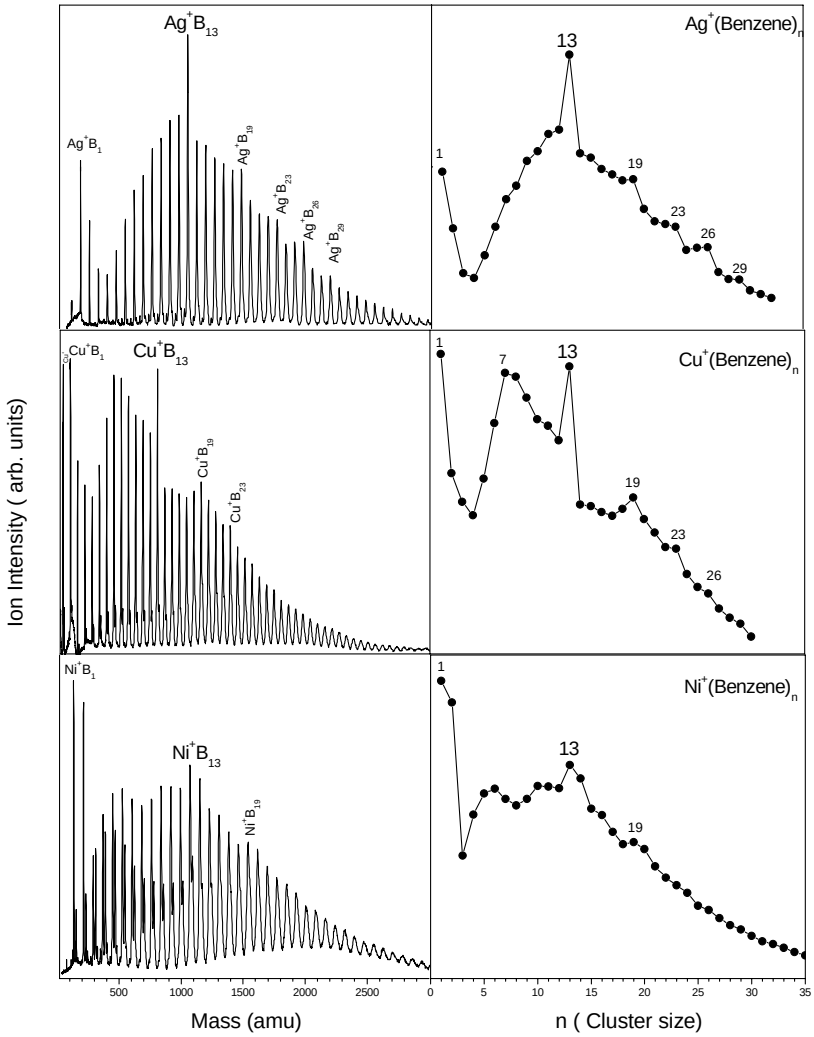

Figure 68: TOF Mass spectra and ion intensity distribution as a function of cluster size of M^+ $(Benzene)_n$ where M = Ni, Cu and Ag.

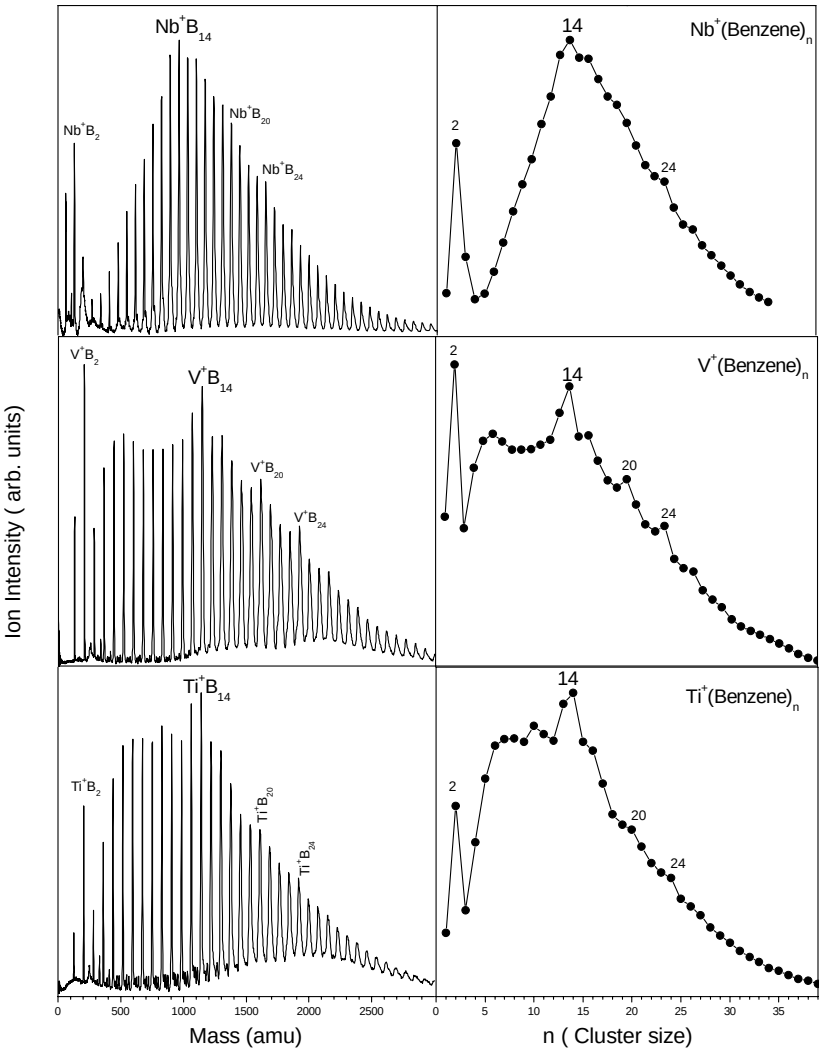

Figure 69: TOF Mass spectra and ion intensity distribution as a function of cluster size of M^+ $(Benzene)_n$ where M = Ti, V and Nb.

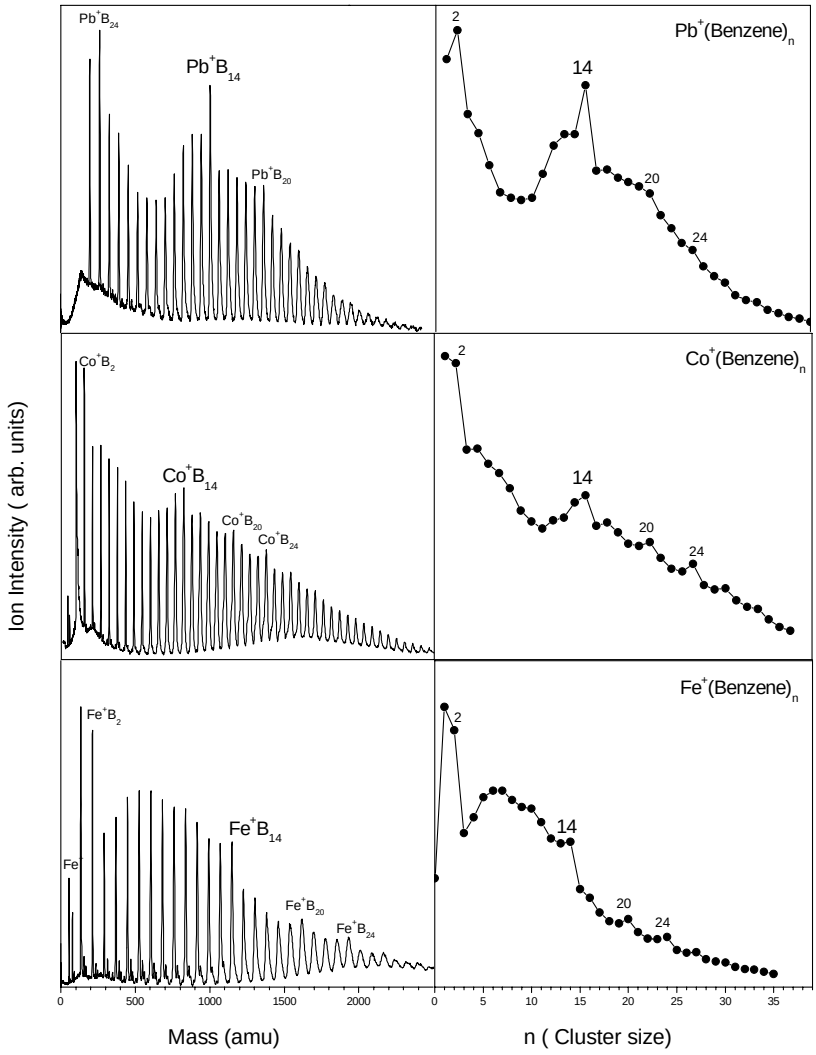

Figure 70: TOF Mass spectra and ion intensity distribution as a function of cluster size of $M^+(Benzene)_n$ where = Fe, Co and Pb.

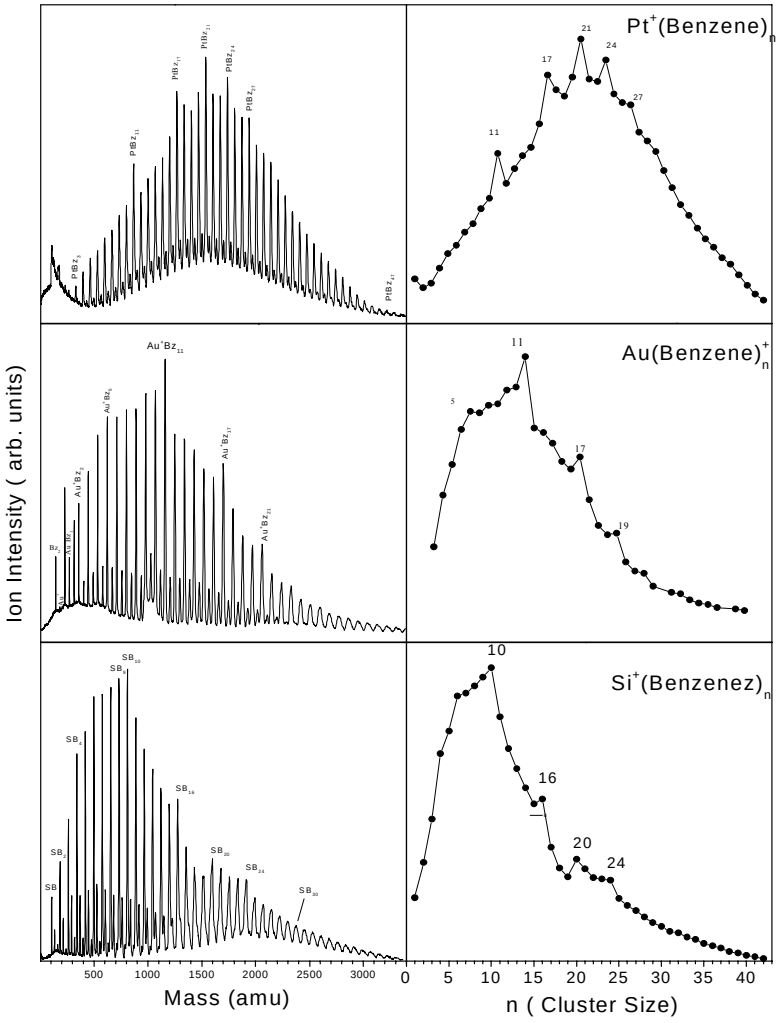

Figure 71: TOF Mass spectra and ion intensity distribution as a function of cluster size of M^+ $(Benzene)_n$ where = Si, Au and Pt.

Table 14: Summary of the observed magic numbers from the LVI-TOF mass spectra of the $M^+(C_6H_6)_n$ clusters

Element	Atomic Radius (A)	IP (eV)	Magic Numbers of Bz
Na	1.9	5.14	3,7,13,19
Mg	1.45	7.65	2,7,13,19
Al	1.18	5.99	1 ,3 ,13 ,19, 23 ,26 ,29
Si	1.11	8.15	10,16,20,24
K	2.43	4.34	1,4,13,19,23
Ca	1.94	6.11	1,3,7,13,19,24,31
Sc	1.84	6.56	2,13,20
Ti	1.76	6.83	2,10,14,16,20,24,27
V	1.71	6.75	2 6 14 20 24 27
Cr	1.66	6.77	1,13,15,17,19,23,26,29
Mn	1.61	7.43	1,7,13,17,19
Fe	1.56	7.90	2 6 14 20 24 27
Co	1.52	7.88	2,7,14,20,24,27
Ni	1.49	7.64	2,6,13,19
Cu	1.45	7.73	1,7,13,19,23
Zn	1.42	9.4	Charge Transfer
Ga	1.36	5.99	1,3,13,19,23
Ge	1.25	7.90	1,3,7,13,17,19,21,26,29
Zr	2.06	6.63	2,13,16,20
Nb	1.98	6.76	2,14,20,24
Ag	1.65	7.58	1,7,13,19,23,26,29
Ba	2.53	5.2	1,3,13,19,21,24
Hf	2.08	6.83	2,13,19,24
W	1.93	7.98	1,4,13,19,23,26
Pt	1.77	9.00	11,17,21,24,27
Au	1.74	9.23	5,11,17,21
Pb	1.54	7.42	2, 14, 20, 24

4.3 Discussion of the Results

Results from the TOF mass spectra and ion intensity distribution as a function of cluster size of M^+ $(benzene)_n$ where M = Na, K, Mg, Ca, Ba, B, Si, Al, Ga, Ge, Sc, Ti, V, Cr, Mn, Fe, Co, Ni, Cu, Zn, Zr, Nb, Ag, Hf, W, Pt, Au and Pb, as shown in Figure 63 - Figure 71 can be divided into three groups according to their magic numbers.

Group 1 represent M^+ $(Benzene)_n$ with magic numbers at n = 14 for M = Ti, V, Fe, Nb and Pb. This group has additional magic numbers at n = 2, 20 and 23. Group 2 has a magic number at n = 13, where M= Na, K, Mg, Ba, Sc, Al, Ca, Ga, Cr, Cu, Ag. In most of these cases Group 2, enhancement in intensity at the smallest cluster size (n = 1) is observed, except for Mg^+ and Sc^+ where mass spectra show enhancement in intensity at n= 2. At higher clusters, Group 2 exhibits strong peaks at n = 19, 24 and 27. Finally, Group 3 exhibits magic numbers at n =10 or 11 as in the case of M= Si, Au, Pt and Hf. This group exhibits no clear magic numbers at small cluster sizes. In all three groups, at larger cluster size the addition of six benzene molecules were noted which created magic numbers at n = 20 for Group 1, at n = 19 for Group 2 and finally at n = 16 or 17 for Group 3. This observation leads us to the conclusion that there are six favorable binding sites after the formation of the primary magic numbers at n = 14 or 13 or 10.

The mass spectrum of the benzene clusters $(C_6H_6)^+_n$ generated by Electron Impact ionization[41] is shown in Figure 72. The benzene cluster cations $(C_6H_6)^+_n$ with an enhanced intensities at n = 2, 14 and 20 were observed. This pattern is similar to that observed with $V^+(C_6H_6)_n$,$Ti^+(C_6H_6)_n$ … etc. (Group 1). However, in the case of neutral benzene clusters,

theoretical calculations suggest that $(benzene)_{13}$ should form a stable structure arising from the arrangement of 12 benzene molecules in an icosahedral pattern around a central molecule[95-98]. This structure has been observed as a magic number in many atomic cluster systems[98]. The atomic icosahedral structure consists of a central atom covered by two staggered five-membered rings along the equator with each pole capped by another atom. Group 1 showed magic numbers at n = 14, 20 and 24. A possible explanation for the stability of these magic numbers is that a metal cation sandwiched between two parallel benzene molecules forms the core ion for an icosahedral structure with the addition of 12 benzene molecules around the core ion. However, Group 2 showed a magic numbers at n = 13, 19 and 23. In this case the icosahedral structure consists of a M^+Bz_1 core surrounded by 12 benzene molecules.

In order to investigate the growth pattern of the magic numbers in the mass spectra and the nature of benzene binding to various metal cations, we collaborated with Dr. Shiv Khanna (VCU. Physics Department) for DFT calculations. Table 15 summarizes the calculated binding energies of one and two benzene molecules attached to the metal cation (M^+). These binding energies were defined as following:

$$BE = E[M^+(C_6H_6)_1] - E[C_6H_6] - E[M^+] \quad \text{for first addition.}$$

$$BE = E[M^+(C_6H_6)_2] - 2*E[C_6H_6] - E[M^+] \quad \text{for second addition}$$

E is the total energy of the ground state structure.

Table 15: Summary of the calculated binding energy of the first and the second addition of benzene to the metal ion.

M^+	Binding Energy (eV)		Ratio of the second addition to the first one
	$M^+(Benzene)_1$	$M^+(Benzene)_2$	
Mg	1.55	2.09	1.35
Al	1.65	2.23	1.35
Si	3.03	3.67	1.21
Ti	3.26	5.84	1.79
V	2.87	6.06	2.11
Fe	3.45	5.88	1.70
Ni	3.41	4.9	1.44
Ag	1.59	2.74	1.72

This table shows that the binding energy for the second addition of benzene molecule is the highest in the case of V^+, Ti^+ and Fe^+. This reveals that the second benzene is stronger than the first one. This may explain the magic number at n = 2 observed in the mass spectra of $M^+(C_6H_6)_n$ for M = V, Ti, Fe. Figure 73 shows the ground state geometries for $M^+(C_6H_6)_2$, for M = V, Al and Si respectively. Interestingly, at smaller cluster sizes, Group 1 shows a magic number at n = 2. This is in agreement with the sandwich structure consisting of a metal cation placed between two parallel benzene molecules.

The $M^+(benzene)_2$ clusters have been well studied both experimentally and theoretically[7,73-94]. In the case of Al^+, Ag^+ and Ni^+ (Group 2), Table 15 shows that the second benzene molecule less bound than Group1. In the case of the Si^+ ion, the binding energy of the first benzene addition is very strong while the second addition of benzene

molecule is the weakest among the other metal cations. In fact, Schwarz *et al* [99] reported the insertion reaction leading to the formation of $HSi^{+}C_6H_5$, when the silicon cation interacts with benzene. It can be inferred that the calculated binding energy and the structure together are responsible for the formation of magic numbers 14, 13, and 10 or 11 in the mass spectra of the $M^{+}(benzene)_n$ clusters..

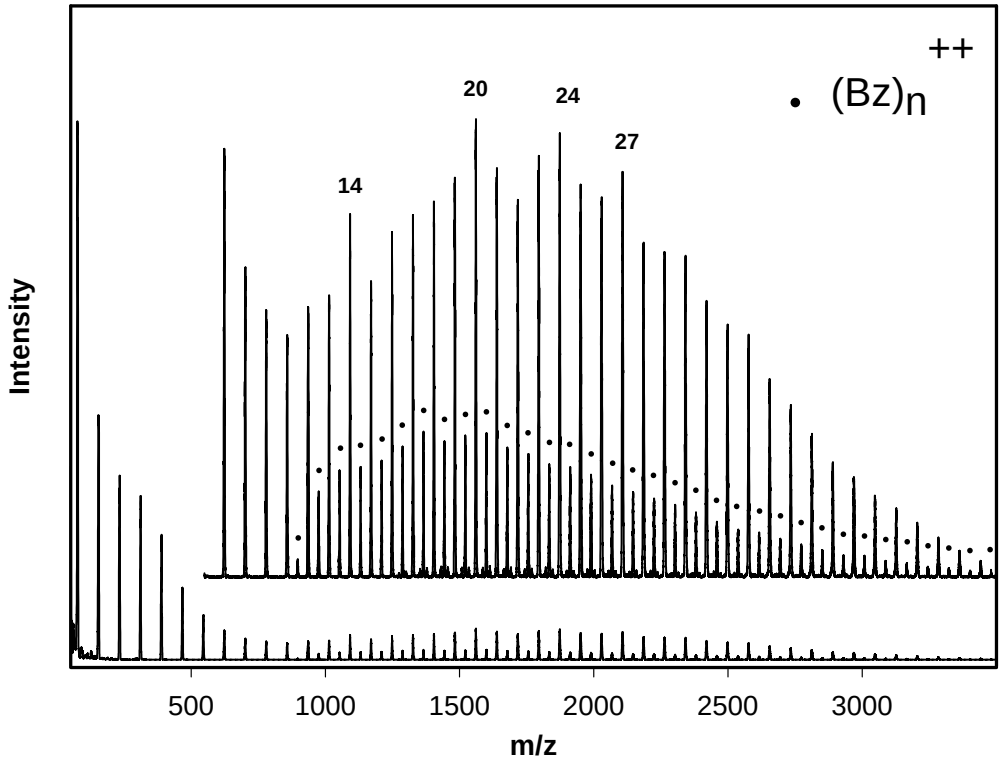

Figure 72: Benzene clusters as obtained by Electron Impact Ionization.

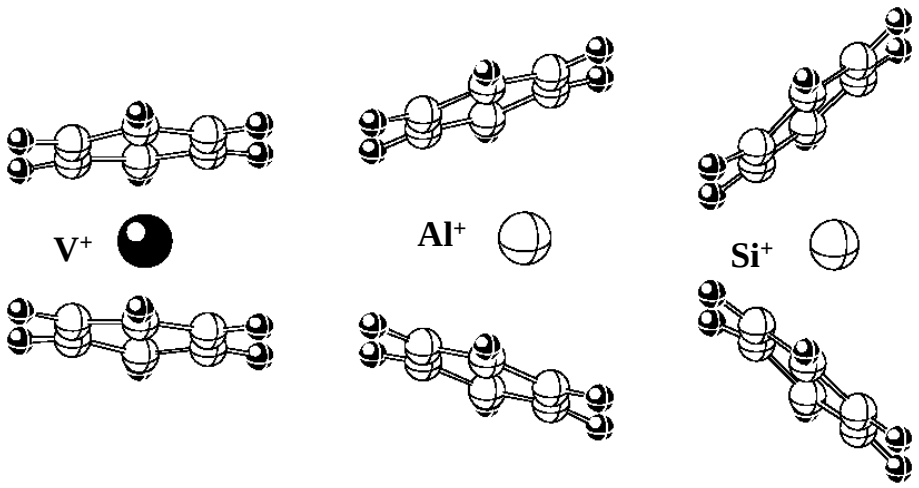

Figure 73: The ground state geometries for $M^{+}(C_6H_6)_2$, for M is V, Al and Si.**(**Density Function Calculations carried by Prof. Shiv Khanna, Department of Physics,VCU.)

The experimental results suggest a very interesting growth pattern for the $M^+(C_6H_6)_n$ series , which, this can be affected by the core ion structure. For example, consider the case of V^+, DFT calculations show that the ground state structure is that V^+ is sandwiched by two benzene molecules. The addition of twelve benzene molecules to $V^+(C_6H_6)_2$ leads to the magic number $V^+(C_6H_6)_{14}$ observed in the mass spectrum. The proposed structure can be viewed as icosahedral structure. This structure requires that the core is a perfect sandwich; any canting in the core will break the symmetry of the icosahedral structure. We propose that this is the case for Group 2, where the core ion is half a sandwich with the metal cation located above the center of the benzene ring. Twelve benzene molecules surround this half sandwich core ion leads to the stable structure of $M^+(C_6H_6)_{13}$.

The TOF mass spectra of Group 1 $M^+(C_6H_6)_n$ showed an intensity dip at n = 3 for all the metal cations studied. This may suggest that the third benzene molecule is not attached to the metal ion M^+, and the result is a benzene-benzene interaction. This is supported by the Duncan's observation [78,79] of a sudden increase in the IR-photodissociation efficiency of the mass selected $V^+(C_6H_6)_n$, at n = 3.

It is interesting to investigate the contribution of the low-lying metal cation excited states, since it can mix with the ground state or compete for the most stable bonding configuration[100,101]. In a different project[102] , we used the mass selected ion mobility system to identify the ground and excited states produced from the Laser Vaporization/Ionization method. Table 16 summarizes the results of various metal cations and their ground and excited state configuration. This table also shows the observed magic

numbers upon the interaction with neutral benzene clusters. Interestingly, when the difference in energy between the ground and excited states is small (~ < 0.35 eV) a magic number at n = 2 and 14 was observed. For example, in the case of the V^+, the difference in energy between $3d^4$ (the ground state) and $3d^34s^1$ (excited state) is 0.337 eV, and the TOF mass spectrum shows magic numbers at n = 2 and 14. However, when this difference in energy is large (> 0.4 eV), the TOF mass spectrum shows magic numbers at n = 1 and 13. For example, for Cu^+, the difference in energy between the $3d^{10}$ (the ground state) and the $3d^94s^1$ (the excited state) is 2.8 eV. This may suggest that the *sd* hybridization effect [100] plays a major role in the sandwich structure formation, that was observed for Group 1. This also explains why the second benzene addition bonds stronger than the first one in Group 1. This is because the energetic cost of *sd* hybridization (small energy) is primarily paid for by the binding energy of the first benzene molecule to the metal cation.

Table 16: Summary of the excited states obtained from theLaser Vaporization/Ionization process[102]

Ion	**Configuration**	**Energy (eV)**	**M^+-Bz magic numbers**
V^+	**$3d^4$** $3d^3 4s$ $3d^3 4s$	**0.026** 0.363 1.104	2, 6,14, 20, 24, 27
Cr^+	**$3d^5$** $3d^4 4s$	**0.000** 1.522	1,3,13,15,17,19, 23,26,29
Ni^+	**$3d^9$** $3d^8 4s$	**0.075** 1.160	2,6,13,19
Fe^+	**$3d^6 4s$** $3d^7$	**0.052** 0.300	2, 6, 14, 20, 24 27
Cu^+	**$3d^{10}$** $3d^9 4s$	**0.000** 2.808	1,3,7,13,19,23
Zr^+	**$4d^2 5s$** $4d^3$	**0.094** 0.406	2,13,16,19
Nb^+	**$4d^4$** $4d^3 5s$	**0.096** 0.421	2,14,20,24
Ag^+	$4d^{10}$ $4d^9 5s$	0.000 5.034	1,3,7,13,19,23, 26, 29

CHAPTER 5 : Solvation of Magnesium cation with clusters of polar molecules

5.1 Introduction

Reactions in solutions are highly dependent upon the medium and among them ion molecule reactions represent the best systems to study solvation effects at a microscopic level[103]. Clusters offer an ideal medium to study the gradual effects of solvation on chemical reactions, which could lead to the stabilization of ionic intermediates[3].

Many groups, using different mass spectrometric techniques, have studied the solvation and the reactivity of water and methanol clusters containing group-II metal ions; magnesium, calcium, or strontium, in both the ground state and the excited electronic state[103-111]. Very intriguing size dependence has been found in the reaction of Mg^+ ion with H_2O and CH_3OH, where the dehydrogenation reaction was observed after the addition of five water molecules to Mg^+.[103-106]

Fuke and Iwata et.al [103-106] studied Mg^+ and Ca^+ with water, where the product $MgOH^+(H2O)_{n-1}$ was exclusively observed [106], for $6 \leq n < 14$ in the mass spectrum. Similar product distributions were also observed for Mg^+ / D_2O, Ca^+ / H_2O, and Ca^+ / D_2O systems. In these systems, ion – molecule reactions within the clusters result in product ion

series, which dominate the mass spectra after certain cluster sizes. This phenomena is known as " Product switching"[105]. Both $M^+(H_2O)_n$ and $MOH^+(H_2O)_{n-1}$, where $M^+ = Mg^+$ or Ca^+ were found to be formed with characteristic size distributions for the product ion switching at two critical sizes (n~5 and 14). On the basis of these results as well as the results on the successive hydration energies of $MgOH^+$, the origin of the first product switching for n ~ 5 was ascribed to the difference in the successive hydration energies of M^+ and MOH^+[109]. With increasing cluster size, the product $MOH^+ \text{-}(H_2O)_{n-1}$ lowers the energy of the system more than $M^+(H_2O)_n$ product, and at $n \geq 5$ the $MOH^+ \text{-}(H_2O)_{n-1}$ becomes the ground state of the system[106]. Castleman et.al [107] used flow tube instruments to examine the effects of solvation on the dehydrogenation reaction of $Mg^+ (H_2O)_n$ to produce $MgOH^+ (H_2O)_{n-1}$, for $n \leq 6$. The reaction was observed to occur spontaneously at room temperature for n > 4. Ligand switching reactions were used to show that Mg^+-OH bonds are stronger than Mg^+H_2O bonds. The results show that the energy required to lose an H atom decreases with the number of water molecules attached because the magnesium ion changes its oxidation state and this results in stronger interactions with the water ligands. Their experimental results differ from the results of Saneketa et.al[105] who observed the first product switching at n = 5, and attributed this result to the low temperature of the cluster beam source. This dehydrogenation reaction was also been observed by Martin Beyer *et.al*.[108] using FTICR.

As for the second product switching for n ~ 15, the origin is not self-evident. Fuke et.al[105] proposed two possible mechanisms; the participation of the Rydberg-type ion-pair state $M^{+2}(H_2O)_n^-$ and the formation of a new reaction product such as $MOH.H_3O^+(H_2O)_{n-2}$. The

former mechanism is based on the results for the photodissociation spectra of $M^+(H_2O)_n$ and is consistent with solution process of metal ions in bulk water. At present, the former mechanism is considered to be much more plausible for understanding the switching. However, they could not rule out the latter mechanism within the experimental data. Sanekata *et al*. also carried out molecular orbital studies to confirm the first product switching[105].

These studies raised an interesting question as to whether cluster reactions would occur in other solvent clusters (e.g., CH_3OH), which may provide valuable information regarding the reaction mechanism. In particular, the substitution of one H in H_2O by a CH_3 group may help to understand the H-elimination behavior of $M^+(H_2O)_n$. As such, the substitution of H by CH_3 offers an opportunity to investigate the structural effects of the molecular clusters on their reactions. It would also be interesting to see whether H- elimination or CH_3- elimination is the dominant process.

Many research laboratories have examined the interaction of Mg^+ with methanol. An early study conducted by Uppal et al[109] using an ICR spectrometer showed no reactivity of Mg^+ ions toward methanol molecules. Kaya et al[112] observed the formation of $Mg^+(CH_3OH)_n$ (n = 1 - 10) in a laser ablation-molecular beam system with a magic number at n = 2. They attributed this magic number to the formation of a first solvation shell of two methanol molecules around the Mg^+ ion. However, Woodward et al.[110] reported the formation other reaction products in addition to $Mg^+(CH_3OH)_n$ (n = 1 - 20) such as, $Mg^+OCH_3(CH_3OH)_{n-1}$, $(CH_3OH)_nH^+$, and $[(CH_3OH)_n(H_2O)]H^+$ (at large n values). Their experiment consisted of a supersonic expansion source for methanol clusters and metal vapor source. The nuetral

$Mg(CH_3OH)_n$ clusters were ionized by electron impact. The main observation was a switching in the dominant product species at specific cluster sizes. They observed that $Mg^+(CH_3OH)_n$ clusters were the dominant species at $n < 3$ while at $n = 4$ the dehydrogenation product, namely $Mg^+OCH_3(CH_3OH)_{n-1}$ became dominant due to the formation of a more polarized ion core, which can be described as $Mg^{2+}–OCH_3^-$. The stability of $Mg^{2+}–OCH_3^-$ was attributed to the stronger interaction between Mg^{2+} and $^-OCH_3$ and the higher enthalpy of solvation for $M^+–^-OCH_3$ than M^+HOCH_2[106].

The switching reaction between $Mg^+(CH_3OH)_n$ and $Mg^+OCH_3(CH_3OH)_{n-1}$ was also studied by Lu et al[111] in a reflectron TOFMS coupled with pulsed supersonic expansion source of methanol clusters and laser ablation source for Mg^+ ions. They observed two product-switching regions. The first product switching region from $Mg^+(CH_3OH)_n$ to $Mg^+OCH_3(CH_3OH)_{n-1}$ at $n = 5$ and the second product switching from $Mg^+OCH_3(CH_3OH)_{n-1}$ to $Mg^+(CH_3OH)_n$ at $n = 15$. They also carried out isotope studies by substituting the H atom in OH and CH_3 groups by D. They found that the OD group shifted the first switching region size from $n = 5$ to $n = 6$, while that of CD_3 had no effect on the switching reaction. The isotope labeling of OH by OD also shifted the second switching from $n = 15$ to $n = 14$ while labeling CH_3 group by CD_3 had no effect. The authors rationalized the shift in the first switching region by suggesting that the OH bond can be broken during the hydrogen elimination and that substituting the OH by OD increases the energy required for the hydrogen elimination and thus $Mg^+(CH_3OH)_n$ required more methanol molecules for switching. Minor reaction products such as $H^+(CH_3OH)_n$, $Mg^+OH(CH_3OH)_{n-1}$, $Mg_2(OCH_3)_2^+(CH_3OH)_{n-2}$, and $Mg_2(OCH_3)_3^+$ -

$(CH_3OH)_{n-3}$ were also observed. The later two products indicated the formation of the dimer ion [Mg_2^+]. The authors explained the formation of $H^+(CH_3OH)_n$ by electron impact ionization where the electrons were supplied from the laser plasma. The CH_3 elimination product ($MgOH^+(CH_3OH)_{n-1}$) was not observed at smaller n and was found to be endothermic by 16 kcal/mol (for n = 1)[113-115]. The authors excluded any contribution from electronically excited state Mg^+ (^2P), which is 102.2 kcal/mol[116] higher in energy than the ground state Mg^+ (^2S), since no $MgOH^+$ was observed. Ab initio calculations at SCF/6-31G* level showed that three CH_3OH molecules formed the first solvation shell around Mg^+. While in $Mg^+OCH_3(CH_3OH)_4$, all the oxygen atoms were found directly bonded to the Mg^+. This structure reflected a Mg^{2+}-like core where 6 ligands formed the first solvation shell for Mg^{2+}. Ab initio calculations also showed a ΔE of 3.237 eV for the hydrogen elimination reaction of $Mg^+(CH_3OH)$. While ΔE was calculated to be 0.055 eV for hydrogen elimination of $Mg^+(CH_3OH)_5$. The sequential binding energies for $Mg^+(CH_3OH)_n$ [n = 1-5] were calculated to be 1.643, 1.269, 0.949, 0.756 and 0.588 eV, respectively. Those values agreed nicely with the bond dissociation energies measured by Anderson et al [117]for $Mg^+(CH_3OH)_n$ [n = 1-3] of 1.51(0.07), 1.25(0.07), and 0.95 (0.09) eV, respectively but were lower than the value reported by Operti et al[114]of 2.65 eV for $Mg^+(CH_3OH)$ which was observed from a photodissociation experiment. The ab initio calculations on $Mg^+OCH_3(CH_3OH)_{n-1}$ showed a more polarizable Mg^+OCH_3 core with charges of 1.9 and –1.3 on Mg^+ and O of OCH_3 respectively compared to values of 0.9 and -0.9 on Mg^+ and O of CH_3OH, respectively. The Mg^+—O distance was shorter in $Mg^+OCH_3(CH_3OH)_{n-1}$ than in $Mg^+(CH_3OH)_n$. Two-cages structure ($[Mg^{+2}(CH_3OH)_n][e^-$

$(CH_3OH)_m]$) were proposed for the second product switching where one cage of methanol molecules is centered around Mg^{+2} and the other cage of methanol molecules trapped the free electron which inhibited the electron transfer to methanol molecules. Then the cages were stabilized by columbic interaction. This proposed structure was based on the ion-pair structure for $Mg^+(H_2O)_n$ [105] and $Sr^+(NH_3)_n$ [118,119]

In this study, the solvation of Mg^+ with polar solvents such as H_2O, CH_3OH, CH_3OCH_3, and CH_3CN were investigated using pulsed supersonic beam expansion coupled with laser vaporization and mass spectrometry techniques. This allows further investigation of the role of polar solvents, role of ground electronic magnesium ion ($Mg^+(^2S)$), and excited electronic magnesium ion ($Mg^+(^2P)$) in the dehydrogenation reaction. Such studies would show whether cluster reaction occurs in other polar solvent clusters (ether and acetonitrile. The results provide valuable information regarding the reaction mechanism. In particular, the substitution of one H in H_2O by a CH_3 group may help to understand the H-elimination behavior of $M^+(H_2O)_n$. As such, the substitution of H by CH_3 offers an opportunity to investigate the structural effects of the molecular clusters on their reaction. It would also be interesting to see whether H- elimination or CH_3- elimination is the dominant process.

5.2 Experimental Results

5.2.1 $Mg^+(H_2O)_n$

Figure 74 displays a typical TOF mass spectrum of water clusters containing Mg^+. The major results can be summarized as following: First, Mg^+ association reactions (1) with water are observed:

$$Mg^+ + H_2O \rightarrow Mg^+(H_2O)_n \quad \ldots\ldots\ldots\ldots\ldots\ldots\ldots\ldots(1)$$

at n = 1-5, with a local maxima (magic number) at n= 4 observed under different experimental conditions such as nozzle width , carrier gas pressure, deflection voltage and the delay time. Second, Figure 74 also shows two switching reactions. The first switching reaction from $Mg^+(H_2O)_n$ to $MgOH^+(H_2O)_{n-1}$. This is observed at $n \geq 6$. A second switching reaction is seen from $MgOH^+(H_2O)_n$ to $Mg^+(H_2O)_{n+2}$ at n = 13 . Interestingly, there is an intensity dip at the end of each cluster size region, where a switching is observed.

5.2.2 $Mg^+(CH_3OH)_n$

The TOF mass spectra of methanol clusters containing Mg^+ are displayed in Figure 75 and Figure 76. The mass spectrum of $Mg^+(CH_3OH)_n$ can be divided into three parts:

First, the association reactions (2) are observed

$$Mg^+ + n\ CH_3OH \rightarrow Mg^+(CH_3OH)_n \quad \ldots\ldots\ldots\ldots\ldots\ldots..(2)$$

at n = 1-5, with a local maximal (magic number) at n= 3, observed under different experimental conditions such as nozzle width , pulser voltage, deflection voltage and the delay time.

Figure 75 shows that the switching reaction (3) to $MgOCH_3$ -$(CH_3OH)_{n-1}$ is observed at n > 6. Cluster size distributions (upper inset in Figure 76) show magic numbers at n= 7, 12 and 14.

$$Mg^+(CH_3OH)_n \rightarrow MgOH^+(CH_3OH)_{n-1} \qquad (3)$$

Also Figure 76 shows a back switching reaction (4) to $Mg^+(CH_3OH)_n$ at $n \geq 15$.

$$MgOH^+(CH_3OH)_m \rightarrow Mg^+(CH_3OH)_n \qquad (4)$$

Finally minor reaction products such as $H^+(CH_3OH)_n$, $Mg^+OH(CH_3OH)_n$, $H^+(CH_3OCH_3)$ and CH_4^+ are also observed as shown in Figure 75.

5.2.3 $Mg^+(CH_3OCH_3)_n$

The TOF mass spectrum of Mg^+ / ether clusters is shown in Figure 77. The spectrum shows the association reaction (5) according to:

$$Mg^+ + n\ CH_3OCH_3 \rightarrow Mg^+(CH_3OCH_3)_n \quad \ldots\ldots\ldots\ldots\ldots(5)$$

Local maxima (magic number) at n= 3,15 and 21 are shown in the cluster ion distribution displayed in the inset of Figure 77. These maxima are observed under different experimental condition such as nozzle width, pulser voltage, deflection and delay time. Figure 6 also shows protonated ether, but no dehydrogenation reaction is observed.

5.2.4 $Mg^+(CH_3CN)_n$

Figure 78 displays the TOF mass spectrum of $Mg^+/(CH_3CN)_n$ clusters system. This mass spectrum shows the association reactions (6).

$$Mg^+ + n\ CH_3CN \rightarrow Mg^+(CH_3CN)_n \qquad (6)$$

Local maxima (magic numbers) at n= 3, 6, 9 and 14 are observed, as shown in the inset of Figure 78. These maxima are observed at different experimental condition such as nozzle regime, pulser voltage, deflection and the delay time. Some other minor products are also observed as shown in Figure 79. This product ions are $MgCN^+(CH_3CN)_n$ and $CH_3^+(CH_3CN)_n$ this product is a result of an eliminations of CH_3 and CN groups, respectively.

5.3 Discussion of the Results

Based on the results, this discussion will focus on three parts First: magic numbers and proposed structures; second: switching reactions, and finally: the origin of protonated clusters. The observed magic numbers in the Mg^+X_n systems where X = H_2O, CH_3OH, CH_3OCH_3 and CH_3CN are shown in Table 17.

Table 17: Summary of the magic numbers obtained from TOFMS.

Solvated Cluster ions	Magic Numbers			
$Mg^+(H_2O)_n$	4	17	19	21
$MgOH^+(H_2O)_n$	5	10	13	
$Mg^+(CH_3OH)_n$	3	16		
$MgOCH_3^+(CH_3OH)_n$	6	11	13	
$Mg^+(CH_3OCH_3)_n$	3	15	21	
$Mg^+(CH_3CN)_n$	3	6	9	14

In the Mg^+ \ water experiments a magic number was revealed at n= 4 for $Mg^+(water)_n$ as shown in Figure 74. This magic number may reflect the first solvation shell. However, the results from other groups suggested that the first solvation shell consists of three water molecules. The structure of $Mg^+(H_2O)_3$ has a pyramidal structure; with all oxygen atoms are pointed directly toward the Mg^+ ion. Comparing $Mg^+(H_2O)_4$ with the well known magic number $H^+(H_2O)_4$, where H_3O^+ is the core ion hydrogen-bonded to three water molecules , we suggest that $(MgOH_2)^+$is the core ion in $Mg^+(H_2O)_4$ and is shielded by three water molecules. This may explain the enhanced intensity of $Mg^+(H_2O)_n$ series at n = 4. In the case of $Mg^+ (M)_n$ where M = CH_3OH, CH_3OCH_3, CH_3CN, the results show magic numbers at n = 3. Theoretical and experimental studies [111]showed that three CH_3OH molecules formed the first solvation shell around Mg^+ where all the oxygen atoms were found directly bonded to the Mg^+ ion. Ab initio calculations done by Dr Yehia Ibrahim (VCU Chemistry Department) show that it is the same case for ether and methanol, as well as the nitrogen atoms in the case of acetonitrile. The lowest energy structures are displayed in Table 18.and Table 20 summarizes the calculated binding energies for Mg^+/ Polar molecules (ether, methanol and acetonitrile). This table shows a sharp drop in the binding energy after the addition of the third molecule, as in the cases of Mg^+/Water and Mg^+/Acetonitrile. This may reflect the formation of the first solvation shell at n = 3. In the case of $Mg^+(CH_3CN)_4$, the calculations showed that there are two possible isomers a and b as shown in Table 18. In isomer a all the N atoms are directly bounded to Mg^+ ion. However, in isomer b only three acetonitrile molecules are directly bonded to Mg^+, forming a solvation shell, and the fourth molecule is outside the shell.

The mass spectra results are consistent with isomer b since the magic number at n = 3 was observed. In comparing Mg^+ (water)$_n$ clusters, with a magic number at n = 4, to the other polar solvent clusters, with the magic number 3, we may conclude that it is the role of hydrogen bonding among water molecules that stabilizes $Mg^+(H_2O)_4$.

Our results indicate two switching reactions. First, the switching reaction from $Mg^+(H_2O)_n$ to $MgOH^+(H_2O)_{n-1}$ at $n \geq 5$, similar to the results obtained by other groups[104]. The ion product corresponds to stabilized Mg^{2+}. This conclusion was based on an energy argument which showed that the production of $MgOH^+(H_2O)_n$ is more favorable at $n \geq 5$. On the other hand, $Mg^+(H_2O)_n$ is energetically more favorable at $n < 5$. This is due to the fact that the endothermic reaction ($Mg^+(H_2O)_1 \rightarrow MgOH^+ + H$) requires ~3.3 eV[107]. Adding five water molecules compensates for this endothermicity. Thus, the ion product $MgOH^+$ becomes dominant in the mass spectrum at $n \geq 5$. All the experimental results are consistent with theoretical calculations which show it is energetically favorable to form Mg^{2+} and OH^- at a higher degree of solvation.[6] Comparing Mg^+ / water clusters to Mg^+ / methanol clusters, they appear to behave in the same manner in terms of the switching reactions. This may lead us to the conclusion that only one H atom is involved in the dehydrogenation reaction. On the other hand, no dehydrogenation reaction was observed in the case of ether or acetonitrile clusters. This may confirm the role of H (in (O-H)) atom in the dehydrogenation reaction. The H atom from the CH_3 group offers no contribution even though it is energetically more favorable. From the Mg^+ /methanol experiment minor reaction products such as $H^+(CH_3OH)_n$, $Mg^+OH(CH_3OH)_n$, $H^+(CH_3OCH_3)$ and CH_4^+ were observed . These series were also observed by Lu et al[111]. The authors explained the

formation of $H^+(CH_3OH)_n$ by electron impact ionization with the electrons supplied from the laser plasma. The CH_3 elimination product ($MgOH^+(CH_3OH)_n$) was not observed at smaller n, and was found to be endothermic by 118 kcal/mol (for n = 1)[113,114]. The authors excluded any contribution from electronically excited state Mg^+ (^2P), since no $MgOH^+$ was observed, which is 102.2 kcal/mol[116] higher in energy than the ground state Mg^+ (^2S). However, our results showed the formation of $MgOH^+$ as shown in Figure 71. To investigate whether if there is any contribution from electronically excited state Mg^+ (^2P), we used our mass-selected ion mobility system [54] to separate ground and electronically excited states of Mg^+. Our results showed only one peak in the arrival time distributions, as shown in Figure77. This peak was assigned to the ground state Mg^+ (^2S). This is direct evidence which confirms the absence of the electronically excited, $Mg^+(^2P)$, which may lead us to a conclusion that the Electron Impact process is responsible for the formation of the minor product ions that are observed in the mass spectra.

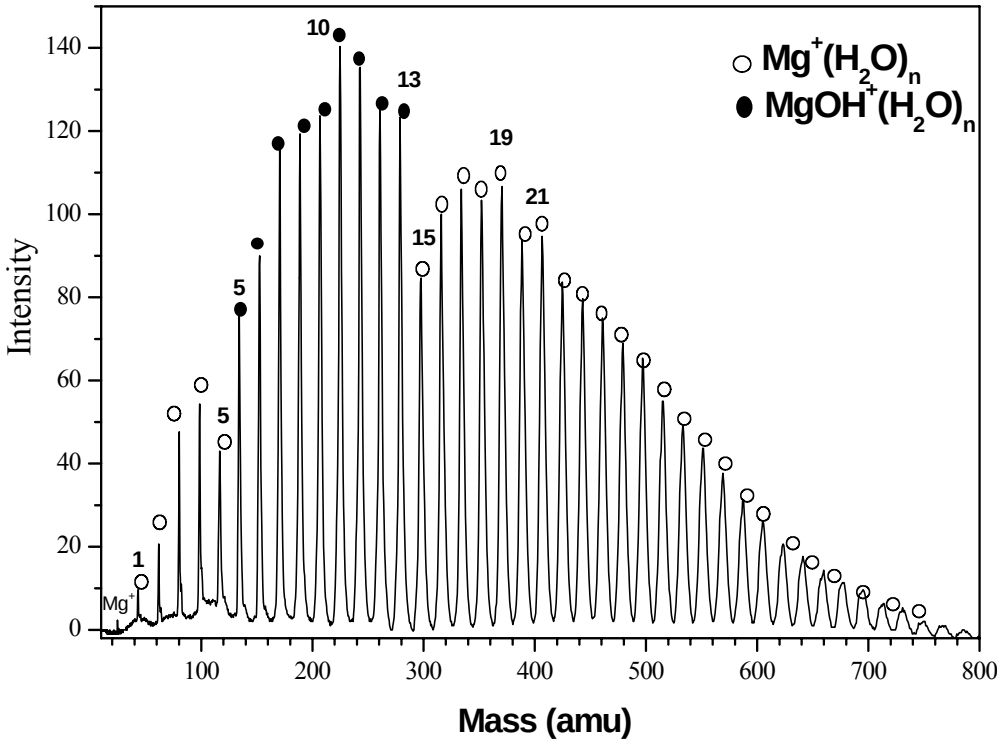

Figure 74: TOF mass spectra of $Mg^{+}(H_2O)_n$

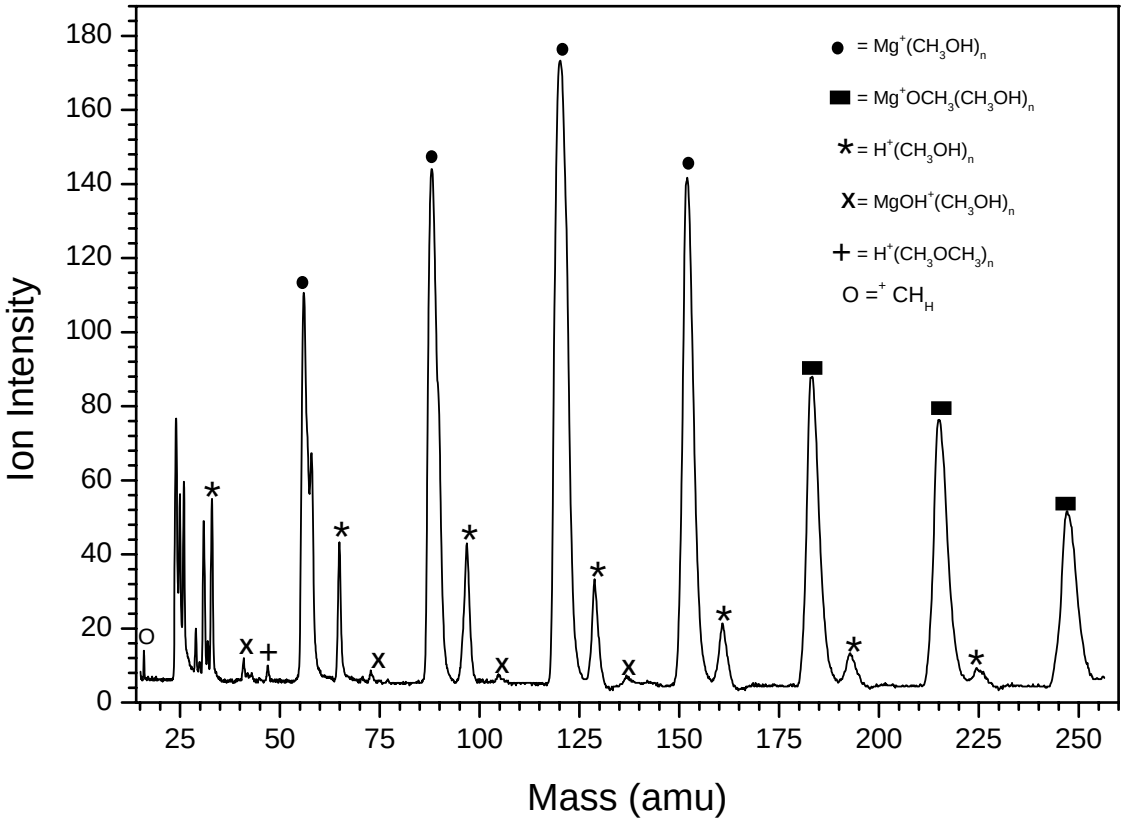

Figure 75: ToF Mass Spectra of $Mg^{+}(CH_3OH)_n$

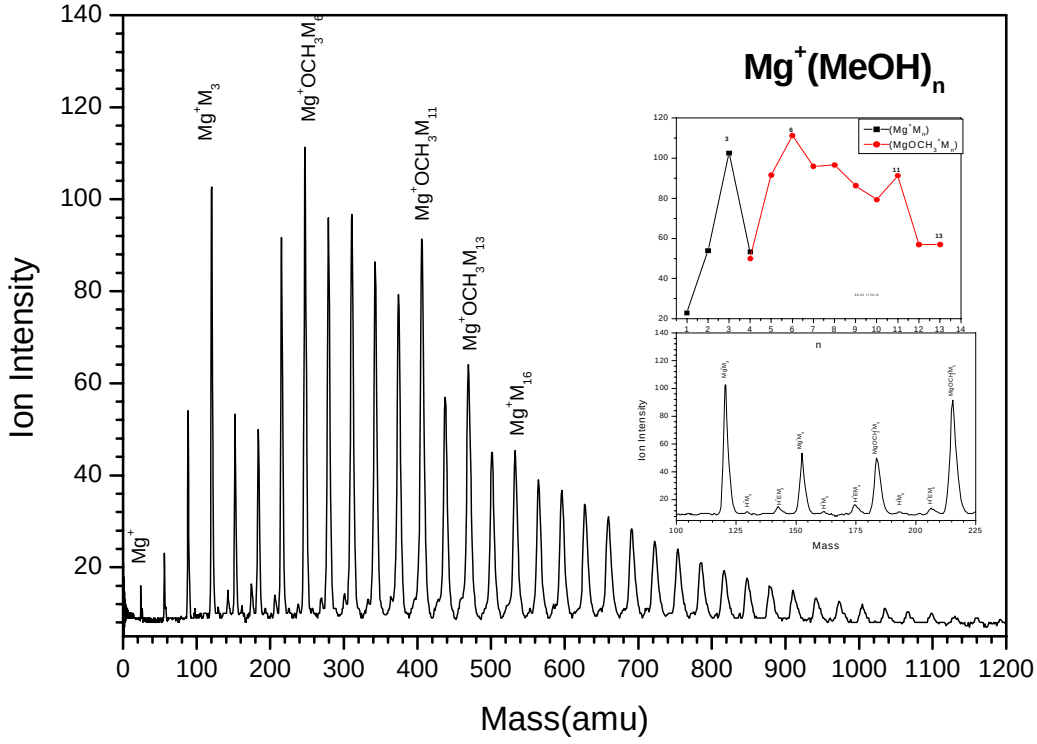

Figure 76: ToF Mass Spectra of $Mg^{+}(CH_3OH)_{n,}$ the upper inset is the ion intensity distribution as a function of cluster size, and the lower inset is TOF mass spectra from 100 amu to 250 amu.

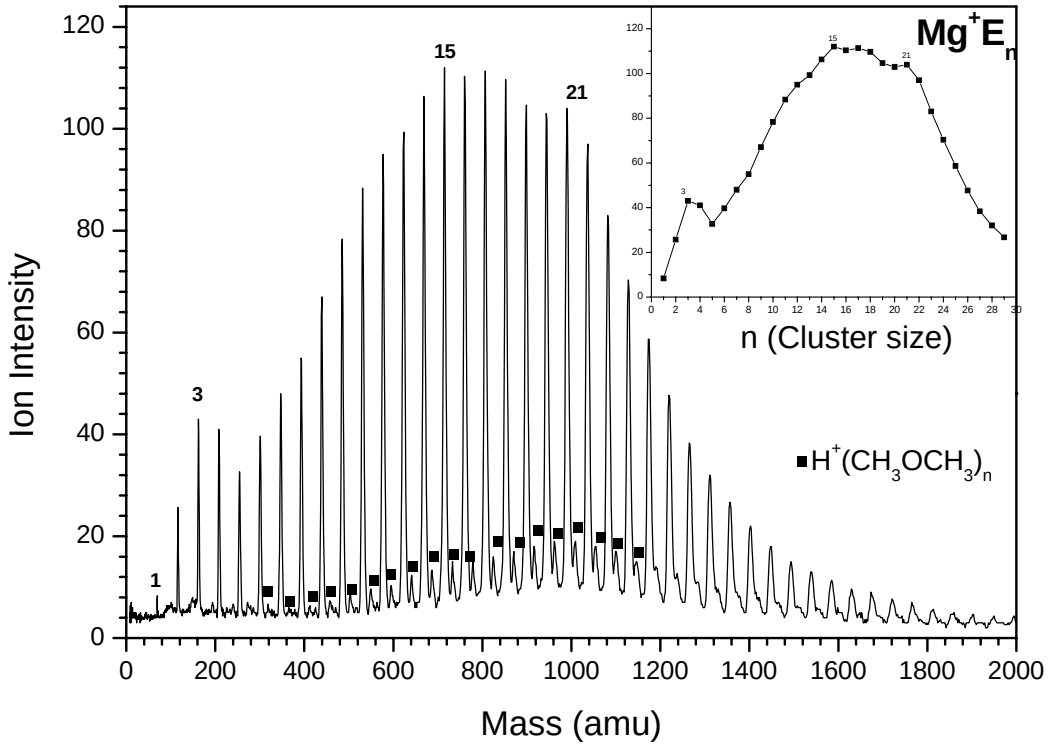

Figure 77: TOF-Mass Spectra of $Mg^+(CH_3OCH_3)_n$, the inset is the ion intensity distribution as a function of cluster size.

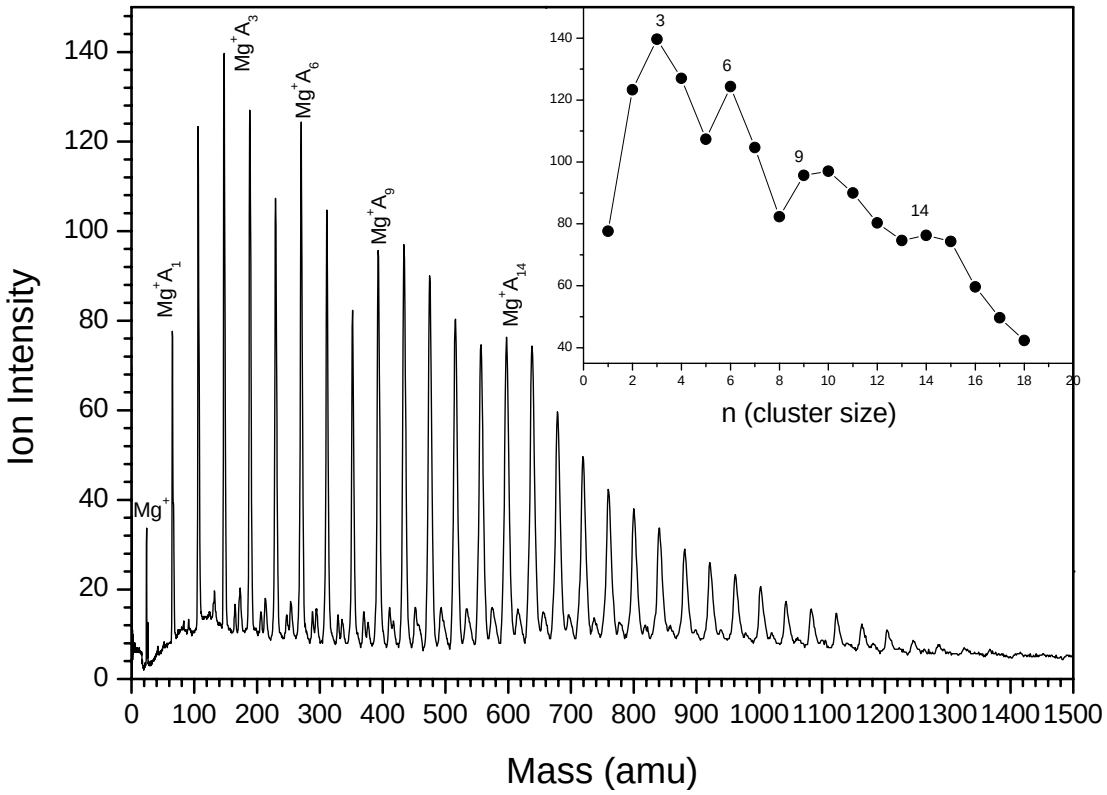

Figure 78: TOF Mass Spectra of $Mg^{+}(CH_3CN)_{n,}$ and the inset is the ion intensity distribution as a function of cluster size

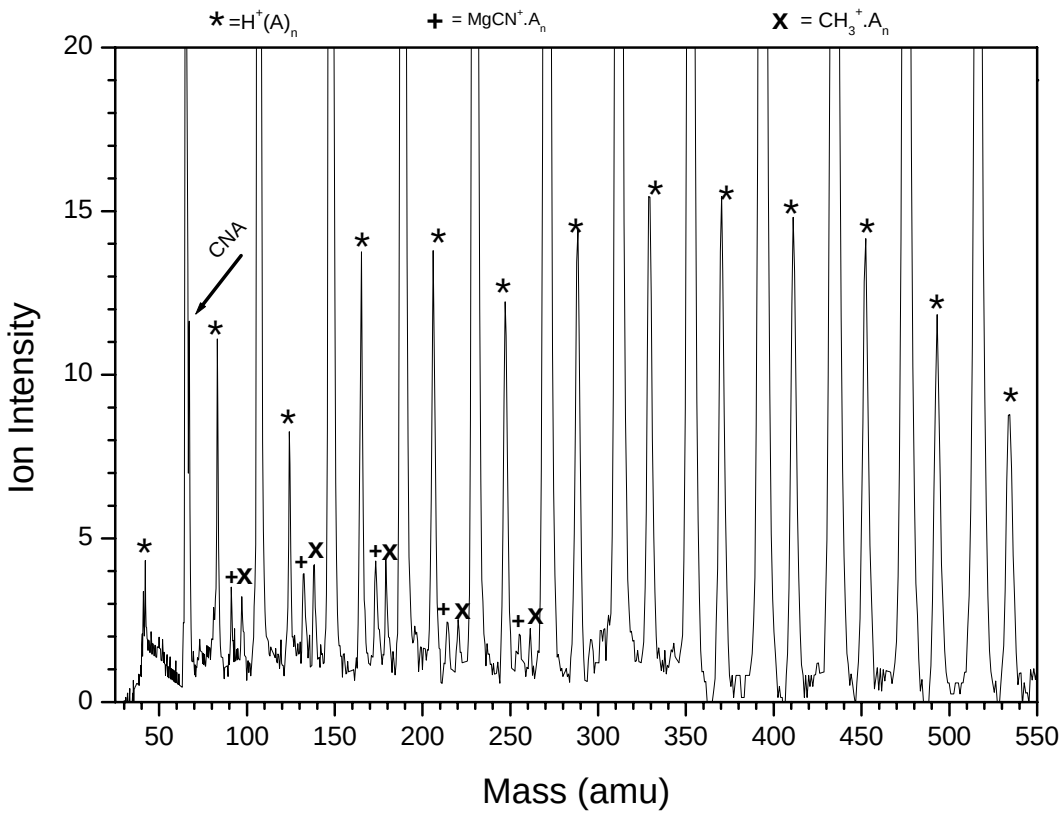

Figure 79: TOF Mass Spectra of $Mg^{+}(CH_3CN)_n$

Table 18: Calculated Structures of $Mg^+(X)_n$ Calculations done at UHF/6-31+G(d,p) level

$Mg^+(CH_3CN)_n$	$Mg^+(CH_3OCH_3)_n$
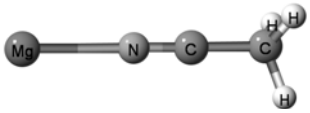 $Mg^+(CH_3CN)_1$	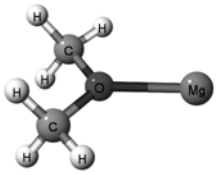 $Mg^+(CH_3OCH_3)_1$
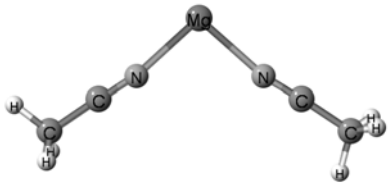 $Mg^+(CH_3CN)_2$	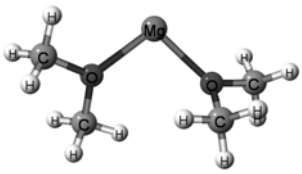 $Mg^+(CH_3OCH_3)_2$
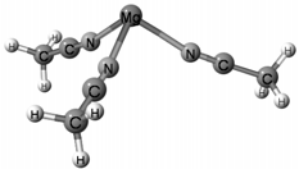 $Mg^+(CH_3CN)_3$	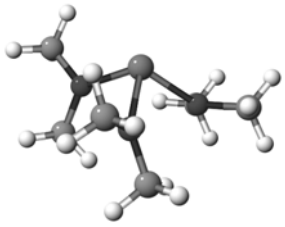 $Mg^+(CH_3OCH_3)_3$
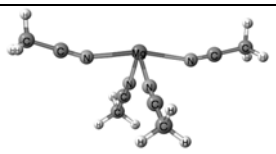 $Mg^+(CH_3CN)_4$ - a	
 $Mg^+(CH_3CN)_4$ - b	

Table 19: Calculated binding energy of $Mg^{+}Xn$ (kcal/mol) done UHF/6-31+G(d,p) level.

Molecule X	n = 1	n = 2	n = 3	n = 4
H_2O[117]	28	22	17	11
CH_3OH [120]	35	29	22	
CH_3OCH_3	40	28	20	
CH_3CN	41	29	22	8

*

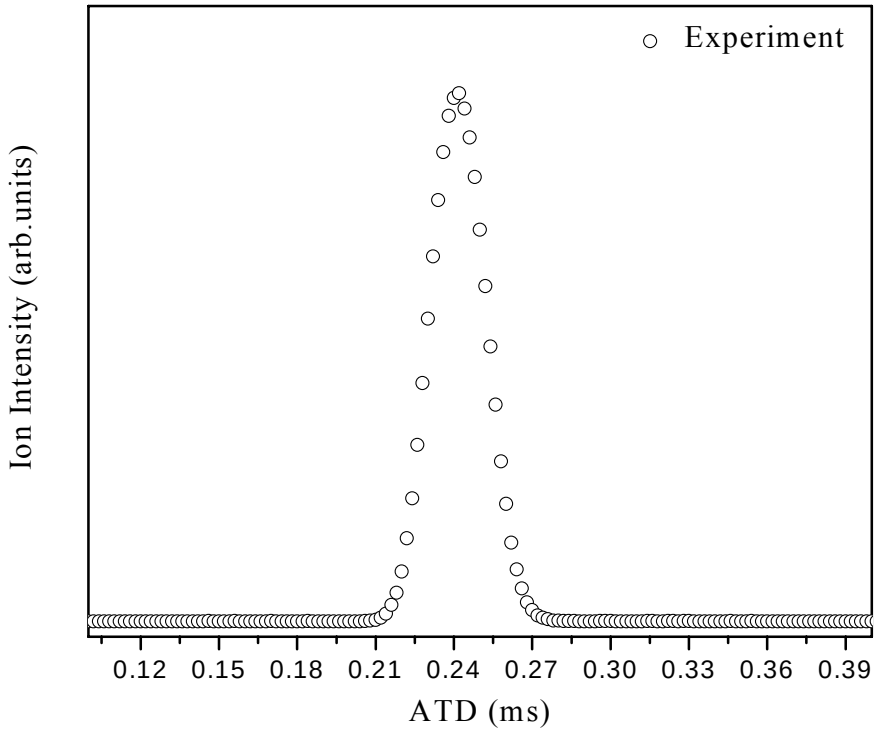

Figure 80: Arrival time distribution of Mg^+ ions, produced from LVI process. The experimental conditions are: 5 μs gate width, drift cell pressure (He) = 2.497 torr, drift cell temperature at 298.25 K and 42 V voltage difference across the cell

CHAPTER 6 Summary and Conclusions

The thermal self-initiated styrene polymerization in the gas phase was presented in Chapter 3. In this study, our experimental approach is based on on-line analysis of the gas phase oligomers by mass-selected ion mobility; this approach is described in Chapter 2. In the experiments, styrene – helium vapor mixture is heated to well-defined temperatures (350 – 370 K) thus allowing the establishment of a distribution of oligomers grown in the vapor phase by the thermal self-initiated process. The vapor mixture is then expanded through a supersonic pulsed nozzle into vacuum thus allowing the adiabatic cooling of the vapor and the quenching of the polymerization process. The clusters (oligomers + monomers) are then ionized by EI, mass selected through a quadrupole mass filter, and injected into a drift cell containing helium buffer gas for the measurement of ion mobility. Ions exiting the cell are mass analyzed and collected as a function of time yielding the arrival time distributions (ATDs) as a function of P/V from which the mobilities and the collision cross sections (Ω) in helium are determined.

The mobility measurements can provide structural information on the ionized oligomers on the basis of their Ω, which depend totally on the geometric shapes of the ions. Theoretical calculations of possible structural candidates of the mass-selected oligomer ions are then used to compute angle-averaged Ω (using the trajectory method) for comparison with the measured ones. The agreement between the measured and calculated Ωs of the candidate structures provides reliable assignments of the structures of the oligomers. Furthermore, collisional-induced dissociation (CID) of the mass-selected

oligomers ions provide further support for the structures obtained from the mobility measurements.

That the oligomer ions represent ionized neutral oligomers formed by vapor phase thermal polymerization is supported by the following considerations: (i) the same ions are observed (although with much weaker intensity) by directly ionizing the heated styrene vapor (with no beam expansion), thus eliminating the possibility of styrene clusters, (ii) the appearance of larger oligomer ions depends on the temperature and the duration of heating of the styrene vapor, (iii) CID experiments of the mass-selected oligomer ions show elimination of specific molecular fragments (end groups) similar to typical polymer fragmentation thus confirming the covalent nature of the oligomer ions and (iv) thermal dissociation experiments at temperatures as high as 470K do not show the typical fragmentation by monomer evaporation expected from molecular cluster ions.

In the case of styrene dimer, DFT calculations [B3LYP/6-31(d,p)] were used to obtain the lowest energy structures of several styrene dimer radical cation isomers (11 most likely isomers were considered). The comparison between the calculated Ω with the measured ones showed that there are three structures present of styrene dimer, 1-phenyl tetralin, 1, 3 diphenylbut-1-ene and 1-methy-3-phenyl-indane. Further evidence supporting these structures comes from the CID results. The mass-selected dimer ion shows fragmentations by the loss of the CH_3 group, which supports the presence of 1, 3 diphenyl but-1-ene and 1-methy-3-phenyl-indane. The loss of the C_6H_6 and C_2H_4 groups supports the presence of 1-phenyltetralin and 1-methy-3-phenyl-indane. Thus, the correlation between calculated and experimental ATD values and the CID results allows us to

determine that gas phase thermal polymerization of styrene involves the 1-phenyltetralin and the 1, 3 diphenyl but-1-ene dimers consistent with Mayo mechanism for the initiation process in the gas phase.

In the case of the styrene trimer, mobility measurements showed that the styrene trimer has the structure of (1-phenyl-4 (1-phenyl ethyltetralin). The calculated ATD for this structure provides an excellent fit to the experimental ATD of the styrene trimer. This suggests that the styrene trimer is a product of the combination of two free radicals ($C_8H_9^{\bullet}$ and $C_{16}H_{15}^{\bullet}$). These two free radicals were proposed by Mayo's mechanism of the thermal polymerization of styrene in the bulk liquids. The dissociation products of the mass selected styrene oligomer ions are consistent with the structures determined with the mobility measurements. Finally, the similarity between the initiation mechanism of the thermal polymerization of styrene in the gas phase and in bulk liquids and solutions is remarkable and implies that the structures of the early oligomers in the gas phase are relevant to the understanding of the polymerization mechanisms in condensed phases. This is a very significant result because it allows oligomer structures generated by different initiation mechanisms to be quickly and reliably determined using the gas phase ion mobility methods. This approach provides a new and general way to study thermally and photochemically initiated gas phase reactions with the simultaneous identifications of the structures of the early reaction products.

In summary, we present here the first direct evidence for the thermal self-initiated polymerization of styrene in the gas phase and establish that the initiation process proceeds

via essentially the same mechanism (the Mayo mechanism) as in condensed phase polymerization. Furthermore, we provide structural identifications of the growing dimers and trimers in the gas phase.

In Chapter 4, we investigate the solvation of atomic metal cations within clusters of benzene molecules. The solvation of a variety of metal ions by benzene clusters has been studied using laser vaporization, cluster beam and time-of-flight mass spectrometry techniques. These techniques are described in Chapter 2. In this work, strong magic numbers have been observed for the metal cation containing benzene clusters containing 10, 13, and 14 molecules depending on the nature of the metal cation involved. The metal cations exhibiting the preference salvation by 14 benzene molecules show strong tendency to form sandwich structures, with two benzene molecules surrounding the metal cation. For V^+, Ti^+, Fe^+,Nb^+ and Co^+, the results are consistent with a sandwich benzene dimer with the metal cation placed inside, and twelve benzene molecules around the $M^+(benzene)_2$ core. For other metal cations such as Al^+, Ga^+, Mg^+, and Si^+, the stable sandwich structures for $M^+(benzene)_n$ are not formed. In these cases, the overall magic number can be 13 or 10 depending on the nature of the interaction between the cation and the benzene molecules.

In summary, the mass spectra of the $M^+(benzene)_n$ can be divided into three groups according to their magic numbers. Group 1 exhibits magic numbers at n = 14, for M = Ti, V, Fe, Nb, Co and Pb. This group has additional magic numbers at n = 2, 20 and 23. Group 2 has a magic number at n = 13, where M= Na, K, Mg, Ba, Sc, Al, Ca, Ga, Cr, Cu,

Ag. In these cases, enhancement in intensity at the smallest cluster size (n = 1) is observed. At higher clusters, Group 2 exhibits peaks at n = 19, 24 and 27. Finally, Group 3 exhibits magic numbers at n =10 or 11 as in the case of M= Si, Au, Pt and Hf.. For Groups 1 and 2 icosahedral structures are proposed, where $M^+(benzene)_2$ or $M^+(benzene)_1$ forms the core ion. This core is surrounded by 12 benzene molecules and resulting in an icosahedral structure.

Finally, in Chapter 5, the work is focused on the investigation of the intracluster ion molecule reactions following the generation of Mg^+ within the polar clusters (water, methanol, ether and acetonitrile). In the case of Mg^+/ water and Mg^+/ methanol, dehydrogenation reactions are observed after the addition of five molecules. However, no dehydrogenation reactions are observed in the case of Mg^+/ ether or Mg^+/ acetonitrile clusters. This confirms the role of the H atom in (O-H) in the dehydrogenation reaction and rules out any contribution from the H atom in the CH_3 group. In addition, the magic numbers in the TOF mass spectra of the Mg^+X_n clusters (X= H_2O, CH_3OH, CH_3OCH_3 and CH_3CN) have been investigated. Our results agree with the Ab initio calculations, which show that for these Mg^+Xn clusters, the first solvation shell consists of three molecules. The structure of $Mg^+(X)_3$ has a pyramidal structure; with all oxygen atoms(or nitrogen atom in the case of acetonitrile) are pointed directly toward the Mg^+ ion.

List of References

List of References

(1) Edelstein, A. S.; Cammarata, R. C.; Editors *Nanomaterials: Synthesis, Properties and Applications*, 1996.

(2) Bernstein, E. R. *Studies in Physical and Theoretical Chemistry, Vol. 68: Atomic and Molecular Clusters*, 1990.

(3) Castleman, A. W., Jr.; Bowen, K. H., Jr. *Journal of Physical Chemistry* **1996**, *100*, 12911.

(4) Castleman, A. W., Jr.; Keesee, R. G. *Annual Review of Physical Chemistry* **1986**, *37*, 525.

(5) Castleman, A. W., Jr.; Keesee, R. G. *Accounts of Chemical Research* **1986**, *19*, 413.

(6) Castleman, A. W.; Wei, S. *Annual Review of Physical Chemistry* **1994**, *45*, 685.

(7) Duncan, M. A. *Annual Review of Physical Chemistry* **1997**, *48*, 69.

(8) Jena, P.; Khanna, S. N.; Rao, B. K.; Editors *Physics and Chemistry of Finite systems: From Clusters to Crystals, Vol. 2. (Proceedings of the NATO Advanced Research Workshop on Physics and Chemistry of Finite Systems: From Clusters to Crystals, Richmond, VA, October 8-12, 1992.) [In: NATO ASI Ser., Ser. C., 1992; 374]*, 1992.

(9) Jortner, J. *Zeitschrift fuer Physik D: Atoms, Molecules and Clusters* **1992**, *24*, 247.

(10) Barr, N. J.; Bengough, W. I.; Beveridge, G.; Park, G. B. *European Polymer Journal* **1978**, *14*, 245.

(11) Brown, W. G. *Journal of the American Chemical Society* **1968**, *90*, 1916.

(12) Buzanowski, W. C.; Graham, J. D.; Priddy, D. B.; Shero, E. *Polymer* **1992**, *33*, 3055.

(13) El-Shall, M. S.; Bahta, A.; Rabeony, H.; Reiss, H. *Journal of Chemical Physics* **1987**, *87*, 1329.

(14) El-Shall, M. S.; Reiss, H. *Journal of Physical Chemistry* **1988**, *92*, 1021.

(15) Groenewold, G. S.; Chess, E. K.; Gross, M. L. *Journal of the American Chemical Society* **1984**, *106*, 539.

(16) Gross, M. L.; Aerni, R. J. *Journal of the American Chemical Society* **1973**, *95*, 7875.

(17) Gross, M. L.; Russell, D. H.; Aerni, R. J.; Bronczyk, S. A. *Journal of the American Chemical Society* **1977**, *99*, 3603.

(18) Kopecky, K. R.; Evani, S. *Canadian Journal of Chemistry* **1969**, *47*, 4049.

(19) Kopecky, K. R.; Evani, S. *Canadian Journal of Chemistry* **1969**, *47*, 4041.

(20) Mayo, F. R. *Journal of the American Chemical Society* **1953**, *75*, 6133.

(21) Mayo, F. R. *Polymer Preprints, American Chemical Society* **1961**, *I 11*, 55.

(22) Mayo, F. R. *Journal of the American Chemical Society* **1968**, *90*, 1289.

(23) Pithawalla, Y. B.; Gao, J.; Yu, Z.; El-Shall, M. S. *Macromolecules* **1996**, *29*, 8558.

(24) Pryor, W. A.; Coco, J. H. *Macromolecules* **1970**, *3*, 500.

(25) Pryor, W. A.; Henderson, R. W.; Patsiga, R. A.; Carroll, N. *Journal of the American Chemical Society* **1966**, *88*, 1199.

(26) Pryor, W. A.; Huang, T.-L. *Macromolecules* **1969**, *2*, 70.

(27) Pryor, W. A.; Lasswell, L. D. *Polymer Preprints (American Chemical Society, Division of Polymer Chemistry)* **1970**, *11*, 713.

(28) Pryor, W. A.; Lasswell, L. D. *Advances in Free-Radical Chemistry (London)* **1975**, *5*, 27.

(29) Reiss, H. *Science* **1987**, *238*, 1368.

(30) Walling, C.; Briggs, E. R.; Mayo, F. R. *Journal of the American Chemical Society* **1946**, *68*, 1145.

(31) Walling, C. T. *Free Radicals in Solution*, 1957.

(32) Pryor, W. A. *Nuova Chimica* **1971**, *47*, 53.

(33) Pryor, W. A. *Introduction To Free Radical Chemistry*, 1966.

(34) Pithawalla, Y. B.; El-Shall, M. S. *ACS Symposium Series* **1998**, *713*, 232.

(35) Kirchner, K.; Patat, F. *Makromolekulare Chemie* **1960**, *37*, 251.

(36) Flory, P. J. *Journal of the American Chemical Society* **1937**, *59*, 241.

(37) Kothe, T.; Fischer, H. *Journal of Polymer Science, Part A: Polymer Chemistry* **2001**, *39*, 4009.

(38) Odian, G. *Principles of Polymerization. 2nd Ed*, 1981.

(39) Ibrahim, Y.; Alsharaeh, E.; Rusyniak, M.; Watson, S.; Meot-Ner, M.; El-Shall, M. S. *Chemical Physics Letters* **2003**, *380*, 21.

(40) Rusyniak, M.; Ibrahim, Y.; Alsharaeh, E.; Meot-Ner, M.; El-Shall, M. S. *Journal of Physical Chemistry A* **2003**, *107*, 7656.

(41) Rusyniak, M. J.; Ibrahim, Y. M.; Wright, D. L.; Khanna, S. N.; El-Shall, M. S. *Journal of the American Chemical Society* **2003**, *125*, 12001.

(42) Mesleh, M. F.; Hunter, J. M.; Shvartsburg, A. A.; Schatz, G. C.; Jarrold, M. F. *Journal of Physical Chemistry* **1996**, *100*, 16082.

(43) Wyttenbach, T.; Helden, G. v.; Batka Jr., J. J.; Carlat, D.; Bowers, M. T. *Journal of the American Society for Mass Spectrometry* **1997**, *8*, 275.

(44) Mason, E. A.; McDaniel, E. W. *Transport Properties of Ions in Gases*; John Wiley & Sons: New York, 1988.

(45) Kohn, W. *Reviews of Modern Physics* **1999**, *71*, 1253.

(46) Kennedy, J. P.; Marechal, E. *Carbocationic Polymerization*, 1982.

(47) Wiley, W. C.; McLaren, I. H. *Journal of Mass Spectrometry* **1997**, *32*, 4.

(48) Wiley, W. C.; McLaren, I. H. *Review of Scientific Instruments* **1955**, *26*, 1150.

(49) Rusyniak, M. Cluster Ion Mobility, Structures, and Binding Energy: Application to the Benzene Cluster System. PhD, Virginia Commonwealth University, 2003.

(50) El-Shall, M. S.; Daly, G. M.; Wright, D. *Journal of Chemical Physics* **2002**, *116*, 10253.

(51) Daly, G. M.; Wright, D.; El-Shall, M. S. *Chemical Physics Letters* **2000**, *331*, 47.

(52) J.B.Anderson; D.P.Wegener; O.F.Hagena *Molecular Beams and Low Density Gasdynamics,*, 1971.

(53) Hercules, D. M.; Day, R. J.; Balasanmugam, K.; Li, C. P. *Analytical Chemistry* **1982**, *54*, 280A.

(54) Ibrahim, Y. M.; Alsharaeh, E. H.; El-Shall, M. S. *Journal of Physical Chemistry B* **2004**, *108*, 3959.

(55) El-Shall, M. S.; Li, S. *Advances in Metal and Semiconductor Clusters* **1998**, *4*, 115.

(56) McDaniel, E. W.; Mason, E. A. *The Mobility and Diffusion of Ions in Gases*; John Wiley & Sons: New York, 1973.

(57) Maxton, P. M.; Schaeffer, M. W.; Felker, P. M. *Chemical Physics Letters* **1995**, *241*, 603.

(58) Hirschfelder, J. O.; Curtiss, C. F.; Bird, R. B. *Molecular theory of Gases and Liquids*; Wiley: New York, 1954.

(59) von Helden, G.; Hsu, M.-T.; Kemper, P. R.; Bowers, M. T. *Journal of Chemical Physics* **1991**, *95*, 3835.

(60) Jarrold, M. F. *Journal of Physical Chemistry* **1995**, *99*, 11.

(61) M. J. Frisch, G. W. T., H. B. Schlegel, G. E. Scuseria, ; M. A. Robb, J. R. C., V. G. Zakrzewski, J. A. Montgomery, Jr., ; R. E. Stratmann, J. C. B., S. Dapprich, J. M. Millam, ; A. D. Daniels, K. N. K., M. C. Strain, O. Farkas, J. Tomasi, ; V. Barone, M. C., R. Cammi, B. Mennucci, C. Pomelli, C. Adamo, ; S. Clifford, J. O., G. A. Petersson, P. Y. Ayala, Q. Cui, ; K. Morokuma, N. R., P. Salvador, J. J. Dannenberg, D. K. Malick, ; A. D. Rabuck, K. R., J. B. Foresman, J. Cioslowski, ; J. V. Ortiz, A. G. B., B. B. Stefanov, G. Liu, A. Liashenko, ; P. Piskorz, I. K., R. Gomperts, R. L. Martin, D. J. Fox, ; T. Keith, M. A. A.-L., C. Y. Peng, A. Nanayakkara, M. Challacombe, ; P. M. W. Gill, B. J., W. Chen, M. W. Wong, J. L. Andres, ; C. Gonzalez, M. H.-G., E. S. Replogle, and J. A. Pople. Gaussian98; Gaussian, Inc.: Pittsburgh PA, 2002.

(62) Alsharaeh, E.; El-Shall, M. S. *Abstracts of Papers, 225th ACS National Meeting, New Orleans, LA, United States, March 23-27, 2003* **2003**, PHYS.

(63) Shvartsburg, A. A.; Jarrold, M. F. *Chemical Physics Letters* **1996**, *261*, 86.

(64) Pryor, W. A.; Fiske, T. R. *Macromolecules* **1969**, *2*, 62.

(65) Chong, Y. K.; Rizzardo, E.; Solomon, D. H. *Journal of the American Chemical Society* **1983**, *105*, 7761.

(66) Johns, S. R.; Rizzardo, E.; Solomon, D. H.; Willing, R. I. *Makromolekulare Chemie, Rapid Communications* **1983**, *4*, 29.

(67) Dugourd, P.; Hudgins, R. R.; Clemmer, D. E.; Jarrold, M. F. *Review of Scientific Instruments* **1997**, *68*, 1122.

(68) Kennedy, J. P. M., E. *Carbocationic Polymerization*; John Wiley & Sons: New York,, 1982.

(69) Gidden, J.; Bowers, M. T.; Jackson, A. T.; Scrivens, J. H. *Journal of the American Society for Mass Spectrometry* **2002**, *13*, 499.

(70) El-Shall, M. S. *Proceedings of the Science and Technology of Atomically Engineered Materials, Richmond, Oct. 30-Nov. 4, 1995* **1996**, 67.

(71) Wilkinson, G.; Rosenblum, M. W.; Woodward, R. B. *Journal of the American Chemical Society* **1952**, *74*, 2125.

(72) Fischer, E. O.; Pfab, W. *Zeitschrift fuer Naturforschung, B: Chemical Sciences* **1952**, *7*, 377.

(73) Meyer, F.; Khan, F. A.; Armentrout, P. B. *Journal of the American Chemical Society* **1995**, *117*, 9740

(74) Afzaal, S.; Freiser, B. S. *Chemical Physics Letters* **1994**, *218*, 254.

(75) Chen, Y.-M.; Armentrout, P. B. *Chemical Physics Letters* **1993**, *210*, 123.

(76) van Heijnsbergen, D.; Jaeger, T. D.; von Helden, G.; Meijer, G.; Duncan, M. A. *Chemical Physics Letters* **2002**, *364*, 345.

(77) van Heijnsbergen, D.; von Helden, G.; Meijer, G.; Maitre, P.; Duncan, M. A. *Journal of the American Chemical Society* **2002**, *124*, 1562.

(78) Duncan, M. A. *International Reviews in Physical Chemistry* **2003**, *22*, 407.

(79) Duncan, M. A., Jr. *Abstracts of Papers, 226th ACS National Meeting, New York, NY, United States, September 7-11, 2003* **2003**.

(80) Buchanan, J. W.; Grieves, G. A.; Reddic, J. E.; Duncan, M. A. *International Journal of Mass Spectrometry* **1999**, *182/183*, 323.

(81) Willey, K. F.; Cheng, P. Y.; Bishop, M. B.; Duncan, M. A. *Journal of the American Chemical Society* **1991**, *113*, 4721.

(82) Bauschlicher, C. W., Jr.; Partridge, H.; Langhoff, S. R. *Journal of Physical Chemistry* **1992**, *96*, 3273.

(83) Hoshino, K.; Kurikawa, T.; Takeda, H.; Nakajima, A.; Kaya, K. *Journal of Physical Chemistry* **1995**, *99*, 3053.

(84) Yasuike, T.; Nakajima, A.; Yabushita, S.; Kaya, K. *Journal of Physical Chemistry A* **1997**, *101*, 5360.

(85) Kurikawa, T.; Takeda, H.; Nakajima, A.; Kaya, K. *Zeitschrift fuer Physik D: Atoms, Molecules and Clusters* **1997**, *40*, 65.

(86) Kurikawa, T.; Negishi, Y.; Hayakawa, F.; Nagao, S.; Miyajima, K.; Nakajima, A.; Kaya, K. *Journal of the American Chemical Society* **1998**, *120*, 11766.

(87) Miyajima, K.; Kurikawa, T.; Hashimoto, M.; Nakajima, A.; Kaya, K. *Chemical Physics Letters* **1999**, *306*, 256.

(88) Kurikawa, T.; Takeda, H.; Hirano, M.; Judai, K.; Arita, T.; Nagao, S.; Nakajima, A.; Kaya, K. *Organometallics* **1999**, *18*, 1430.

(89) Nagao, S.; Kato, A.; Nakajima, A.; Kaya, K. *Transactions of the Materials Research Society of Japan* **2000**, *25*, 959.

(90) Nagao, S.; Kato, A.; Nakajima, A.; Kaya, K. *Journal of the American Chemical Society* **2000**, *122*, 4221.

(91) Nakajima, A.; Kaya, K. *Journal of Physical Chemistry A* **2000**, *104*, 176.

(92) Nakajima, A.; Kaya, K. *NATO Science Series, II: Mathematics, Physics and Chemistry* **2002**, *57*, 173.

(93) Miyajima, K.; Muraoka, K.; Hashimoto, M.; Yasuike, T.; Yabushita, S.; Nakajima, A.; Kaya, K. *Journal of Physical Chemistry A* **2002**, *106*, 10777.

(94) Weis, P.; Kemper, P. R.; Bowers, M. T. *Journal of Physical Chemistry A* **1997**, *101*, 8207.

(95) Martin, T. P. B., T.; Gohlich, H.; Lange, T. *J. Phys. Chem* **1991**, *95*, 6421.

(96) Ingolfsson, O. W., A. M. *Journal of Chemical Physics* **2002**, *117*, 3721.

(97) van de Waal, B. W. *Journal of Chemical Physics* **1983**, *79*, 3948.

(98) van de Waal, B. W. *Chemical Physics Letters* **1986**, *123*, 69.

(99) Srinivas, R.; Hrusak, J.; Suelzle, D.; Boehme, D. K.; Schwarz, H. *Journal of the American Chemical Society* **1992**, *114*, 2802.

(100) Rodgers, M. T.; Stanley, J. R.; Amunugama, R. *Journal of the American Chemical Society* **2000**, *122*, 10969.

(101) Rodgers, M. T.; Armentrout, P. B. *Mass Spectrometry Reviews* **2000**, *19*, 215.

(102) Ibrahim, Y. Ion Mobility Studies of The Electronic States of Transition Metal Cations and Ion-Molecules Reactions, Virginia Commonwealth university, 2003.

(103) Soep, B.; Elhanine, M.; Schulz, C. P. *Chemical Physics Letters* **2000**, *327*, 365.

(104) Misaizu, F.; Sanekata, M.; Fuke, K.; Iwata, S. *Journal of Chemical Physics* **1994**, *100*, 1161.

(105) Sanekata, M.; Misaizu, F.; Fuke, K.; Iwata, S.; Hashimoto, K. *Journal of the American Chemical Society* **1995**, *117*, 747.

(106) Watanabe, H.; Iwata, S.; Hashimoto, K.; Misaizu, F.; Fuke, K. *Journal of the American Chemical Society* **1995**, *117*, 755.

(107) Harms, A. C.; Khanna, S. N.; Chen, B.; Castleman, A. W., Jr. *Journal of Chemical Physics* **1994**, *100*, 3540.

(108) Berg, C.; Beyer, M.; Achatz, U.; Joos, S.; Niedner-Schatteburg, G.; Bondybey, V. E. *Chemical Physics* **1998**, *239*, 379.

(109) Uppal, J. S.; Staley, R. H. *Journal of the American Chemical Society* **1982**, *104*, 1229.

(110) Woodward, C. A.; Dobson, M. P.; Stace, A. J. *Journal of Physical Chemistry A* **1997**, *101*, 2279.

(111) Lu, W.; Yang, S. *Journal of Physical Chemistry A* **1998**, *102*, 825.

(112) Kaya, T.; Horiki, Y.; Kobayashi, M.; Shinohara, H.; Sato, H. *Chemical Physics Letters* **1992**, *200*, 435.

(113) Lide, D. R.; Editor *Handbook of Chemistry and Physics: 77th Edition*, 1996.

(114) Operti, L.; Tews, E. C.; MacMahon, T. J.; Freiser, B. S. *Journal of the American Chemical Society* **1989**, *111*, 9152.

(115) Operti, L.; Tews, E. C.; Freiser, B. S. *Journal of the American Chemical Society* **1988**, *110*, 3847.

(116) Moore, C. E. *U.S. Natl. Bur. Standards Circ.* **1949**, *467*, 309 pp.

(117) Andersen, A.; Muntean, F.; Walter, D.; Rue, C.; Armentrout, P. B. *Journal of Physical Chemistry A* **2000**, *104*, 692.

(118) Donnelly, S. G.; Schmuttenmaer, C. A.; Qian, J.; Farrar, J. M. *Journal of the Chemical Society, Faraday Transactions* **1993**, *89*, 1457.

(119) Donnelly, S. G.; Farrar, J. M. *Journal of Chemical Physics* **1993**, *98*, 5450.

(120) Dalleska, N. F. T., B. L.; Armentrout, P. B. *Journal of Physical Chemistry* **1994**, *98*, 4191.

APPENDIX A

Water Clusters Containing Metal Cations

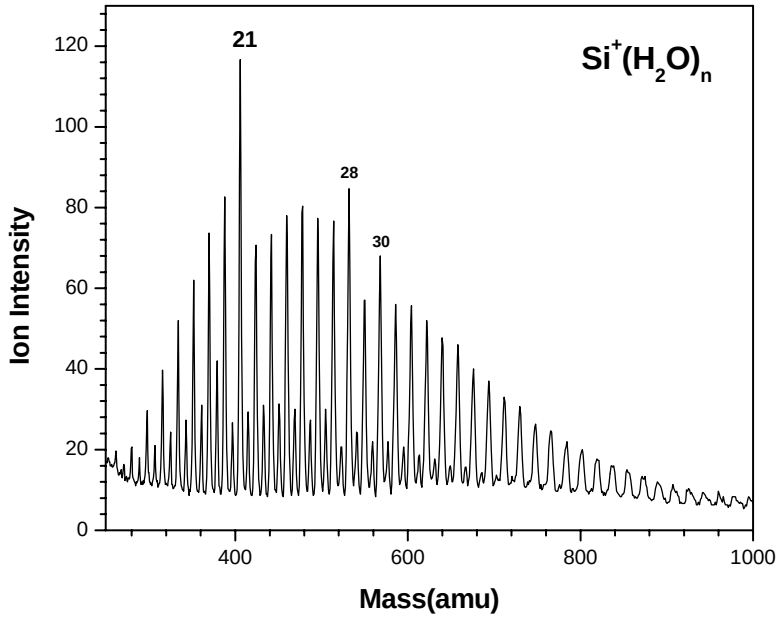

Figure 81: TOF mass spectra of $Si^+(H_2O)_n$

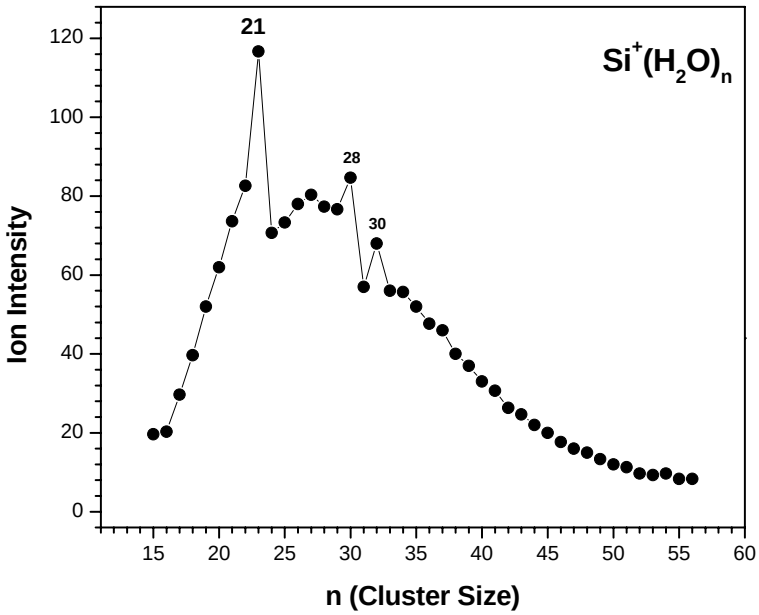

Figure 82: $Si^+(H_2O)_{n,}$ ion intensity distribution as a function of cluster size

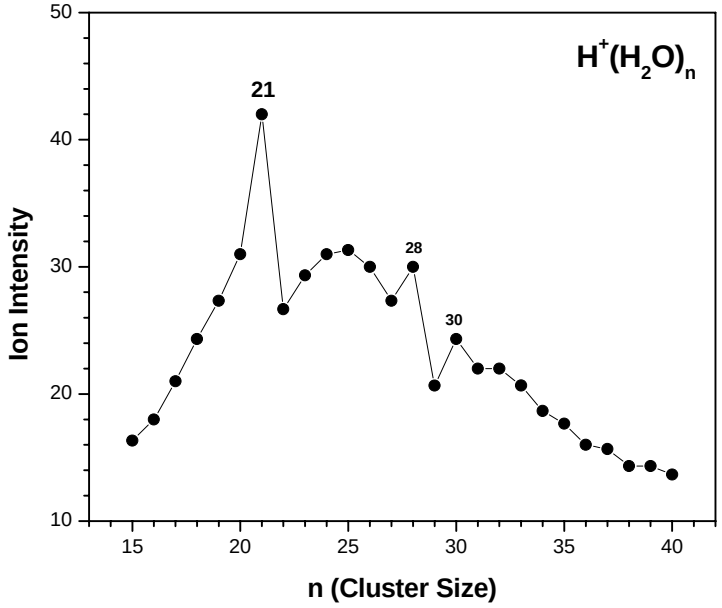

Figure 83: $H^+(H_2O)_{n,}$ ion intensity distribution as a function of cluster size

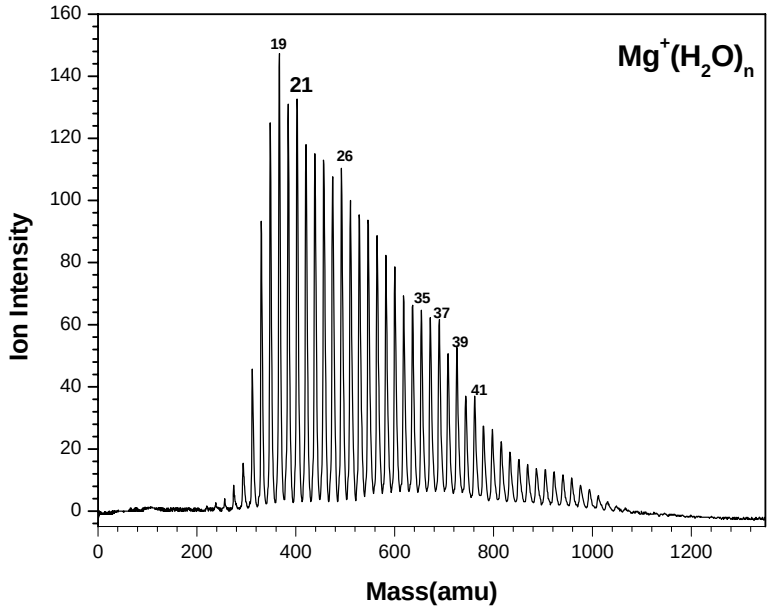

Figure 84: TOF mass spectra of $Mg^{+}(H_2O)_n$

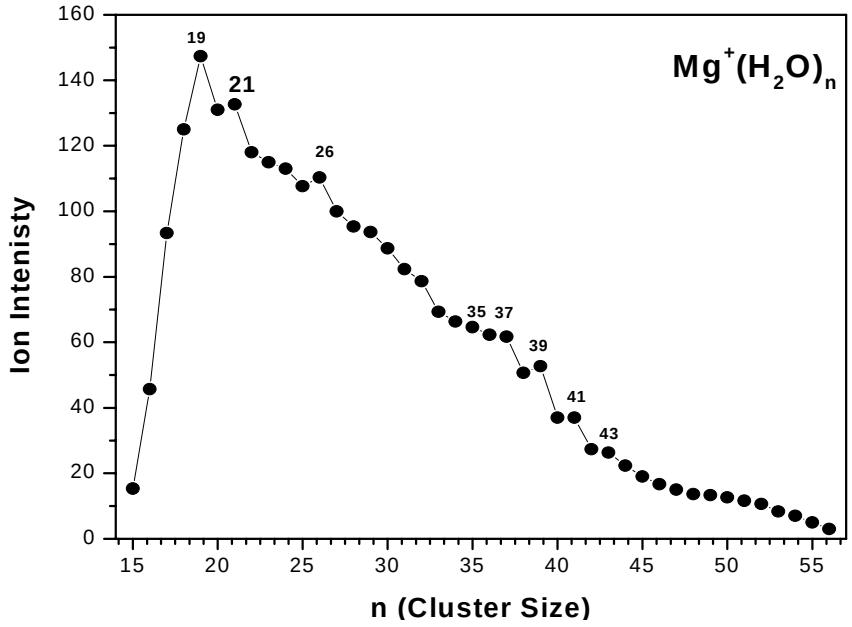

Figure 85: $Mg^{+}(H_2O)_{n,}$ ion intensity distribution as a function of cluster size

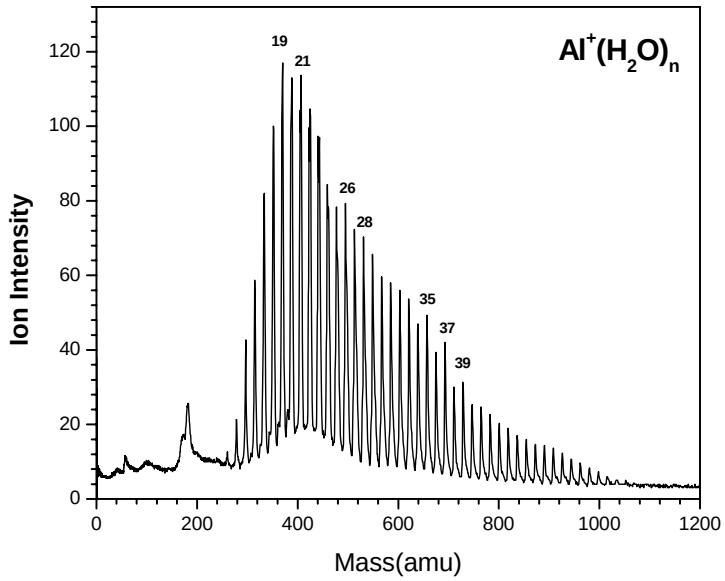

Figure 86: TOF mass spectra of $Al^+(H_2O)_n$

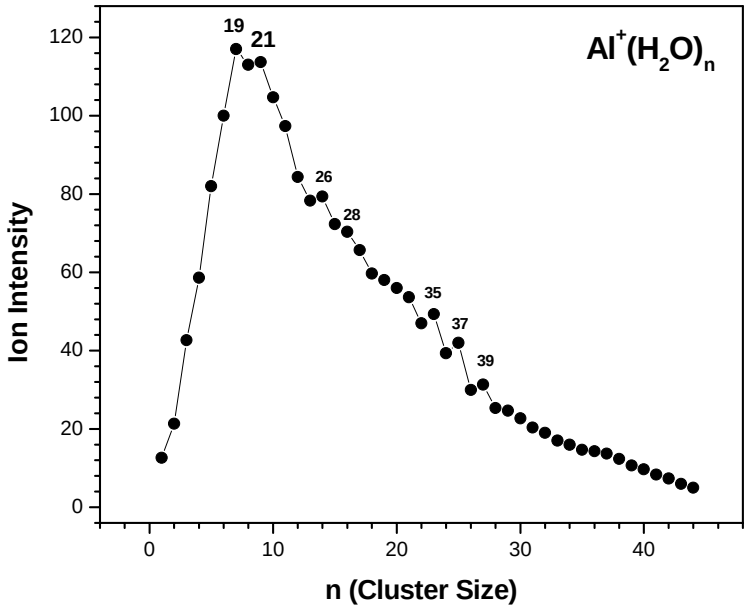

Figure 87: $Al^+(H_2O)_{n,}$ ion intensity distribution as a function of cluster size.

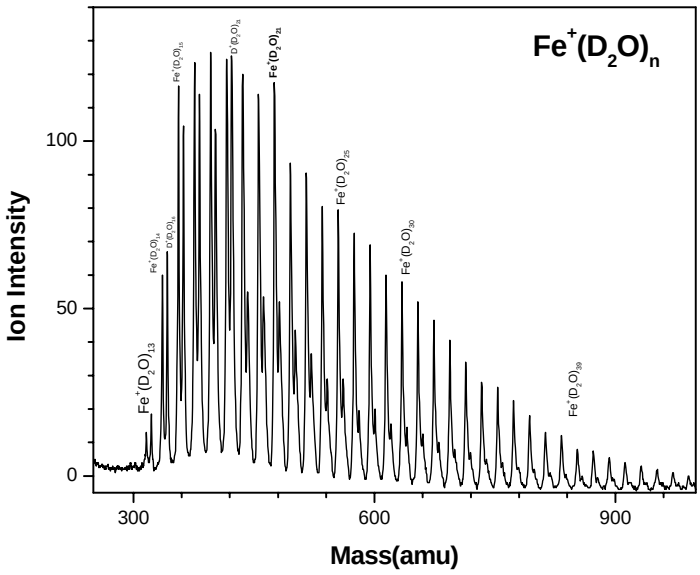

Figure 88: TOF mass spectra of $Fe^{+}(D_2O)_n$

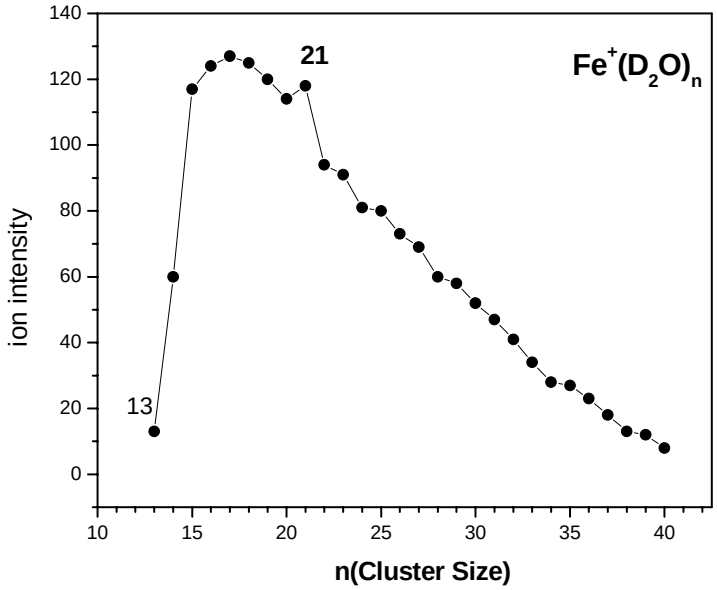

Figure 89: $Fe^{+}(D_2O)_{n,}$ ion intensity distribution as a function of cluster size

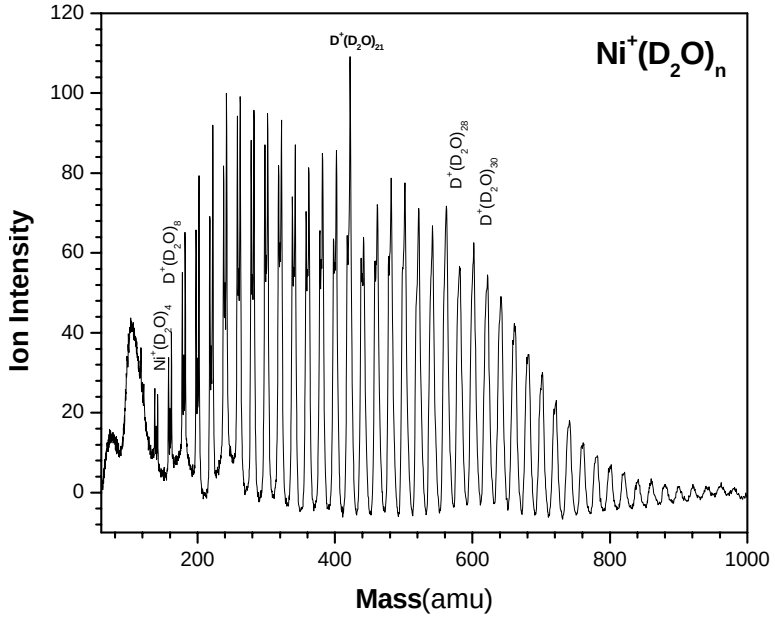

Figure 90: TOF mass spectra of $Ni^{+}(D_2O)_n$

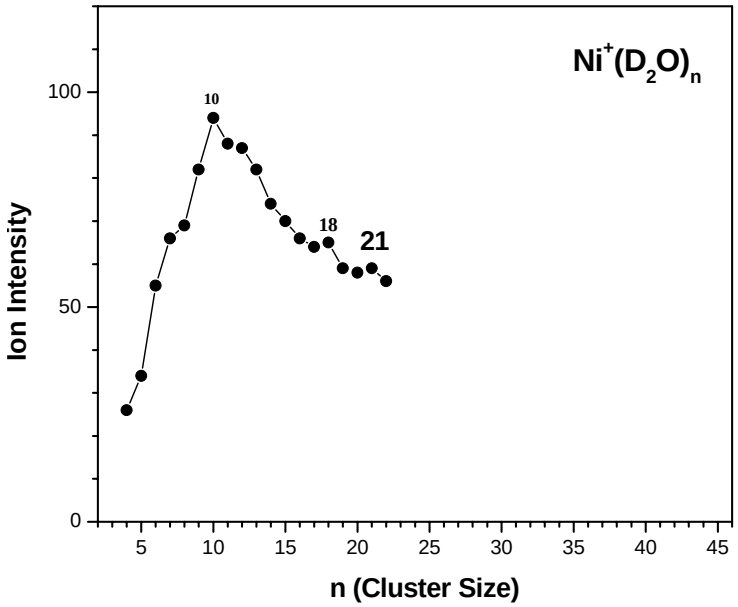

Figure 91: $Ni^{+}(D_2O)_n$, ion intensity distribution as a function of cluster size

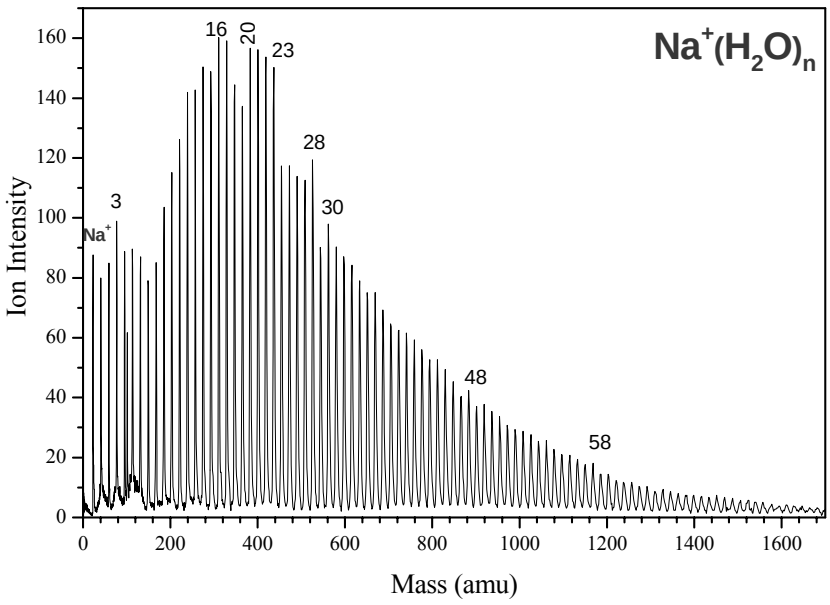

Figure 92: TOF mass spectra of $Na^+(H_2O)_n$

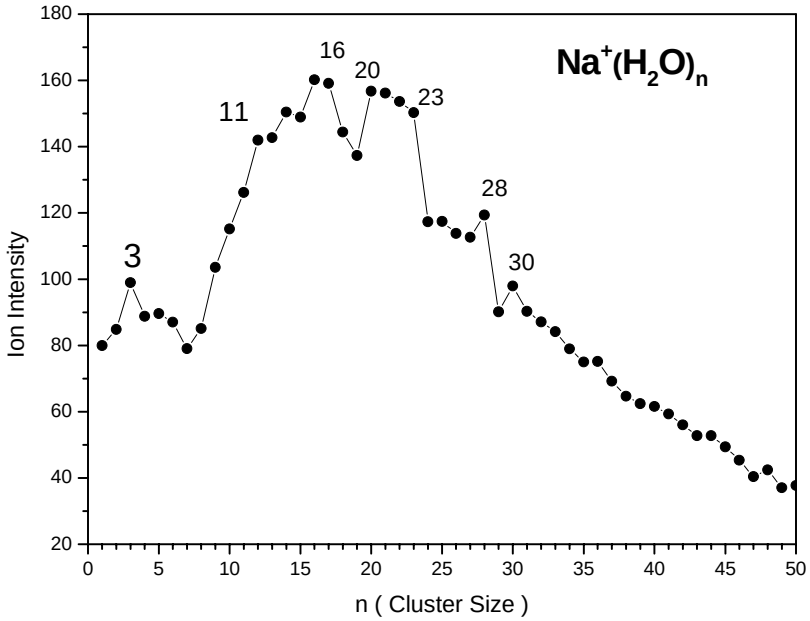

Figure 93: $Na^+(H_2O)_n$, ion intensity distribution as a function of cluster size

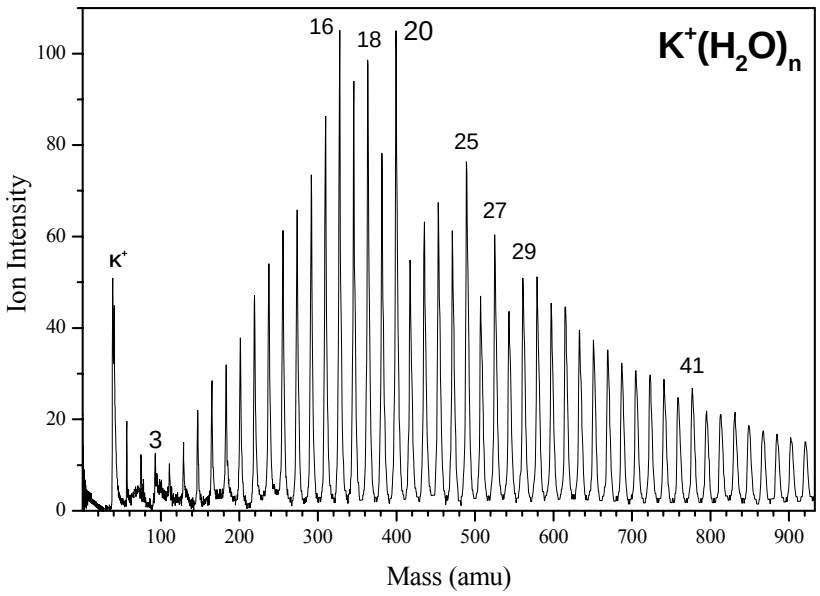

Figure 94: TOF mass spectra of $K^+(H_2O)_n$

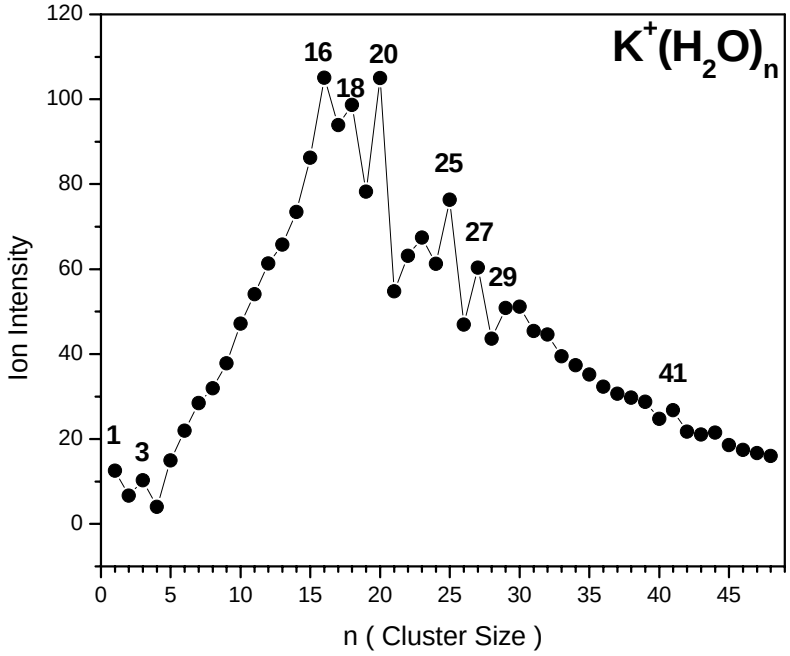

Figure 95: $K^+(H_2O)_n$, ion intensity distribution as a function of cluster size

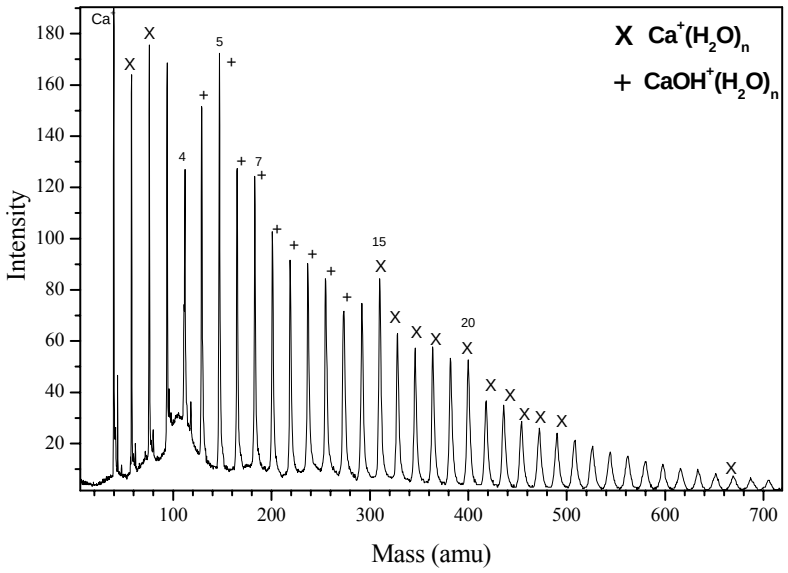

Figure 96: TOF mass spectra of $Ca^{+}(H_2O)_n$

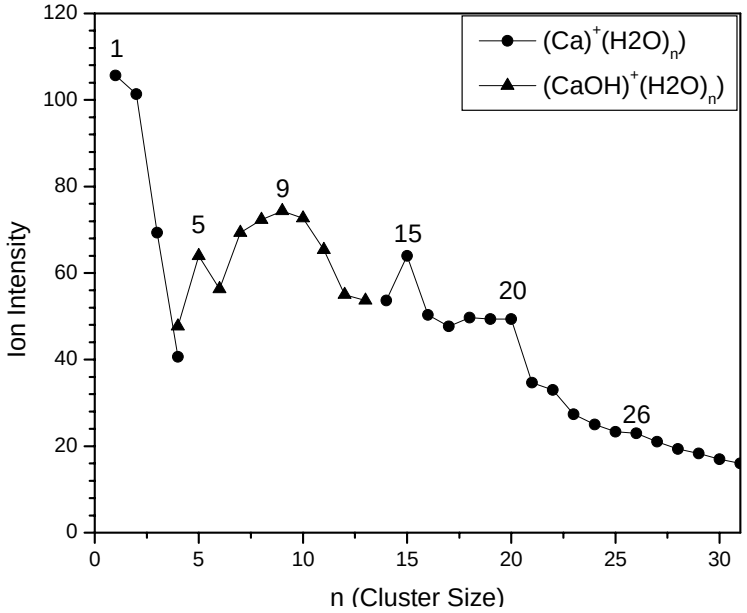

Figure 97: $Ca^{+}(H_2O)_{n,}$ ion intensity distribution as a function of cluster size

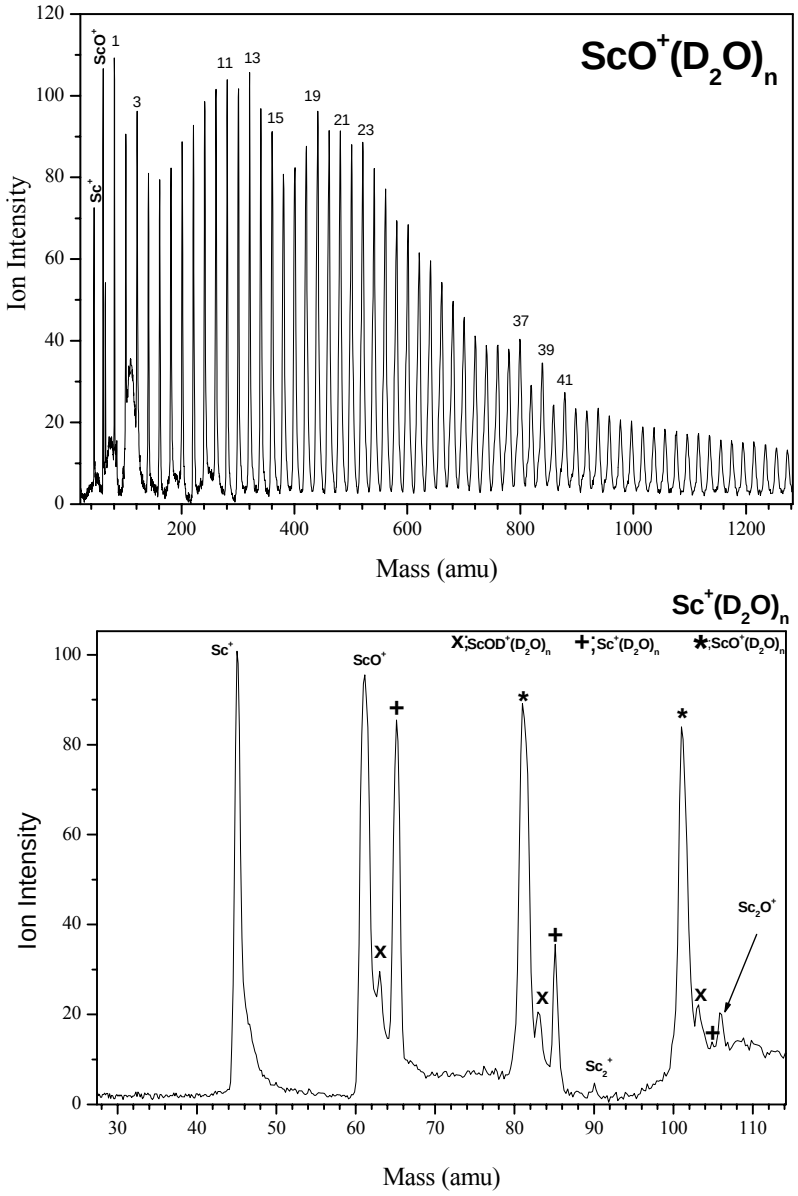

Figure 98: TOF mass spectra of $Sc^{+}(D_2O)_n$

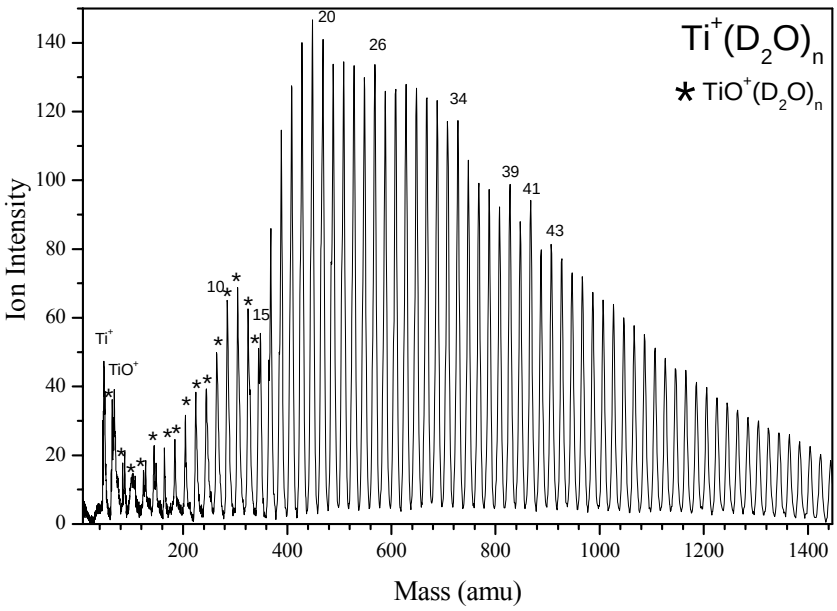

Figure 99: TOF mass spectra of $Ti^{+}(D_2O)_n$

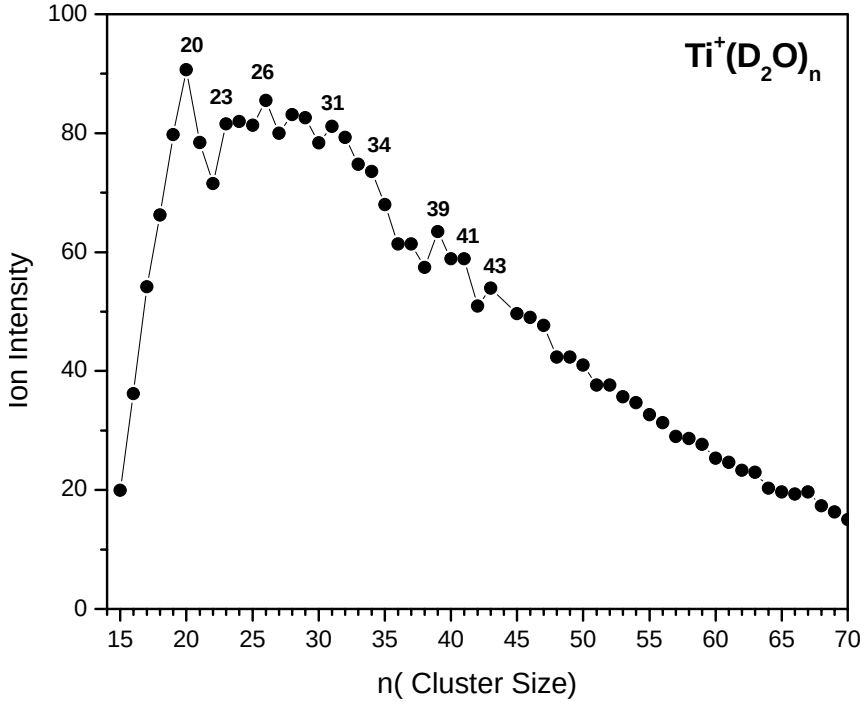

Figure 100: $Ti^{+}(D_2O)_{n,}$ ion intensity distribution as a function of cluster size.

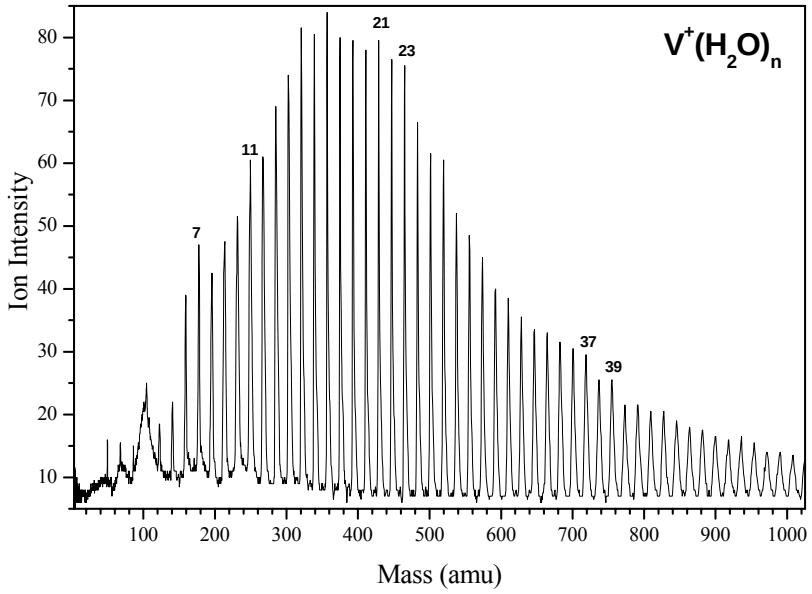

Figure 101: TOF mass spectra of $V^+(H_2O)_n$.

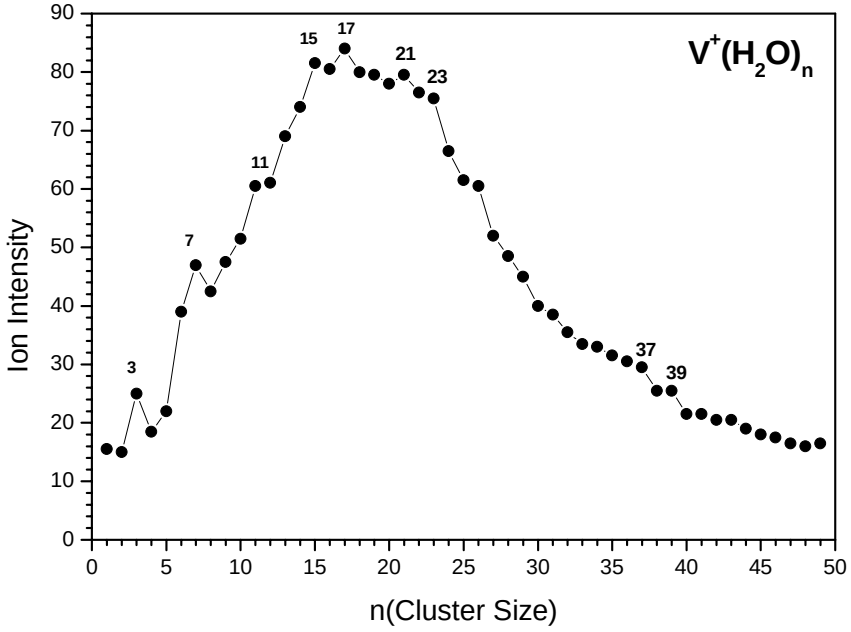

Figure 102: $V^+(H_2O)_n$, ion intensity distribution as a function of cluster size.

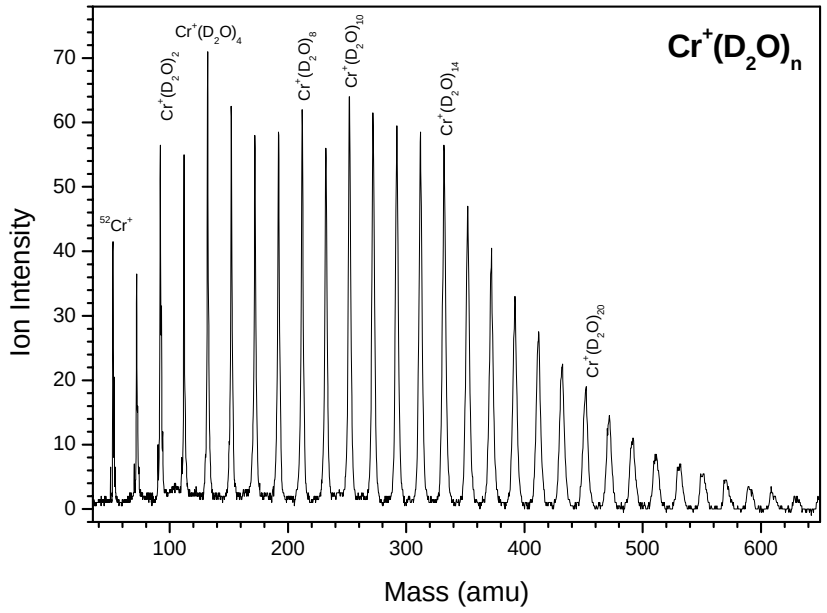

Figure 103: TOF mass spectra of $Cr^{+}(D_2O)_n$.

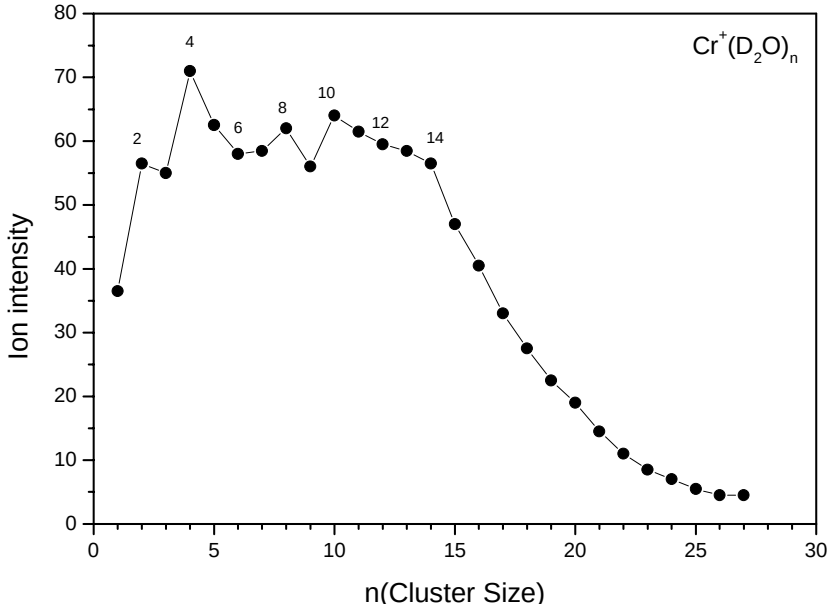

Figure 104: $Cr^{+}(D_2O)_{n,}$ ion intensity distribution as a function of cluster size.

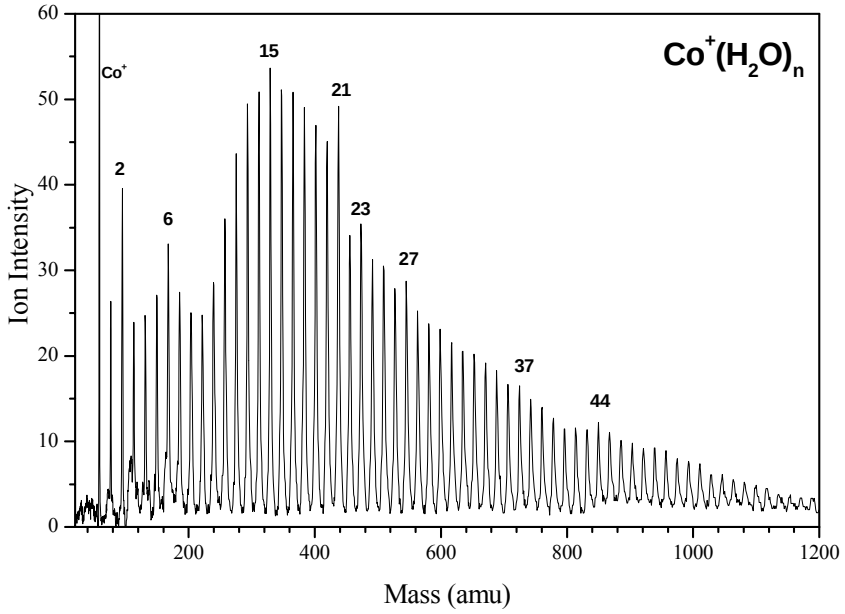

Figure 105: TOF mass spectra of $Co^{+}(H_2O)_n$.

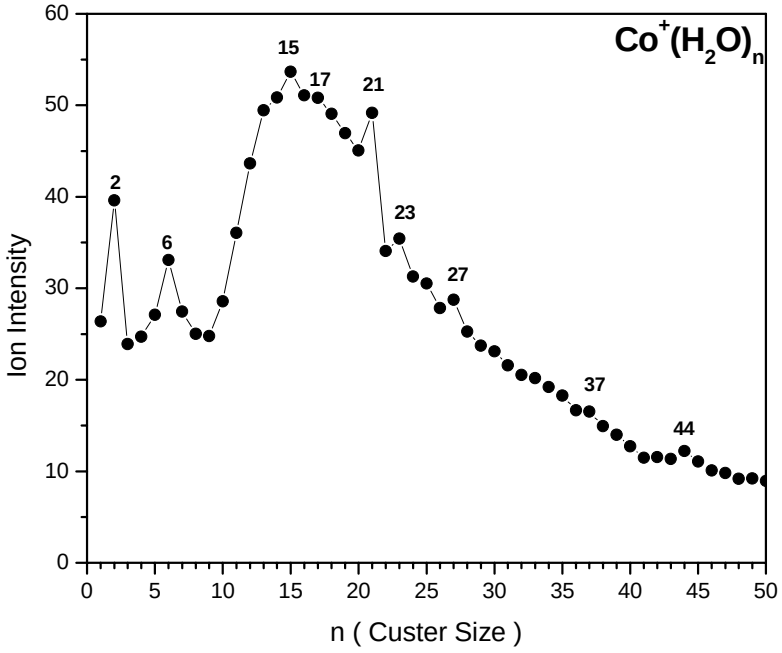

Figure 106: $Cr^{+}(H_2O)_{n,}$ ion intensity distribution as a function of cluster size.

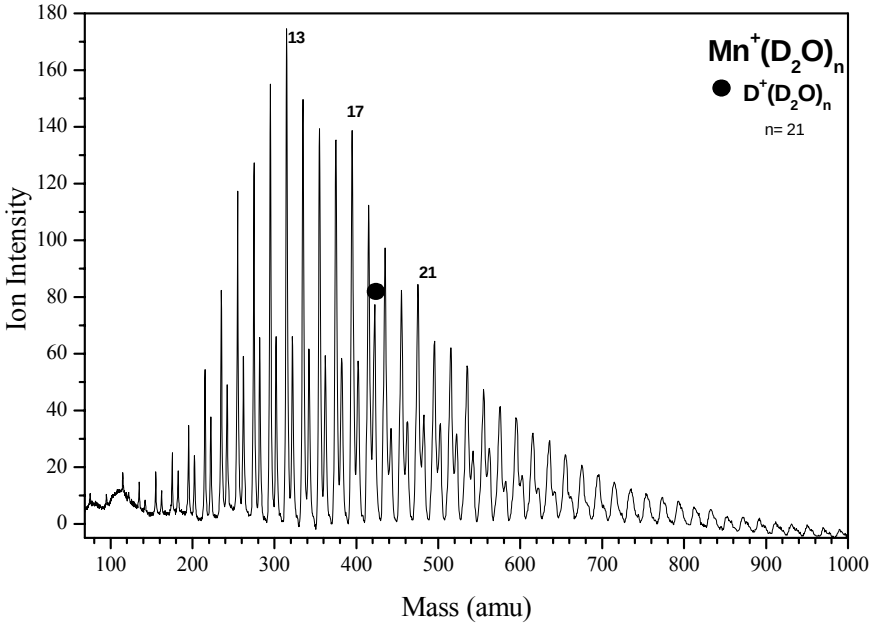

Figure 107: TOF mass spectra of $Mn^{+}(D_2O)_n$.

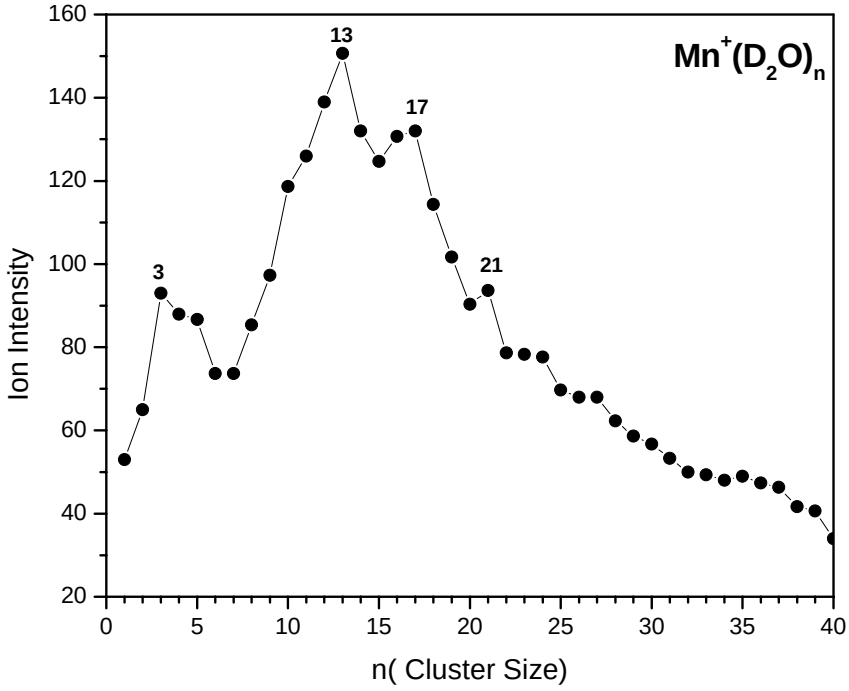

Figure 108: $Mn^{+}(D_2O)_{n,}$ ion intensity distribution as a function of cluster size.

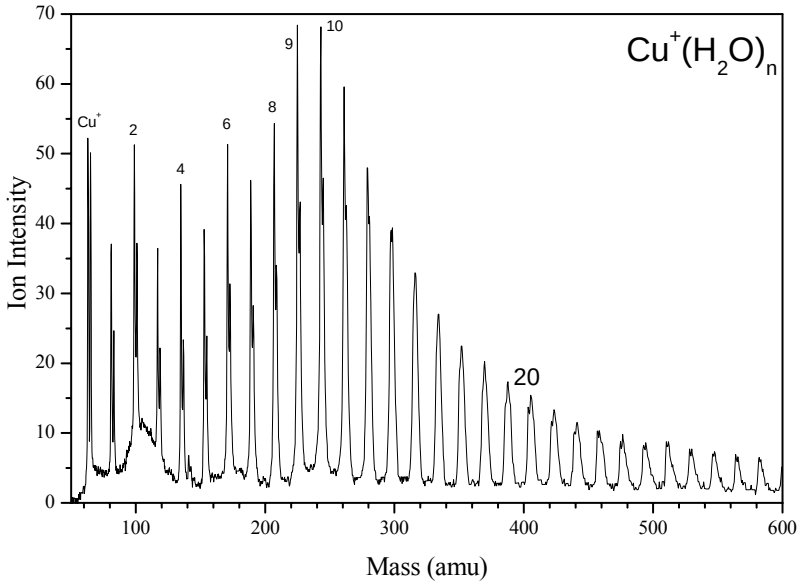

Figure 109: TOF mass spectra of $Cu^{+}(H_2O)_n$

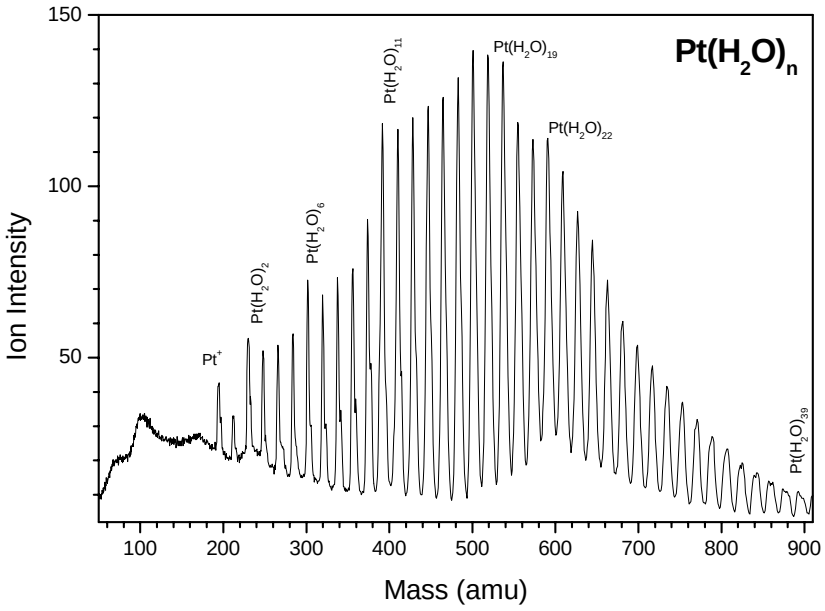

Figure 110: TOF mass spectra of $Pt^{+}(H_2O)_n$

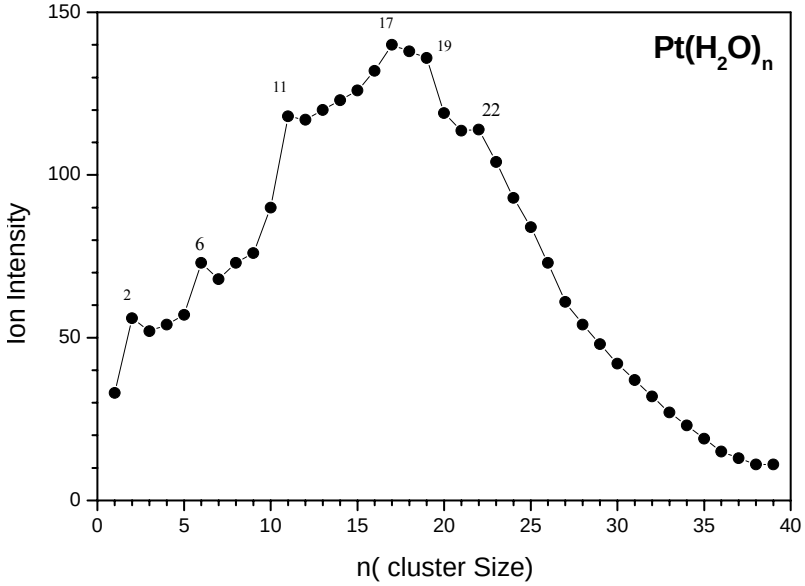

Figure 111: $Pt^{+}(H_2O)_{n,}$ ion intensity distribution as a function of cluster size.

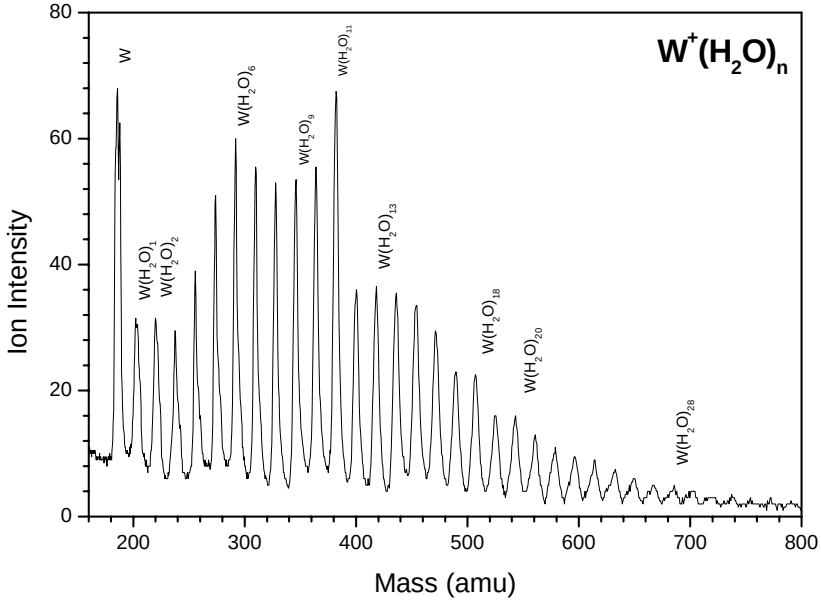

Figure 112: TOF mass spectra of $W^{+}(H_2O)_n$

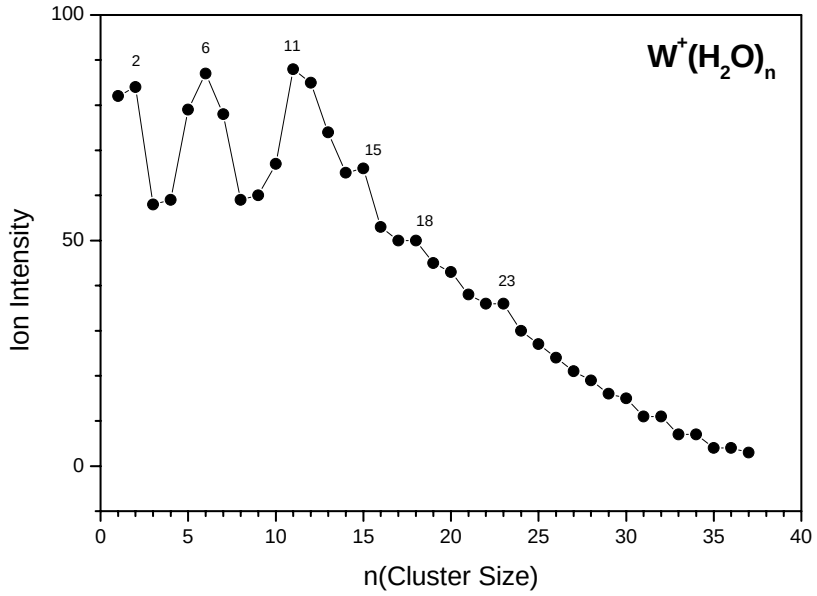

Figure 113: $W^{+}(H_2O)_{n,}$ ion intensity distribution as a function of cluster size.

VITA

Edreese Housni Alsharaeh was born on December 16, 1971 in Irbid, Jordan. He earned his B. Sc. in Chemistry from Jordan University of Science and Technology, and his M. Sc. in Organic Chemistry on 1997. Since 1999, he is pursuing his Ph. D. degree in Physical Chemistry from Virginia Commonwealth University

EDUCATION

1999 - present	**Virginia Commonwealth University**, Richmond, VA Ph.D. candidate in Physical Chemistry –(Anticipated): Decembert /2004 Advisor - Dr. M. Samy El-Shall GPA: 3.89
1994 - 1997	**Tennessee State University**, Nashville, TN. M.S Degree - December 1997 " Synthesis and Characterization of Copolymer polyvinylidene Chloride, Methyl Methylacrylate, and Itaconic Acid" Advisor: Dr. Edward Covington GPA: 3.5
1989 - 1993	**Jordan University of Science and Technology**, Irbid, Jordan Bachelor of Science, Major: Chemistry, August, 1993

TEACHING EXPERIENCE

1999 - present	**Teaching Assistant**, **Virginia Commonwealth University**, Richmond, VA Instructor of General Chemistry recitation 101, 102 level, Physical, Analytical chemistry and Instrumental Analysis Laboratories 300 and 400 levels
1995 - 1997	Teaching Assistant, Tennessee State University, Nashville, TN

RESEARCH EXPERIENCE

1999-present Research involves structural information, mechanism of formation and the observed fragmentation pathway of the growing styrene Oligomers via thermally self-initiated polymerization in the gas phase. In addition, the research involves reactions and solvations of Atomic Metal Cations within Molecular Clusters and Mass Selected-Cluster Ion Mobility Mass Spectrometer for structural characterizations and binding energies of gas phase molecular cluster ions. This involves a variety of experimental techniques (molecular beams, lasers, electron impact, Time of flight, CID, Quadruple and Ion mobility mass spectrometry (MS/MS).

994 –1997 Research on the synthesis and characterization of co-polymers, using DSC and FTIR. **Tennessee State University**, Nashville, TN

Summer 1992 Internship with **Jordan Oil Refinery** CO.LTD. Research and development Laboratories.

AWARDS

Virginia Commonwealth University Fellowship, 2003/2004
Graduate Teaching Assistantship, 1999/2003
Graduate School Research Fellowship (2004)

AFFILIATION

American Chemical Society

Publications:

1. M. Samy El-Shall, Victor Abdelsayed, Yezdi B. Pithawalla, **Edreese Alsharaeh**, and Seetharama C. Deevi, "Vapor Phase Growth and Assembly of Metallic, Intermetallic, Carbon, and Silicon Nanoparticle Filaments", J. Phys. Chem. B, 2003, 107: 2882-2886.

2. Rusyniak, M., Ibrahim, Y., **Alsharaeh, E**., Moet-Ner (Mautner) M. and El-Shall, M. S "Mass -Selected Ion Mobility Studies of the isomerization of the Benzene Radical cation and Binding Energy of the Benzene Dimer Cation. Separation of Isomeric Ions By Dimer Formation" J. Phys. Chem. A, 2003, 107: 7656-7666.

3. Ibrahim, Y., **Alsharaeh, E.**, Rusyniak, M., Moet-Ner (Mautner)M., Watson, S. and El-Shall, M. S." Separation of Isomers by Dimer Formation : Isomerically Pure benzene$^+$ and Toluene$^+$ Ions, and Their Dimers. *Ab initio* Calculations on $(Benzene)_2^+$": Chem. Phys. Lett. 2003, 380: 21-28.

4. Momoh, Paul O.; El-Shall, Sammy M.; **Alsharaeh, Edreese**. **S**olvated iron and nickel ions, Fe+ (H_2O)n, Ni+ (H_2O)n using time of flight mass spectrometry (TOF-MS). Abstracts of Papers, 223rd ACS National Meeting, Orlando, FL, United States, April 7-11, 2002 (2002),CHED-857.

5 Ibrahim, Y.M., **Alsharaeh, E.H**., and El-Shall, M.S., Evidence for Penning Ionizationin the Generation of Electronically Excited States of Transition Metal Cations by Laser Vaporization. Journal of Physical Chemistry B, 2004. 108(13): p. 3959-62.

6. Ibrahim, Yehia; **Alsharaeh, Edreese;** Dias, Keith; Meot-Ner, Michael; El-Shall, M. Samy.Stepwise Hydration and Multibody Deprotonation with Steep Negative Temperature Dependence in the Benzene$^+$/Water System. Journal of the American Chemical Society (2004), 126(40), 12766-12767

7. **Edreese H. Alsharaeh**, Yehia M. Ibrahim and M. Samy El-Shall, Direct Evidence for the Gas Phase Thermal Polymerization of Styrene. Determination of the Initiation Mechanism and the Structures of the Early Oligomers by Ion Mobility .(submitted to Journal of the American Chemical Society)(communication)

SELECTED PRESENTATIONS:

November 2002" Reactions and Solvations of Atomic Metal Cations within Water and Benzene Clusters"**Edreese Alsharaeh**, M. Samy El-Shall,(Talk). 55th Southeast Regional Meeting of the American Chemical Society, Charleston, SC. Presentation in the Division of Physical Chemistry.

March 2003" Electronic States of Second- Row transition Metal Cations and Ion Mobilities of Metal Cation-Benzene Clusters,"Ibrahim Yehia, **Edreese Alsharaeh**, M. Samy El-Shall,(Poster Presentation). Gordon Research Conference on Gaseous ions: Structures, Energetics & Reactions, Ventura, Ca. March, 2003.

March 2003 **Alsharaeh, E.** and El-Shall, M.S., *Solvation of atomic metal cations within benzene and water clusters.* Abstracts of Papers, 225th ACS National Meeting, New Orleans, LA, United States, March 23-27, 2003, 2003: p. PHYS-510.

November 2004" Reactions and Solvations of Atomic Metal Cations within Water and Benzene Clusters"**Edreese Alsharaeh**, M. Samy El-Shall,(Talk). 57th Southeast Regional Meeting of the American Chemical Society, Durham, NC Presentation in the Division of Physical Chemistry.